Femtosecond Stimulated Resonance Raman Spectroscopy: Towards Mapping the Primary Steps in Biological Photoreceptors

D I S S E R T A T I O N

zur Erlangung des akademischen Grades

(Dr. rer. nat.)
im Fach Chemie

eingereicht an der
Mathematisch-Naturwissenschaftlichen Fakultät I
Humboldt-Universität zu Berlin

von
Dipl.-Chem. Alexander Weigel

Präsident der Humboldt-Universität zu Berlin:
Prof. Dr. Jan-Hendrik Olbertz

Dekan der Mathematisch-Naturwissenschaftlichen Fakultät I:
Prof. Dr. Andreas Herrmann

Gutachter:
1. Prof. Dr. Nikolaus Ernsting
2. Prof. Dr. Peter Hildebrandt
3. Prof. Dr. Klaus Rademann

eingereicht am: 23. Dezember 2010
Tag der mündlichen Prüfung: 17. Februar 2011

Für meine Eltern und für Alexandra.

„Es gibt ein großes und doch ganz alltägliches Geheimnis. Alle Menschen haben daran teil, jeder kennt es, aber die wenigsten denken je darüber nach. Die meisten Leute nehmen es einfach so hin und wundern sich kein bißchen darüber. Dieses Geheimnis ist die Zeit."

(*Momo*, Michael Ende)

Abstract

Femtosecond Stimulated Raman Spectroscopy is a powerful tool that allows to study the vibrational evolution of an excited chromophore directly in time. One perspective of this method is the elucidation of structural relaxation in biological photoreceptors. In this work the technique was built up and advanced towards applications to flavin-based proteins.

Tunable Raman pulses were generated in a newly developed narrowband optical parametric amplifier (*nb*-OPA). These pulses provided the basis for transient Raman measurements with ~ 10 cm^{-1} spectral and 50–100 fs temporal resolution. The signal/noise ratio in these experiments allows to increase the number of transient spectra collected, by more than a factor of 10 compared to previous work.

Resonance conditions strongly affect the appearance of the stimulated Raman spectra from an electronically excited state. The tunable Raman source was used to explore this effect to find optimal conditions. The charactistic spectral shape under typical resonance conditions was reproduced by simulations.

Excited-state dynamics were first investigated for the model photoswitch **stilbene**, starting from both the *cis* and the *trans* isomers. Decay, spectral shift, and narrowing of individual bands provided insight into the vibrational relaxation of the excited chromophore. Wavepacket motion was seen as oscillations of the Raman bands, and evidence for anharmonic coupling between different modes was found.

Another chromophore that undergoes isomerization upon light excitation is the **"parent" cyanine**, 1,1'-diethyl-2,2'-pyrido cyanine iodide (PC). For this molecule the isomerization reaction could be followed to the ground state. From a global data analysis Raman spectra were obtained for the Franck-Condon region, the intermediately populated hot ground state, and the isomerization products.

As a basis for experiments on flavoproteins the excited-state properties of the **pure flavin chromophore** were studied in solution. Transient absorption and fluorescence experiments suggest an influence of dynamic polar solvation on the electronic properties of the excited state, and solvent-controled $\pi\pi^*$-nπ^* coupling is offered as an explanation. Raman spectra from the flavin excited state were recorded and the vibrational bands assigned. Population depletion by the Raman pulse was identified as a potential artefact in time-dependent measurements, but the effect was also used to mark wavepacket motion in the excited state.

The application of the developed femtosecond stimulated Raman spectrometer to biological samples is demonstrated in a first FSRS experiment on **glucose oxidase** as a model flavoprotein. Spectra from the excited state were recorded, and the spectral evolution was followed in time. With transient absorption spectroscopy the BlrB-L66F and Slr1694-Y8F **BLUF** (Blue Light Using FAD) photoreceptor mutants were studied; signaling state formation and flavin reduction by a semiconserved tryptophan were seen, respectively.

Zusammenfassung

Femtosekundenaufgelöste Stimulierte Raman-Spektroskopie (FSRS) ist ein leistungsfähiges Werkzeug, das es erlaubt, die Schwingungsentwicklung eines angeregten Chromophors in Echtzeit zu studieren. Eine Perspektive dieser Methode ist die Aufklärung struktureller Relaxation in biologischen Photorezeptoren. In dieser Arbeit wurde die Technik aufgebaut und weiterentwickelt, hin zu einer Anwendung auf flavinbasierte Photorezeptoren.

Durchstimmbare Ramanimpulse wurden in einem neu entwickelten schmalbandigen optisch-parametrischen Verstärker erzeugt und bildeten die Grundlage für transiente Ramanmessungen mit einer spektralen Auflösung von $\sim$ 10 cm^{-1} und einer zeitlichen Auflösung von 50–100 fs. Das Signal/Rausch-Verhältnis in diesen Experimenten erlaubt es, die Anzahl von Spektren in einer zeitaufgelösten Messung um mehr als einen Faktor zehn gegenüber vorherigen Arbeiten zu erhöhen.

Die **Resonanzbedingungen** beeinflussen stark das Erscheinungsbild von stimulierten Ramanspektren aus einem elektronisch angeregten Zustand. Die durchstimmbare Ramanquelle wurde dazu genutzt, diesen Effekt zu erforschen, um optimale Bedingungen zu finden. Die charakteristische spektrale Linienform wurde für typische Resonanzbedingungen mit Simulationen reproduziert.

Angeregte-Zustandsdynamik wurde zuerst für den Modellphotoschalter **Stilben** untersucht, ausgehend sowohl vom *cis*-, als auch vom *trans*-Isomer. Anhand der Intensitätsabnahme des Signals sowie der spektralen Verschiebung und Bandenverschmälerung konnten Einblicke in die Schwingungsrelaxation des angeregten Chromophors erhalten werden. Wellenpaketbewegung wurde als Oszillation der Ramanbanden beobachtet, und Anzeichen für die anharmonische Kopplung zwischen Moden wurden gefunden.

Ein weiterer Chromophor, der unter Lichteinwirkung isomerisiert, ist das **„Mutter"-Cyanin** 1,1'-Diethyl-2,2'-pyridocyaniniodid (PC). Für dieses Molekül konnte die Isomierungsreaktion in den Grundzustand hinein verfolgt werden. Aus einer globalen Datenanalyse wurden Ramanspektren des Franck-Condon-Zustandes, des intermediär bevölkerten heissen Grundzustandes und der Isomerisierungsprodukte erhalten.

Als Grundlage für Experimente an Flavoproteinen wurden die Eigenschaften des angeregten Zustandes des **reinen Flavinchromophors** in Lösung studiert. Transiente Absorptions- und Fluoreszenzexperimente weisen auf den Einfluss von dynamischer polarer Solvatation auf die elektronischen Eigenschaften des angeregten Zustandes hin. Lösungsmittelkontrollierte $\pi\pi^*$-nπ^*-Kopplung wird als Erklärung vorgeschlagen. Es wurden Ramanspektren des angeregten Zustandes von Flavin aufgenommen und die Schwingungsbanden zugeordnet. Populationsverminderung durch den Ramanimpuls wurde als potentielles Artefakt in zeitaufgelösten Messungen identifiziert. Der Effekt wurde aber auch genutzt, um Wellenpaketbewegung im angeregten Zustand zu markieren.

Die Anwendung des entwickelten femtosekundenaufgelösten stimulierten Ramanspektrometers auf biologische Proben wurde in einem ersten FSRS-Experiment an

Glucose Oxidase als Modell-Flavoprotein demonstriert. Spektren vom angeregten Zustand wurden aufgenommen und die spektrale Entwicklung in der Zeit verfolgt. Die **BLUF** (*Blue Light Using Flavin*) Photorezeptor-Mutanten BlrB-L66F und Slr1694-Y8F wurden mit transienten Absorptionsmessungen untersucht. Dabei wurde die Bildung des Signalzustandes bzw. eine intermediäre Reduktion des Flavins durch ein nahegelegenes Tryptophan beobachtet

Contents

1 Introduction **1**

2 Nonlinear Spectroscopy **7**
2.1 Theoretical Background 8
2.1.1 The Density Matrix 8
2.1.2 Description of Mixed Systems 8
2.1.3 Time Evolution of a System 10
2.1.4 The Induced Polarization 12
2.1.5 Relaxation 13
2.1.6 Propagation of the Electric Field through a Medium 15
2.1.7 Homodyne and Heterodyne Detection 16
2.1.8 Absorption of a Weak Probe 17
2.2 Linear Spectroscopy 18
2.2.1 Absorption 18
2.2.2 Stimulated and Spontaneous Transitions 19
2.3 Transient Absorption 21
2.4 Femtosecond Stimulated Resonance Raman Spectroscopy 26
2.4.1 Theoretical Description of FSRS Bandshapes 26
Formalism 26
A compact form for the bandshape 30
2.4.2 Simulation of FSRS Bandshapes for Typical Resonance Conditions 31
$\mathbf{f} \leftarrow \mathbf{e}$ Resonance 32
$\mathbf{e} \rightarrow \mathbf{g}$ resonance 33
Simulataneous $f \leftarrow e$ and $e \rightarrow g$ resonance 34
$\mathbf{e} \leftarrow \mathbf{g}$ resonance. 34
Summary of expected Raman contributions 34
Comparison to Spontaneous Raman Spectroscopy 35

3 Experimental Section **37**
3.1 Linear Absorption and Fluorescence 37
3.2 Generation of Ultrashort Laser Pulses 37
3.2.1 Titanium-sapphire based laser systems 37
3.2.2 Nonlinear light conversion 38
3.3 Fluorescence Upconversion 39
3.4 Single-Shot Referencing in Transient Absorption and Raman Spectroscopy 40

3.5 The Femtosecond Stimulated Raman Spectrometer . . . 44
3.5.1 The Narrow-band Optical Parametric Amplifier . . . 44
3.5.2 Measurement Details . . . 47
3.5.3 Spectral Calibration . . . 48
3.5.4 Subtraction of Solvent Features . . . 49
3.5.5 Background Correction . . . 50
Generation of a Spectral Basis to the Raman Signal . . . 50
Generation of the Background Spectrum . . . 54
Noise Reduction for Small Signals . . . 56
Characteristics of the Background Correction Algorithm . . . 56
3.6 Data Analysis . . . 57
3.6.1 Multiexponential Fits . . . 57
3.6.2 Global Analysis and Kinetic Models . . . 58
3.6.3 Maximum Entropy Analysis . . . 60

4 Excited Stilbene: IVR and Solvation Studied by FSRR Spectroscopy 61
4.1 Introduction . . . 61
4.2 Experimental Details . . . 63
4.2.1 Transient absorption Spectroscopy . . . 63
4.2.2 Transient Raman Spectroscopy . . . 63
4.2.3 Chemicals . . . 63
4.3 Results . . . 63
4.3.1 Resonance Conditions . . . 63
4.3.2 *trans*-Stilbene . . . 64
4.3.3 *cis*-Stilbene . . . 67
4.4 Discussion . . . 69
4.4.1 *trans*-Stilbene . . . 69
Transient Spectra and Band Assignment . . . 69
Raman Intensities . . . 72
Evolution of the Inverted Raman Signals . . . 76
Band Shifts and Frequency Oscillations . . . 78
Band Widths . . . 82
4.4.2 *cis*-Stilbene . . . 83
Spectral Evolution . . . 83
Raman Band Shapes and Resonance Conditions . . . 84
Changes within the first 0.15 ps . . . 85
Intensity Oscillations . . . 87
4.5 Conclusions . . . 87

5 Structural Changes upon Internal Conversion of a "Parent Cyanine" 91
5.1 Introduction . . . 91
5.2 Materials and Methods . . . 91
5.2.1 Synthesis and Characterization . . . 91
5.2.2 Transient Absorption . . . 92

5.2.3 Fluorescence Upconversion . . . 93
5.2.4 Femtosecond Stimulated Raman Scattering (FSRS) . . . 93
5.2.5 Quantum-chemical Calculations . . . 93
5.3 Results and Discussion . . . 94
5.3.1 Transient Absorption . . . 94
5.3.2 Transient Fluorescence Upconversion . . . 96
5.3.3 Femtosecond Stimulated Raman Spectroscopy . . . 97
Resonance Conditions . . . 97
Decomposition of the Raman Signal . . . 98
Spectral Evolution . . . 100
Global Analysis and Raman Spectra of the involved Species . . . 100
5.3.4 Mechanistic Conclusions from Quantum-chemical Calculations . . . 100
Resonance Raman Spectra . . . 100
Potential Energy Surfaces and Model . . . 101
5.4 Conclusions . . . 103

6 Excited Flavin: A Femtosecond Stimulated Raman Study 105
6.1 Introduction . . . 105
6.2 Experimental Details . . . 108
6.2.1 Transient Absorption Spectroscopy . . . 108
6.2.2 Transient Fluorescence Spectroscopy . . . 108
6.2.3 Transient Raman spectroscopy . . . 109
6.2.4 Other Experimental Details. . . . 109
6.2.5 Spectral Fits . . . 109
6.2.6 Chemicals . . . 110
6.3 Quantum Chemical Calculations . . . 110
6.3.1 Methods and Models . . . 110
6.3.2 Vibrational Assignment . . . 111
6.4 Experimental Results . . . 112
6.4.1 Resonance Conditions. . . . 112
6.4.2 Evolution of Induced Absorption Spectra . . . 114
6.4.3 Evolution of Fluorescence Spectra . . . 116
6.4.4 Femtosecond Stimulated Raman Spectra . . . 117
6.5 Discussion . . . 122
6.5.1 Assignment of FSRS Bands Based on Quantum Chemistry . . . 122
Ground state vibrations . . . 122
Excited state vibrations . . . 129
6.5.2 Raman Band Shapes . . . 130
6.5.3 Vibrational Spectroscopy in Time . . . 131
6.5.4 Relaxation of Excited Flavin Seen by Transient Absorption and Fluorescence . . . 137
6.5.5 Decomposition of Transient Absorption Spectra . . . 144
6.6 Outlook . . . 148

6.7 Supporting Material . . . 149
6.7.1 Transient Absorption . . . 149
6.7.2 Fluorescence Upconversion . . . 152
6.7.3 Excited State Absorption Spectra . . . 153
6.7.4 Femtosecond Stimulated Resonance Raman Spectroscopy . . . 153

7 Light-Induced Changes in BLUF Photoreceptors 157
7.1 Introduction . . . 157
7.2 Experimental Details . . . 161
7.2.1 Transient Absorption . . . 161
7.2.2 Biological Samples . . . 161
7.2.3 Resonance Conditions . . . 161
7.3 BlrB-L66F: Formation of the Signaling State without Detectable Intermediates . . . 162
7.3.1 Results . . . 162
7.3.2 Discussion . . . 164
Temporal Characterization . . . 164
Mechanism of the BlrB-L66F Photocycle . . . 166
7.4 Slr1694-Y8F: Reduction of Flavin by a Tryptophan Residue . . . 168
7.4.1 Results . . . 168
7.4.2 Discussion . . . 169
Temporal Characterization . . . 170
Global Analysis and Mechanism . . . 171
7.5 Conclusions . . . 176

8 Outlook: Femtosecond Stimulated Raman Spectroscopy of Glucose Oxidase 179
8.1 Introduction . . . 179
8.2 Experimental Details . . . 180
8.3 Results . . . 180

9 Conclusions 183

1 Introduction

Light serves in nature not only as the essential energy source, but can also be harmful. Many organisms have developed complex receptor systems that allow to adequately react to small changes of the incident light. In plants, for example, the absorption spectra of blue- and red-light receptors overlap with those of the photosysnthesis pigments so that a control of the bioproduction is possible. Sensing of the stimulus generally involves the photoexcitation of a chromophore, which then induces a chain of reactions that lead to the formation of the signaling state. Initial steps involve processes like conformational change, for example *cis/trans* isomerization, electron and proton transfer, or the formation or breaking of bonds. To trace such reactions in real time one has to achieve a temporal resolution on the time scale of atomic motion, *i.e.* femtoseconds to picoseconds.

Within the last decades femtosecond spectroscopy has become an indispenable tool to study early reaction dynamics of photoexcited molecules in the gas phase,[1] solution,[2] and in biological environments.[3] One of the most employed techniques is to measure time-dependent absorption changes induced by an optical pump pulse.[4] This method is particularly useful to explore electronic changes that occur along the relaxation pathway. A major challenge in protein spectroscopy is the elucidation of conformational change upon light activation. Absorption spectra in solution are generally broad and do not provide enough information to reveal structural details. In BLUF photoreceptors, for example, the formation of the signaling state leads only to a 10–15 nm red-shift of the absorption spectrum (see Chapter 7), which is explained by changes of the hydrogen-bond network. To reveal the underlying conformational evolution, techniques are required that are more sensitive to structural changes.

X-ray crystallography is the ultimate tool to obtain precise structural information, but the temporal resolution of bright sources (synchrotons) is still limited to 100 ps.[5] Higher time resolution can be obtained in laboratory-scale X-ray and electron diffraction experiments, but at cost of decreasing the photon flux by several orders of magnitude. Taken together with difficulties in sample preparation, X-ray crystallography is still far from solving structures of a reacting protein in real-time. It should also be kept in mind that the geometrical confinement in the crystal may impede conformational changes, which are essential for the formation of the signaling state in solution.

Vibrational spectroscopy is currently the most promising approach to capture structural changes in biological samples on the femtosecond to picosecond time scale. By studying the time-dependent behavior of individual vibrational bands, the molecular

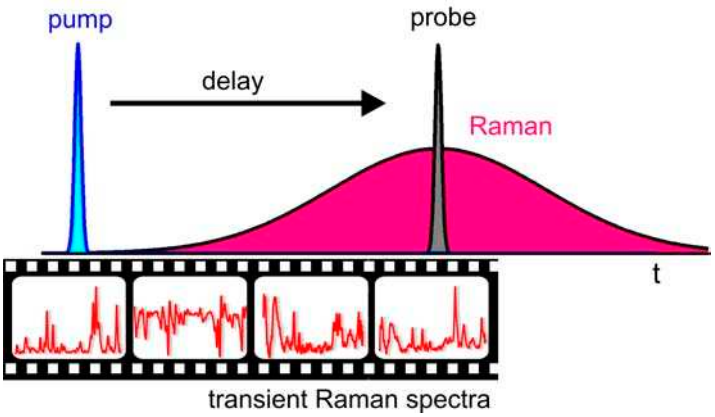

Figure 1.1: Scheme of a femtosecond stimulated Raman experiment. The delay between pump and Raman/probe is scanned, and a transient Raman spectrum is recorded at each delay time. The temporal resolution is determined by the pump-probe cross-correlation, but the spectral resolution is limited by the spectral width of the Raman pulse.

evolution is mapped along the normal coordinates. The recent availability of femtosecond infrared pulses has stimulated intense research in the field of ultrafast infrared spectroscopy.[6] However, the generation and detection of infrared pulses is demanding, and the teporal resolution is typically restricted to above 200 fs. Moreover, the applied probe pulses have only a bandwidth of less than 300 cm^{-1}, and frequencies below 1000 cm^{-1} are not accessed by the nonlinear processes used for pulse generation. The strongest drawback of ultrafast infrared spectroscopy is the overwhelming absorption of the water bending mode around 1645 cm^{-1}, which usually prohibits the measurement of proteins under physiological conditions.

Raman spectroscopy can circumvent many of the pitfalls of infrared experiments.[7] The Raman beam can be applied in the visible, and the detection window can span in a single measurement the full vibrational spectrum down to lowest frequencies. Raman scattering in resonance with electronic transitions is enhanced by several orders of magnitude. This allows to discriminate the vibrational signature of the chromophore against the scattering from a large excess of solvent molecules. Another advantage is that water is a weak Raman scatterer and does not interfere with measurements.

High spectral resolution in Raman spectroscopy requires narrowband Raman pulses. Due to the time-bandwidth relationship, such pulses inherently have picosecond duration. Therefore, spontaneous Raman experiments in a pump-probe arrangement can not achieve femtosecond time resolution. This fundamental limitation can be overcome by applying a third, ultrashort probe pulse that stimulates the Raman transition, see Figure 1.1.[7] Now the spectral resolution is still determined by the bandwidth of the Raman pulse, but the temporal resolution depends —as in a transient absorption experiment— on the cross-correlation of the short pump and probe pulses. In this way detailed vibra-

Table 1.1: Overview of recent femtosecond stimulated Raman experiments and comparison to this work.[a]

year	sample	ϵ[b]	λ_R[c]	resolution[d]	N[e]
		previous publications			
1999	DCM [8]	42500 [9]	794.7	25	4
2003	β-carotene [10]	134400 [11]	793	17	50
2005	rhodopsin [12]	41200 [13]	805	< 15	11
2005	bacteriorhodopsin [14]	58276 [15]	809	8	35
2006	*o*-nitrobenzaldehyde [16]	17750 [17]	387.5	12	9
2006	pure $CDCl_3$ [18]		800	< 15	8
2008	β-carotene [19]	134400 [11]	560/590*	34	30
2008	rhodamine 6G [20]	105000 [9]	540–580*	34	8
2008	phytochrome [21]	85000 [22]	792	18	20
2009	GFP [23]	55000 [24]	790–795	15	13
2010	*o*-nitrotoluene [25]	5500 [25]	388	30	40
		this work			
	trans-stilbene	24000 [26]	580/620*	12/7.5	660
	cis-stilbene	9350 [26]	620*	7.5	660
	PC	31000 [27]	520*	11	660
	FAD in water	11300 [28]	500/523/776*	12/20/5.5	660
	FAD in glucose oxidase	12590 [29]	521*	12	660

a abbreviations:
DCM – 4-dicyanomethylene-2-methyl-6-*p*-dimethylaminostyryl-4H-Pyran, GFP – Green Fluorescent Protein, PC – 1,1'-diethyl-2,2'-pyrido cyanine iodide, FAD – flavin adenine dinucleotide.
b extinction coefficient in $cm^{-1}M^{-1}$ for the lowest absorption band, or the absorption band that was excited in the experiment.
c wavelength of the Raman pulses in nm. Stars mark measurements with tunable Raman pulses.
d in cm^{-1}
e approximate number of points in time, for which Raman spectra were collected in an individual measurement.

tional spectra can be recorded with femtosecond resolution. An additional feature of this technique is that Raman scattering is only detected in the direction of the stimulating probe pulse, so that background from spontaneous fluorescence is suppressed.

The development of femtosecond stimulated Raman spectroscopy is sketched by the representative experiments in Table 1.1. The principle was first demonstrated in 1999 in

measurements on the laser dye DCM by Yoshizawa and Kurosawa.[8] The technique was was mainly developed thereafter in the group of R. Mathies, and applied to a number of chromophores.[10,12,14,18–21,23] Great attention has been paid to the investigation of the internal conversion in β-carotene,[10,19]. More recently also the dynamics of the proteins rhodopsin, bacteriorhodopsin, phytochrome, and GFP were studied.[12,14,21,23] The current work develops femtosecond stimulated Raman spectroscopy for the application to flavoproteins, for example BLUF domains.

The intensity of the scattered Raman signal depends on various parameters. To give an idea about the electronic properties of the measured samples, the molar extinction coefficient ϵ for the lowest band, or the transition that is excited in the experiment, is given in Table 1.1 as well. A comparison of the values suggests already that the detection of flavin (here flavin adenine dinucleotide, FAD) is challenging.

Resonance enhancement can greatly improve the signal, but to explore the optimum conditions, a tunable Raman pulse is required. In the majority of the previous experiments Raman pulses were obtained by filtering part of the laser system output. Thus, the resulting pulses were limited to a narrow spectral region around the 800 nm fundametal. The group of P. Gilch also demonstrated narrowband second harmonic generation, yielding Raman pulses around 400 nm.[16] Up to now only few experiments were reported with wavelength-tunable Raman pulses (tunability is marked in Table 1.1 by an asterisk).[19,20] These experiments were based on a narrowband optical parametric amplifier (*nb*-OPA). However, the conversion efficiency of this device was low, and the bandwidth of the pulses limited the spectral resolution to 34 cm^{-1}. To study the details of protein relaxation, higher resolution is required. Therefore, in the current work a *nb*-OPA is developed which efficiently provides tunable Raman pulses with spectral widths around 10 cm^{-1}.

Femtosecond resolution is the prerequisite to study ultrafast reactions in real time. The underlying processes, however, are only captured with precision if a sufficient number of spectra, N, is collected at different delay times. A comparison of the values in Table 1.1 shows that due to limitations by signal/noise previous experiments typically recorded less than 50 spectra in time. In this work, the number transient spectra was increased more than 10-fold, thus coming closer to the idea of "making a molecular movie" in Raman spectroscopy.

The work is arranged as follows:

In **Chapter 2** the theoretical background for transient absorption, fluorescence, and Raman experiments is described. Depending on the resonance conditions, stimulated Raman spectra from the excited state differ in shape from sponaneous Raman spectra. Simulations for typical conditions are shown, and the third-order contributions are discussed.

Experimental details are given in **Chapter 3**; the main focus is set to the Raman spectrometer and the analysis of the measured spectra. The transient evolution of the Raman

signal is only revealed, if the sequential background is subtracted in each spectrum consistently. A suitable algorithm is presented.

As a model compound for photoisomerization, stilbene is studied in **Chapter 4**, and relaxation processes on the excited-state potential energy surface are elucidated.

1,1'-diethyl-2,2'-pyrido cyanine iodide (PC) can be seen as a "parent cyanine", and it undergoes photoinduced *cis*/*trans* isomerization as well. Time-resolved optical and vibrational spectroscopy on this dye is shown in **Chapter 5**. In contrast to stilbene, the resonance conditions allow here to follow the internal conversion of the excited molecule to the ground state where the isomerization occurs.

Flavin is the chromophore in a number of photoreceptors. In **Chapter 6** the properties of unbound flavin in solution are studied by a combination of transient absorption, fluorescence, and Raman spectroscopies. Vibrational bands are assigned on the basis of quantum-chemical calculations. To prepare for future Ramman experiments on flavoproteins, the effect of resonance conditions is explored, and artefacts by population depletion are discussed. As an alternative to frequency-domain Raman spectroscopy, the identification of excited-state vibrations in time domain is shown.

As an outlook, the application of femtosecond stimulated Raman spectroscopy to flavoproteins is demonstrated in **Chapter 8**. Glucose oxidase is used as a model compound.

Finally the main conclusions are summarized in **Chapter 9**.

2 Nonlinear Spectroscopy

The regime of femtosecond time resolution is not achieved by common electronic detection techniques. Thus, most experimental approaches translate ultrashort time spans into differences in the optical pathlengths of two or more short light pulses. Typically, a femtosecond pump pulse induces a perturbation of the system at a well defined point in time; in the visible, for example, it drives an electronic transition. A pulse or pulse sequence then captures the evolution of the induced spectral changes as a function of delay time. In such scheme, the detected signal inherently depends to higher order on the electric field.

A theoretical description of the nonlinear signal is achieved by time-domain perturbation theory. A response function formalism was developed by Mukamel *et al.* and applied to a variety of spectroscopic techniques, including transient absorption and fluorescence spectroscopy.[30–34] These concepts were further refined to achieve a unified description of third-order sequential and coherent contributions to broadband transient absorption spectroscopy.[35–40] The femtosecond stimulated resonance Raman (FSRR) signal has been treated in semiclassical and quantum-mechanical terms.[14,20,41–45] Previous simulations simplified the system and included only limited resonance to other electronic states. Experimentally, however, the shape of FSRR bands may be complicated and depends strongly on measurement parameters and resonance conditions.[14,20,46] Interpretation of the complex spectral and temporal characteristics of FSRR measurements requires further understanding of the underlying processes.

Here transient absorption and Raman signals are treated to third order. The reader is introduced into the response function method[30] and its application to linear and transient absorption spectroscopy is presented.[35–40] With the support of A. Dobryakov[1] the formalism was extended to describe FSRR spectroscopy under simultaneous resonce with multiple electronic states. The transient Raman signal is simulated for typical conditions, and the band shapes are discussed.

[1] Third-order Raman signals were simulated by A. Dobryakov; Chemical Department, Humboldt-Universität zu Berlin, Brook-Taylor Str. 2, 12489 Berlin.

2.1 Theoretical Background

2.1.1 The Density Matrix

A quantum system, for which the complete information is known, is determined by its wave function $\Psi(x,t) = \langle x|\Psi\rangle$. Its evolution in time obeys the *Schrödinger equation*,

$$\frac{d}{dt}|\Psi\rangle = -\frac{i}{\hbar}\mathcal{H}|\Psi\rangle, \tag{2.1}$$

where $\mathcal{H}$ is the quantum-mechanical Hamiltonian of the system. In a physical experiment the wavefunction is not measured directly, but a quantity which depends its square. The expectation value of an observable O is given by

$$\langle O\rangle = \langle\Psi|O|\Psi\rangle. \tag{2.2}$$

Similarly, the probability $p(a)$ that the system is in specific state $|a\rangle$ is

$$p(a) = \langle a|\Psi\rangle\langle\Psi|a\rangle. \tag{2.3}$$

This suggests the introduction of a new operator, the density operator ρ, as

$$\rho = |\Psi\rangle\langle\Psi| \tag{2.4}$$

In the matrix representation, the diagonal elements $\rho_{aa} = \langle a|\Psi\rangle\langle\Psi|a\rangle$ directly give the probability for the system to be in state $|a\rangle$. Off-diagonal elements ρ_{ab} exist only for a coherent superposition of states $|a\rangle$ and $|b\rangle$. The expectation value $\langle O\rangle$ depends linearly on the density matrix via

$$\langle O\rangle = \mathrm{Tr}\left(O\rho\right), \tag{2.5}$$

where $\mathrm{Tr}(\dots) = \sum_i \langle i|\dots|i\rangle$ denotes the trace operation. Starting from the Schrödinger equation (2.1), an equation of motion can also be derived for the density operator, the *Quantum Liouville Equation*:

$$\frac{d}{dt}\rho = -\frac{i}{\hbar}\left[\mathcal{H},\rho\right] = -\frac{i}{\hbar}\left(\mathcal{H}\rho - \rho\mathcal{H}\right). \tag{2.6}$$

This equation is formally isomorph to the Schrödinger equation. Note, however, that the Hamiltonian acts on both sides of the density operator in equation (2.6).

2.1.2 Description of Mixed Systems

The density operator provides a direct connection between quantum mechanics and classical concepts. Despite significant advances in single-molecule spectroscopy,[47–50] most physical experiments still investigate ensemble properties. In general, the system can represented by a mixture of pure states $|\Psi_1\rangle$, $|\Psi_2\rangle$ …, $|\Psi_n\rangle$, which are populated with the probabilities $P(1)$, $P(2)$,…, $P(n)$; the expectation of an observable O is then

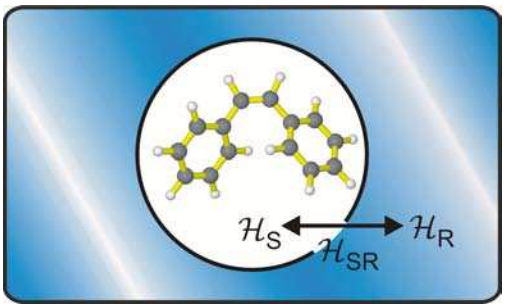

Figure 2.1: Typical situation in condensed-phase chemistry. The system (Hamiltonian $\mathcal{H}_S$) is surrounded by a reservoir, described by $\mathcal{H}_R$. System-reservoir coupling is included via $\mathcal{H}_{SR}$

obtained from the non-coherent superposition

$$\langle O\rangle = \sum_m P(m)\langle\Psi_m|O|\Psi_m\rangle = \sum_m P(m)\mathrm{Tr}\,(O\rho_m)..\tag{2.7}$$

Therefore, in contrast to the wave function, the density operator ρ of a mixture can be described as the weighted statistical average over the individual density operators ρ_m,

$$\rho = \sum_m P(m)\rho_m.\tag{2.8}$$

The diagonal elements $\rho_{aa} = \sum_m P(m)p_m(a)$ are the probabilities that the pure state $|a\rangle$ is contained in the statistical mixture described by ρ, and are also termed the *population* of $|i\rangle$.

In condensed phase, figure 2.1, the investigated molecules are surrounded by solvent bulk. It is usually not necessary to describe the complete solvent environment in detail, but one will attempt to reduce the system to the chromophor and maybe the first solvent shell, and seek the maximum extent of information only for this reduced system. It appears natural to devide the Hamiltonian into a system part $\mathcal{H}_S$, a reservoir part $\mathcal{H}_R$ which describes the pure solvent, and a part $\mathcal{H}_{SR}$ describing the interaction between the two,

$$\mathcal{H} = \mathcal{H}_S + \mathcal{H}_R + \mathcal{H}_{SR}\tag{2.9}$$

When, for example, a chromophor solution is irradiated with visible light, the solvent reservoir is typically transparent. The corresponding operator O_S thus only acts on the system. While such separation is possible for the Hamiltonian, the eigenvectors of the total Hamiltonian generally do not factorize into a system eigenvector $|a\rangle$ and a reservoir eigenvector $|\alpha\rangle$. Nonetheless, the vectors $|\alpha a\rangle$ may serve as a complete basis for the joint system-reservoir wavevector $|\Psi_m\rangle$. The expectation value of the operator

O_S is then given by

$$\langle O_S \rangle = \mathrm{Tr}\left(\rho O_S\right) = \sum_{\alpha,a} \langle a\alpha|\rho O_S|\alpha a\rangle. \tag{2.10}$$

Since O_S does not act on $|\alpha\rangle$, equation 2.10 can be rearranged to

$$\begin{aligned} \langle O_S \rangle &= \sum_a \langle a| \sum_\alpha \langle \alpha|\rho|\alpha\rangle O_S|a\rangle, \\ &= \sum_a \langle a|\rho_r O_S|a\rangle = \mathrm{Tr}_S\left(\rho_r O_S\right), \end{aligned} \tag{2.11}$$

with the *reduced density operator* $\rho_r = \mathrm{Tr}_R(\rho)$. Tr_S and Tr_R denote the partial traces over the system and reservoir coordinates, respectively. The last equation strongly simplifies the problem, as now knowledge of the reduced density operator ρ_r is sufficient to calculate the expectation value of any operator that exclusively acts on the system degrees of freedom.

2.1.3 Time Evolution of a System

For solving the equations of motion (2.1) and (2.6), we seek expressions for the time-dependent wavefunction $\Psi(t)$ and density operator $\rho(t)$. Let us recall the time-dependent Schrödinger equation 2.1:

$$i\hbar \frac{d}{dt}|\Psi(t)\rangle = \mathcal{H}|\Psi(t)\rangle. \tag{2.1}$$

This differential equation suggests that there exists a linear operator $\mathcal{U}(t, t_0)$, which allows to propagate the system in time and transforms the state vector $|\Psi(t_0)\rangle$ at an arbitrary time t_0 to the state vector $|\Psi(t)\rangle$ at a later time t,

$$|\Psi(t)\rangle = \mathcal{U}(t, t_0)|\Psi(t_0)\rangle. \tag{2.12}$$

This operator is called the *time evolution operator*. Only in this case, which is conservative, *i.e.* whose Hamiltonian is time-independent, the previous equation is solved by[2]

$$\mathcal{U}_0(t, t_0) = \mathrm{e}^{-\frac{i}{\hbar}\mathcal{H}\cdot(t-t_0)}. \tag{2.13}$$

In spectroscopy, the free evolution of the chromophor is perturbed by an incoming light field. This interaction is usually weak enough that perturbation theory is valid. The full Hamiltonian $\mathcal{H}(t)$ may then be devided into a time-independent part $\mathcal{H}_0$ and a

[2] To describe a physical experiment, the time-evolution operator $\mathcal{U}_0(t, t_0)$ should be replaced by the Green function $\mathcal{G}(t, t_0) = \Theta(t - t_0)\mathcal{U}_0(t, t_0)$. The Heaviside step function $\Theta(t - t_0)$ sets the evolution for $t < t_0$ to zero, thus preventing a physically meaningless backwards evolution in time.

time-dependent part $\mathcal{V}(t)$,

$$\mathcal{H}(t) = \mathcal{H}_0 + \mathcal{V}(t). \tag{2.14}$$

The interaction Hamiltonian $\mathcal{V}(t)$ is commonly described in the *dipole approximation*, thereby neglecting magnetic and higher-order multipole contributions, [51]

$$\mathcal{V}(t) = -\mu E(t), \tag{2.15}$$

where μ is the electric dipole operator, and E is the electric field.

Within this framework, the treatment of the time-dependent wavefunction is facilitated by a transformation to the interaction picture: [30,51]

$$|\Psi_I\rangle \equiv \mathcal{U}_0^\dagger(t, t_0)|\Psi\rangle, \tag{2.16}$$

where $\mathcal{U}_0^\dagger(t, t_0)$ is the Hermitian conjugate of the time evolution operator for the conservative system. The density matrix in the interaction picture is defined as

$$\rho_I = \mathcal{U}_0^\dagger(t, t_0)\rho\mathcal{U}_0(t, t_0). \tag{2.17}$$

The transformation should not affect the expectation value of a physical observable O. As a consequence, also the operator O is changed in the interaction picture and becomes time-dependent,

$$O_I = \mathcal{U}_0^\dagger(t, t_0)O\mathcal{U}_0(t, t_0). \tag{2.18}$$

In the interaction picture, the Schrödinger equation simplifies to

$$\frac{d}{dt}|\Psi_I\rangle = -\frac{i}{\hbar}\mathcal{V}_i|\Psi_I\rangle. \tag{2.19}$$

Similarly the Quantum Liouville equation can be written as

$$\frac{d}{dt}\rho_I = -\frac{i}{\hbar}[\mathcal{V}_I, \rho]. \tag{2.20}$$

These equations of motion do not depend any more on the full Hamiltonian $\mathcal{H}$, but only on the weak perturbation $\mathcal{V}_I$. Therefore, expansion into a series and suitable truncation becomes feasible. Time integration of equation (2.20) gives

$$\rho_I(t) = \rho_I(0) - \frac{i}{\hbar}\int_0^\infty d\tau[\mathcal{V}_I(\tau), \rho(\tau)]. \tag{2.21}$$

Upon iterative insertion of the density matrix one finally obtains

$$\rho_I(t) = \rho_I^{(0)}(t) + \sum_{n=1}^{\infty}\left(-\frac{i}{\hbar}\right)^n \int_0^t d\tau_n \int_0^{\tau_n} d\tau_{n-1} \ldots \int_0^{\tau_2} d\tau_2 \times [\mathcal{V}_I(\tau_n), [\mathcal{V}_I(\tau_{n-1}), \ldots [\mathcal{V}_I(\tau_1), \rho_I(-\infty)] \ldots]], \tag{2.22}$$

where $\rho(-\infty)$ is the equilibrium density matrix before the interaction with the light field. The density operator may be transformed back to the Schrödinger picture. By further changing the integration variables from time points τ_i to time spans t_i with $\tau_i = t_i - t_{i-1}$, equation 2.22 can be rewritten as

$$\rho(t) = \rho^{(0)}(t) + \sum_{n=1}^{\infty} \left(-\frac{i}{\hbar}\right)^n \int_0^t \int_0^t \dots \int_0^t dt_n dt_{n-1} \dots dt_1 \times \mathcal{U}_0(t,t_0)[\mathcal{V}_I(t_n),[\mathcal{V}_I(t_{n-1}),\dots[\mathcal{V}_I(t_1),\rho(-\infty)]\dots]]\mathcal{U}^\dagger(t,t_0). \tag{2.23}$$

2.1.4 The Induced Polarization

The incoming electric fields induce a time-dependent polarization $P(t)$, which is to first order the expectation value of the dipole operator,

$$P(t) = \mathrm{Tr}\left(\mu\rho(t)\right). \tag{2.24}$$

Equation (2.23) suggests that the polarization may be expanded into a series,

$$P(t) = P^{(1)} + P^{(2)} + \dots \tag{2.25}$$

The nth order polarization can then be expressed by

$$P^{(n)} = \int_0^\infty \int_0^\infty \dots \int_0^\infty dt_n dt_{n-1} \dots dt_1 \times R^{(n)}(t_n, t_{n-1}, \dots t_1) E^{(n)}(t, t_n, t_{n-1}, \dots t_1). \tag{2.26}$$

Here the interaction Hamiltonian $\mathcal{V}_I(t) = -\mu_I(t)E(t)$ was inserted, and the time-orderd product of electric fields was collected in the term $E^n(t, t_n, t_{n-1}, \dots t_1)$,

$$E^n(t, t_n, t_{n-1}, \dots, t_1) = E(t-t_n)E(t-t_n-t_{n-1})\dots E(t-t_n-t_{n-1}-\dots t_1). \tag{2.27}$$

The action of the dipole operators $\mu_I(t_i)$ on the equilibrium density matrix is contained in the nth response function $R^{(n)}(t_n, t_{n-1}, \dots t_1)$,

$$R^{(n)}(t_n, t_{n-1}, \dots t_1) = \left(\frac{i}{\hbar}\right)^n \mathrm{Tr}\left(\mu_I(t)[\mu_I(\tau_n),[\mu_I(\tau_{n-1}),\dots[\mu_I(t_1),\rho(-\infty)]\dots]]\right). \tag{2.28}$$

Evaluation of the nested commtutators in the last equation produces 2^n terms, each corresponding to a different interaction pathway.

As an example, consider the third-order response function $R^{(3)}(t_3, t_2, t_1)$. It may be written as the sum of eight dipole correlation functions $R^{(3)}_{[k]}$, which are parewise complex

conjugate to each other,

$$R^{(n)}(t_3,t_2,t_1) = \sum_{[k]=1}^{8} R^{(3)}_{[k]}, \tag{2.29}$$

where

$$R^{(3)}_1(t_3,t_2,t_1) = -\frac{i}{\hbar^3}\sum_{a,b,c,d} p(a)\mu_{ab}\mu_{bc}\mu_{cd}\mu_{da}I_{dc}(t_3)I_{db}(t_2)I_{da}(t_1), \tag{2.30a}$$

$$R^{(3)}_2(t_3,t_2,t_1) = -\frac{i}{\hbar^3}\sum_{a,b,c,d} p(a)\mu_{ab}\mu_{bc}\mu_{cd}\mu_{da}I_{dc}(t_3)I_{db}(t_2)I_{ab}(t_1), \tag{2.30b}$$

$$R^{(3)}_3(t_3,t_2,t_1) = -\frac{i}{\hbar^3}\sum_{a,b,c,d} p(a)\mu_{ab}\mu_{bc}\mu_{cd}\mu_{da}I_{dc}(t_3)I_{ac}(t_2)I_{ab}(t_1), \tag{2.30c}$$

$$R^{(3)}_4(t_3,t_2,t_1) = -\frac{i}{\hbar^3}\sum_{a,b,c,d} p(a)\mu_{ab}\mu_{bc}\mu_{cd}\mu_{da}I_{ba}(t_3)I_{ca}(t_2)I_{da}(t_1), \tag{2.30d}$$

$$R^{(3)}_5(t_3,t_2,t_1) = \frac{i}{\hbar^3}\sum_{a,b,c,d} p(a)\mu_{ab}\mu_{bc}\mu_{cd}\mu_{da}I_{cb}(t_3)I_{db}(t_2)I_{ab}(t_1), \tag{2.30e}$$

$$R^{(3)}_6(t_3,t_2,t_1) = \frac{i}{\hbar^3}\sum_{a,b,c,d} p(a)\mu_{ab}\mu_{bc}\mu_{cd}\mu_{da}I_{cb}(t_3)I_{db}(t_2)I_{da}(t_1), \tag{2.30f}$$

$$R^{(3)}_7(t_3,t_2,t_1) = \frac{i}{\hbar^3}\sum_{a,b,c,d} p(a)\mu_{ab}\mu_{bc}\mu_{cd}\mu_{da}I_{cb}(t_3)I_{ca}(t_2)I_{da}(t_1), \tag{2.30g}$$

$$R^{(3)}_8(t_3,t_2,t_1) = \frac{i}{\hbar^3}\sum_{a,b,c,d} p(a)\mu_{ab}\mu_{bc}\mu_{cd}\mu_{da}I_{ad}(t_3)I_{ac}(t_2)I_{ab}(t_1). \tag{2.30h}$$

The auxiliary function $I_{ij}(t)$ describes the evolution of the system upon dipole interaction. In the formalism developed so far, a system prepared in the superposition state $|i\rangle\langle j|$ evolves according to

$$I_{ij}(t) = \exp\left[-i\omega_{ij}t\right]. \tag{2.31}$$

Here ω_{ij} is the transition frequency between states $|i\rangle$ and $|j\rangle$.

2.1.5 Relaxation

The previous treatment did not consider relaxation effects. They are included here by the dephasing rate Γ_{ij}. The auxiliary function $I_{ij}(t)$ can then be expressed in terms of the complex frequency $\widetilde{\omega}_{ij} = \omega_{ij} - i\Gamma_{ij}$:

$$I_{ij} = \exp\left[-i\widetilde{\omega}_{ij}t\right]. \tag{2.32}$$

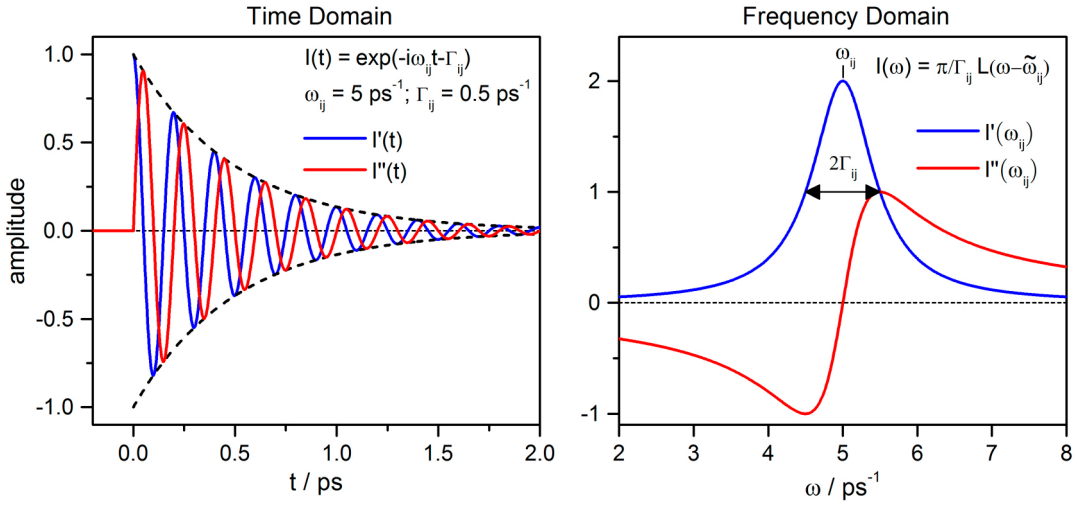

Figure 2.2: Time domain (left) and frequency domain representations of the Green function I_{ij} for the model parameters ω_{ij} and Γ_{ij} given in the inset. Real parts are shown in blue, imaginary parts in red.

In the *Bloch* approximation, the dephasing rate Γ_{ij} may be written as[30]

$$\Gamma_{ij} = \frac{1}{2}(\gamma_i + \gamma_j) + \widetilde{\Gamma}_{ij}. \tag{2.33}$$

Here population decay of the states $|i\rangle$ and $|j\rangle$ is described by the rates γ_i and γ_j, corresponding to the inverse lifetimes of the states. The environment is considered in the homogeneous limit, *i.e.* it is is assumed that it affects the chromophore by rapid fluctuations. These fluctuations induce a dephasing of the coherence $|i\rangle\langle j|$, characterized by the pure dephasing rate $\widetilde{\Gamma}_{ij}$. When performing the Fourier transform of the damped oscillation $I_{ij}(t)$ in positive time direction, one obtains

$$\int_{-\infty}^{\infty} dt\ I_{ij}(t)e^{i\omega t} = (\pi/\Gamma_{ij})L(\omega - \widetilde{\omega}_{ij}), \tag{2.34}$$
$$L(\omega - \widetilde{\omega}_{ij}) = i\Gamma_{ij}/\pi(\omega - \widetilde{\omega}_{ij}).$$

The function $L(\omega - \widetilde{\omega}_{ij})$ is a dimensionless complex Lorentzian, with the real and imaginary parts

$$L'(\omega - \widetilde{\omega}_{ij}) = \mathrm{Re}\,(L(\omega - \widetilde{\omega}_{ij}) = \frac{\Gamma_{ij}^2/\pi}{(\omega - \omega_{ij})^2 + \Gamma_{ij}^2}, \tag{2.35a}$$

$$L''(\omega - \widetilde{\omega}_{ij}) = \mathrm{Im}\,(L(\omega - \widetilde{\omega}_{ij}) = \frac{(\omega - \omega_{ij})\Gamma_{ij}/\pi}{(\omega - \omega_{ij}\Gamma_{ij})^2 + \Gamma_{ij}^2}. \tag{2.35b}$$

As shown in Figure 2.2, $L'(\omega-\widetilde{\omega}_{ij})$ is purely positive and peaks at the resonance frequency ω_{ij} and has a width $2\Gamma_{ij}$, whereas $L''(\omega-\widetilde{\omega}_{ij})$ changes sign and goes through zero at ω_{ij}.

Additional broadening may be introduced by static inhomogeneities of the solvent shell. This effect may be incorporated by convolution of the homogeneous polarization with a (Gaussian) distribution function,[30]

$$\langle P^{(n)}(\omega_{ij})\rangle = (1/\sqrt{2\pi}\Delta)\int_{-\infty}^{\infty} d\omega'\ P^{(n)}(\omega_{ij}+\omega')\exp\Big[-(\omega'/\Delta)^2/2\Big]. \tag{2.36}$$

More generally, solvent fluctuations may occur on a time scale which is in between the homogeneous (ultrafast) and the heterogeneous (static) limit. The solvent will then have a time-dependent effect on the evolution of the system. Theoretically such situation can be treated by performing the *Cumulant expansion* of the response function, and describing solvent motion in the *Brownian oscillator* model.[30] The randomization of solvent perturbations induced by dipole transitions is in this context described by the complex solvation correlation function. Its real part describes dephasing, whereas the imaginary part introduces a frequency shift that corresponds to the solvent-induced Stokes shift.

2.1.6 Propagation of the Electric Field through a Medium

In a non-magnetic medium without electric charges the polarization $P(\mathbf{r},t)$ is connected to the electric field $E(\mathbf{r},t)$ by the Maxwell wave equation:[3]

$$\left(\nabla^2-\frac{1}{c^2}\frac{\partial^2}{\partial t^2}\right)E(\mathbf{r},t)=\frac{1}{\epsilon_0 c^2}\frac{\partial^2}{\partial t^2}P(\mathbf{r},t). \tag{2.37}$$

This second-order differential equation may be solved by expressing the electric field and the polarization as plane waves. Under phase-matching conditions the electric field and polarization can be written in the complex notation

$$E(\mathbf{r},t)=\widetilde{E}(\mathbf{r},t)\exp\left(-i\omega t+i\mathbf{kr}\right)+cc.=\mathcal{E}(\mathbf{r},t)+\mathcal{E}^*(\mathbf{r},t), \tag{2.38a}$$
$$P(\mathbf{r},t)=\widetilde{P}(\mathbf{r},t)\exp\left(-i\omega t+i\mathbf{kr}\right)+cc.=\mathcal{P}(\mathbf{r},t)+\mathcal{P}^*(\mathbf{r},t), \tag{2.38b}$$

where the complex amplitudes carry a phase factor ϕ,

$$\widetilde{E}(\mathbf{r},t)=E_0(\mathbf{r},t)e^{i\phi}, \tag{2.39}$$
$$\widetilde{P}(\mathbf{r},t)=P_0(\mathbf{r},t)e^{i\phi}. \tag{2.40}$$

The notation of the electric field terms is not uniform in literature. To describe the complex amplitudes some authors introduce an additional factor of 1/2, which then has to be taken into account in the subsequent equations. Here the following conventions

[3] All equations are given in SI units.

are made: the complex electric field amplitudes are denoted by $\widetilde{E}$ and $\widetilde{E}^*$; their absolute value is E_0, and it is assumed that $E_0(t)$ has its maximum at $t = 0$. The electric field is written in equation (2.38a) as the sum of two complex conjugate terms, each describing an oscillation in the complex plane. These complex field terms are represented by the caligraphic letters $\mathcal{E}$ and $\mathcal{E}^*$. The same notation is used for the polarization. The Fourier transform operation $FT(\dots)$ interconverts expressions between time and frequency, and also between coordinate and momentum space. The actual space is indicates by the arguments t/ω and $\mathbf{r}/\mathbf{k}$.

Orientational effects are omitted here for simplicity. Typically, the field and polarization envelopes $E_0(\mathbf{r}, t)$ and $P_0(\mathbf{r}, t)$ change only slowly on the time scale of an oscillation period, and the temporal and spatial second derivative of the envelopes is set to zero; this is the *slowly varying envelope approximation*. For the component propagating in z direction equation (2.37) the simplifies under phase-matching conditions to

$$\frac{\partial}{\partial z}\widetilde{E}(z,t) = \frac{ik_z}{2\epsilon_0}\widetilde{P}(z,t). \tag{2.41}$$

2.1.7 Homodyne and Heterodyne Detection

Optical detectors are usually square-law devices, which means that not the electric field wave itself but the time-integrated intensity $I(\mathbf{k}, \omega)$ is measured. Two different approaches exist for the detection of the induced optical changes. In *homodyne* detection, the intensity of the generated electric signal field $E(\mathbf{k}, \omega)$ is measured directly as

$$I(\mathbf{k}, \omega) = 2c\epsilon_0|\widetilde{E}(\mathbf{k}, \omega)|^2. \tag{2.42}$$

In a higher-order experiment with non-collinear arrangement, the signal electric field may separated from the incoming beams by its propagation direction. Phase matching requires that the wave vector of the signal field $\mathbf{k_S}$ is the sum of the wave vectors of the incoming fields $\mathbf{k_i}$ involved in the nonlinear process,

$$\mathbf{k} = \sum_i \mathbf{k_i}. \tag{2.43}$$

Homodyne dection has the advantage that under apropriate conditions background-free measurements are possible. It has been successfully applied, for example, in four-wave mixing and photon-echo spectroscopy. The recorded intensity depends on the square of the signal electric field.

In another approach, *heterodyne* detection, the signal field E is mixed with a weak probe field E_{LO}, which is also denoted as the local-oscillator field, referring to the terminology in radio technology. The measured intensity is then

$$\begin{aligned} I(\mathbf{k}, \omega) &= 2c\epsilon_0|\widetilde{E}_{LO}(\mathbf{k_{LO}}, \omega_{LO}) + \widetilde{E}(\mathbf{k}, \omega)|^2 \\ &= I_{LO}(\mathbf{k_{LO}}, \omega_{LO}) + I(\mathbf{k}, \omega) + 4c\epsilon_0 \mathrm{Re}\left[\widetilde{E}^*_{LO}(\mathbf{k_{LO}}, \omega_{LO})\widetilde{E}(\mathbf{k}, \omega)\right]. \end{aligned} \tag{2.44}$$

Since the signal field is usually small, the contribution of $I(\mathbf{k},\omega)$ can be neglected, so that the intensity change in a heterodyne experiment depends linearly on the signal field. In linear absorption, pump-probe and stimulated Raman spectroscopy the signal field is generated along the direction of the incoming probe field, so that interference takes place. Therefore these experiments are intrinsically heterodyne.

2.1.8 Absorption of a Weak Probe

When light passes through a sample, its intensity and oscillation phase may change. Propagation in z direction is in the slowly varying amplitude approximationby quantified by Equation (2.41) . Multiplication with the complex conjugate field amplitude $\widetilde{E}^*(z,t) = E_0(z,t)e^{-i\phi}$ yields

$$E_0\frac{\partial}{\partial z}E_0 + iE_0^2\frac{\partial}{\partial z}\phi = \frac{i\omega}{2c\epsilon_0}\widetilde{E}^*\widetilde{P}, \tag{2.45}$$

where $k_z = \omega/c$ was used, thereby neglecting the refractive index dependence. With $I(z,t) = 2\epsilon_0 cE_0(z,t)^2$, the changes of intensity and phase for a single absorbing system can be expressed via the real and imaginary part of the last equation:

$$\frac{\partial I}{\partial z} = -2\omega\ \mathrm{Im}\left(\widetilde{E}^*(z,t)\widetilde{P}(z,t)\right), \tag{2.46a}$$

$$\frac{\partial \phi}{\partial z} = \frac{\omega}{I(z,t)}\mathrm{Re}\left(\widetilde{E}^*(z,t)\widetilde{P}(z,t)\right). \tag{2.46b}$$

When light with an initial intensity spectrum $I(0,\omega)$ passes a sample, its intensity $I(z,t)$ changes exponentially with the pathlength z, according to the *Beer-Lambert* law:

$$I(z,\omega) = I(0,\omega)e^{-\sigma_A(\omega)\mathscr{N}z}, \tag{2.47}$$

where $\mathscr{N} = N/V$ is the number density of the chromophore, and $\sigma_A(\omega)$ is its absorption cross section. Experimental results are usually discussed in terms of the extinction or optical density

$$OD(z,\omega) = \lg\frac{I(0,\omega)}{I(z,\omega)} = \lg(e)\ \sigma_A\mathscr{N}z. \tag{2.48}$$

Since

$$OD(z,\omega) = -\lg(e)\frac{z}{I}\frac{\partial I}{\partial z}, \tag{2.49}$$

the measured optical density spectrum is related to the induced polarization via

$$OD(z,\omega) = \lg(e)z\mathscr{N}\frac{2\omega}{I(z,\omega)}\mathrm{Im}\left(\widetilde{E}^*(z,\omega)\widetilde{P}(z,\omega)\right). \tag{2.50}$$

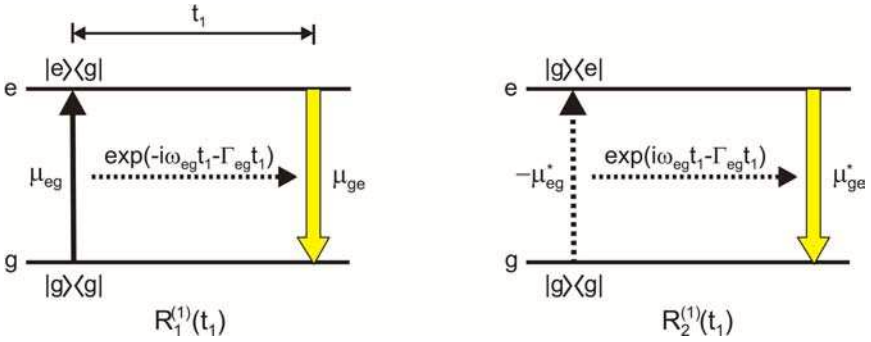

Figure 2.3: Energy ladder diagrams of the pathways $R^{(1)}_{[k]}$ that contribute to linear absorption in a two-level system. Dipole action on the ket (dashed arrow) or bra (full arrow) side prepares the system in the electronic coherence $|e\rangle\langle g|$ or $|g\rangle\langle e|$. It then evolves with $I_{eg}(t_1) = \exp[-i\omega_{eg}t_1 - \Gamma_{eg}t_1]$, $I_{ge}(t_1) = \exp[i\omega_{eg}t_1 - \Gamma_{eg}t_1]$. The last arrow corresponds to the dipole transition needed to evaluate the signal polarization.

2.2 Linear Spectroscopy

2.2.1 Absorption

In linear absorption, interaction with the electric field $E(\mathbf{r}, t - t_1)$ induces at time $t - t_1$ an electronic coherence between the ground state $|g\rangle$ and the excited state $|e\rangle$. The induced polarization at time t is given by the convolution of the electric field with the first-order response function $R^{(1)}(t_1)$,

$$P^{(1)}(\mathbf{r}, t) = \int_0^\infty dt_1 R^{(1)}(\mathbf{r}, t_1) E^{(1)}(\mathbf{r}, t - t_1) = \sum_{[k]} \int_0^\infty dt_1 R^{(1)}_{[k]}(\mathbf{r}, t_1) E(\mathbf{r}, t - t_1). \quad (2.51)$$

The pathways $R^{(n)}_{[k]}$ that contribute to an n^{th} order signal can be presented pictorially by energy ladder diagrams. To describe linear absorption, consider a two level system, which consists of the ground state g and an excited state e, Figure 2.3. In the diagram, time moves from left to right, and interactions with the dipole operator μ_{eg} are represented by vertical arrows. Full arrows correspond to action of the dipole operator on the ket side, dashed arrows indicate action on the bra side; the last arrow corresponds to the dipole transition needed to evaluate the signal polarization. As seen in Figure 2.3, the response to a first-order perturbation is described by the two complex-conjugate pathways

$$R^{(1)}_1(t_1) = \frac{i}{\hbar} p(g) |\mu_{eg}|^2 I_{eg}(t_1), \quad (2.52a)$$

$$R^{(1)}_2(t_1) = -\frac{i}{\hbar} p(g) |\mu_{eg}|^2 I_{ge}(t_1), \quad (2.52b)$$

where the factor $p(g)$ denotes the population of the ground state. In the Bloch approximation

$$I_{eg} = I_{ge}^{*} = \exp\left[-i\omega_{eg}t_1 - \Gamma_{eg}t_1\right]. \tag{2.53}$$

The electric field term $E^{(1)}(t-t_1)$ in $\mathbf{k}$ direction is equal to the light field of the probe beam,

$$E^{(1)}(\mathbf{k}, t-t_1) = \widetilde{E}(t-t_1)\exp\left[-i\Omega(t-t_1) + \mathbf{kr}\right] + cc. \tag{2.54}$$

For the calculation of the measured signal, Equation (2.50), only the complex amplitude $\widetilde{P}(k,\omega)$ of the induced polarization needs to be known. Hence, it is sufficient to evaluate the polarization with the complex part $\mathcal{E}(\mathbf{k}, t-t_1)$ of the electric field. Multiplication of $\mathcal{E}^{(1)}(\mathbf{k}, t-t_1)$ with the dipole correlation function $R_1^{(1)}(t_1)$ yields a term, which oscillates slowly in t_1 with the difference frequency $\Omega - \omega_{eg}$, whereas multiplication with $R_2^{(1)}(t_1)$ leads to a term, which oscillates rapidly with the sum frequency $\Omega + \omega_{eg}$. When performing the time integration in Equation (2.51), under near-resonance conditions only the slowly varying term from the pathway $R_1^{(1)}(t_1)$ will give a significant contribution. Upon Fourier transformation of the polarization wave $\mathcal{P}(\mathbf{k}, t)$, the convolution can be written as a product,

$$\mathcal{P}(\mathbf{k}, \omega) = R_1^{(1)}(\omega)\mathcal{E}(\mathbf{k}, \omega). \tag{2.55}$$

The linear absorption signal is finally obtained by inserting this result into Equation (2.50) and multiplying by the number N of absorbing molecules:

$$OD^{(1)}(z,\omega) = \lg(e) z \mathscr{N} \frac{\omega p(g)\pi}{\epsilon_0 c\hbar\Gamma_{eg}} |\mu_{eg}|^2 L'(\omega - \widetilde{\omega}_{eg}). \tag{2.56}$$

Its profile is given by the real part of the Lorentzian $L(\omega - \widetilde{\omega}_{eg})$, as defined in Equation (2.35a).

2.2.2 Stimulated and Spontaneous Transitions

Absorption, the transition from a state g to a higher electronic state e under consumption of a photon, is stimulated by the incoming light field and can thus be understood as a first-order reaction with respect to the photon density of the incoming beam. The probability w_{eg} that a single molecule absorbs a photon is proportional to the energy density $\rho(\nu) = I/c$ of the incoming light at frequency $\nu = \omega/2\pi$ via

$$w_{eg} = B_{eg}\rho(\nu). \tag{2.57}$$

The proportionality constant B_{eg} is the *Einstein coefficient for absorption.* It is related to the absorption cross section $\sigma_A(\nu)$ by[52]

$$B_{eg} = \frac{c}{h} \int \frac{\sigma_A}{\nu} d\nu. \tag{2.58}$$

The incoming radiation can also induce a transition to a lower-lying electronic state, *i.e.* in this case the $e \rightarrow g$ transition. The probability w_{ge} for unit population of the state e is

$$w_{ge} = B_{ge}\rho(\nu), \tag{2.59}$$

where B_{ge} is the *Einstein coefficient for stimulated emission.* It can be shown[51] that the coeficients B_{eg} and B_{ge} are equal,

$$B_{ge} = B_{eg} = B. \tag{2.60}$$

Experimentally observed absorption or emission bands can be analyzed by forming the band integral

$$BI = \int \frac{\sigma(\nu)}{\nu} d\nu = \int \frac{\sigma(\lambda)}{\lambda} d\lambda. \tag{2.61}$$

This quantity is proportional to the Einstein coefficient B that characterizes the transition. Furthermore, the band integral is insensitive to thermal relaxation of the molecule in a pure electronic state, when integrating over the full vibronic band envelope.[52,53] A spectral comparison of absorption and stimulated emission bands is achieved by plotting the band shape functions $\sigma(\nu)/\nu$.

In addition to stimulated emission, a chromophore in the excited state may also be de-excited by the spontaneous emission of a photon; this process is independent of the incident light. Nonetheless, it may be understood as emission which is stimulated by fluctuations of the vacuum field.[4] The probability for the spontaneous emission of a photon, w_{ge}^{sp} is given by the *Einstein coeffecient* A,

$$w_{ge}^{sp} = A. \tag{2.62}$$

A rigorous treatment requires a quantum-mechanical description of the electric field. A single mode of $E(\mathbf{r}, t)$ may be represented in the second quantization formalism via the creation and anihilation operators $a_2^\dagger$ and a_2,

$$E(\mathbf{r}, t) = i\sqrt{\frac{2\pi\hbar\omega_2}{v}} \left(a_2 \exp\left[-i(\omega_2 t - \mathbf{kr})\right] - a_2^\dagger \exp\left[i(\omega_2 t - \mathbf{kr})\right] \right), \tag{2.63}$$

with the quantization volume v. It can be shown[51] that the coefficient A for spontaneous

[4] Note that the vacuum field can not induce transitions to higher-lying states, since these processes require the absorption of a photon.

emission is, is related to that of stimulated emission, B, via

$$A = \frac{8\pi h\nu^3}{c^3} B. \tag{2.64}$$

In contrast to absorption, spontaneous fluorescence is usually measured directly with a detector that is sensitive to the number of emitted photons. The recorded photon distribution $F(\nu)$ can be converted into (relative) cross section spectra for stimulated emission, σ_{SE}, by multiplication with $1/\nu^2$.

The formalism presented above is not limited to optical absorption and fluorescence, but is valid also for other processes like stimulated and spontaneous Raman scattering.

2.3 Transient Absorption

In a transient absorption experiment, a pump pulse is applied and the induced absorption of a probe pulse is measured at a specific delay time t_d. A chopper extincts every second pump pulse, and the transient absorption signal is the induced difference spectrum. In an isotropic sample, the lowest-order signal contribution is of third-order,

$$\Delta OD(\omega_2, t_d) = \lg(e) z \mathscr{N} \frac{2\omega_2}{I} \mathrm{Im}\left(\widetilde{E}_2^*(\omega_2)\widetilde{P}^{(3)}(\omega_2, t_d)\right). \tag{2.65}$$

The third-order polarization spectrum $\mathcal{P}^{(3)}(\omega_2, t_d)$ is taken in the probe direction $\mathbf{k_2} = -\mathbf{k_1} + \mathbf{k_1} + \mathbf{k_2}$. It may be expressed by its Fourier transform as

$$\mathcal{P}^{(3)}(\omega_2, t_d) = \mathrm{FT}\left(\mathcal{P}^{(3)}(\mathbf{k_2}, t, t_d)\right) = \int_{-\infty}^{\infty} dt\ \mathcal{P}^{(3)}(\mathbf{k_2}, t, t_d) \exp[i\omega_2 t], \tag{2.66}$$

In the dipole approximation the nonlinear polarization $P^{(3)}(\mathbf{r}, t, t_d)$ is given by

$$P^{(3)}(\mathbf{r}, t, t_d) = \int_0^{\infty} dt_3 \int_0^{\infty} dt_2 \int_0^{\infty} dt_1 R^{(3)}(t_3, t_2, t_1) E^{(3)}(\mathbf{r}, t, t_3, t_2, t_1), \tag{2.67}$$

where $R^{(3)}(t_3, t_2, t_1)$ is the third-order nonlinear response function and $E^{(3)}(t, t_3, t_2, t_1)$ is the three-fold electric field product

$$E^{(3)}(\mathbf{r}, t, t_3, t_2, t_1) = E(\mathbf{r}, t - t_3 - t_2 - t_1) E(\mathbf{r}, t - t_3 - t_2) E(\mathbf{r}, t - t_3). \tag{2.68}$$

The total electric field at time t is given by the sum of the pump and probe pulse fields $E_1(\mathbf{r}, t + t_d)$ and $E_2(\mathbf{r}, t)$,

$$E(\mathbf{r}, t) = E_1(\mathbf{r}, t + t_d) + E_2(\mathbf{r}, t). \tag{2.69}$$

The effective field product $\mathcal{E}^{(3)}(\mathbf{k_2}, t, t_3, t_2, t_1)$ in $\mathbf{k_2}$ direction is obtained by insertion into equation (2.68) and collecting the terms with $\exp(i\mathbf{k_2 r})$. It is the sum of six time-ordered

terms,

$$\mathcal{E}^{(3)}(\mathbf{k_2},t,t_3,t_2,t_1) = \mathcal{E}_S^{(3)}(\mathbf{k_2},t,t_3,t_2,t_1) + \mathcal{E}_C^{(3)}(\mathbf{k_2},t,t_3,t_2,t_1) + \mathcal{E}_D^{(3)}(\mathbf{k_2},t,t_3,t_2,t_1),$$
$$\mathcal{E}_{S,C,D}^{(3)} = \mathcal{E}_{S_A,C_A,D_A}^{(3)} + \mathcal{E}_{S_B,C_B,D_B}^{(3)}, \tag{2.70}$$

where

$$\mathcal{E}_{S_A}^{(3)}(t,t_3,t_2,t_1) = \mathcal{E}_2(t-t_3)\mathcal{E}_1^*(t-t_3-t_2+t_d)\mathcal{E}_1(t-t_3-t_2-t_1+t_d), \tag{2.71a}$$
$$\mathcal{E}_{S_B}^{(3)}(t,t_3,t_2,t_1) = \mathcal{E}_2(t-t_3)\mathcal{E}_1(t-t_3-t_2+t_d)\mathcal{E}_1^*(t-t_3-t_2-t_1+t_d), \tag{2.71b}$$
$$\mathcal{E}_{C_A}^{(3)}(t,t_3,t_2,t_1) = \mathcal{E}_1(t-t_3+t_d)\mathcal{E}_2(t-t_3-t_2)\mathcal{E}_1^*(t-t_3-t_2-t_1+t_d), \tag{2.71c}$$
$$\mathcal{E}_{C_B}^{(3)}(t,t_3,t_2,t_1) = \mathcal{E}_1(t-t_3+t_d)\mathcal{E}_1^*(t-t_3-t_2+t_d)\mathcal{E}_2(t-t_3-t_2-t_1), \tag{2.71d}$$
$$\mathcal{E}_{D_A}^{(3)}(t,t_3,t_2,t_1) = \mathcal{E}_1^*(t-t_3+t_d)\mathcal{E}_2(t-t_3-t_2)\mathcal{E}_1(t-t_3-t_2-t_1+t_d), \tag{2.71e}$$
$$\mathcal{E}_{D_B}^{(3)}(t,t_3,t_2,t_1) = \mathcal{E}_1^*(t-t_3+t_d)\mathcal{E}_1(t-t_3-t_2+t_d)\mathcal{E}_2(t-t_3-t_2-t_1), \tag{2.71f}$$

The term $\mathcal{E}_S^{(3)}$ in equation (2.70) describes the sequential contribution, where the sample interacts first twice with the pump and then with the probe field. The terms $\mathcal{E}_C^{(3)}$ and $\mathcal{E}_D^{(3)}$ correspond to the coherent contribution, where the sample interacts with the interference of pump and probe fields. Note that in the description of ref. 30, the double coherent term $\mathcal{E}_D^{(3)}$ is omitted. By inserting the previous result into equations (2.65) and (2.66), also a transient absorption spectrum $\Delta OD(\omega_2,t_d)$ may be separated into sequential and coherent spectra,

$$\Delta OD(\omega_2,t_d) = \Delta OD_S(\omega_2,t_d) + \Delta OD_C(\omega_2,t_d) + \Delta OD_D(\omega_2,t_d). \tag{2.72}$$

$\Delta OD_C(\omega_2,t_d)$ and $\Delta OD_D(\omega_2,t_d)$ contain contributions from stimulated Raman scattering, two-photon absorption, and perturbed free induction decay.[35,36,39,54,55] If the electronic coherence time is short compared to the pulse duration, these signals appear only during the cross-correlation time of pump and probe pulses, giving rise to a 'coherent spike' around zero delay time. Such coherent contributions will be considered in the context of femtosecond stimulated resonance Raman (FSRR) spectroscopy. Here the discussion is focused on the sequential part $\Delta OD_S(\omega_2,t_d)$, which dominates the signal for temporally well-separated pump and probe pulses. The first two interactions with the pump field generate electronic population, whose evolution is queried by interaction with the delayed probe field. The signal $\Delta OD_S(\omega_2,t_d)$ is determined by the third-order polarization spectra $\mathcal{P}_S^{(3)}(\omega_2,t_d)$. The relevant nonlinear response function $R^{(3)}(t_3,t_2,t_1)$ is expressed by the sum over all third-order pathways $R_{[k]}^{(3)}(t_3,t_2,t_1)$:

$$\mathcal{P}_S^{(3)}(\omega_2,t_d) = \sum_{[k]} \int_0^\infty dt_3 \int_0^\infty dt_2 \int_0^\infty dt_1 \; R_{[k]}^{(3)}(t_3,t_2,t_1)\mathrm{FT}\left[\mathcal{E}_S^{(3)}(t,t_3,t_2,t_1)\right]. \tag{2.73}$$

A pathway $[k]$ is specified by subscripts $[mn, kl, pq]$ and corresponds to a third-order sequence of the general form

$$|g\rangle\langle g| \xrightarrow{\mu_{ab}} |m\rangle\langle n| \xrightarrow{\mu_{cd}} |k\rangle\langle l| \xrightarrow{\mu_{ef}} |p\rangle\langle q|. \tag{2.74}$$

In the Bloch approximation the third order response function of the $[k]$th pathway is given by

$$R^{(3)}_{S[k]}(t_3, t_2, t_1) = -\frac{i}{\hbar^3} p(g) \widehat{\mu}_{[k]} \exp\left[-i\widetilde{\omega}_{mn} t_3 - i\widetilde{\omega}_{kl} t_2 - i\widetilde{\omega}_{pq}\right]. \tag{2.75}$$

Here the product of the dipole matrix elements, $\mu_{fe}\mu_{ef}\mu_{cd}\mu_{ab}$, is collected in the operator $\widehat{\mu}$.

For well separated pulses of negligible duration, the sequential contribution to transient absorption may be factorized into a term that describes the time-dependent population $p(j, t_d)$ change of state $|j\rangle$ and the associated first-order spectrum $\Delta D^{(1)}_j(\omega_2, 0)$,

$$\Delta OD^{(3)}_S(\omega_2, t_d) = \sum_j p(j, t_d) \Delta D^{(1)}_j(\omega_2, 0), \tag{2.76}$$

with

$$\Delta D^{(1)}_j(\omega_2, 0) = \sum_i \lg(e) z \mathscr{N} \frac{\omega\pi}{\epsilon_0 c\hbar\Gamma_{ij}} |\mu_{ij}|^2 L'(\omega - \widetilde{\omega}_{ij}). \tag{2.77}$$

Thus by analyzing the temporal evolution of the induced absorption spectrum, one may draw conclusions about the flow of the intermediately created populations $p(j, t_d)$. The time-dependence of $p(j, t_d)$ depends on the mechanism of excited-state relaxation. In Section 3.6 it will be shown that the evolution of transient populations can be described in most cases by the sum of exponential terms, weighted by the amplitudes a_i,

$$p(j, t_d) = \sum_n a_n \exp\left(-t/\tau_n\right)). \tag{2.78}$$

A typical transient absorption experiment may be modelled by considering a system of three electronic states g, e, and f, each with vibrational structure distinguished by primes (g', e', f'). Pathways that contribute to the sequential transient-absorption signal are illustrated as energy-ladder diagrams in figure 2.4. For simplicity only sequences are shown that start from the lowest vibrational level in the ground state. The pathways may be classified according to the way in which system is prepared. In the bleaching process (BL) the pump pulse modifies the population in the ground electronic state. The probe induces the $e \leftarrow g$ coherence, resulting in an emissive polarization wave. Other processes involve the transfer of population to the excited state. The probe field may then drive the $f \leftarrow e$ or the $e \rightarrow g'$ transition, corresponding to excited-state absorption (ESA) or stimulated emission (SE).

As an example, the transient-absorption spectrum of riboflavin in DMSO at delay $t_d = 0.4$ ps is shown in figure 2.4 and compared to the stationary absorption and emis-

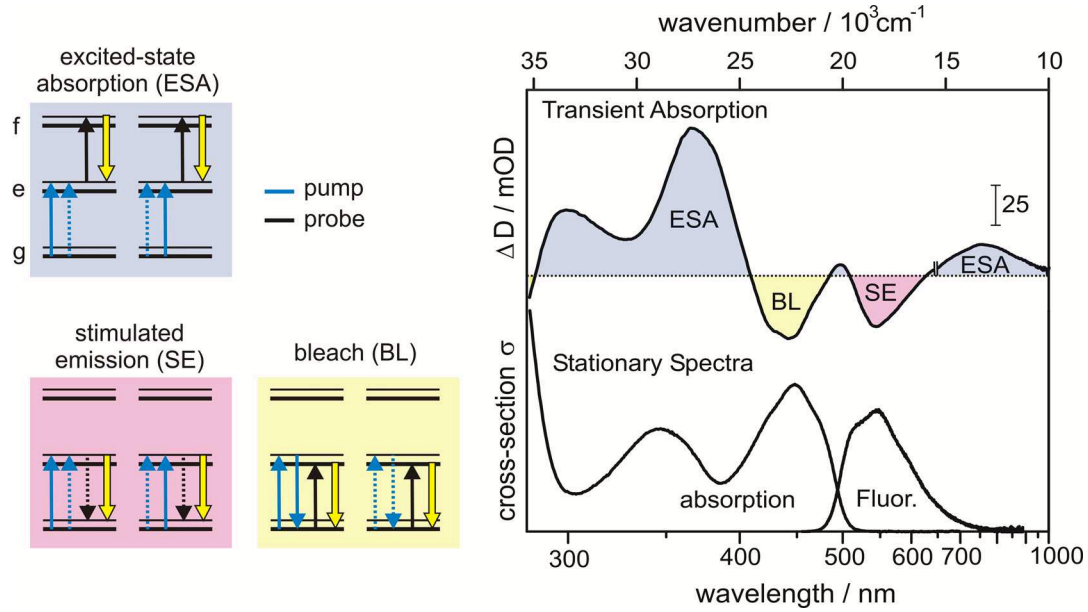

Figure 2.4: The transient absorption signal. Left: Energy ladder diagrams representing the sequential pathways that contribute to the transient absorption signal. Right: Typical transient absorption signal of riboflavin in DMSO upon excitation with 440 nm at a delay of $t_d = 0.4$ ps, compared to stationary absorption and emission cross-section spectra.

sion cross-section spectra. The excited-state absorption (ESA) gives rise to positive bands, which are overlayed with negative signals from bleach (BL) and stimulated emission (SE). Note that the contributions monitor evolution of the excited molecule from different viewpoints: ESA and SE report on the population and spectroscopic properties of excited states. On the other hand, BL reflects a lack of population in the fully equilibrated electronic ground state and has the shape of the negative ground-state absorption spectrum.

At early delay times, the pulse duration should be taken into account for a description of the sequential contribution. The pulse envelope is in many cases well described by a Gaussian of width $\tau_{1,2}$. The pump and probe electric field terms are then

$$\mathcal{E}_1(\mathbf{k_1}, t + t_d) = \exp\left[-(t + t_d)^2/2\tau_1^2 - i\Omega_1(t + t_d) + i\mathbf{k_1 r}\right], \tag{2.79a}$$

$$\mathcal{E}_2(\mathbf{k_2}, t) = \exp\left[t^2/2\tau_2^2 - i\Omega_1(t) + i\mathbf{k_2 r}\right]. \tag{2.79b}$$

After performing the Fourier transform, equation (2.73) can be solved analytically.[35,38,39] If electronic dephasing is fast compared to the pulse durations, i.e. $\Gamma_{pq} \to \infty$, the sequential transient absorption signal from population transfer may be written as the convolution of the impulsively generated signal, equation (2.76), with the temporal

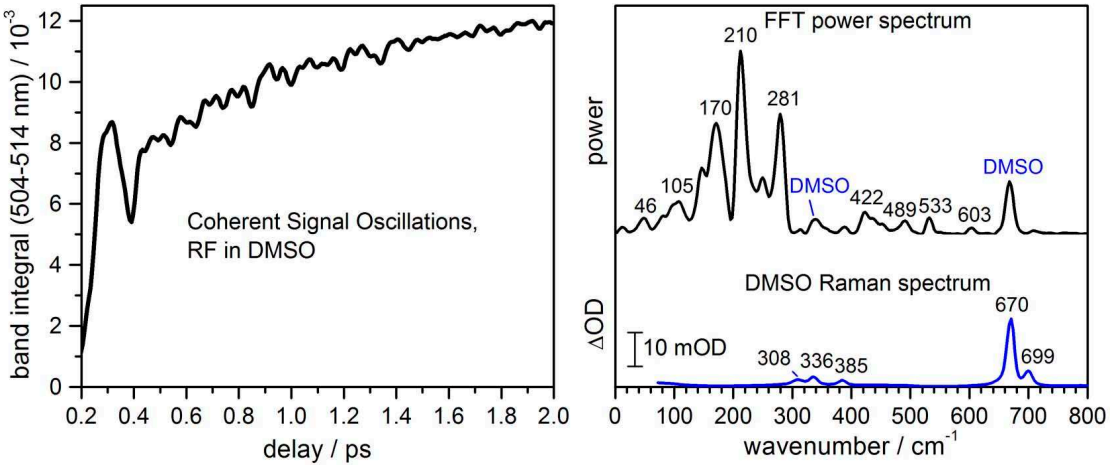

Figure 2.5: Oscillatory modulation of the transient absorption signal of riboflavin in DMSO by impulsive stimulated Raman scattering (SR). The sample was excited with 400 nm pump pulses. Left: Transient absorption band integral over the region 504–514 nm. Right: Fourier power spectrum of the oscillations (top) and stimulated Raman spectrum of DMSO (bottom).

apparatus function $F_{cc}(t)$,

$$\Delta OD_S^{(3)}(\omega_2, t_d) = \sum_j \left[\int_{-\infty}^{\infty} dt' F_{cc}(t') p(j, td - t') \right] \Delta D_j^{(1)}(\omega_2, 0). \tag{2.80}$$

Impulsive stimulated Raman scattering (SR) gives additional contributions to the sequential signal. It arises from the intrinsic spectral width of the femtosecond pump pulses, which allows the first two electric field interactions (mn, kl) to occur with diffent transition frequencies. This generates a vibrational coherence in the ground or excited state, off which the probe field is scattered. Motion of the prepared vibrational wavepacket around a potential minimum induces oscillatory modulation of the transient absorption signal with the vibrational frequency $\omega_{vib} = \omega_{kl}$. The accessible frequency range is limited by the spectral width of the pump pulse. For the time-resolved experiments presented in this work, typically vibrations along low-frequency modes up to ~ 700 cm^{-1} are excited. The spectral amplitude of coherent oscillations is determined by a combination of real and imaginary parts of the complex Lorentzians that characterize the involved transitions.[39] Therefore, the oscillation phase typically varies across a transient-absorption band, so that not only the signal amplitude, but also its spectral position is modulated.

Experimentally observed oscillations of the transient absorption signal are shown in figure 2.5 for riboflavin in DMSO. The continuous rise is clearly modulated by oscillations. Fourier transform reveals the spectrum of contributing low-frequency vibrations. Hence, transient absorption spectroscopy allows to perform vibrational spectroscopy in

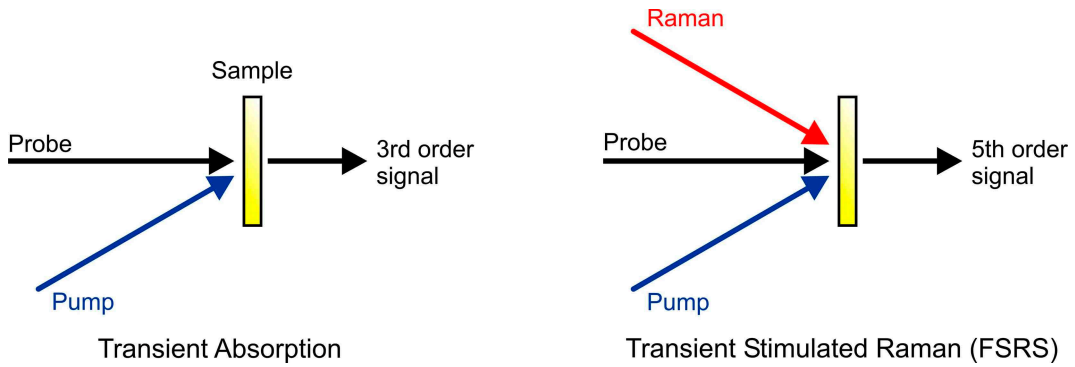

Figure 2.6: Comparison of femtosecond-resolved transient absorption and stimulated Raman spectroscopy (FSRS).

time domain. The previous discussion focussed on resonance transitions, but also under non-resonant conditions impulsive stimulated Raman scattering may prepare wave packets in the electronic ground state. Whereas this contribution is negligible for the chromophor, it plays a role for solvent, which is present in large excess. Comparison of the Fourier power spectrum in 2.5 with the Raman spectrum of DMSO identifies bands around 670 cm^{-1} and 336 cm^{-1} as originating from solvent oscillations. In the discussion of femtosecond stimulated resonance Raman spectroscopy on the flavin chromophor, it will be shown that the Fourier power spectrum of Raman background oscillations is inherently free from solvent contributions.

2.4 Femtosecond Stimulated Resonance Raman Spectroscopy

To achieve femtosecond resolution in Raman spectroscopy, the limitations imposed by the time-bandwith relation of the Raman pulse must be overcome. The problem can be solved by stimulating the Raman scattering with an ultrashort probe pulse.[8,16,18,19] The detection scheme of an actinic pump pulse and a delayed probe pulse is already realized in a transient absorption experiment. This setup can be converted into a transient stimulated Raman spectrometer by applying an additional Raman pulse, which temporally coincides with the probe pulse, see figure 2.6. When scanning the delay time t_d, now the vibrational evolution of the system can be studied by acquiring stimulated Raman spectra. Both Raman and pump beam are chopped in an appropriate sequence (see Chapter 3), so that the lowest contribution to the calculated signal is of fifth order.

2.4.1 Theoretical Description of FSRS Bandshapes

Formalism

The actinic pump pulse prepares the system with populations $p(j,t)$ in vibronic states j. For simplicity let us assume that the subsequent scattering events are well separated in time by the delay t_d. The quantity of interest is the transient Raman spectrum

$R(\omega_2, t_d) = -\Delta OD^{(5)}(\omega_2, t_d)$, induced by the actinic pump and measured at t_d by the coinciding Raman and probe pulses as function of probe frequency ω_2. Let us concentrate on coherence only, *i.e.* after a background due to population transfer among states a has been subtracted. The stimulated Raman signal can then be written as

$$R(\omega_2, t_d) = -\sum_a p(j, t_d)\Delta D^{(3)}(\omega_2, 0), \tag{2.81}$$

with

$$\Delta D^{(3)}(\omega_2, 0) = \lg(e) z \mathscr{N} \frac{2\omega_2}{I} \mathrm{Im}\left(\widetilde{E}_2^*(\omega_2)\widetilde{P}^{(3)}(\omega_2)\right). \tag{2.82}$$

The 0 in $\Delta^{(3)}(\omega_2, 0)$ indicates that the probe pulse has zero delay with respect to the Raman pulse, *i.e.* that both pulses are coincident. Similar to transient absorption, the third-order induced polarization can be written in the form

$$P^{(3)}(\mathbf{r}, t, t_d) = \int_0^\infty dt_3 \int_0^\infty dt_2 \int_0^\infty dt_1 R^{(3)}(t_3, t_2, t_1) E^{(3)}(\mathbf{r}, t, t_3, t_2, t_1), \tag{2.83}$$

where $R^{(3)}(t_3, t_2, t_1)$ is the third order nonlinear response function , but without the population factor, and $E^{(3)}(\mathbf{r}, t, t_3, t_2, t_1)$ is the three-fold electric field product. The Raman experiment focuses on the coherent contribution to the third-order polarization, *i.e.* terms, in which the last interaction takes place with the Raman electric field. The effective field product $\mathcal{E}^{(3)}(\mathbf{k_2}, t, t_3, t_2, t_1)$ in probe direction $\mathbf{k_2}$ can be written in the form

$$\mathcal{E}^{(3)}(\mathbf{k_2}, t, t_3, t_2, t_1) = \mathcal{E}_A(t, t_3, t_2, t_1) + \mathcal{E}_B(t, t_3, t_2, t_1), \tag{2.84}$$

where

$$\mathcal{E}_A(t, t_3, t_2, t_1) = \mathcal{E}_1(t - t_3)\mathcal{E}_2(t - t_3 - t_2)\mathcal{E}_1^*(t - t_3 - t_2 - t_1),$$
$$\mathcal{E}_B(t, t_3, t_2, t_1) = \mathcal{E}_1(t - t_3)\mathcal{E}_1^*(t - t_3 - t_2)\mathcal{E}_2(t - t_3 - t_2 - t_1).$$

Here $\mathcal{E}_1(t)$ and $\mathcal{E}_2(t)$ in (2.84) represent the Raman and probe pulses,

$$\mathcal{E}_{1,2}(\mathbf{r}, t) = \widetilde{E}_{1,2}(\mathbf{r}, t) \exp\left[-i\Omega_{1,2}t + i\mathbf{k_{1,2}}\mathbf{r}\right]. \tag{2.85}$$

The third-order signal $\Delta D^{(3)}(\omega_2, 0)$ depends on the polarization spectra $\mathcal{P}(\omega_2, 0)$. It is expressed here in terms of the sum over all resonant third-order pathways $R^{(3)}_{[k]}(t_3, t_2, t_1)$:

$$\mathcal{P}^{(3)}(\omega_2, 0) = \sum_{[k]} \int_0^\infty dt_3 \int_0^\infty dt_2 \int_0^\infty dt_1 R^{(3)}_{[k]}(t_3, t_2, t_1) FT\left(\mathcal{E}^{(3)}(\mathbf{k_2}, t, t_3, t_2, t_1)\right) \tag{2.86}$$

Performing the Fourier transform $FT\left(\mathcal{E}^{(3)}(\mathbf{k_2},t,t_3,t_2,t_1)\right) = I_{A,B}(\mathbf{k_2},t_3,t_2,t_1)$ of the 3-fold field products, results in

$$I_A(\mathbf{k_2},t_3,t_2,t_1) = \exp\left[i\omega_2(t_3+t_2) - i\Omega_1(t_2+t_1) + i\mathbf{k_2}\mathbf{r}\right]$$
$$\times \int_{-\infty}^{\infty} dt\ \widetilde{E}_1(t+t_2)\widetilde{E}_2(t)\widetilde{E}_1^*(t-t_1)\exp\left[i(\omega_2-\Omega_2)t\right], \tag{2.87}$$
$$I_B(\mathbf{k_2},t_3,t_2,t_1) = \exp\left[i\omega_2(t_3+t_2+t_1) - i\Omega_1 t_2 + i\mathbf{k_2}\mathbf{r}\right]$$
$$\times \int_{-\infty}^{\infty} dt\ \widetilde{E}_1(t+t_2+t_1)\widetilde{E}_1^*(t+t_1)\widetilde{E}_2(t)\exp\left[i(\omega_2-\Omega_2)t\right]. \tag{2.88}$$

Exact forms for $FT\left(\mathcal{E}^{(3)}(t,t_3,t_2,t_1)\right)$ were given in refs. 35–40, and the reader is referred to these papers for details. Here the coherent Raman signal is calculated using two-sided exponentials for the Raman pulse envelope, $\mathcal{E}_1(\mathbf{r},t) = \exp\left(-|t|/\tau_1 + i\mathbf{k_1}\mathbf{r}\right)$. This form is preferred over a Gaussian since it allows to find the simplest analytic expression. When the probe is a δ pulse, $\mathcal{E}_2(\mathbf{r},t) = \delta(t)\exp\left(i\mathbf{k_2}\mathbf{r}\right)$, equations (2.87) and (2.88) may be written as

$$I_A(\mathbf{k_2},t_3,t_2,t_1) =$$
$$\exp\left[i\omega_2 t_3 + i(\omega_2 - \Omega_1 + i/\tau_1)t_2 - i(\Omega_1 - i/\tau_1)t_1 + i\mathbf{k_2}\mathbf{r}\right], \tag{2.89}$$
$$I_B(\mathbf{k_2},t_3,t_2,t_1) =$$
$$\exp\left[i\omega_2 t_3 + i(\omega_2 - \Omega_1 + i/\tau_1)t_2 + i(\omega_2 + 2i/\tau_1)t_1 + \mathbf{k_2}\mathbf{r}\right]. \tag{2.90}$$

Having considered the applied electric fields, we turn to the molecular response functions $R^{(3)}_{[k]}$ in equation (2.86). As before, the Bloch approximation may be applied, so that [35–40]

$$R^{(3)}_{[k]}(t_3,t_2,t_1) = -\frac{i}{\hbar^3}\widehat{\mu}_{[k]}\exp\left[-i\widetilde{\omega}_{mn}t_3 - i\widetilde{\omega}_{kl}t_2 - i\widetilde{\omega}_{pq}t_1\right], \tag{2.91}$$

with complex frequency $\widetilde{\omega}_{ab} = \omega_{ab} - i\Gamma_{ab}$ and the transition frequency ω_{ab}.

Time integration is carried out analytically and the induced signal is expressed by auxiliary functions $F_{A,B}(mn,kl,pq)$,

$$\Delta D^{(3)}(\omega_2,0) = \lg(e)z\mathcal{N}\frac{2\omega}{I\hbar^3}\sum_{[k]}\left(\widehat{\mu}_A F_A(mn,kl,pq) + \widehat{\mu}_B F_B(mn,kl,pq)\right), \tag{2.92}$$

with

$$F_{A,B}(mn,kl,pq) = -\pi^3/\left(\widetilde{\Gamma}_{mn}\widetilde{\Gamma}_{kl}\widetilde{\Gamma}^{A,B}_{pq}\right)\mathrm{Im}\left(f_{mn}\times g_{kl}\times h^{A,B}_{pq}\right), \tag{2.93}$$

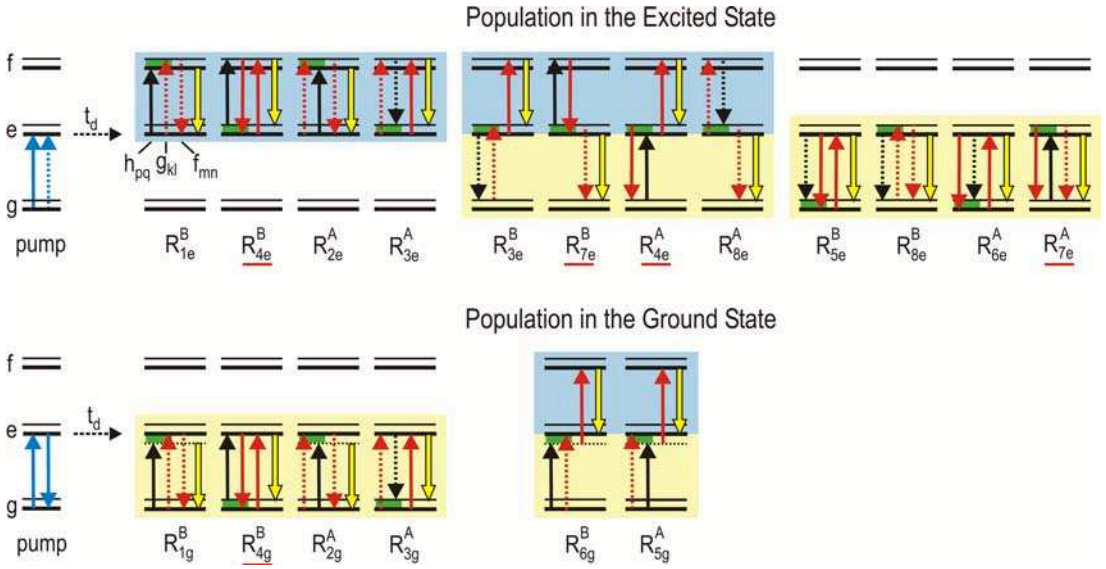

Figure 2.7: Ladder diagrams representing the main interaction pathways for femtosecond stimulated Raman scattering of a model system with three electronic states. Sequences are named according to ref. 30; superscripts A (Raman first) and B (probe first) denote the interaction order. Pathways that need an excited vibrational level for resonance are underlined red. Dashed arrows represent bra-side, and full arrows ket-side interaction. The actinic pump pulse (blue) prepares population either in the ground state g or electronic excited state e. After a time delay t_d, interaction of the sample with the Raman (red) and probe (black) electric fields involves transitions to a higher excited state f (blue shaded) and/or to the ground state g (yellow shaded). The intermediate vibrational coherence is indicated by a green shaded area.

$$L_{mn} = \frac{\widetilde{\Gamma}_{mn}/\pi}{\omega_2 - \omega_{mn} + i\widetilde{\Gamma}_{mn}}, \qquad L_{kl} = \frac{\widetilde{\Gamma}_{kl}/\pi}{\omega_2 - \Omega_1 - \omega_{kl} + i\widetilde{\Gamma}_{kl}},$$
$$L^A_{pq} = \frac{\widetilde{\Gamma}^A_{pq}/\pi}{\Omega_1 + \omega_{pq} + i\widetilde{\Gamma}^A_{pq}}, \qquad L^B_{pq} = \frac{\widetilde{\Gamma}^B_{pq}/\pi}{\omega_2 - \omega_{pq} + i\Gamma^B_{pq}},$$

and

$$\widetilde{\Gamma}_{mn} = \Gamma_{mn}, \qquad \widetilde{\Gamma}_{kl} = \Gamma_{kl} + 1/\tau_1, \qquad \widetilde{\Gamma}^A_{pq} = -\Gamma_{pq} - 1/\tau_1, \qquad \widetilde{\Gamma}^B_{pq} = \Gamma_{pq} + 2/\tau_1.$$

A pictorial representation of the pathways that contribute to the signal is provided by the ladder diagrams of 2.7. Consider a system of three electronic states g, e, and f with vibrational structure. Two interactions with the actinic pump pulse (blue) prepare the system with transient population in the ground state g or in the first excited state e. For the generation of the stimulated Raman signal, the detection geometry requires two conjugate interactions with the Raman electric field (red) and one with the probe field (black). The superscripts A and B distinguish whether the first interaction takes place

with the Raman or probe pulse.

A compact form for the bandshape

The induced polarization which causes the transient signal is the sum over the possible vibronic pathways $[k]$ (see (2.86)) where all vibrational manifolds $g(\nu_g, \nu'_g, \dots)$, $e(\nu_e, \nu'_e, \dots)$, $f(\nu_f, \nu'_f, \dots)$ are included. Let us focus on the Raman pathways in 2.7. For a discussion of the signal shape we calculate the auxiliary functions $F_{A,B}(mn, kl, pq)$ in equation (2.93) for temporally long Raman pulses, i.e. in the limit $\tau_1 \to \infty$.

The third-order transitions may be classified according to the density matrix elements that are prepared. The first and third electric field interactions, characterized by subscripts mn and pq, generate electronic coherence. We introduce the detuning of the Raman frequency from the electronic transitions involved ,

$$\begin{aligned} \delta^A_{pq} &= \Omega_1 + \omega_{pq}, \quad \delta^B_{pq} = \Omega_1 - \omega_{pq}, \\ \delta^A_{mn} &= \delta^B_{mn} = \Omega_1 - \omega_{mn} = \delta_{mn}. \end{aligned} \tag{2.94}$$

Dephasing of electronic coherence typically takes place in 10 fs at room temperature. We assume here that the electronic dephasing rates are equal,

$$\Gamma_{mn} = \Gamma_{pq} = \Gamma_{el}. \tag{2.95}$$

The second electric-field interaction, characterized by the subscripts kl, prepares a vibrational coherence, indicated by the green-shaded area in 2.7. The frequency ω_{vib} of the vibration is given by

$$\omega_{vib} = -\omega_{kl}. \tag{2.96}$$

We further introduce the vibrational dephasing rate

$$\Gamma_{vib} = \Gamma_{kl}. \tag{2.97}$$

Vibrational dephasing is typically much slower than electronic dephasing and may take picoseconds if dominated by pure dephasing.

The Raman signal can now be calculated by taking the imaginary part in (2.93). In the limit $\tau_1 \to \infty$ the auxiliary functions can be presented as the product of the real parts of the three Lorentzians L_{ab}, multiplied by a second-order polynomial:

$$F_{A,B}(mn, kl, pq) = \frac{\pi^3}{\Gamma^4_{el}\Gamma^2_{vib}} \left(a_{A,B}\ x^2 + b_{A,B}\ x + c_{A,B}\right) L'_{mn} L'_{kl} L'^{A,B}_{pq}, \tag{2.98}$$

where $x = \omega_2 - \Omega_1$ is the Raman detuning. The Lorentzians L'_{mn} and $L'^{A,B}_{pq}$ are deter-

mined by the electronic resonance conditions:

$$L'_{mn} = \frac{\Gamma_{el}^2/\pi}{(x+\delta_{mn})^2 + \Gamma_{el}^2},$$
$$L'^{A}_{pq} = \frac{\Gamma_{el}^2/\pi}{{\delta^A_{pq}}^2 + \Gamma_{el}^2}, \qquad L'^{B}_{pq} = \frac{\Gamma_{el}^2/\pi}{\left(x+\delta^B_{pq}\right)^2 + \Gamma_{el}^2}. \tag{2.99}$$

The vibrational coherence gives rise to the Lorentzian L_{kl},

$$L_{kl} = \frac{\Gamma_{vib}^2/\pi}{(x+\omega_{vib})^2 + \Gamma_{vib}^2}. \tag{2.100}$$

Since usually $\Gamma_{vib} \ll \Gamma_{el}$, the position and width of a Raman band is given by L'_{kl}, whereas L'_{mn} and $L'^{A,B}_{pq}$ modify its amplitude. The shape of the Raman band may change upon multiplication with the second-order polynomial. The parameters are

$$\begin{aligned}
a_A &= \Gamma_{el}, \quad a_B = 2\Gamma_{el} + \Gamma_{vib},\\
b_A &= \Gamma_{el}\left(\omega_{vib} + \delta_{mn} - \delta^A_{pq}\right) - \Gamma_{vib}\delta^A_{pq},\\
b_B &= \Gamma_{el}\left(2\omega_{vib} + \delta_{mn} + \delta^B_{pq}\right) + \Gamma_{vib}\left(\delta_{mn} + \delta^B_{pq}\right),\\
c_A &= -\Gamma_{el}^2\Gamma_{vib} + \Gamma_{el}\omega_{vib}\left(\delta_{mn} - \delta^A_{pq}\right) - \Gamma_{vib}\delta_{mn}\delta^A_{pq},\\
c_B &= -\Gamma_{el}^2\Gamma_{vib} + \Gamma_{el}\omega_{vib}\left(\delta_{mn} + \delta^B_{pq}B\right) + \Gamma_{vib}\delta_{mn}\delta^B_{pq}.
\end{aligned} \tag{2.101}$$

Depending on the roots of the polynomial, the Raman signal may change sign. If the polynomial passes through zero at the vibrational resonance frequency ω_{vib}, the band has dispersive appearance with a negative and positive lobe. For given system parameters the polynomial depends on the resonance conditions, expressed by the detunings δ_{mn} and $\delta^{A,B}_{pq}$. Note that for pathways R^A the detuning difference $\delta_{mn} - \delta^A_{pq}$ enters, but for pathways R^B the sum of the detunings $\delta_{mn} + \delta^B_{pq}$ is formed in (2.101). If the Raman pulse is resonant only with a single electronic transition, for example $f \leftarrow e$ or $e \rightarrow g$ (yellow or blue shaded in 2.7), detunings δ_{mn} and δ^A_{pq} are equal for R^A. In the limit $\Gamma_{vib} \rightarrow 0$ the shape and direction of the Raman bands do not depend on the resonance conditions for these pathways. In contrast, all pathways R^B are sensitive to resonance detuning.

2.4.2 Simulation of FSRS Bandshapes for Typical Resonance Conditions

For a discussion of the major trends, the Raman signal $R(\nu)$ is now simulated according to (2.81) and (2.92) for a system of displaced harmonic oscillators; results are shown in 2.8. For simplicity we use a single vibrational mode which has the frequencies $\nu_g = \omega_{vib,g}/2\pi = 1000\ \mathrm{cm}^{-1}$, $\nu_e = 980\ \mathrm{cm}^{-1}$, and $\nu_f = 960\ \mathrm{cm}^{-1}$ in the g, e, and f electronic states, respectively. We discuss the effect of Raman resonance with stimulated emission $e \rightarrow f$, bleach $e \leftarrow g$ or excited-state absorption $f \leftarrow e$. The following

common parameters are chosen: vibrational lifetime $\tau_{aa'} = 1/\gamma_{aa'} = 5$ ps except stated otherwise; pure vibrational dephasing rate $\widehat{\Gamma}_{vib} = (5 \text{ ps})^{-1}$, electronic dephasing rate $\widehat{\Gamma}_{el} = (0.010 \text{ ps})^{-1}$; potential minima displacement $\Delta_{eg} = \Delta_{fe} = \sqrt{2}$; Raman pulse duration $\tau_1 = 2$ ps. We set the $f \leftarrow e$ (0-0) transition to 19000 cm^{-1} (526 nm). The $f - e$ (0-0) energy displacement and the Raman frequency $\nu_R = \Omega_1/2\pi$ are adjusted to model different resonance conditions, 2.8 b. The effect of vibrational excitation is assessed by placing population $p(j, t_d)$ either in the lowest vibrational level (2.8b, top), or the first excited vibrational level (2.8b, bottom) of S_1.

Only those pathways were included in the simulation that may give rise to spectrally sharp Raman features on the Stokes side; the corresponding diagrams were shown in 2.7. Starting from the excited state e the diagrams have been ordered according to the involved electronic states: the pathways may include transitions to a higher electronic state f (blue shaded), to the ground state g (yellow) or to both states (blue/yellow). Sequences that require the system to be in a vibrationally excited state are underlined red. Actinic excitation may deposits excess energy in the Franck-Condon active modes, which is dissipated by intramolecular vibrational redistribution and vibrational cooling. Similarly, internal conversion to the ground state leaves the molecule with population in higher vibrational levels. For the molecule at room temperature, modes > 200 cm^{-1} are in the vibrational ground state, and the underlined diagrams no longer contribute to the signal for these modes.

f ← e Resonance

Consider first a situation in which the Raman pulse is only resonant with an $f \leftarrow e$ excited-state absorption but not with the $e \rightarrow g$ stimulated emission. Such conditions are found for *trans*-stilbene (Chapter 4 and flavin for Raman excitation at 776 nm (Chapter 6). In the simulation we set the Raman frequency to $\nu_R = 20000$ cm^{-1} (500 nm), and move the $e \rightarrow g$ transition out of resonance to $\nu_{eg} = 40000$ cm^{-1}. If e is populated in its lowest vibrational state, only R^B_{1e}, R^A_{2e}, and R^A_{3e} affect the signal, 2.8 b (top left). All three pathways result in positive bands of approximately equal height. R^A_{3e} (blue) describes conventional Stokes scattering in the excited state e and corresponds to the RRS(I) term in ref.[41]. R^B_{1e} (black) and R^A_{2e} (red) have been designated as hot luminescence, HL(III) and HL(IV).[20,41] In these cases vibrational coherence is generated in the higher excited state, and the corresponding band is determined by the vibrational properties of S_n; hence a peak at ν_n is observed. Such pathways can only contribute if the S_n state is resonant and posesses a lifetime that is long enough. 2.8 a shows the dependence of the signal on the vibrational lifetime $\tau_{aa'}$. Starting from $\tau_{aa'} = 1$ ps, shortening of the vibrational lifetime of f leads to broadening of the band at ν_f. At $\tau_{ff'} = 0.1$ ps this band can not be distinguished any more from a broad background in the experiment. Similarly, we are also able to suppress the band at ν_e by decreasing the vibrational lifetime of e. Higher excited electronic states often interconvert to the first excited state within < 0.1 ps, facilitated by a high density of vibronic states. Then the contributions of R^B_{1e} and R^A_{2e} to the background-corrected signal are negligible. If the state e is vibrationally excited, R^B_{4e} also contributes (2.8 b, bottom left). This pathway has been assigned to

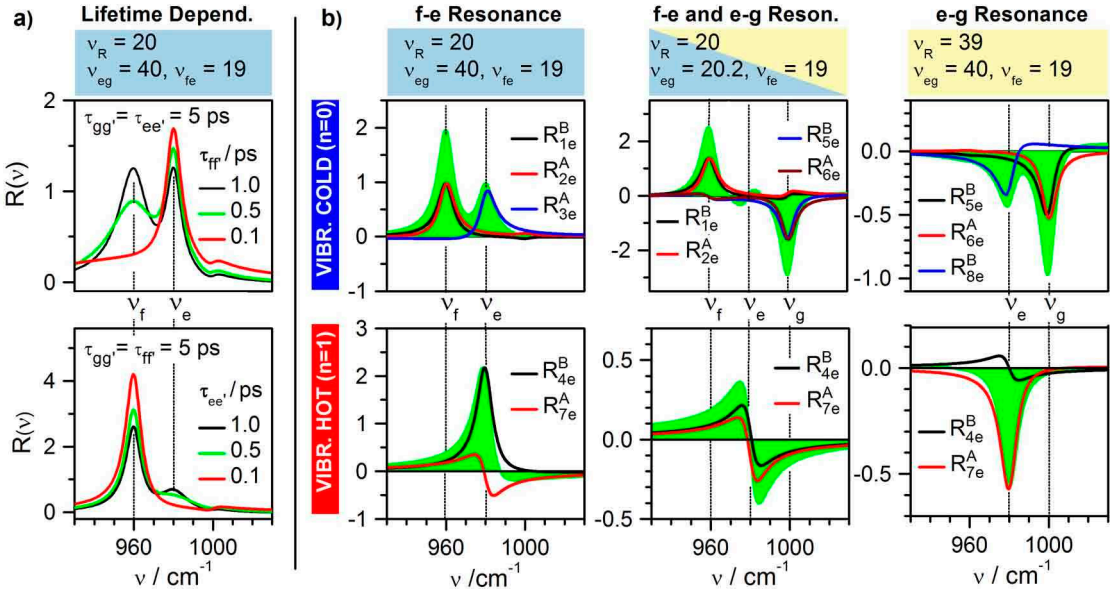

Figure 2.8: Simulation of the FSRR signal under different conditions. The Raman frequency $\nu_R = \Omega_1/2\pi$ and the frequencies of the $e - g$ and $f - e$ (0-0) transitions are given in 10^3 cm^{-1}. a) Dependence of the band shape on the vibrational lifetime $\tau_{aa'} = 1/\gamma_{aa'}$ in the f (top) and e (bottom) excited states. b) Dependence on the resonance conditions. The full signal is given in green, and the main contributions from the diagrams in 2.7 are shown. Signals were simulated with the population either in the lowest vibrational level (top) or in the first excited vibrational level (bottom) of S_1. All vibrational lifetimes were set to $\tau_{gg'} = 5$ ps.

inverse Raman scattering, IRS(I) in ref. 41, and it is made responsible for negative FSRR signals in the low-frequency region of *trans*-stilbene (Chapter 4). In the current simulation a strong positive band is seen at ν_e instead (black). As explained before, signals from R^B pathways are sensitive to changes in the Raman resonance detunig.

e → g resonance

If the Raman pulse is resonant only with the stimulated emission $e \rightarrow g$, but not with excited-state absorption, the signal is dominated by R^B_{5e}, R^B_{8e}, R^A_{6e}, and R^A_{7e}. This situation is found for cyanine in the excited state (Chapter 5). It is modelled by keeping the parameters for the system ($\nu(S_0S_1) = 40000$ cm^{-1}, $\nu(S_1S_n) = 19000$ cm^{-1}) and changing the Raman frequency to $\nu_R = 39000$ cm^{-1}. The obtained Raman bands in 2.8 b, right, resemble the signal for $f \leftarrow e$ resonance, with the difference that contributions from the resonant state appear now at ν_g and the complete signal has opposite sign. R^B_{5e} (top, black) and R^A_{6e} (top, red) are the counterparts of R^B_{1e} and R^A_{2e}. In contrast to S_n, however, the ground electronic state does not decay, and these diagrams must be taken into account. In FSRS experiments on other systems, dispersive signals at the positions

of ground state were found and assigned to such pathways.[14,20] The diagrams R_{8e}^{B} (top, blue) and R_{7e}^{A} (bottom, red) are the counterparts of the inverse Raman pathway R_{4e}^{B} and the conventional Raman scattering term R_{3e}^{A}. Note that R_{7e}^{A} requires the system to be vibrationally excited, while R_{8e}^{B} may start from the lowest vibrational state.

Simulataneous $f \leftarrow e$ and $e \rightarrow g$ resonance

This situation is encountered, when excited flavin interacts with Raman pulses at 500 and 523 nm (Chapter 6). For simulation, we set the Raman frequency to 20000 cm^{-1}, spectrally overlapping with excited-state absorption ($\nu_{fe} = 19000$ cm^{-1}) and stimulated emission ($\nu_{eg} = 20200$ cm^{-1}). In addition to all diagrams discussed above, sequences with mixed transitions are expected to play a role. Corresponding pathways are R_{3e}^{B} and R_{8e}^{A}, and if the system is vibrationally excited, R_{7e}^{B} and R_{4e}^{A}. These action sequences are controlled by the vibrational properties of e. The simulation in 2.8 b (middle) indicates that the signal mainly comprises contributions that involve pure $e \rightarrow g$ or $f \leftarrow e$ transitions. For the vibrationally cold system a strong positive signal from R_{1e}^{B} and R_{2e}^{A} is found at ν_f; as discussed before, for rapid internal conversion of higher electronic states this band is broad and does not survive the background correction. However the negative band at ν_g from R_{5e}^{B} and R_{6e}^{A} will also contribute. Signals from R_{3e}^{A} and R_{8e}^{B} (not shown) partly cancel each other and result in a small dispersive feature at ν_e. For the vibrationally excited molecule, R_{4e}^{B} (black) and R_{7e}^{A} (red) also lead to a small dispersive-shaped signal. The actual shape FSRR signal from population in the state e will be affected by subtle differences in the involved transitions for each individual mode.

e $\leftarrow$ g resonance.

When the Raman pulses are resonant with the ground state-absorption, as for example in experiments on cyanine (Chapter 5) and flavin (Chapter 6) with Raman pulses at 500 nm, transient population in the ground state (or "Bleach", 2.7, panel b) gives rise to additional contributions. The pathways R_{1g}^{B}, R_{4g}^{B}, R_{2g}^{A}, and R_{3g}^{A} are analogues to the blue-shaded diagrams for initial preparation in the first excited state e. At room temperature, contribution of R_{4e}^{B} is negligible. Apart from R_{3g}^{A}, all other sequences generate vibrational coherence in e. If the Raman pulse overlaps with the red edge of the $e \leftarrow g$ absorption band, these pathways should be negligible, and the signal should be dominated by the R_{3g}^{A} diagram. This pathway corresponds to conventional ground-state resonance Raman scattering on the Stokes side (the simulation is not shown).

Summary of expected Raman contributions

(i) Raman signals from vibrations in the excited state e. The shape is controlled by the $f - e$ and $e - g$ resonance conditions for each individual mode.

(ii) A negative bleach signal. The shape is given by the ground-state Raman spectrum and does not change with time. As in transient absorption, the bleach intensity reports on the amount of population which is depleted from the ground state.

(iii) A (negative) signal at ground-state vibrational frequencies, originating from population in the excited state e. The signal differs from the bleach contribution in that the system adopts the excited-state geometry. Therefore frequencies and band shapes may change after excitation, thus reporting on the excited-state relaxation of the molecule.

Comparison to Spontaneous Raman Spectroscopy

Spontaneous Raman Spectroscopy only measures Raman emission. The previous simulations indicate that for a system in the excited state only the blue-shaded pathways in Figure 2.7 contribute to a spontaneous Raman signal. In the spontaneous Raman process the vacuum electric field plays the role of the probe pulse and stimulates the scattering event.[30] As a consequence, pathways, in which the probe pulse induces an intermediate transition to a higher electronic state, can not contribute to the signal. Therefore, a spontaneous transient Raman spectrum on the Stokes side is dominated by the pathway R^A_{3e}. Similarly, a spontaneous Raman spectrum from the ground state is purely determined by R^A_{3g}.

3 Experimental Section

Details of stationary and time-resolved measurements, and the subsequent data analysis are described. I focus on the implementation of femtosecond stimulated Raman spectroscopy. A key development is a narrowband optical parametric amplifier that provides tunable Raman pulses with spectral widths around 10 cm^{-1}. High time resolution is the prerequisite to detect ultrafast evolution, but to truly capture molecular motion with precision, a sufficient number of frames has to be recorded in time. In previous Raman experiments typically not more than 50 transient spectra were obtained in a single experiment, thereby only highlighting the main trends. In this work spectra up to 660 steps in time are recorded in each measurement, providing detailed insight into the temporal relaxation. A procedure was developed to remove the background from all transient spectra of a data set consistently. The background correction is facilitated by switching during a measurement between two frequency-shifted Raman pulses on a shot-to-shot basis.

3.1 Linear Absorption and Fluorescence

UV-vis absorption spectra were scanned on a Varian Cary 300. Fluorescence spectra were obtained on a Spex Fluorolog-2 spectrofluorimeter, and corrected for instrumental factors, and converted into cross sections for stimulated emission σ_{SE}.[56] It is these spectra which are called "fluorescenc", whereas "stimulated emission" (SE) refers exclusively to the $S_1 \rightarrow S_0$ part of transient absorption spectra. Fluorescence quantum yields were measured relative to aqueous quinine sulfate[57] and rhodamine 101 in ethanol[58] as fluorescence standards.

3.2 Generation of Ultrashort Laser Pulses

3.2.1 Titanium-sapphire based laser systems

Because time and spectral domain are related via the Fourier transform, a short laser pulse inherently posesses a broad spectrum and *vice versa*. To generate ultrashort pulses, the laser medium should therefore allow the amplification of modes in a wide frequency range. However, stable pulse trains are only obtained if a fixed phase relationship is established between the modes (*mode locking*). Modern femtosecond laser systems mostly use titanium-doped sapphire (Ti:Sa) crystals as gain medium. This material allows light amplification over a broad spectral range beween 680 and 1100 nm,[59] and mode locking is achieved via the nonlinear Kerr effect: at high light intensities, the refractivity of Ti:Sa becomes intensity-dependent. This leads to an effective self-focusing of the beam. Note

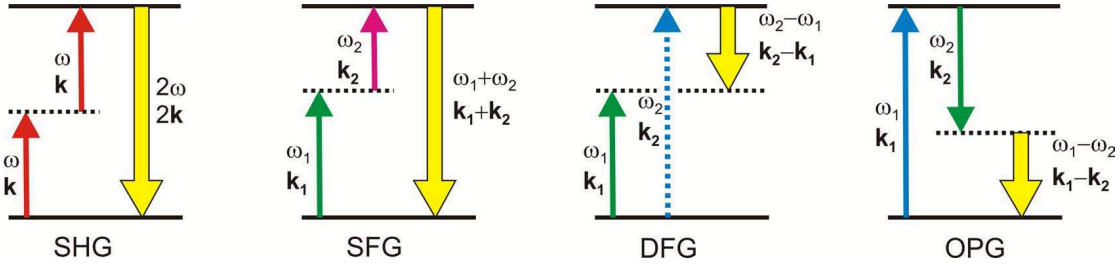

Figure 3.1: Energy-ladder diagrams representing the second-order processes in non-isotropic media: second harmonic generation (SHG), sum frequency generation (SFG), difference frequency generation (DFG), and optical parametric generation (OPG).

that the highest peak intensities are encountered if the modes are phase-locked, because the total energy is then confined to narrow pulses in time. By an aperture inside the laser a preferred amplification of self-focused pulses is achieved, so that mode-locking is favoured. The output of the oscillator can then be amplified in a second Ti:Sa crystal (*Chirped Pulse Amplification, CPA*).

The current experiments were performed with the following Ti:Sa laser systems:

- Femtolasers *sPro*, a multipass amplifier system generating 750 μJ pulses around 800 nm with durations of 50 fs, at a repetition rate of 500–1000 Hz.

- Clark-MXR *CPA 2001*, a regenerative amplifier systeme providing 800 μJ pulses around 776 nm with durations of 130 fs, at a repetition rate of 920 Hz.

3.2.2 Nonlinear light conversion

The output of Ti:Sa lasers is limited to the spectral range around 800 nm. Pulses at other wavelengths can be generated in nonlinear optical materials. Most commonly, second-order processes are used. In the formalism developed in the previous chapter, the induced second-order polarization can be written as

$$P^{(2)}(\mathbf{r},t,0) = \int_0^\infty dt_2 \int_0^\infty dt_1 R^{(2)}(t_2,t_1) E^{(2)}(\mathbf{r},t,t_2,t_1), \tag{3.1}$$

with the second-order field product

$$E^{(2)}(\mathbf{r},t,t_2,t_1) = E(\mathbf{r},t-t_2-t_1)E(\mathbf{r},t-t_2). \tag{3.2}$$

As before, the total electric field at time t is the sum of the electric fields $E_{1,2}$ of the incoming pulses:

$$E(\mathbf{r},t) = \widetilde{E}_1(\mathbf{r},t)\exp\left(-i\omega_1 t + i\mathbf{k_1}\mathbf{r}\right) + \widetilde{E}_2(\mathbf{r},t)\exp\left(-i\omega_2 + i\mathbf{k_2}\mathbf{r}\right) + cc. \tag{3.3}$$

Energy-ladder diagrams of pathways for commonly applied processes are shown in 3.1. Note that, in contrast to third-order spectroscopy, the electric signal field is always generated with the sum or difference of the frequencies and k-vectors of the incoming pulses. Consider now propagation of the generated signal field through the nonlinear material in z direction. For a description, the phase mismatch $\Delta k = k_z - k_{z,1} - k_{z,2}$ needs to be taken into account. The Maxwell wave equation in the slowly varying envelope approximation is then given by

$$\frac{\partial}{\partial z}\widetilde{E}(z,t) = \frac{ik_z}{2\epsilon_0}\widetilde{P}(z,t)e^{-i\Delta kz}. \tag{3.4}$$

Efficient conversion requires phase matching, *i.e* $\Delta k = 0$. Since the wavenumber k is connected to the frequency by $k = \omega/(nc_0)$ and the frequencies of the involved light fields are different, phase matching has to be achieved via the adjustment of the refractive index n. In practice, birefringent crystals are used, and phase matching is adjusted by tuning the angle of the optical axis. One of the most employed materials for light conversion in the UV-vis spectral range is β-BaB_2O_4 (BBO). It combines high conversion efficiency with a wide transparency range and high damage threshold.

By combination of the second-order processes in figure 3.1 pulses over the full range from the UV to the far infrared can be produced. Conversion with tunable output frequencies can be achieved with parametric amplification. In parametric generation (OPG) an incident *pump* pulse with frequency ω_1 is split into two pulses: the *signal* with frequency ω_2 and the *idler* with frequency $\omega_1 - \omega_2$. The process can be stimulated by a *seed* pulse, thus defining the frequencies of the output pulses.

White light continuum can be generated by focusing ultrashort light pulses into a material like sapphire or CaF_2. Spectral broadening is induced by a number of higher-order processes like self-phase modulation, stimulated Raman emission, and multi-photon ionization. [60,61]

3.3 Fluorescence Upconversion

The broadband fluorescence-upconversion was already described in references [62–64]. The setup is based on theFemtolasers *sPro* system. Measurements are recorded with actinic excitation at two different wavelengths: pulses at 400 nm (4 μJ, 40 fs) are generated by frequency-doubling part of the fundamental; 440–450 nm pulses (0.5 μJ, 50 fs) are provided by a *TOPAS* (Light Conversion) in combination with frequency mixing. The pump beam is focused with the lens L_1 to a diameter of 80 μm onto a 0.5 mm sample cell. The fluorescence is collected with an off-axis Schwarzschild objective (M_2 and M_3) and 1:7 imaged onto a KDP crystal (0.3 mm, 65°). For gating the 1340 nm idler pulses from the *TOPAS* are used. Spatial separation of the upconverted beam is assured by overlapping fluorescence and gate beams at an angle of 20° on the KDP crystal. In this geometry, optimal time resolution is only reached if the wave fronts of the incident pulses are matched. In the setup the gate pulses are simultaneously compressed and have their pulse front tilted with a combination of the three prisms P_1–P_3 (SF59)

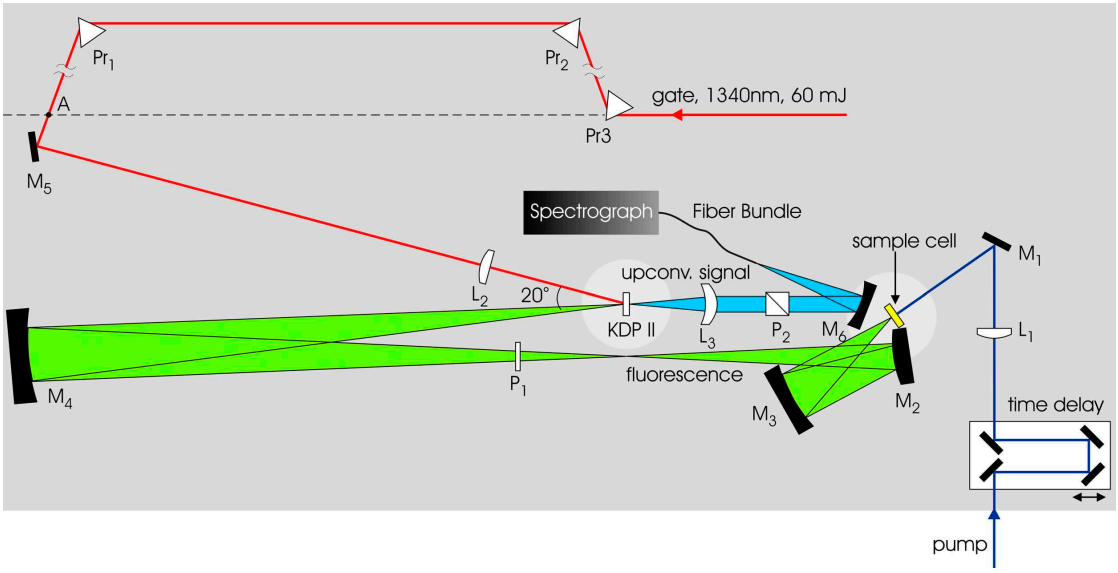

Figure 3.2: The fluorescence upconversion setup

and a 140 mm lens, L_2. The upconverted signal is imaged onto a fiber, dispersed in a prism or grating spectrograph, and detected with a CCD camera (ANDOR *NEWTON*). Recorded spectra are corrected for instrumental factors such that transient spectra at long delay times match the stationary fluorescence. The temporal apparatus function is limited by the pump and gate pulse durations, and the adjustment of the wave front tilt. Depending on the experimental conditions, it is described by a Gaussian of 80–350 fs width (FWHM).

3.4 Single-Shot Referencing in Transient Absorption and Raman Spectroscopy

Femtosecond transient-absorption and stimulated Raman spectroscopy are strongly related from a conceptual point of view: it becomes possible to measure time-resolved Raman scattering in a pump-probe experiment by applying an additional narrow-band Raman pulse (although the experimental realization is not trivial). It is advantageous to use a common measurement setup, to achieve mutual improvements in both techniques.

The available spectroscopic information depends on the balance between spectral coverage and resolution. Vibronic bands in transient-absorption spectroscopy are usually broadened in solution, and a reliable distinction between different potential intermediates requires broadband detection. An optical probe of up to 22000 cm^{-1} spectral width is provided here by multi-filament supercontinuum pulses, which are generated when focusing femtosecond pulses into a CaF_2 crystal. When handling the resulting inhomogeneous and divergent beam, accurate imaging of the spot from the CaF_2 crystal onto the sample cell and the detection array is necessary to avoid spectral and temporal

artefacts. For many Raman-spectroscopic applications, on the other hand, the most important vibrations are found in the region 0-1700 cm^{-1} relative to the Raman pulse. This range covers C=C and C=O stretch, as well as bending, deformation and torsion modes. Experimentally, such spectral width is already accessible directly with a non-collinear optical parametric amplifier. To discriminate between individual vibrational bands and capture subtle spectral shifts, the resolution should reach the order of 10 cm^{-1}.

Small signal amplitudes make noise reduction an important issue in nonlinear spectroscopy. Transient absorption depends to the third order on the incoming electric field, and the induced intensity changes in the probe pulse amount to only several percent at most. Femtosecond stimulated Raman spectroscopy is even a fifth-order experiment, and the signals are typically 100 times weaker than in pump-probe spectroscopy. The main source of noise are variations of the laser intensity and beam position, leading to continuum fluctuation of 1–10% between each shot. The corresponding noise may be reduced by monitoring the fluctuations in a reference experiment. Setups which were described recently,[65,66] use subsequent sample and reference pulses of the probe beam. With this approach the correlation between two successive laser pulses is exploited.[67] The signal/noise ratio can be further improved by extensive averaging. However, when working with biological samples, laser irradition, mechanical forces, and interaction with interfaces constantly expose the sample to stress, so that measurement is often a race against time. Single-shot referencing can significantly reduce the necessary number of sample averages, since high precision can be obtained even if successive probe pulses are uncorrelated. The measurement geometry is the result of constant improvement over a decade, and is further detailed in ref.[68].

Two identical setups are used. One is driven by the Femtolasers *sPro* system. Pulses for continuum generation (20 μJ) are usually taken from the frequency-doubled beam. Pump pulses (0.6 μJ) are conveniently generated at 400 nm or 267 nm, and other pump wavelengths are reached by parametric optical amplification (Light Conversion *TOPAS*). The other setup is driven by the Clark-MXR *CPA 2001* system. In this case, 30 fs probe pulses are generated at 520 nm in a 2-stage non-collinear optical parametric amplifier (Jobin Yvon *NOPA*). The 0.6 μJ pump pulses are generated in a 1-stage NOPA, followed by frequency doubling when necessary. The relative delay of the pump pulses is controlled by a delay stage (Physik Instrumente *M-531.5IM*).

The spectrograph setup is sketched schematically in Figure 3.3. Supercontinuum light is generated by focussing the probe pulses just before a 1 mm CaF_2 plate with a fused silica lens (f = 200 mm). The plate remains stationary during an acquisition sequence, but it is translated in both directions orthogonal to the beam by about 100 μm whenever the delay stage moves to a new position. (Rotation of the plate is avoided because of an intensity dependence on rotation angle, due to nonlinear interactions.) The continuum extends a full angle of about 6°, as found by an aperture stop before field mirror M_1. Residual laser light close to the optical axis is absorbed by a central stop. Multifilament generation results in a speckle pattern of about 2–6 homogeneous zones at M_1 which should be stable during the acquisition sequence. By optimizing the input beam diameter (~6 mm) and lens plate distance, measurement of transient optical density is possible from the near-IR to 270 nm. Optical relay of the supercontinuum is

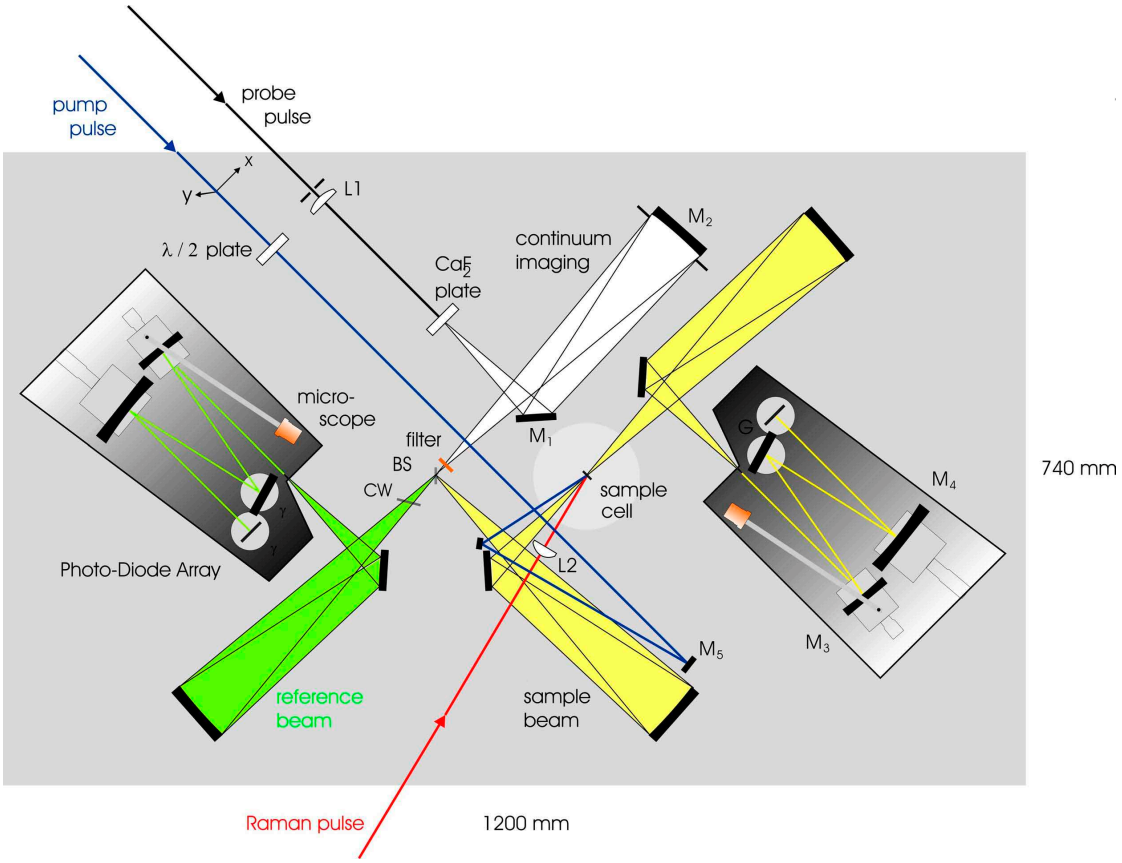

Figure 3.3: Setup for transient absorption and Raman spectroscopy. Multifilament supercontinuum generation extends the probe range from the visible into the UV to ~270 nm, but it requires optics for a 6° full solid angle at the source. For Raman spectroscopy alternatively the output of a non-collinear optical parametric amplifier is used directly. Mirror objectives allow 50 μm spot size in the sample cell and upon entrance into two spectrographs. Apertures and slits are avoided after the beam splitter BS (for notations see text).

achieved by repeated use of a 1:1 objective in an off-axis Schwarzschild arrangement. All mirrors are aluminium coated with enhancement optimized around 300 nm. The first objective images the supercontinuum source 1 mm in front of beam splitter BS. About 20 mm before the beam splitter, the light passes through a color filter which is made with a flow cell (0.3 mm internal path length between 0.2 mm thick fused silica windows). BS has approximately 40% transmission and 40% reflection for the front surface of a fused silica substrate. Light reflected from the front surface is used for optical probing and transmitted light for reference, as shown in Figure 3.3. In this arrangement, a lateral displacement of the source leads to equivalent displacements on the entrance planes of the two spectrographs. A counter-wedge (CW) in the reference beam cancels the angular dispersion which is caused by BS, and its partial reflection balances the additional losses

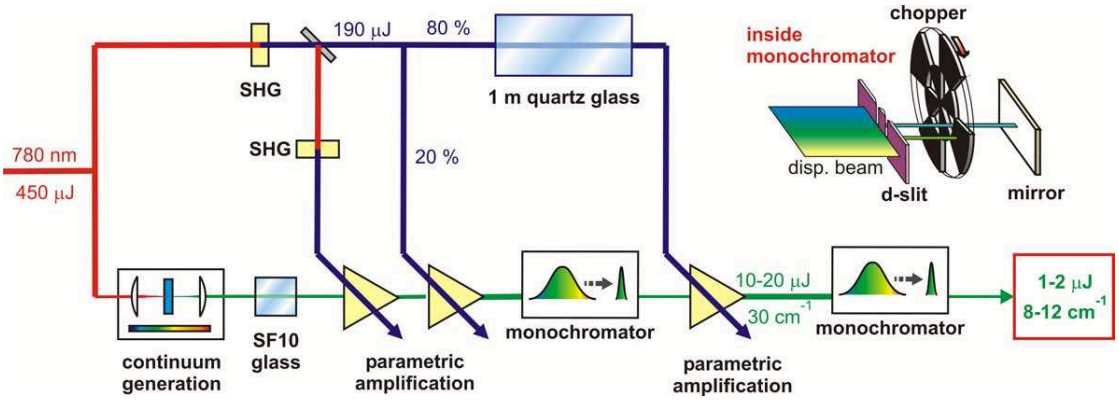

Figure 3.4: Setup of the narrowband Raman-NOPA. A white-light continuum is generated, chirped through 5 mm SF10 glass, and amplified parametrically in 2 stages. It is then filtered in a monochromator and further amplified parametrically. For this stage the pump beam is stretched by passing it through 1 m of quartz glass. The NOPA output is tunable from 480 to 700 nm, typical output powers of 10-20 *mu*J at 30 cm^{-1} spectral width (FWHM) have been obtained in the range 500-620 nm . A second monochromator further narrows the spectrum to 8-12 cm^{-1}. As shown in the inset, the monochromators contain double slits enabling the generation of pulses at two different wavelengths shifted by 30-40 cm^{-1}. They are selected in the first monochromator via a chopper (chopping pattern simplified in the scheme).

in the sample beam.

The spectrographs employ a Czerny-Turner mount of a ruled plane grating. For transient absorption, gratings with about 200 lines/mm are used (for example NEWPORT *53-346R*) to map continuum in the range 270–690 nm onto the 1/2" photodiode-array (see below). Alternatively, the probe light is dispersed in double-prism spectrographs, which provide higher transmission in the near-infrared spectral range, and allow to cover the range 330–1030 nm. For the dispersion of Raman spectra gratings with 2400 lines/mm (NEWPORT) are used. Each spectrograph is equipped with a microscope which can be swivelled into the beam. It allows to adjust the supercontinuum alignment and monitor the pump-probe overlap region in the flow cell. Inside the spectrographs the dispersed probe light is detected with NMOS linear image sensors with 512 pixels (HAMAMATSU *S3904-512Q*). Typically 50 spectra are averaged at 660 points in time. The full delay time window is covered by recording measurement runs with different time steps between 6 and 1000 fs. Data from approximately 5–10 measurement runs is averaged to give the final signal.

3.5 The Femtosecond Stimulated Raman Spectrometer

3.5.1 The Narrow-band Optical Parametric Amplifier

The aquisition of Raman spectra with high frequency resolution and decent signal/noise requires a source for spectrally narrow Raman pulses of reasonable brightness. Around 776 nm, these requirements can be easily met by filtering part of the output of the Clark *CPA2001* amplifier system in a monochromator. With this approach Raman pulses with energies of 3.7 μJ and spectral widths of 5.5 cm^{-1} are achieved. However, the simulation of Raman signals in chapter 2.4.2 and the experimental Raman spectra of flavin in chapter 6 demonstrate that the measured signal strongly depends on the resonance conditions of the Raman pulse. To study and optimize resonance conditions, it is necessary to generate Raman pulses also at other wavelengths. This can be achieved by applying nonlinear optical processes. Narrowband pulses at 400 nm were previously obtained by sum frequency generation of counter-chirped fundamental pulses.[16] Whereas this approach is limited to a narrow frequency range around 400 nm, optical parametric amplification is a convenient tool to provide tunable pulses in the visible and near-infrared region.[69,70] Nowadays, sub-10 fs pulses can be routinely obtained, spanning a frequency range of several thousand wavenumbers at a time.[71–74] In comparison, the development of amplification schemes for the creation of spectrally narrow pulses still lags behind. The conversion process is usually not efficient enough that filtering of the output pulses of optical parametric amplifiers would be a conceivable approach to obtain spectrally narrow pulses. In a recent publication by Shim *et al.* the direct amplifation of narrowband pulses was demonstrated.[75] The obtained output pulses featured energies of up to 2.5 μJ and a spectral width of 36 cm^{-1}. However, the total conversion efficiency was small, considering that input pulse energies of 800 μJ were necessary.

Raman spectra of chromophores with low symmetry are higly congested. Hence, for a reliable tracking of relaxation in biological photoreceptors, one should strive for an improvement of the spectral resolution to ~10 cm^{-1} . On the other hand, in the current experiment only 450 μJ of the the fundamental was available for the generation of Raman pulses. A key requirement was therefore the development of an efficient narrow-band optical parametric amplifier (*nb*-OPA).

The setup of the *nb*-OPA is presented in 3.4; it is pumped by a 450 μJ portion of the Clark *CPA 2001* output. The first part of the setup resembles a common two-stage non-collinear optical parametric amplification in a 2 mm BBO crystal (type I, $\theta = 29°$).[70] A small fraction (ca. 2%) of the incoming light is separated with a beam splitter and focused with a lens (f = 50 mm) into a 2 mm thick sapphire plate to generate a continuum; the white light is recollimated with a second lens (f = 50 mm) and focused into the BBO crystal for amplification. In order to decrease the spectral width of the amplified beam, the continuum seed is chirped by 5 cm of SF10 glass. The residual ~98 % of the fundamental is frequency doubled in a 2 mm thick BBO crystal (type I, $\theta = 29°$) resulting in 190 μJ of blue light. Optimal conversion is achieved by decreasing the near-infrared beam size with a 2:1 telescope to a diameter of 3 mm. For pumping the first stage it is sufficient to separate the residual from the previous second-harmonic

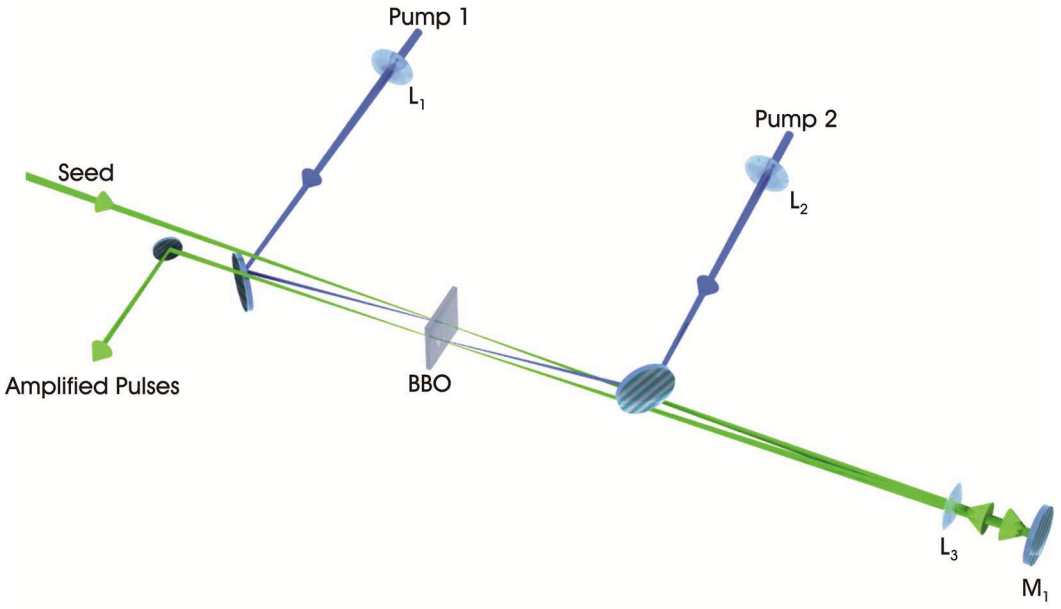

Figure 3.5: First two stages of amplification in the *nb*-OPA. The 400 nm pump beams are focused 1 cm in front of the BBO crystal (2 mm, 29°) with lenses L_1 and L_2 ($f = 200$ mm). The continuum seed ist focused into the BBO and overlapped with pump 1 for amplification. Thereafter, it is passed a second time through the crystal, thereby collimated and refocused with lens L_3 ($f = 200$ mm).

generation with a dielectric mirror and frequency-double it again in another BBO crystal. For the subsequent amplification stage 20% of the main blue light is separated with a beam splitter. Both amplification stages were realized in the nonlinear crystal with a folded geometry (see figure 3.5). The seed is collimated after the first pass through the crystal with lens L_3 ($f = 200$ mm) and back-reflected by mirror M_1 to pass the crystal a second time, thereby again being focused by lens L_3. The pump beams are focused with lenses L_1 and L_2 ($f = 200$ mm) to points 1 cm before the BBO crystal, and overlapped with the seed inside the crystal. Typically, 11 μJ of visible pulses with a bandwidth of 100 cm^{-1} are obtained. Due to the time-bandwidth relationship the minimal spectral width is limited by the pump pulse duration. As already demonstrated by Mathies *et al.*, temporal stretching of the blue light pulse enables the amplification of a narrowband seed.[75] Here, temporal broadening is achieved by passing the residual blue light through 1 m of quartz glass. Experimentally, this is realized by sending the blue light five times through a quartz block with 20 cm length (Heraeus *HOMISIL*), whoose end surface are cut at Brewster angle. To avoid continuum generation inside the glass, the beam diameter is enlarged with a telescope to 30 mm. The outcoming pulses are then used to drive the third amplification stage. As seed, the output from the previous amplification stage is filtered in a grating monochromator. The monochromator has a conventional 4f arrangement, consisting of a holographic grating with 2400 lines/mm (Newport), a lens

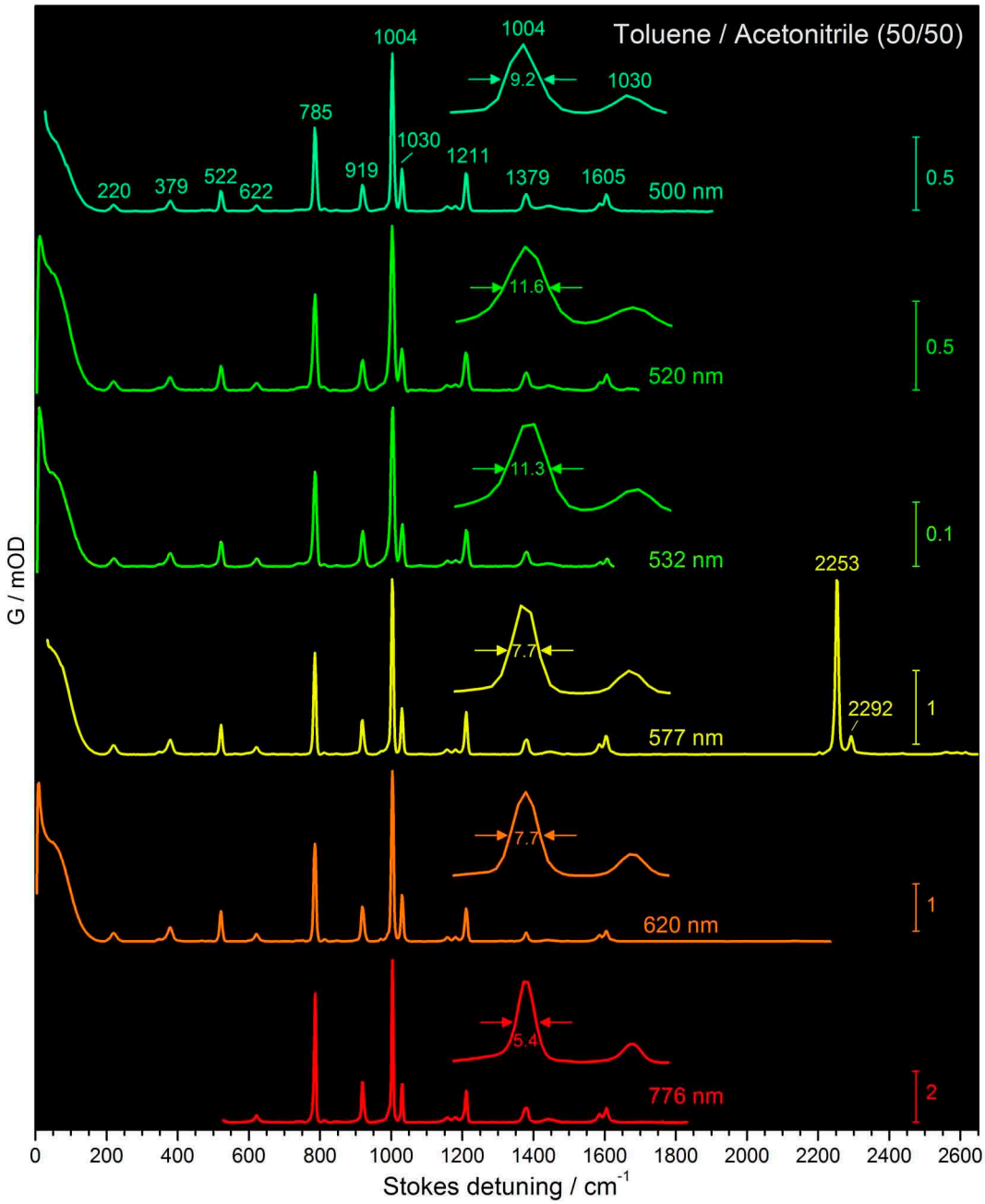

Figure 3.6: Tunability of the Raman pulse demonstrated for stimulated state Raman spectra of a toluene/acetonitrile (50/50) mixture. Insets show the width of the 1004 cm^{-1} band.

with f = 300 mm, and a back-reflecting mirror. Amplification of the narrowband seed in a 2 mm BBO crystal (type I, $\theta = 29°$) with nearly collinear pump/seed geometry results

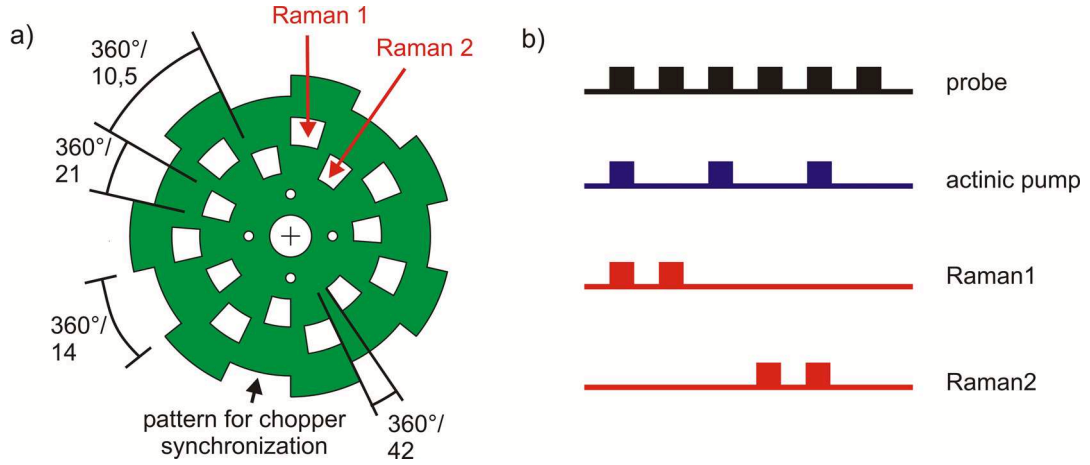

Figure 3.7: a)Layout of the chopper wheel in the *nb*-OPA. Designed for a NEW FOCUS chopper model *3501*, model 3501. b) Raman pulse sequence: In a repeated cycle of 6 submeasurements, transient absorption, ground and transient Raman spectra can be obtained. The sequence was achieved with two choppers: one in the monochromator of the narrowband OPA and one in the pump beam. Each square represents a single pulse.

in 10-20 μJ of visible pulses with 30 cm^{-1} spectral width (FWHM). In a second grating monochromator the pulses are further filtered to match the resolution of the Raman spectrograph (7.5–15 cm^{-1} in the visible), leaving 1–2 μJ pulse energy. The tunability of the Raman pulses is demonstrated in figure 3.6 for stimulated Raman spectra of a toluene/acetonitrile (50/50) mixture. A close-up of the 1004 cm^{-1} band in the inset shows the spectral resolution.

To facilitate the evaluation, the monochromators are equipped with a double slit (3.4, inset), enabling the amplification of the seed at two wavelengths which differ by 30–60 cm^{-1}. A chopper (NEW FOCUS *3501*) in the *nb*-OPA selects between the two (Raman1 and Raman2); for the design of the chopper wheel see figure 3.7a.

3.5.2 Measurement Details

Raman measurements were performed by overlapping 0.5–1.2 μJ of the narrowband pulses with the pump and probe beams on the sample cell. The delay between probe and Raman pulses is adjusted for maximum signal intensity. Spectra are acquired at two Raman wavelengths (Raman1, Raman2), which are selected by the chopper within the *nb*-OPA. In combination with a chopper in the pump beam, a repeated cycle of six different pulse sequences is generated, see figure 3.7 b. From the measured intensities transient absorption (TAS), ground (G) and transient (Σ) Raman spectra can be

obtained with consecutive shots in the same experiment,

$$TAS = -\log\left(I_{pu+pr}/I_{pr}\right), \tag{3.5a}$$

$$G^{(1/2)} = \log\left(I_{R1/2+pr}/I_{pr}\right), \tag{3.5b}$$

$$\Sigma^{(1/2)} = \log\left(I_{pu+R1/2+pr}/I_{R1/2+pr}\right) + TAS. \tag{3.5c}$$

Here the intensities I are reference-corrected, i.e. $I = I_{signal}/I_{reference}$, and the indices correspond to Raman1/2 (R1/2), probe (pr) or pump (pu) beam turned on, respectively. As the signal amplitude is small, S_{GR} and S_{TR} approximately equal the Raman gain, the quantity presented in publications of the Mathies group.[19] In the calculation of Σ, equation (3.5c), the stationary Raman signal G of both solvent and solute is implicitly removed.

Scattering at the sample cell surfaces causes an emissive-like feature around the Raman pump wavelength which appears in the ground state spectra only (excited-state spectra involve a subtraction). To remove this artefact from spectra extending to lowest Stokes frequencies (< 100 cm^{-1}), after each measurement the Raman pulses are delayed by 13 ps with respect to the probe pulses. Loss of temporal overlap causes the Raman spectrum to vanish, while the stray light is unaffected and may be subtracted from the previous measurement. Some raw spectra show a ripple in the baseline which originates from interference at the thin sample cell windows. The ripple is removed by a Fourier filter.

The following notations are used subsequently:

$\Sigma^{(i)}(t, \widetilde{\nu})$	Raman-induced change in transient absorption spectrum at delay time t (equation (3.5c); i refers to Raman1 or Raman2),
$\widetilde{\nu}$	measured optical frequency,
$\widetilde{\nu}^{(i)}$	measured optical center frequency of Raman1 or Raman2 excitation pulses, respectively,
ν	Stokes detuning, $\widetilde{\nu}^{(i)} - \widetilde{\nu}$.

The dependence on detuning ν or delay time t will not be written explicitly if misunderstanding is unlikely.

3.5.3 Spectral Calibration

The absolute frequency scale $\widetilde{\nu}$ and the optical center frequencies $\widetilde{\nu}^{(i)}$ are determined with the atomic lines of neon and mercury in combination with Raman shift standards (ASTM E 1840, cyclohexane and a 50/50(v/v) toluene/acetonitrile mixture, see 3.6). The signal is usually plotted against Stokes detuning ν.

The spectral range can be extended by combining measurements with different detection windows. Usually, measurements are scaled to equal amplitudes for bands in the overlap region (see 3.8 top, shaded grey). Measurements of *trans*-stilbene in acetonitrile

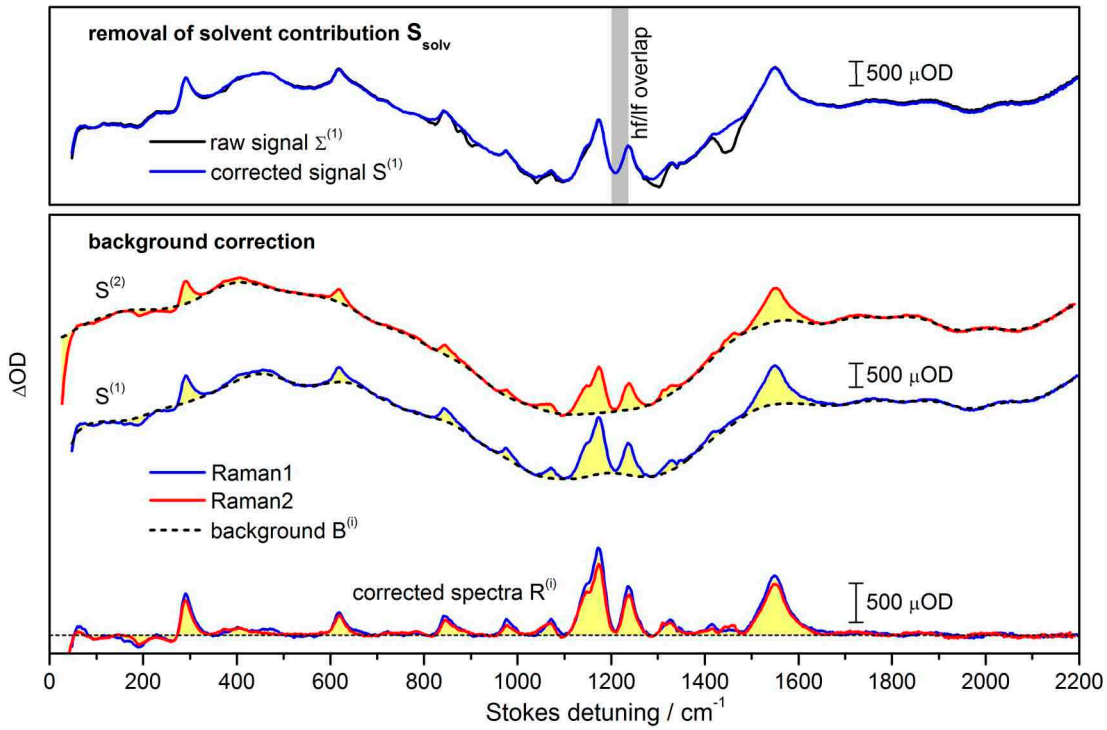

Figure 3.8: Summary of signal processing, illustrated for *trans*-stilbene in *n*-hexane at 0.5 ps delay. *Upper panel*: The raw signal for low- and high-frequency region is merged (given in black for Raman1, $\Sigma^{(1)}$); the spectral overlap is marked by the grey shaded area. A contamination with ground-state solvent spectra is removed resulting in the spectrum $S^{(1)}$ (blue). *Lower panel*: The signals $S^{(1)}$ and $S^{(2)}$ (blue and red, respectively) are corrected for a slowly varying background $B^{(1)}$ and $B^{(2)}$(dashed black) leaving the Raman spectra $R^{(1)}$ and $R^{(2)}$.

lack a similar band in the overlap region. They are instead scaled with the help of stationary solvent Raman spectra and the transient absorption amplitude.

3.5.4 Subtraction of Solvent Features

The extraction of the Raman signal from the measured data is summarized in 3.8 with *trans*-stilbene in *n*-hexane as an example. The raw signal $\Sigma^{(i)}$, by construction, has the non-resonant solvent signal $G^{(i)}$ already subtracted. In addition to the stilbene spectral information $S^{(i)}$, however, it contains a further transient contribution $S^{(i)}_{solv}$ from the solvent,

$$\Sigma^{(i)}(\nu) = S^{(i)}(\nu) + S^{(i)}_{solv}(\nu). \tag{3.6}$$

The non-resonant $S^{(i)}_{solv}$ can have different origins: (i) incomplete subtraction of the strong stationary solvent spectrum due to detector nonlinearity, (ii) nonlinear pump/Raman

pump/probe interactions, and (iii) formation of vibrationally excited solvent molecules by impulsive Raman scattering of the actinic pump pulse.

At each delay time the transient solvent signal is modeled as the scaled stationary Raman spectrum $G^{(i)}_{solv}$, shifted by a small frequency displacent $\delta\nu$. Then the pure solute signal is obtained as

$$S^{(i)}(\nu) = \Sigma^{(i)}(\nu) - \lambda G^{(i)}_{solv}(\nu + \delta\nu), \tag{3.7}$$

with optimized λ; $\delta\nu$. This correction is demonstrated in 3.8, *top*.

3.5.5 Background Correction

The signal $S^{(i)}$ comprises the transient Raman signal $R^{(i)}$ superimposed on a slowly varying background $B^{(i)}$ from further nonlinear interactions. In previous publications the background has been modelled by splines or polynomials.[16,19] The performance of this correction depends on the actual background that is described. Whereas such an approach is well suited for stationary Raman spectroscopy, in transient Raman spectroscopy it is important to remove the background at all delay times consistently. Note that during an FSRS measurement the background may vary significantly, since it represents mainly a bleach of the transient absorption signal induced by the Raman pump. In particular, wave packet motion in the ground or excited state causes an oscillatory modulation of the Raman background. Any correction method that relies on a description of the background shape translates deviations from the model function directly into fluctuations of the Raman baseline. Since the background is large compared to the signal, this may render an analysis of the temporal evolution of the Raman spectra impossible. In this view it appears advantageous to derive the baseline position from a description of the Raman signal itself. In this work a correction procedure was developed, in which global analysis is used to obtain a spectral basis set to the Raman signal.

Generation of a Spectral Basis to the Raman Signal

In contrast to the Raman signal itself, the background is rather insensitive to small changes of the Raman center frequency $\widetilde{\nu}^{(i)}$. For an ideal measurement one expects a linear shift response of $R^{(i)}$ while the background $B^{(i)}$ stays constant,

$$S^{(1)}(\widetilde{\nu}) = R^{(1)}(\widetilde{\nu}) + B^{(1)}(\widetilde{\nu}), \tag{3.8}$$

$$\begin{aligned} S^{(2)}(\widetilde{\nu}) &= R^{(2)}(\widetilde{\nu}) + B^{(2)}(\widetilde{\nu}) \\ &= R^{(1)}(\widetilde{\nu} + \widetilde{\nu}^{(2)} - \widetilde{\nu}^{(1)}) + B^{(1)}(\widetilde{\nu}). \end{aligned} \tag{3.9}$$

Hence, recording spectra with two frequency-shifted pulses can help to identify the Raman features $R^{(i)}$. In the setup presented above, a chopper switches between the two Raman frequencies on a shot-to-shot basis, thus maximizing the correlation of background fluctuations. Both spectra are compared in 3.8, middle, as a function of Stokes

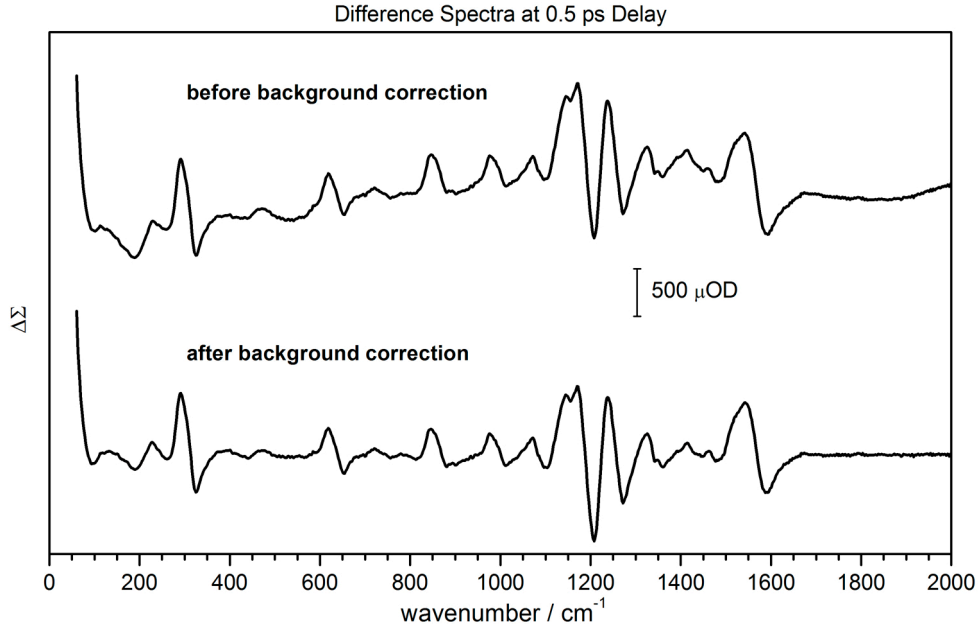

Figure 3.9: Difference Spectra of *trans*-stilbene in *n*-hexane at 0.5 ps delay, given in the Stokes-shift scale ($\widetilde{\nu}^{(1)} - \widetilde{\nu}$) of Raman1.

detuning ν. The similarity of the estimated background spectra (dashed black) is evident. If they were exactly equal, a formation of the difference spectrum ΔS would cancel the two contributions, leaving only the Raman features,

$$\begin{aligned} \Delta S(\widetilde{\nu}) &= S^{(1)}(\widetilde{\nu}) - S^{(2)}(\widetilde{\nu}) \\ &= R^{(1)}(\widetilde{\nu}) - R^{(2)}(\widetilde{\nu}). \end{aligned} \tag{3.10}$$

As shown in 3.9, top, the experimentally obtained difference spectrum ΔS still bears a non-vanishing background. The residual may result either from changes in the nonlinear interaction or from small deviations in the experimental conditions between the two Raman experiments. As a consequence, the equality of $B^{(1)}$ and $B^{(2)}$ was not assumed for background correction, and the $B^{(i)}$ were determined individually. The strong correlation between $R^{(1)}$ and $R^{(2)}$, however, was used to identify the Raman features.

The temporal evolution of a Raman band may be reproduced reliably only with a consistent data treatment over all delay times. In previous publications the background has been modeled by splines.[16] [19] To extract Raman peaks, which evolve gradually on a fluctuating background, it seems advantageous to describe the Raman signal itself. Here the transient Raman spectra are approximated by a linear combination of spectral basis functions. This allows an initial background guess which is then refined. As an example *trans*-stilbene measured in *n*-hexane with 6 fs steps is discussed (*cf.* 3.8).

Starting from $S^{(i)}$ we search for an approximation to $R^{(i)}$ which takes into account

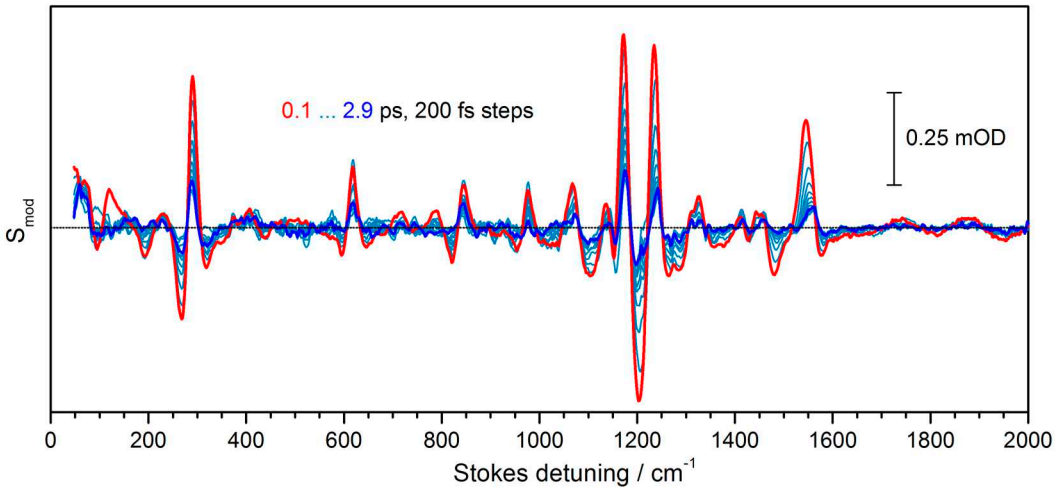

Figure 3.10: Modified Raman signal $S_{mod}(\nu) = \left(S^{(1)}(\nu) + S^{(2)}(\nu)\right)/2$ of *trans*-stilbene in *n*-hexane at different delay times.

the temporal evolution of the Raman signal. An operation is required that allows to extract the time-dependence of the Raman features $R^{(i)}(t)$. One choice would be the frequency derivative $\frac{dS^{(i)}}{d\nu}$, since the background may be assumed to change only slowly with frequency. This would, however, enhance the baseline noise, and therefore a different approach was chosen: a 30-point (60-80 cm^{-1}) moving average $\mathbf{A}_{30}$ is applied to $S^{(i)}$ and subtracted, to obtain

$$S^{(i)}_{mod} = S^{(i)} - \mathbf{A}_{30}S^{(i)}. \tag{3.11}$$

In a summation the moving average works distributively, hence

$$\mathbf{A}_{30}S^{(i)} = \mathbf{A}_{30}R^{(i)} + \mathbf{A}_{30}B^{(i)}. \tag{3.12}$$

As the background may be assumed to vary only slowly with frequency, $\mathbf{A}_{30}B^{(i)} \approx B^{(i)}$ and

$$S^{(i)}_{mod} = R^{(i)} - \mathbf{A}_{30}R^{(i)}. \tag{3.13}$$

3.10 demonstrates that the modified spectra reflect the Raman spectral evolution, although the signal shape is distorted.

A global multiexponential analysis is now performed on $S^{(i)}_{mod}$, as described in Section 3.6.2. In the current example (3.10), $S^{(i)}_{mod}$ is fitted with two exponential functions (τ_1 = 0.35 ps, τ_2 = 1.1 ps) and an offset ($\tau_3 = \infty$); the exponential sum is convoluted with a Gaussian system response of 0.15 ps full width at half maximum. Next, a three-state model is introduced assuming that the states interconvert according to the formal kinetic

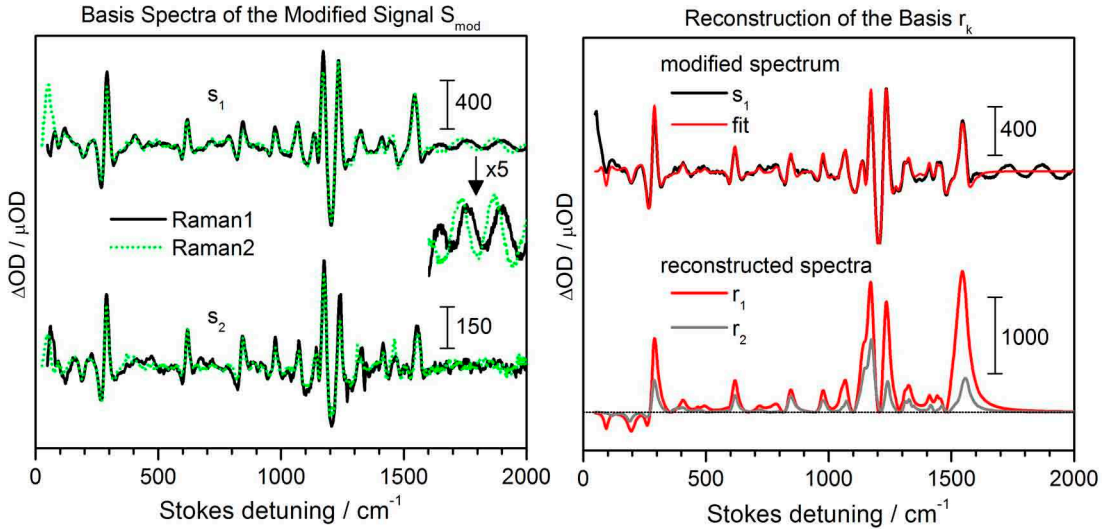

Figure 3.11: Basis spectra $s_k^{(i)}$ (for Raman1 and Raman2) as derived from a global fit of the modified Raman signal $S_{mod}^{(i)}$ of *trans*-stilbene in *n*-hexane with 0.35 and 1.1 ps decay times. *Right*: Fit of s_k exemplified for s_1 (*top*, Raman1 and Raman2 averaged), and reconstruction of the Raman spectra r_1 and r_2.

sequence 1→2→3. The exponential description of $S_{mod}^{(i)}$ is then transformed[76] into

$$S_{mod}^{(i)}(\nu,t) = a_1(t)s_1^{(i)}(\nu) + a_2(t)s_2^{(i)}(\nu) + a_3(t)s_3^{(i)}(\nu). \tag{3.14}$$

Here the basis spectra $s_k^{(i)}(\nu)$ (commonly refered to as *evolution associated spectra*) are time-independent; the time-dependence is captured by the (relative) populations $a_k(t)$, which apply to both Raman1- and Raman2-generated transient spectra. Finally, the spectral basis is reduced to those spectra which describe the dominant spectral changes clearest, in the present example s_1 and s_2.[1] The spectra s_1 and s_2 are compared in 3.11, *left* (note that $s_k^{(1)}$ and $s_k^{(2)}$ are shown as a function of Stokes shift ν). The Raman features are clearly visible and highly reproduced for both excitation wavelengths.

The spectra $S_{mod}^{(i)}$ are now expressed in the reduced basis by fitting their coefficients $a'_k(t)$ at each delaytime,

$$S_{mod}^{(i)}(\nu,t) = a'_1(t)s_1^{(i)}(\nu) + a'_2(t)s_2^{(i)}(\nu). \tag{3.15}$$

[1] For the correction of the *trans*-stilbene measurement discussed here, s_1 and s_2 form a sufficient basis. The offset s_3 could be included as well but was dismissed due to the lower signal/noise level.

Similarly, the Raman spectra can be expanded in a basis $r_k^{(i)}$ as

$$R^{(i)}(\nu,t) = a_1'(t)r_1^{(i)}(\nu) + a_2'(t)r_2^{(i)}(\nu). \tag{3.16}$$

The basis spectra are related via

$$s_k^{(i)}(\nu) = r_k^{(i)}(\nu) - \mathbf{A}_{30}r_k^{(i)}(\nu). \tag{3.17}$$

For reconstruction (3.11, *right*), every $r_k^{(i)}$ is described by a sum of Lorentzians L_j and their first derivatives,

$$r_k^{(i)}(\nu) = \sum_j \left(c_j L_j(\nu) + d_j \frac{dL_j(\nu)}{d\nu} \right). \tag{3.18}$$

The coefficients c_j and d_j, and the spectral positions and widths of the Lorentzians are determined by fitting the basis spectra $s_j^{(i)}$ for both Raman wavelengths ($i = 1, 2$) simultaneously. In the fit the equality of $s_k^{(1)}(\nu)$ and $s_k^{(2)}(\nu)$ on the Stokes detuning scale is introduced,

$$\begin{aligned} s_k(\nu) = \sum_j \Big[& c_j(L_j(\nu) - \mathbf{A}_{30}L_j(\nu)) \\ & + d_j \left(\frac{dL_j(\nu)}{d\nu} - \mathbf{A}_{30}\frac{dL_j(\nu)}{d\nu} \right) \Big]. \end{aligned} \tag{3.19}$$

The shifted Raman spectra are used to identify the Raman features. For example, the oscillatory features at frequencies > 1700 cm^{-1} can be assigned to background noise. As positive and negative peaks contribute to the signal, this reconstruction is not unique and has to be guided by comparison to the raw data. The information available for the fitting procedure depends on the length of the applied moving average. If the moving average window is smaller, background rejection is stronger and the shape in spectrally congested regions becomes clearer. On the other hand, also the amplitude of broad Raman bands will be reduced, and their reconstruction becomes more difficult.

Generation of the Background Spectrum

An approximation to the Raman spectrum $R^{(i)}$ at each delay time (here denoted as $R_{appr}^{(i)}$) is now constructed by inserting $r_k^{(i)}$ into equation 3.16. Subtraction from the initial signal $S^{(i)}$ then gives an approximation to the background spectrum.

$$B_{appr}^{(i)} = S^{(i)} - R_{appr}^{(i)}. \tag{3.20}$$

By smoothing this spectrum with a 30-point moving average, one arrives at the final estimate for the background

$$B^{(i)} = \mathbf{A}_{30}B_{appr}^{(i)}. \tag{3.21}$$

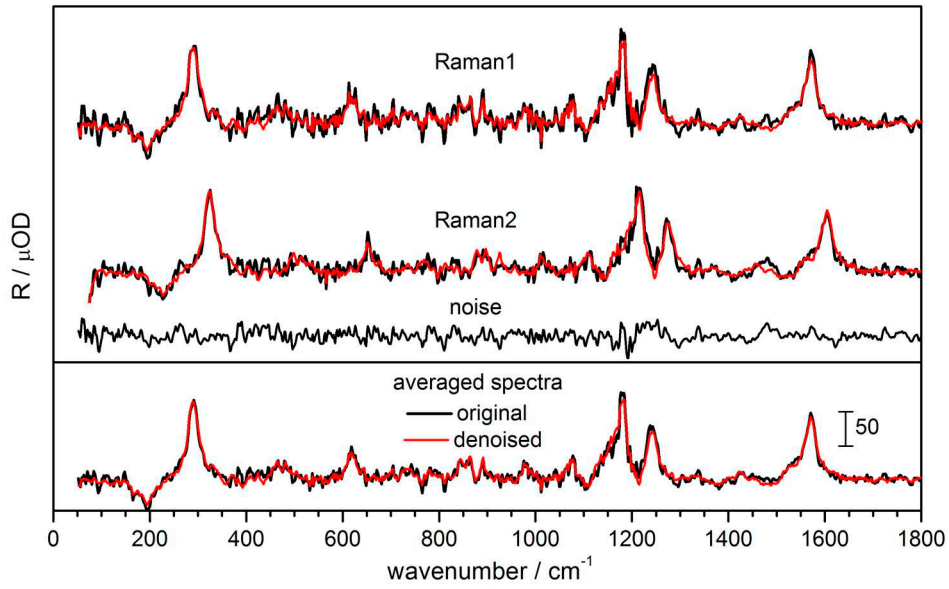

Figure 3.12: Transient Raman spectra of trans-stilbene in *n*-hexane at 60 ps delay (black), and spectra after subtracting a noise guess S_{noise} which is common for both signals, Raman1 and Raman2.

The Raman spectrum $R^{(i)}$ is obtained as

$$R^{(i)} = S^{(i)} - B^{(i)}. \tag{3.22}$$

Spectrally sharp features which were not reproduced by the base spectra, enter the signal during this step due to the previous smoothing of the background. The background and the retrieved signals are also shown in 3.8.

The dependence of the Raman peak positions on the excitation wavelength was used here to improve the signal recognition during the fitting of the basis spectra $s_k^{(i)}$. In an alternative approach, the Raman spectra can be reconstructed from the difference spectra ΔS (eq. 3.10), thus profiting from the inherent reduction of the background.[77,78] In stationary Raman spectroscopy this technique has been widely applied for fluorescence rejection (Shifted Excitation Raman Difference Spectroscopy, SERDS).[79,80] In the present work, however, difference formation does not completely cancel the background. The residual background and the complicated signal shape hamper spectral reconstruction. In 3.9 the difference spectra at 0.5 ps delay before and after background correction are compared. Clearly all spectral features are preserved, and the shape as well as the amplitudes are reproduced. In future, an inclusion of the difference spectrum into the correction algorithm may further reduce background artefacts.

Noise Reduction for Small Signals

For small signals at long delay times, the identitity of $R^{(1)}(\nu)$ and $R^{(2)}(\nu)$ on the Stokes-shift scale allows to guess the pixel-dependent correlated noise (3.12). The denoised spectrum R_{dn} is initially approximated as the average over $R^{(1)}$ and $R^{(2)}$, smoothed by a 4-point moving average.

$$R_{dn}(\nu) = \mathbf{A}_4 \left((R^{(1)}(\nu) + R^{(2)}(\nu))/2 \right). \tag{3.23}$$

It is subtracted from the individual Raman signals R_1 and R_2. The residuals are then averaged on the absolute frequency scale to achieve an estimate for the noise which is common to both Raman spectra,

$$\begin{aligned} S_{noise}(\widetilde{\nu}) = \; & \Big(R^1(\widetilde{\nu}) - R_{dn}(\nu + \widetilde{\nu}^{(1)}) \\ & + R^{(2)}(\widetilde{\nu}) - R_{dn}(\nu + \widetilde{\nu}^{(2)}) \Big) /2. \end{aligned} \tag{3.24}$$

On this basis, a new approximation for the denoised spectrum is obtained, and the procedure iterated:

$$\begin{aligned} R_{dn,new}(\nu) = \; & \Big((R^{(1)}(\nu) - S_{noise}(\widetilde{\nu}^{(1)} - \widetilde{\nu}) \\ & + R^{(2)}(\nu) - S_{noise}(\widetilde{\nu}^{(2)} - \widetilde{\nu}) \Big) /2. \end{aligned} \tag{3.25}$$

The algorithm slightly improves the signal/noise level while the difference spectrum stays unchanged. It is only applicable in the case of small signal/noise ratios (for example at long delay times) and if the Raman signal is equally reproduced in both R_1 and R_2.

Characteristics of the Background Correction Algorithm

In conclusion, the use of a spectral basis set to correct time-dependent Raman data has several advantages:

(i) The evolution is treated in a uniform way over all delay times. This allows to process large data sets (here typically 660 delay times) without manual adjustment.

(ii) Base spectra obtained from global analysis profit from a signal/noise improvement which allows to identify the Raman bands better.

(iii) The signal $R^{(i)}$ can be extracted from a changing background. Transient absorption artefacts like oscillations from wavepacket motion are removed.

(iv) Within the limitation of the moving average length, all sharp spectral features are retained, even if they are not included in the intermediate description by base spectra. This is demonstrated by the oscillations of individual bands and the ultrafast spectral shift of the 200 cm^{-1} mode.

The effect of background correction errors on the observables discussed in the main part is now estimated.

Raman Intensities. Insufficient reconstruction may lead to errors in the baseline position and result in systematic distortion of individual Raman bands. These deviations may be identified in the evolution associated spectra of a global fit. The general trends are therefore expected to be reproduced.

Time Constants and Frequencies. The Raman signals are extracted at each delay time individually. Therefore the main temporal behaviour is recovered, and errors in the baseline estimation will only have minor influence on characteristic temporal parameters like decay times and oscillation frequencies.

Spectral Positions. The time-dependent frequency shift is obtained from a Lorentzian fit, which may be systematicly affected by asymmetric band distorsions. Nonetheless, the relative temporal evolution is preserved. The Raman peak maxima themselves are insensitive to changes of a slowly varying background and can be discussed with high confidence.

Band Widths. On account of our spectral resolution and signal/noise ratio, only relative band width changes are discussed in this work. On this level, the effect of slowly varying background residues may be regarded to be negligible.

3.6 Data Analysis

3.6.1 Multiexponential Fits

The signal from a time-resolved experiment can be understood as the impulsively rising molecular evolution convoluted with temporal apparatus function (see Chapter 2). The molecular relaxation is generally captured by a sum of exponential functions, and the apparatus function is descriped by a Gaussian $G(t)$. A time trace is fitted to the function

$$S_{exp}(t) = G(t) \otimes \left(\Theta(t) \sum_i A_i e^{-t/\tau_i} \right), \tag{3.26}$$

where τ_i are the decay times and $\Theta(t)$ is the Heaviside step function. Oscillations of the signal were included as the sum over damped cosine function with phases ϕ_j,

$$S_{osc}(t) = G(t) \otimes \left(\sum_j A_j e^{-t/\tau_j} \cos(\omega_j t + \phi) \right). \tag{3.27}$$

To improve the speed the fitting algorithm the phase-shifted cosined was expressed as the sum of $\sin(\omega t)$ and $\cos(\omega t)$ functions for each frequency with zero initial phase. The pure cosine oscillation was then reconstructed from the sum-angle trigonometric relationships, and the time-zero phase of the pure cosine function can then be obtained between 0 and

2π with avoidance of intrinsic phase uncertainty resulting from the symmetry of the cosine function.

Transient absorption traces show a coherent contribution around time zero. It is modeled by a Gaussian with the width of the temporal apparatus function, and its derivatives up to fourth order.[35]

3.6.2 Global Analysis and Kinetic Models

The majority of photochemical processes on the femtosecond to picosecond time scale can be described as a combination of first-order or pseudo first-order reaction steps. A common goal in a kinetic analysis is the determination of the spectra $\epsilon_i(\lambda)$ associated with the intermediate species. This can be achieved performing the exponential analysis depicted above simultaneously for the time traces at all individual wavelengths with a common set of exponential functions. An analogue to equation (3.26) is obtained by replacing amplitudes A_i by amplitude spectra $\mathbf{A_i}(\lambda)$:

$$\mathbf{S}(\lambda, t) = \sum_i \mathbf{A_i}(\lambda) e^{-t/\tau_i}. \tag{3.28}$$

For the reconstruction of the species associated spectra I follow a procedure presented by Szundi *et al.*.[76] The time dependent species concentrations are collected in the vector $\mathbf{c}$. The reaction scheme is described by a set of first-order differential equations,

$$\frac{d}{dt}\mathbf{c}(t) = \mathbf{K}\mathbf{c}(t), \tag{3.29}$$

where $\mathbf{K}$ is the model-specific kinetic matrix. As an example, consider the sequential interconversion of three species 1, 2, and 3 with the microscopic rate constants k_1 and k_2:

$$A \xrightarrow{k_1} B \xrightarrow{k_2} C. \tag{3.30}$$

This corresponds to the kinetic matrix

$$\mathbf{K} = \begin{pmatrix} -k_1 & 0 & 0 \\ k_1 & -k_2 & 0 \\ 0 & k_2 & 0 \end{pmatrix}. \tag{3.31}$$

Equation (3.29) is solved by a sum of exponential functions,

$$\mathbf{c}(t) = \sum_i f_i \mathbf{V}_i e^{\alpha_{ii} t}. \tag{3.32}$$

The exponents α_{ii} are the eigenvalues of the kinetic matrix $\mathbf{K}$, obtained from a diagonalization with unitary matrices $\mathbf{V} = (\mathbf{V_1}, \mathbf{V_2} \dots)$,

$$\alpha = \mathbf{V}^{-1}\mathbf{K}\mathbf{V} \tag{3.33}$$

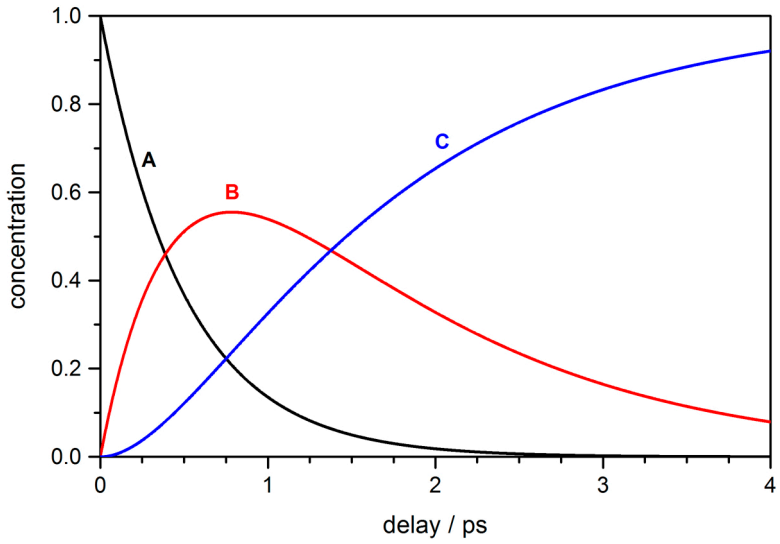

Figure 3.13: Time-dependent concentrations of the species in the sequential model $A \xrightarrow{k_1} B \xrightarrow{k_2} C$, with rate constants $k_1 = 2$ ps^{-1} and $k_2 = 0.5$ ps^{-1} and the initial concentrations $c_A(0) = 1$, $c_B(0) = 0$, $c_C(0) = 0$.

In the special case of sequential interconversion, the exponents are equal to the negative rate constants, *i.e.* $\alpha_{11} = -k_1$, $\alpha_{22} = -k_2$, and $\alpha_{33} = 0$ (the last term is included to describe the long-time offset). In the general case, α_{ii} is a combination of the microscopic rates. The normalization factors f_i are obtained from the concentrations at time zero,

$$\mathbf{f} = \mathbf{V}^{-1}\mathbf{c}(0). \tag{3.34}$$

A typical choice $\mathbf{c}(0)$ in photoinduced experiment is the normalized concentration vector

$$\mathbf{c}(0) = \begin{pmatrix} 1 \\ 0 \\ 0 \end{pmatrix}. \tag{3.35}$$

For the chosen example the time-dependent concentrations then

$$\mathbf{c}(t) = \begin{pmatrix} e^{-k_1 t} \\ k_1/(k_2 - k_1)\left(e^{-k_1 t} - e^{-k_2 t}\right) \\ 1/(k_1 - k_2)\left(k_2 e^{-k_1 t} - k_1 e^{-k_2 t}\right) + 1 \end{pmatrix}. \tag{3.36}$$

Concentration traces for species A, B, and C are modelled in figure 3.13 for the rate constants $k_1 = 2$ ps^{-1} and $k_2 = 0.5$ ps^{-1}.

The time-dependent spectral contribution of the species i, $\mathbf{S_i}(\lambda, t)$, scales with its

concentration,

$$\mathbf{S_i}(\lambda) = c_i(t)\epsilon(\lambda). \tag{3.37}$$

Comparison of equation (3.32) with equation (3.28) shows that

$$\alpha_i = -1/\tau_i \quad \text{and} \quad \epsilon(\lambda) f_i \mathbf{V_i} = \mathbf{A_i}. \tag{3.38}$$

The species associated spectra (SAS) are thus obtained as

$$\epsilon_\mathbf{i}(\lambda) = f_i^{-1} \mathbf{A_i} \mathbf{V_i}^{-1}. \tag{3.39}$$

For the above example with sequential interconversion the species associated spectra are related to the exponential amplitudes via

$$\epsilon_\mathbf{1}(\lambda) = \mathbf{A_1}(\lambda) + \mathbf{A_2}(\lambda) + \mathbf{A_3}(\lambda), \tag{3.40a}$$

$$\epsilon_\mathbf{2}(\lambda) = \frac{\tau_1}{1/\tau_1 - 1/\tau_2}\mathbf{A_2}(\lambda) + \mathbf{A_3}(\lambda), \tag{3.40b}$$

$$\epsilon_\mathbf{3}(\lambda) = \mathbf{A_3}(\lambda). \tag{3.40c}$$

The species of a kinetic do not necessarily have to represent actual intermediates in a physical sense. A sequential model, for example, also gives a summary of the spectral evolution in a measurement. The species then correspond to characteristic spectra that dominate at different delay times. This property was applied in section 3.5.5 to obtain a spectral basis set to the Raman signal.

3.6.3 Maximum Entropy Analysis

Setting the number of exponentials in a multi-exponential fit introduces constraints the data analysis. In practice, a time trace is described with an increasing number of decay functions, until the fit does not improve further. The ultimate goal is to relate the temporal evolution to a distribution of lifetimes $f(\log \tau)$. A quasi-continuous decay time distribution can be obtained by fitting the experimental trace to a large number of time constants. In the presence of noise, however, the solution is not unique, *i.e.* a variety of diffent distributions f yield descriptions of the experimental data with similar χ^2 values. In this case, the obtained solution depends on the choice of the initial parameters. The experimental uncertainty can be taken into account by the entropy $H(f)$ of the distribution f,[81] which is defined by

$$H(f) = -\sum_i f_i \ln f_i. \tag{3.41}$$

Among the many solutions with equal χ^2 the most probable solution for f is the one which maximizes the entropy.

4 Excited Stilbene: Intramolecular Vibrational Redistribution and Solvation Studied by Femtosecond Stimulated Raman Spectroscopy

4.1 Introduction

Photoinduced *cis-trans* isomerization about a C=C double bond is widely used by nature to trigger a response to an external light stimulus. Prominent examples include the vision process, phototaxis, control of germination, and photoinduced ion-pumping.[82,83] As a model system for olefinic photoisomerization, stilbene (1,2-diphenylethene) has attracted immense attention.[84] Irradiation of either conformer at wavelengths around 300 nm produces *cis*- and *trans*-stilbene with comparable yields (Figure 4.1). The reaction pathway in the electronically excited state S_1 follows torsion around the central ethylenic bond, accompanied by rotation of the phenylic residues.[85,86] This motion proceeds until a 90° twisted geometry is reached that allows internal conversion via a phantom state p to the ground state potential energy surfaces of *cis* and *trans* isomers.[87] For *trans*-stilbene, isomerization is hindered by a ~ 1200 cm^{-1} activation barrier on the S_1 potential energy surface[86] resulting in an excited-state lifetime on the order of 100 ps.[85,88,89] In contrast, *cis*-stilbene exhibits only a shallow minimum in S_1 and conversion is complete after 1 ps.[90–94]

The outcome of an isomerization reaction is primed by the relaxation pathway on the excited state potential. Tailored pulses made it possible for a variety of molecules to prepare wave packets appropriate for driving reactions into a specific direction.[95–99] The efficiency of such quantum control experiments depends on the interaction of vibrational modes and the flow of excess energy at earliest times. For *cis*-stilbene, recent pump/dump experiments could follow the temporal evolution of a low-frequency oscillation with femtosecond resolution.[100] A gradual frequency downshift of this mode was correlated to twisting of the molecule on its way to the conical intersection. An integral view of structural relaxation, however, necessitates consideration of the full vibrational evolution, and not of just one spectator mode. Such broad spectral windows are naturally obtained with frequency-domain spectroscopy. Spontaneous Raman scattering, although restricted to picosecond resolution, has improved our molecular understanding significantly. With this technique the cooling dynamics of excited *trans*-stilbene was followed on the 10 ps time scale.[102–107] A linear relationship between frequency shift and bandwidth of the ethylenic stretching mode was observed, having a characteristic depen-

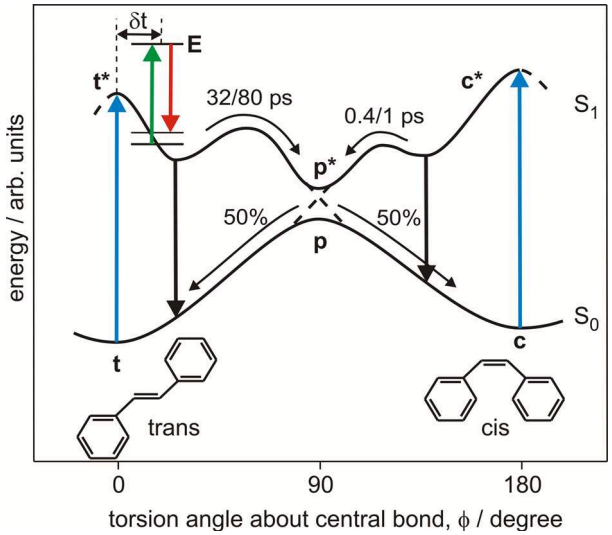

Figure 4.1: Simplified scheme of the ground and excited state potential energy surfaces of stilbene along the reaction coordinate, and the femtosecond stimulated Raman process: blue – actinic pump, green – Raman, red – stimulating probe pulses; δt denotes the variable delay. Excited state lifetimes are given for acetonitrile/*n*-hexane solution at room temperature.[85,89,91,93,101]

dence on solvent and temperature. Based on this observation, an equilibrium of S_1 with a nearby zwitterionic state was proposed: the polarization-exchange model.[104,108–110] This model can also explain an observed proportionality between the induced Raman changes and the isomerization rate of *trans*-stilbene.[104] But limited temporal resolution prevented these experiments from tracing the relaxation back to the subpicosecond regime. Thus, also for the short-lived excited state of *cis*-stilbene, only time-averaged spontaneous Raman spectra have generally been reported.[111,112] The initial time scale is dominated by intramolecular vibrational redistribation (IVR) which smears out the originally imposed vibrational information.[53,113,114]

Here, femtosecond stimulated Raman spectroscopy is used to track ultrafast evolution in excited stilbene. In both, *trans* and *cis* isomers, the relaxation of individual modes is scrutinized. A broad dectection range combined with sufficient spectral and temporal resolution allows to monitor the flow of excess energy within the vibrational manifold. Molecular processes are distinguished by three time-dependent observables: the Raman intensity, the frequency shift of the peaks, and the spectral width of the bands. Wavepacket motion is observed as oscillation of Raman bands, and due to anharmonic coupling the peak positions of high-frequency modes are also modulated. Static and dynamic influences of polar solvation are discussed by comparing results in *n*-hexane and acetonitrile solution.

4.2 Experimental Details

4.2.1 Transient absorption Spectroscopy

Transient absorption spectra were provided by Sergey Kovalenko;[1] they were measured with the setup which is based on the FEMTOLASERS *sPro* system. The chromophore was excited with 0.5 μJ pulses at 283 nm pulses generated in a *TOPAS* (LIGHTCONVERSION). Between 350 and 675 nm the temporal apparatus function is well described by a Gaussian with 60 fs width.

4.2.2 Transient Raman Spectroscopy

Narrowband Raman pulses at 575 and 620 nm were provided by the home-built optical parametric amplifier (see Section 3.5.1). From the output, 0.5 μJ were used for the experiment; the spectral width of the pulses was 7.5–12 cm^{-1}. After time-zero correction for the probe pulse chirp, the temporal resolution was 120–150 fs (fwhm of apparatus function).

4.2.3 Chemicals

Trans-stilbene (Fluka, 97%) and *cis*-stilbene (Fluka, 96%) were used as received. All solutions were prepared in fluorescence grade solvents (Merck). In agreement with the known sample impurity, for *cis*-stilbene measurements $\sim$ 3% contamination by signal from the *trans*-conformer can be identified at delay times $>$ 1 ps. This shows that additional product accumulation during acquisition is negligible. Results for pure *cis*-stilbene are obtained by substracting the evolution of *trans*-stilbene.

4.3 Results

4.3.1 Resonance Conditions

Resonance conditions can be seen in Figure 4.2 where the Raman wavelengths are shown together with the stationary and transient optical spectra. For *trans*-stilbene (blue), Raman pulses were tuned to 575 nm for measurements in acetonitrile and to 620 nm in *n*-hexane. At the chosen wavelengths only the excited-state absorption (t*) is resonant; the reactant and product ground states absorb exclusively in the UV. The corresponding signals, being non-resonant, are expected to be orders of magnitude smaller than that from t* and can therefore be neglected. Thus, the transient Raman evolution of *trans*-stilbene will solely reflect the motion of the molecule on the S_1 surface. All *cis*-stilbene measurements were taken with 620 nm Raman excitation. Under such conditions not only overlap with ground state absorption, but also with the band of the by-product DHP (4a,4b-dihydrophenanthrene) and the excited state absorption from the excited phantom state p* are avoided. The emission spectrum of the *cis* isomer, however, covers the

[1] Sergey Kovalenko, Department of Chemistry, Humboldt-Universität zu Berlin, Brook-Taylor-Str. 2, 12489 Berlin.

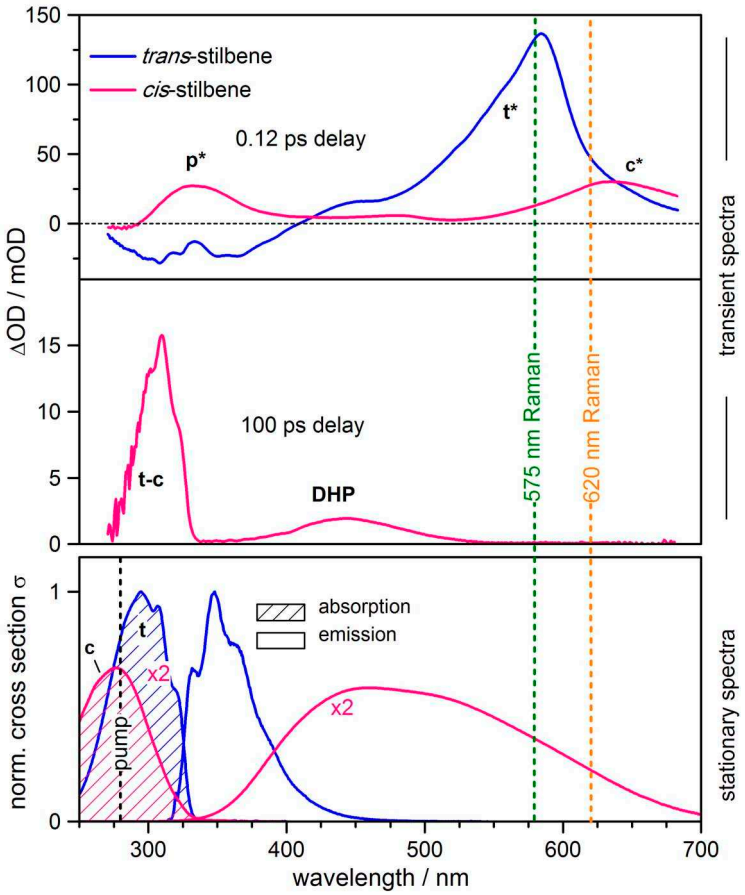

Figure 4.2: Transient absorption (*top* and *middle*) and ground state absorption and emission (*bottom*) spectra of *trans*- and *cis*-stilbene in *n*-hexane. In acetonitrile spectral features are similar. The *cis*-stilbene fluorescence spectrum was taken from ref. 85. Excitation and Raman pump wavelenths are indicated by vertical lines. **c/c*** – ground/excited state *cis*-stilbene absorption, **t/t*** –ground/excited state *trans*-stilbene absorption, **DHP** –absorption of 4a,4b-dihydrophenanthrene, **p*** –excited state absorption of the phantom state.[87]

full visible region. Femtosecond-resolved fluorescence experiments find already at early times a signal that resembles the stationary emission spectrum.[64] Therefore additional resonance with the $S_1 \rightarrow S_0$ transition has to be taken into account for *cis*-stilbene.

4.3.2 *trans*-Stilbene

Transient Raman spectra of *trans*-stilbene in *n*-hexane and acetonitrile are shown in Figure 4.3. Due to improved resonance the initial signal is 4–5 times stronger in acetonitrile compared to *n*-hexane; otherwise the spectra in both solvents are qualitatively similar. It may be concluded that the difference in Raman wavelength does not impose further

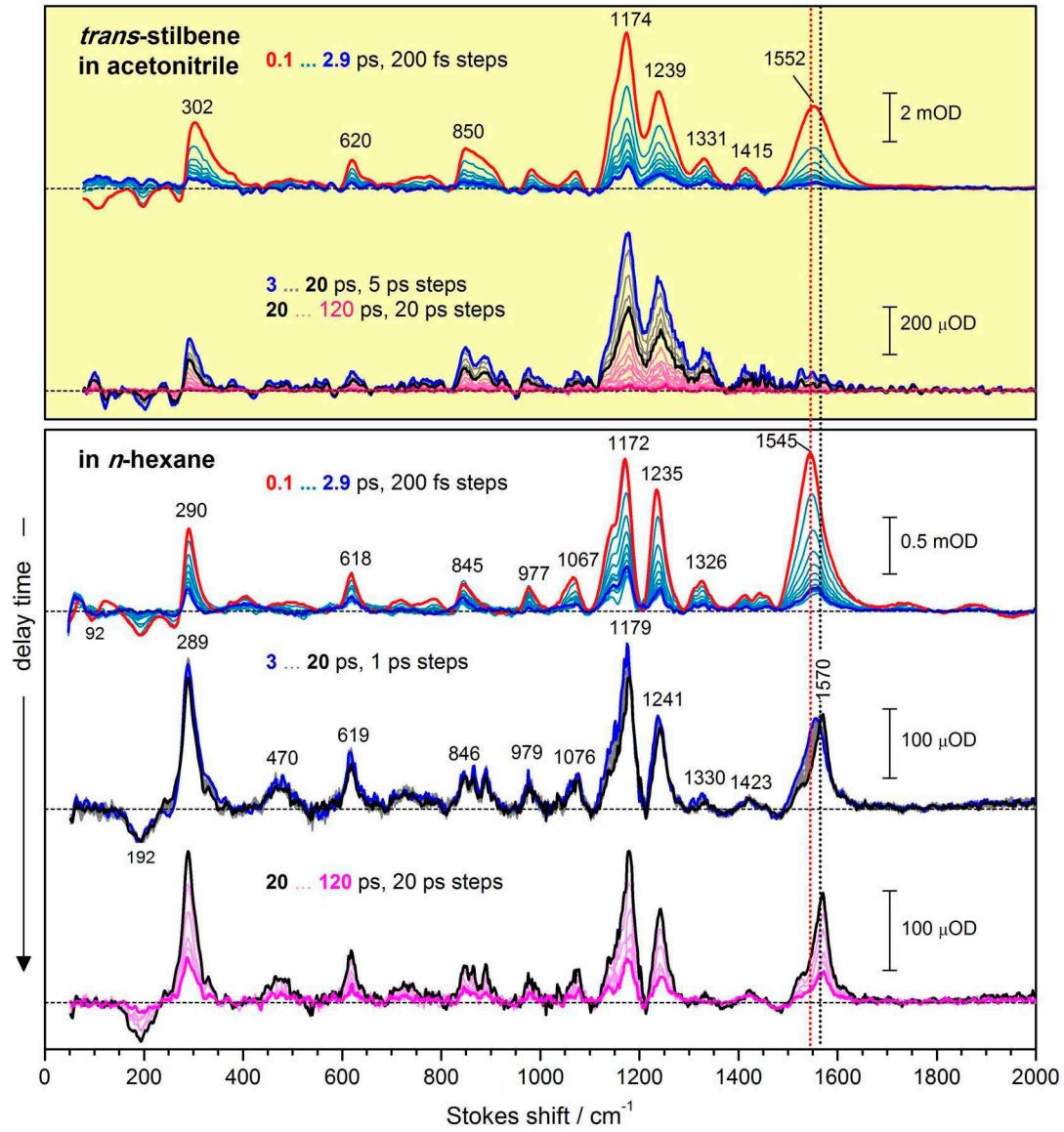

Figure 4.3: Transient resonance Raman spectra of *trans*-stilbene in acetonitrile (top; acetonitrile solutions are generally marked yellow) and in *n*-hexane (bottom) after excitation at 280 nm. Measurements up to 2.9 ps were obtained under parallel polarization conditions, signals at longer delay times are given for magic angle conditions. The peak positions of the main bands are indicated. The positions of the C=C stretching band around 1550 cm^{-1} in *n*-hexane at time zero and 20 ps delay are shown as vertical dotted lines (red and black, respectively).

effects on the signal. Already directly after excitation (at 0.1 ps delay, red line) a well resolved Raman spectrum is observed. The appearance of the spectrum stays similar

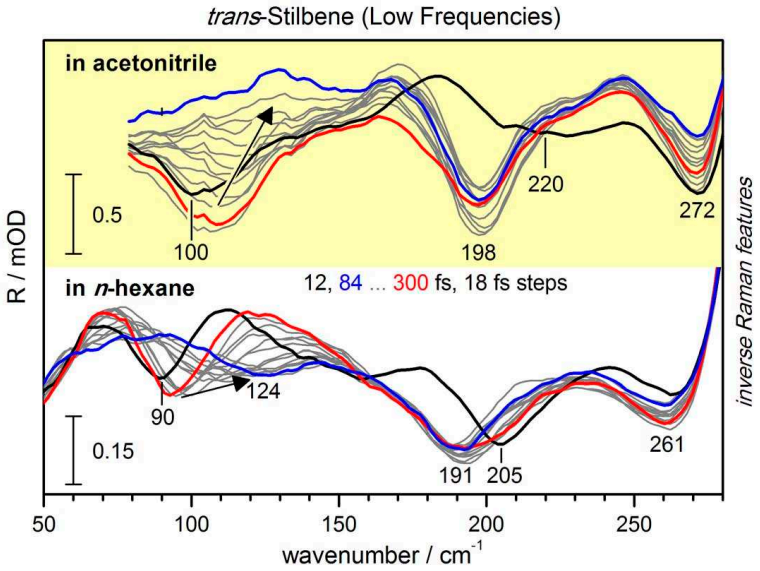

Figure 4.4: Low-frequency region of the transient Raman evolution of *trans*-stilbene in acetonitrile and in *n*-hexane after excitation with 280 nm under parallel polarization conditions.

during the complete evolution although gradual changes in intensity as well as in shift and width of the peaks can be discerned. Most strikingly, during the first picosecond the overall signal intensity decreases by almost one order of magnitude. Neither by transient absorption nor time-resolved fluorescence a significant decay of *trans*-stilbene excited-state population is observed on this time scale.[53,114] Thus the rapid signal decay may be attributed to a decrease of Raman cross-section. As an alternative explation in Chapter 6 depletion of population by the Raman pulse is offered.

The spectral evolution in both solvents is described next. In *n*-hexane the whole spectrum decays in a relatively uniform way, although within the first 0.3 ps bands with frequencies >1000 cm^{-1} decrease slightly stronger compared to the low-frequency part of the spectrum. In acetonitrile the spectral shape resembles that in *n*-hexane solution, but bands are broader at the beginning. Like in *n*-hexane the Raman intensity decreases significantly during the first picosecond. Here the decay of the 1550 cm^{-1} band deviates even stronger from the rest of the spectrum; it vanishes almost completely during the initial relaxation phase. Shift of Raman peak positions accompanies the amplitude decay in *n*-hexane. This effect is most clearly observed as an upshift of the high-frequency modes, especially for the ν(C=C) mode around 1550 cm^{-1} which shifts by +10 cm^{-1}. When further increasing the delay up to 20 ps (middle lower panel) this shift proceeds while the signal amplitude does not change significantly. Until 120 ps the complete signal decays with constant shape indicating population loss from the excited state. In acetonitrile the spectral positions of the Raman bands do not exhibit prominent change upon relaxation. In particular, the high-frequency ν(C=C) mode approaches its final position around 1550 cm^{-1} already at 100 fs delay, and no prominent upshift such

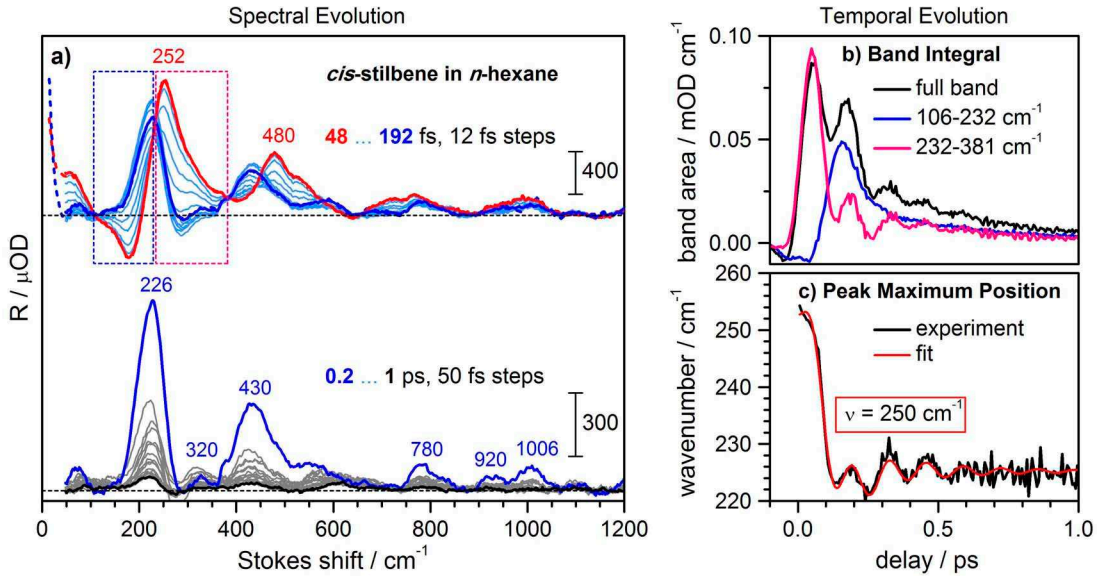

Figure 4.5: Transient Raman evolution of *cis*-stilbene in *n*-hexane after excitation at 280 nm under parallel polarization conditions. a) Spectral evolution. The solvent Raman signal and 3 % *trans*-stilbene contribution was subtracted. b) Temporal evolution of the band integral 106-381 cm^{-1} (black) and the high- and low-frequency part (blue and magenta respectively) as marked in subfigure a). c) Temporal evolution and fit of the peak maximum position for the 226-252 cm^{-1} peak. Fitting parameters: $\nu_1 = 80$ cm^{-1}, $\gamma_1 = 80$ fs; $\nu_2 = 252$ cm^{-1}, $\gamma_2 = 0.3$ ps, shift within cross-correlation.

as in *n*-hexane occurs. The decay of the Raman spectra at later delay times is faster in acetonitrile than in *n*-hexane, and the signal goes nearly to zero at 120 ps.

Negative (absorptive) Raman features are observed below 300 cm^{-1} in both solvents while bands at higher frequencies are purely positive. The low-frequency evolution during the first 0.3 ps is shown in Figure 4.4. At 12 fs delay negative dips in the baseline are observed at 90 and 205 cm^{-1} in *n*-hexane (100 and 220 cm^{-1} in acetonitrile). During temporal overlap between actinic pump and probe pulses, the band at 204(220) cm^{-1} disappears and a new dip at 191(198) cm^{-1} evolves. This band is observed throughout the measurement and decays together with the rest of the spectrum. The behavior of the feature around 100 cm^{-1} is completely different. It has an initial minimum at 90(100) cm^{-1} and decays to the baseline already within 0.3 ps. During this time the band continuously shifts to higher frequencies, to a final position around 120 cm^{-1}. In addition to the two bands outlined above the $\sim$ 290 cm^{-1} peak bears a negative side lobe at 261 (272) cm^{-1}, which decays during the first picoseconds.

4.3.3 *cis*-Stilbene

The transient spectral evolution of *cis*-stilbene in *n*-hexane and acetonitrile is shown in Figures 4.5a and 4.6a. Compared to *trans*-stilbene, the signal is significantly broader

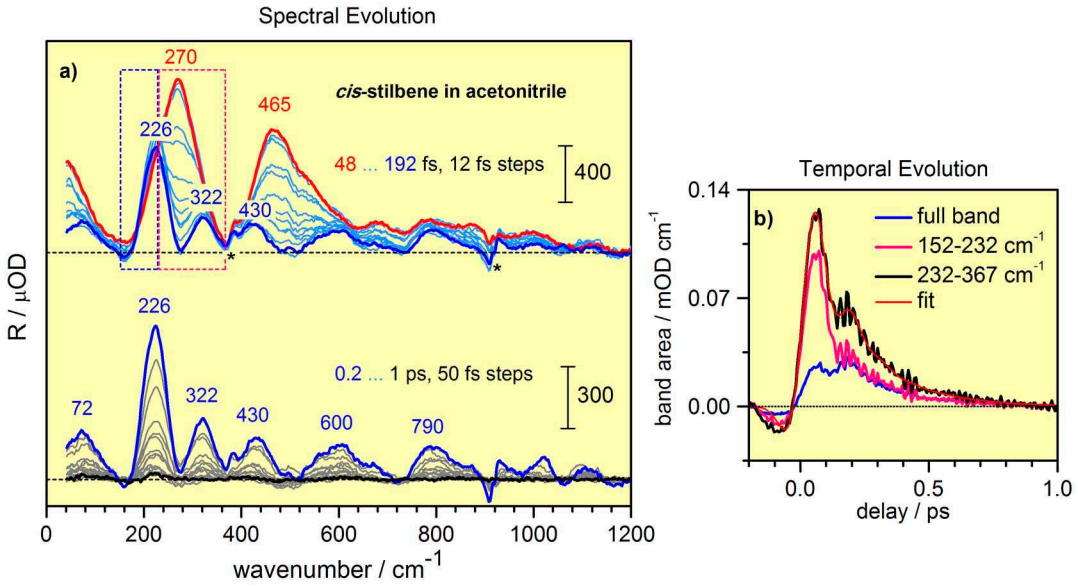

Figure 4.6: Transient Raman evolution of *cis*-stilbene in acetonitrile after excitation at 280 nm under parallel polarization conditions. a) Spectral evolution. Asterisks mark artefacts from insufficient solvent subtraction. b) Temporal evolution of the 152-367 cm^{-1} band integral (black) and the low- and high-frequency part (blue and magenta, respectively). Red: 152-367 cm^{-1} band integral over a global fit with one exponential decay ($\tau = 0.2$ ps) and two oscillations ($\nu_1 = 70$ cm^{-1}, $\gamma_1 = 0.07$ ps and $\nu_2 = 264$ cm^{-1}, $\gamma_2 = 0.08$ ps).

and the intensity of high-frequency modes weaker. Directly after excitation (48 fs delay, red line) the spectrum is dominated by two bands at 252 (270) and 480 (465) cm^{-1} in *n*-hexane (acetonitrile). The signal at earliest times shows dispersive-like lineshapes around 210 cm^{-1} in *n*-hexane. During the first 0.15 ps strong changes take place. The initial signal decays while a new spectrum with major bands around 226 and 430 cm^{-1} appears. Similar changes are observed in the lower frequency range: the initial band at 45–60 cm^{-1} decays and leaves a peak around 84 cm^{-1}. The behavior resembles qualitatively the evolution of the 200 cm^{-1} band in *trans*-stilbene; further common features will become clear in the discussion. On the high-frequency side additional bands up to 1000 cm^{-1} can be distinguished after ultrashort relaxation. Thereafter the full spectrum decays within the first picosecond in both solvents. The band integral over the region 106-381 cm^{-1} (Figure 4.5b, black) reveals a decay time on the order of 0.5 ps in *n*-hexane. Strong oscillations are superimposed on the decay. They are located around the position of the initial 252 cm^{-1} band as can be seen from the comparison of the high- and low-frequency part of the band integral (magenta and blue lines in Figure 4.5b, respectively). Ultrafast spectral changes are reflected by a 0.1 ps delayed rise of the low-frequency edge (blue). The dynamics described above can also be followed by monitoring the maximum of the 252 cm^{-1} band (Figure 4.5c). Here again, oscillations

with a frequency of 250 cm^{-1} are evident. In acetonitrile a similar evolution is observed; however the full decay is shortened to approximately 0.2 ps, and the oscillations are less discernable from the signal.

4.4 Discussion

4.4.1 *trans*-Stilbene

Transient Spectra and Band Assignment

Peak positions directly after actinic excitation and at delay times > 20 ps are summarized in Table 4.1. The spectra at long delay times compare well to literature data obtained from picosecond spontaneous Raman spectroscopy under resonance and non-resonance conditions.[107,115–117] This suggests that the signal >270 cm^{-1} resembles conventional Stokes spectra. The Raman pulses are only resonant with a higher excited S_n state, so that only the blue shaded diagrams in Figure 2.7 (Section 2.4) have to be considered. From the simulations in Section 2.4 Raman emission at the S_1 state vibrational frequencies is expected, mainly originating from the pathway R^A_{3e}. Since S_n should posess a short lifetime on the 0.1 ps time scale, signals from hot luminescence, R^B_{1e} and R^A_{2e} will be broad and are removed during background correction. The R^B_{4e} interaction starts from a vibrationally excited state on the Stokes side. For modes with frequencies >200 cm^{-1}, at room temperature mainly the vibrational ground state is populated. Therefore after vibrational cooling, R^B_{4e} is expected to affect only the sub-200 cm^{-1} part of the spectrum. The inverse Raman bands around 100 and 200 cm^{-1} suggest a change of the polynomial prefactor in equation (2.98). This agrees with the finding that the polynomial is most sensitive to resonance conditions in pathways where the sample interacts with the probe pulse first (indicated by the superscript B). At earlier delay times, R^B_{4e} may also have contributions to bands that are vibrationally excited by Franck-Condon transitions or during intramolecular relaxation. In this context the dip at 260–270 cm^{-1} may be interpreted as the originating from an R^B_{4e} contribution of the vibrationally excited $\sim$ 290 cm^{-1} mode. The picosecond decay of this signal agrees with the return of the population to the vibrational ground state. For the higher-frequency modes similar behavior is not resolved.

The band assignment is discussed next. From ^{13}C substitution experiments, significant involvement of ethylenic carbon atoms was identified for the modes at 1570 , 1528, 1241, 1179, 1150, and 846 cm^{-1} (refering to the fully relaxed spectrum in *n*-hexane).[117] Vibrational modes >1300 cm^{-1} contain C=C stretching contributions. In particular, for the strongly shifting band around 1550 cm^{-1} two underlying bands can be distinguished after thermalization. The peak at 1570 cm^{-1} is attributed to the ethylenic C=C stretching mode ν_8 while the shoulder at 1528 cm^{-1} corresponds to the phenylic C=C stretching mode ν_9. The assignment follows the consensus in the literature[115,120] although, based on recent calculations, an alternative assignment to ν_7 (1570 cm^{-1}) and ν_8 (1528 cm^{-1}) was suggested.[118] The region from 1000 to 1300 cm^{-1} is dominated by C-H bending modes (ν_{14}–ν_{18}). The 619 cm, 846 and 979 cm^{-1} bands correspond to deformations

Table 4.1: Transient Raman peak positions of *trans*-stilbene excited in acetonitrile and *n*-hexane, with mode assignments. Band positions are given for time zero and after full vibrational relaxation (> 20 ps delay). Literature values refer to picosecond-resolved spontaneous Raman measurements. ip/oop – in plane/out of plane.

Raman band positions / cm^{-1}					**Assignment**		
in acn		**in *n*-hexane**					
at t$_0$	**after rel.**	**at t$_0$**	**after rel.**	**literature**[a]	**symmetry**	**mode**[b]	**motion**[b]
100		90		83	a_u	$\nu_{37} + \nu_{36}$,	phenyl/ethylene torsion
				95		$2\nu_{37}$	
200	193	205	192	197	a_g	ν_{25}	ip C_{et}=C_{et}-C_Φ bend
303	291	290	289	285	a_g	ν_{24}	ip/oop bend
482		480	470				
620	619	617	619	619	a_g	ν_{22}	ring deformation
770		752	752				
851	849	844	846	844	a_g	ν_{21}	C_{et}=C_{et}-C_Φ bend + ring breathing
981	975	977	979	978	a_g	ν_{20}	trig. ring deform.
1067	1071	1064	1076	1077	a_g	ν_{18}	C_Φ-H bend
1145	1145	1146	1150	1148	a_g	ν_{16}	C_Φ-H bend
1172	1179	1172	1179	1179	a_g	ν_{15}	C_Φ-H bend + C_{et}-C_Φ stretch
1237	1242	1233	1241	1241	a_g	ν_{14}	C_{et}-H bend
1329	1331	1322	1330	1334	a_g	ν_{12}	ring vibration
1415	1418	1406/1446	1423/1450	1421	a_g	ν_{11}, ν_{10}	ring vibration
			1528	1534	a_g	ν_9	C_Φ-C_Φ stretch
1553	1550	1543	1570	1566	a_g	ν_8	C_{et}=C_{et} stretch

a Values for the low-frequency a_u modes were deduced from the fluorescence excitation spectrum of jet-cooled *trans*-stilbene.[86] Frequencies >190 cm^{-1} are taken from spontaneous resonance Raman measurements with 593 nm excitation at 10 ps delay.[115]
b according to refs. 115,118–120.

of the phenyl rings (ν_{20}–ν_{22}), while the signal at 289 cm^{-1} is assigned to in-plane and out-of-plane bending of the phenyl moieties (ν_{24}). The negative band at 192 cm^{-1} corresponds to an in plane bending of the phenyl groups towards the central ethylenic moiety (ν_{25}). The C_{et}=C_{et}-C_Φ angle decreases upon $S_1 \leftarrow S_0$ transition, rendering this mode highly Franck-Condon active.[119]

For *trans*-stilbene C_{2h} symmetry has been established.[119,121,122] As a consequence Raman transitions are formally allowed only for a_g and b_g modes. Enhancement of a Raman signal by resonance with a single electronic state further requires a change of the polarizability along the normal coordinate due to this transition; this is satisfied if a shift between the potential minima exists. Under the assumption that Herzberg-Teller coupling can be neglected and the molecular symmetry stays unchanged, only totally symmetric modes will be observed in resonance Raman spectroscopy.[123] In accordance, all modes previously discussed have a_g symmetry. The 90 cm^{-1} band, however, forms an exception, since from calculations no a_g vibrations are expected below 192 cm^{-1}.[118] This band has not been observed in spontaneous Raman experiments before,[115] and it decays already within the first picosecond. An unequivocal assignment can not be given here but several candidates for this band are discussed.

A phenyl torsion mode of b_g symmetry (ν_{48}) with a frequency of 112 cm^{-1} was identified in laser-induced fluorescence measurements.[121] This mode may become active in resonance Raman spectroscopy if the Raman transition is affected by electronic or vibrational mixing of states.

Combinations of the a_u symmetric torsion modes ν_{36} and ν_{37} dominate the low-frequency region of fluorescence excitation spectra.[121,122] In particular, ν_{37} describes in the ground state an in-phase phenyl torsion at very low frequency (~ 10 cm^{-1}) which is strongly anharmonic. Upon transition to the S_1 state this mode gains significant ethylenic torsion character and is upshifted to 48 cm^{-1}.[118,119,121] Due to the large frequency change between S_0 and S_1 and a considerable Duschinsky effect the mode has strong Franck-Condon activity. Although fundamentals of a_u symmetry are formally not Raman active, their higher harmonics and combinations, which lead to even changes of vibrational quanta, are totally symmetric and thus Raman allowed.[124] The 90 cm^{-1} band could then correspond to the second harmonic $2\nu_{37}$ or to the combination $\nu_{37}+\nu_{36}$.

Difference frequency generation offers an additional pathway for the generation of the 90 cm^{-1} signal. As discussed above, the 290 cm^{-1} mode ν_{24} is proposed to be vibrationally excited at early delay times. Combination with ν_{25} may then result in a Raman band around 90 cm^{-1} ($\nu_{24}-\nu_{25}$). In femtosecond stimulated Raman spectroscopy vibrational coupling and cascaded Raman sequences have been discussed as suitable schemes for difference frequency formation.[18,125,126] In the subsequent analysis evidence for coupling of high-frequency modes to vibrations with 57 and 90 cm^{-1} will be shown, while they are unaffected by ν_{25} and ν_{24}. This contradicts a generation of the 90 cm^{-1} signal by difference frequency formation. Instead, the assignment of the coupling vibrations to ν_{37} and $2\nu_{37}/\nu_{37}+\nu_{36}$ appears reasonable.

The interplay of modes and the influence of a polar solvent shell is now studied in detail by separating the spectral changes into three time-dependent observables: the Raman intensity, the frequency shift of the peaks, and the spectral widths of bands.

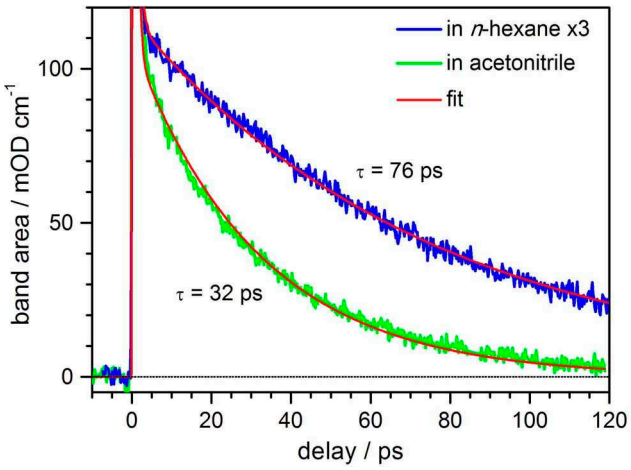

Figure 4.7: Time-dependent integral over the full *trans*-stilbene spectrum in acetonitrile and in *n*-hexane after excitation at 280 nm. The traces are fitted with biexponential functions (red); the long decaytimes are given (short decaytimes: 0.6-0.7 ps).

Raman Intensities

Integration over individual Raman bands allows to investigate the temporal evolution of the intensity without contamination from spectral shift and narrowing phenomena. At longer delay times the spectrum stays unchanged and its decay is monitored by integrating over the full spectral window (Figure 4.7). An exponential fit gives decay times of 32 ps in acetonitrile and 76 ps in *n*-hexane which agree well with the lifetimes of the S_1 state derived from other methods (*cf.* Figure 4.1).[93,101] Additional spectral changes that take place on the 10 ps time scale do not affect, within precision, the Raman intensity. The complete signal decay shows that, under the current resonance conditions, the Raman signal does not trace the population flow beyond the isomerization barrier. Subsequent transition to the ground electronic state is adequately monitored by transient absorption spectroscopy.[127] The femtosecond resonance Raman experiment allows on the other hand an investigation of the relaxation from the Franck-Condon region of the S_1 state to its potential minimum.

Information about the initial relaxation is obtained from the individual band integrals in Figure 4.8. Let us begin the discussion with *trans*-stilbene in *n*-hexane. As reasoned above, the sub-picosecond evolution is not caused by population loss from isomerization. Furthermore, solvation effects are negligible in the nonpolar solvent *n*-hexane.[128] The observed changes may therefore reflect vibrational relaxation in the S_1 state. The sub-picosecond time scale is characteristic for intramolecular vibrational redistribution (IVR).[113] Excitation prepares the molecule with vibrational excess energy concentrated in the optically active modes. In stilbene the $S_1 \leftarrow S_0$ ($\pi\ \pi^*$) transition mainly affects the ethylene and phenyl stretching modes ν_8 and ν_9 which are represented by the broad Raman band around 1550 cm^{-1}.[118] Gas phase fluorescence excitation spectra revealed additional principle transitions for the following a_g modes: The C_{et}-H bending modes

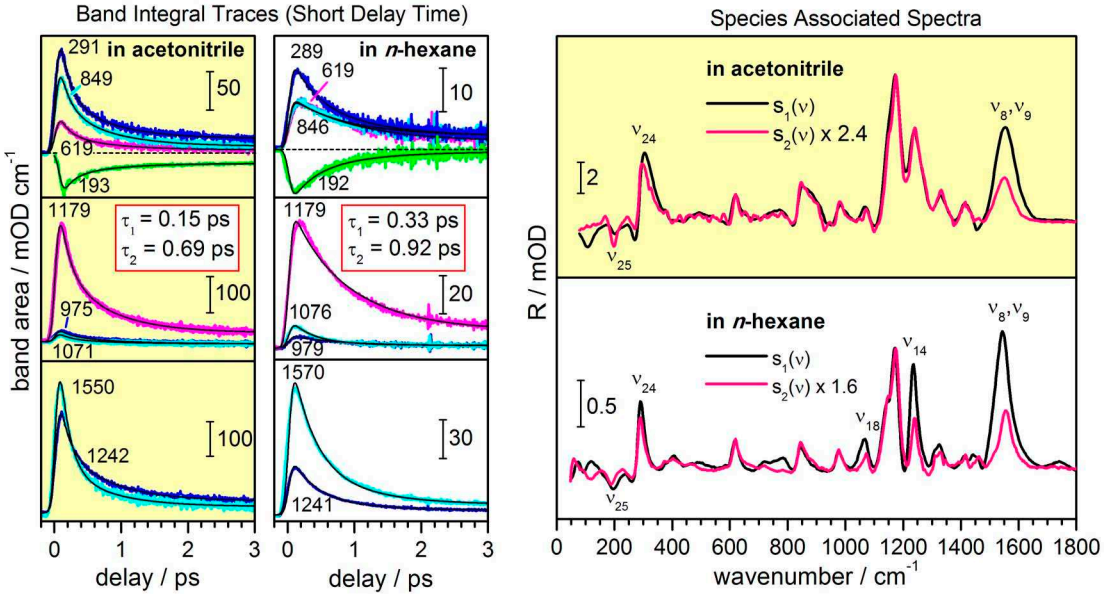

Figure 4.8: Left: Time-dependent spectral integrals of *trans*-stilbene in acetonitrile and in *n*-hexane after excitation at 280 nm for the first 3 ps. The evolution of every mode is well reproduced by a global exponential fit (black lines); decay times are given as insets. The 193 cm^{-1} trace in acetonitrile was corrected for underlying background. Right: Species Associated Spectra for a formal sequential model $1 \rightarrow 2 \rightarrow 3$ where the conversion times were taken from the global fit. The spectra $s_2(\nu)$ are scaled to equal intensities for the 619 cm^{-1} band.

ν_{13} (not observed) and ν_{14} (1241 cm^{-1}), the ring deformation modes ν_{20} (979 cm^{-1}) and ν_{21} (846 cm^{-1}), and the C_{et}=C_{et} bending mode ν_{25} (192 cm^{-1}).[118,119,121] During IVR the excess energy is distributed over the full vibrational manifold, leading to a molecule which is in thermal equilibrium internally, at high temperature. Within this model, the prominent ultrafast loss of Raman cross-section for the 1570 cm^{-1} band can be explained by decrease of Franck-Condon overlap with the resonant electronic state S_n as population drains out of the originally excited vibrational states in S_1. The origin of the concomitant unspecific signal decay of the other modes, however, remains unclear.

Intramolecular vibrational redistribution requires coupling between the normal modes of the system. The actual energy flow depends on the coupling strength and the number of modes which are accessible for energy exchange. As each mode may in principal behave differently, the decay of the band integral traces in Figure 4.8 was analyzed individually. The signal $S(t)$ is described as the weighted sum of exponential functions convoluted with the system response G(t), see Section 3.6. As an example we discuss results for the 1570 cm^{-1} band. The signal can be modelled by a biexpontial fit (Figure 4.9, *left*, yellow bars), but the decay times $\tau_1 = 0.28$ ps and $\tau_2 = 0.71$ ps are not well defined by the original signal: the Raman intensity decay is reproduced with equal χ^2 by the broad distribution given in red, which was found by maximum entropy methods

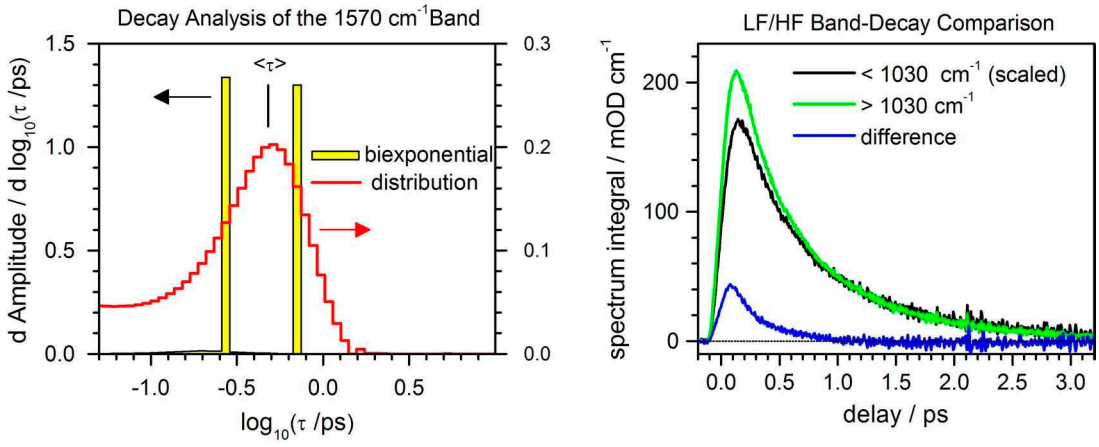

Figure 4.9: Band integral analysis for *trans*-stilbene in *n*-hexane. Left: Exponential analysis of the 1570 cm^{-1} band integral in Figure 4.8. Right: Integrated signal for the spectral regions 250–1030 cm^{-1} (black) and 1030–1700 cm^{-1} (green) after subtraction of the long-time offset. The low frequency band integral was scaled by a factor of three.

(see Section 3.6). From similar comparisons for all modes, it is concluded that, at this stage, the only significant descriptor of the initial Raman loss dynamics is given by the correlation time $\langle\tau\rangle$:

$$\langle\tau\rangle = \frac{\sum_j A_j \tau_j}{\sum_k A_k}. \tag{4.1}$$

The obtained values are compared in Table 4.2. The signal/noise level is also given as the deconvoluted amplitude at $t = 0$ ps, divided by 2σ, where σ is the rms deviation of the optimal fit. The correlation times range between 0.5 and 0.7 ps. With femtosecond pump-depletion spectroscopy and resonance-enhanced multiphoton ionization on *trans*-stilbene vapour, a time constant of 0.65 ps has been observed for the initial process.[114] The similarity with the present data supports the assignment to IVR and suggests that the *n*-hexane solvation shell does not affect IVR significantly. The decay, however, is not uniform: Raman bands > 1000 cm^{-1} decay faster ($\sim$ 0.5 ps) than bands < 1000 cm^{-1} ($\sim$ 0.65 ps). In order to test the significance of this observation the transient evolution is integrated over the spectral regions 250–1030 cm^{-1} and 1030–1700 cm^{-1}. The fast decaying parts of the resulting traces are given in Figure 4.9; to facilitate comparison, the long-time signal was subtracted. From 0.8 ps onwards low- and high-frequency traces show virtually identical temporal evolution. In contrast, at early times bands > 1030 cm^{-1} are subject to an additional intensity loss on the time scale of 0.3 ps. Interpreted in terms of IVR, one may conclude that despite the individuality of vibrations, the

Table 4.2: Results from the maximum-entropy analysis of the fast intensity decay for *trans*-stilbene in *n*-hexane: Signal/Noise S/N and correlation time $\langle\tau\rangle$.

mode	**frequency / cm^{-1}**	**S/N**	$\langle\tau\rangle$ **/ ps**
ν_{25}	192	6.4	0.61
ν_{24}	289	11	0.55
ν_{22}	619	5.8	0.68
ν_{21}	846	8.0	0.68
ν_{20}	979	4.6	0.64
ν_{18}	1076	13	0.38
ν_{15},ν_{16}	1179	34	0.49
ν_{14}	1241	60	0.49
ν_8,ν_9	1570	90	0.48

redistribution may be devided into a fast and a slower process.

$$1 \xrightarrow{\tau_1} 2 \xrightarrow{\tau_2} 3.$$

Here 1 corresponds to the system prepared by Franck-Condon transition at zero delay time and 3 to the internally equilibrated molecule. From a global fit of the band integrals in Figure 4.8 time constants of $\tau_1 = 0.33$ ps and $\tau_2 = 0.92$ ps are obtained. The transient Raman signal is now described at each individual frequency ν as (see Section 3.6.2)

$$S(\nu, t) = a_1(t)s_1(\nu) + a_2(t)s_2(\nu) + a_3(t)s_3(\nu), \tag{4.2}$$

where $s_i(\nu)$ is the spectrum of the virtual state i; its population dynamics is given by $a_i(t)$. The Species Associated Spectra $s_1(\nu)$ and $s_2(\nu)$ reflect the spectral changes during the evolution with $\tau_1 = 0.33$ ps. They are compared in Figure 4.8 (bottom right), scaled to equal intensity for the 619 cm^{-1} band. The strongest intensity loss during the fast IVR step is found for the following bands: 1570 cm^{-1} (ν_8, ν_9), 1241 cm^{-1} (ν_{14}), 1076 cm^{-1} (ν_{18}), 289 cm^{-1} (ν_{24}) and 192 cm^{-1} (ν_{25}).

In this view, Raman intensity serves as an indicator for the progress of IVR. There seems to exist a correlation between the extent of initial intensity decay and Franck-Condon activity (see above). Here the following interpretation is suggested: the actinic pump pulse prepares the Franck-Condon modes in vibrationally excited states. Energy redistribution through inter-mode coupling is most efficient within a subset of modes which is probably governed by symmetry constraints. This preferential IVR is dominant during the fast 0.33 ps relaxation while equilibration over the full vibrational manifold is slower (0.92 ps).

Solvation effects are negligible in *n*-hexane, but in acetonitrile polar solvation should be taken into account. A global fit of the band integral traces in Figure 4.8 (left) gives decay times of $\tau_1 = 0.15$ and $\tau_2 = 0.69$ ps in acetonitrile. In contrast to *n*-hexane solution,

the two decay components can be distinguished directly in the signal. As before, for the longer decay (τ_2) no significant changes of the relative band intensities are resolved. For a discussion of the 0.15 ps evolution, the Species Associated Spectra $s_1(\nu)$ and $s_2(\nu)$ are compared in Figure 4.8 (top right), again scaled to equal intensities for the 619 cm^{-1} band. A completely uniform decay of the spectrum is observed in the region 400–1450 cm^{-1}. Strong additional intensity loss with $\tau_1 = 0.15$ ps is found for the 1550 cm^{-1} band which corresponds to the highly Frack-Condon active modes ν_8 and ν_9. Smaller changes are seen for bands at 291 cm^{-1} (ν_{24}) and 193 cm^{-1} (ν_{25}).

In a polar environment the apparent acceleration of the relaxation in this model suggests that the inter-mode coupling becomes more efficient. This would allow fast energy redistribution over a large vibrational manifold and could explain the uniform signal decay which is observed already at earliest times. Vibrational relaxation may be facilitated if the solvent environment breaks symmetry restrictions. In *n*-hexane, the $\pi\pi^*$ excitation prepares the molecule in a state with biradicalic character. The polarization exchange model proposes that the biradicalic form is in equilibrium with a nearby zwitterionic state.[104,108–110] A polar solvent like acetonitrile can shift the equilibrium towards the ionic form, stabilizing stilbene in a momentarily polarized state. The concomitant breakage of symmetry may facilitate IVR. In agreement with this concept, transient infrared experiments have found symmetry-forbidden bands for *trans*-stilbene in acetonitrile.[129]

Dynamic reorientation of the solvent environment around the excited molecule may affect the transient spectral evolution. Time-resolved fluorescence measurements found a typical solvation time of 0.63 ps for acetonitrile.[128,130] The decay with $\tau_2 = 0.69$ ps may therefore be attributed to dynamic solvation by acetonitrile instead of a second IVR process. The strong decay of the 1550 cm^{-1} band then indicates that the ethylenic stretching mode is affected by the polar solvent surrounding differently. More insight will be obtained from an analysis of the peak frequencies.

An alternative mechanism for subpicosecond decay of Raman signals arises from the evaluation of experiments on the flavin chromophore (Chapter 6): population depletion from the excited state induced by the intense Raman pulse. The initial decay characteristics are in this model mainly determined by the measuremenent conditions like Raman pulse duration and temporal overlap with the probe pulse. To explain differences in the evolution of the high- and low-frequency regions, one would have to consider the temporal phase: for a chirped probe pulse individual frequencies overlap at different delay times with the Raman pulse. Only depletion by the part of the Raman pulse that preceeds the probe pulse can affect the measurement. Then the temporal evolution at early delay times would become frequency-dependent. A definite assignment of the effects observed here requires further experiments in future that systematically vary the measurement parameters.

Evolution of the Inverted Raman Signals

Strong intensity oscillations overlay the exponential evolution of the Raman signals below 250 cm^{-1}. Figures 4.4 and 4.11 show the residuals obtained after fitting single time traces in the low-frequency range with the parameters from the previous analysis of band

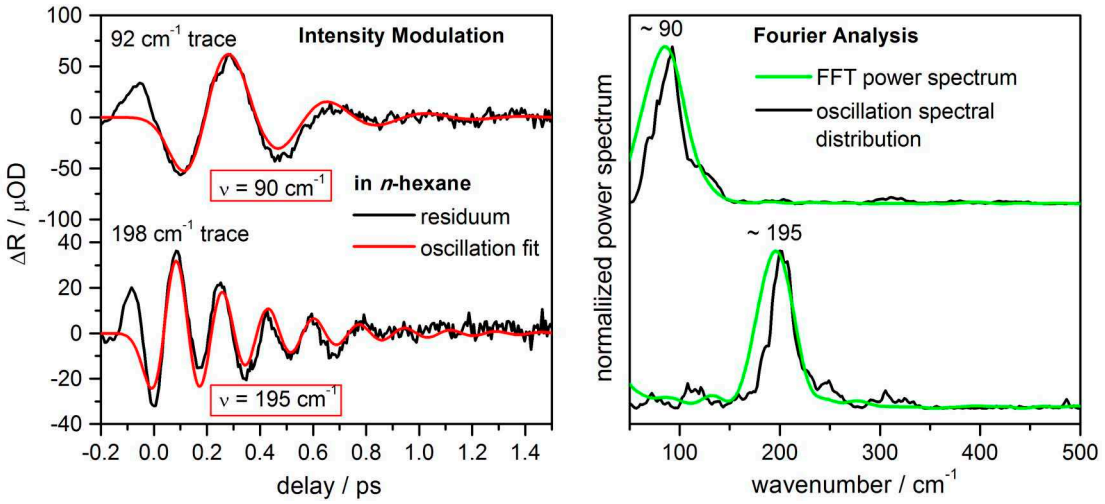

Figure 4.10: Left: Residuals from a global exponential fit of the Raman spectral evolution of *trans*-stilbene in *n*-hexane, with decay times taken from the band integral analysis. Signals (black) were smoothed by a Sawitzky-Golay filter for presentation. In red: oscillation fits with the parameters $\nu_1 = 90$ cm^{-1}, $\gamma_1 = 0.27$ ps, and $\nu_2 = 195$ cm^{-1}, $\gamma_2 = 0.33$ ps, respectively. Right: FFT power spectra (green, normalized) of the experimental residues shown to the left. The normalized power distributions of the 90 and 195 cm^{-1} oscillations as a function of Stokes detuning are given in black.

integrals. [2] Strikingly, the intensities oscillate with the pertinent mode frequency (90 or 195 cm^{-1} in *n*-hexane; 100 or 206 cm^{-1} in acetonitrile. Figure 4.4, right, demonstrates that these modulations are restricted to the Raman bands of the respective modes (black line). The large difference in the oscillation frequency of adjacent bands confirms that these features are not artefacts from insuffiently subtracted transient absorption signals. Modulations in Raman intensity, as observed here, were proposed theoretically for wavepacket dynamics.[41] It is therefore concluded that the oscillatory modulations derive from wavepacket motion along the potentials of the 90 and 190 cm^{-1} modes. In acetonitrile these frequencies are slightly higher, implying that the C=C-C$_\Phi$ bending and phenyl/ethylene torsional modes are stiffened through solvation.

The observation that the 90 cm^{-1} signal oscillates with its pertinent frequency does not provide a sufficient criterium for a definite assignment. The fundamental ν_{48} as well as the combination modes $2\nu_{37}$ / $\nu_{37}+\nu_{36}$ and $\nu_{24}-\nu_{25}$ may exhibit such behavior.[125] An assignment to combinations of ν_{37}, however, is supported by the strong Franck-Condon activity of this mode. The frequency shift of the 90 cm^{-1} band on the time scale of IVR may then be explained by the large anharmonicity of ν_{37}. The influence that anharmonicity imposes on the peak frequency is amplified upon formation of combination modes or higher harmonics. Relaxation on such a potential should also affect the Frack-

[2] For the description of *trans*-stilbene in acetonitrile around time zero, a coherent term has to be added (grey in Figure 4.11), which is modeled by the weighted sum of a Gaussian and its first derivative.

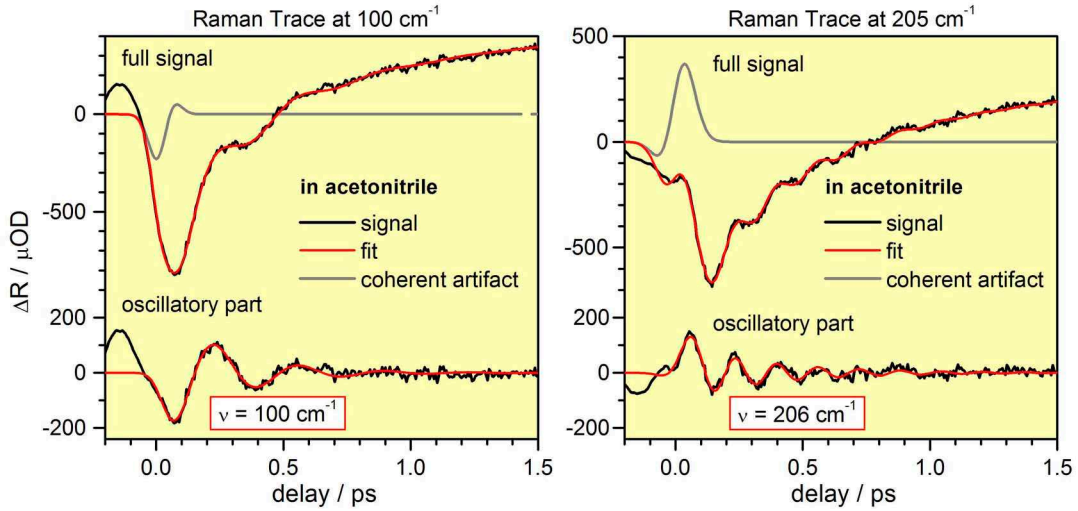

Figure 4.11: Time traces of *trans*-stilbene in acetonitrile at 100 cm^{-1} (left) and 205 cm^{-1} (right). The full signal (top of each panel) was fitted with two exponential functions, one damped oscillation and a coherent artifact around time zero. The oscillatory part and its fit is shown at the bottom of each panel.

Condon overlap with higher electronic states and inter-vibrational coupling. This may readily explain the sub-picosecond decay of the 90 cm^{-1} band.

In terms of third-order signal description, Raman bands below 200 cm^{-1} are assigned to the pathway R^{B}_{4e}. As shown in Section 2.4.1 contributions to transient Raman bands can be described as the product of three Lorentzian functions multiplied with a second-order polynomial, which modifies the spectral shape of the bands. Since the polynomial prefactor is most sensitive to resonance conditions for B-type interaction sequences, it appears reasonable that the R^{B}_{4e} signal responds strongly to wavepacket motion on the excited-state potential. The spectral evolution of the low-frequency bands may then also be understood solely as a change of the signal shape without a shift of the vibrational frequency itself. Note that a single experiment can not easily distinguish between a change of the Raman band shape and a spectral shift of the underlying frequencies. To solve this ambiguity, future experiments should rigorously explore the subtle effects of resonance changes for each system individually. One can avoid the problem by favoring by the experimental conditions third-order pathways of the A type, since their contribution to the signal is less affected by resonance detuning. The high-frequency bands in the *trans*-stilbene measurements, for example, mainly arise from the R^{A}_{3e} pathway, so that stronger spectral shifts like that observed for the 1570 cm^{-1} C=C stretching band may be assigned confidently to changes of the vibrational frequency.

Band Shifts and Frequency Oscillations

Lorentzian spectral fits to the dominant transient Raman bands are obtained for each delay time. The time-dependent positions of representative peaks are compared in Fig-

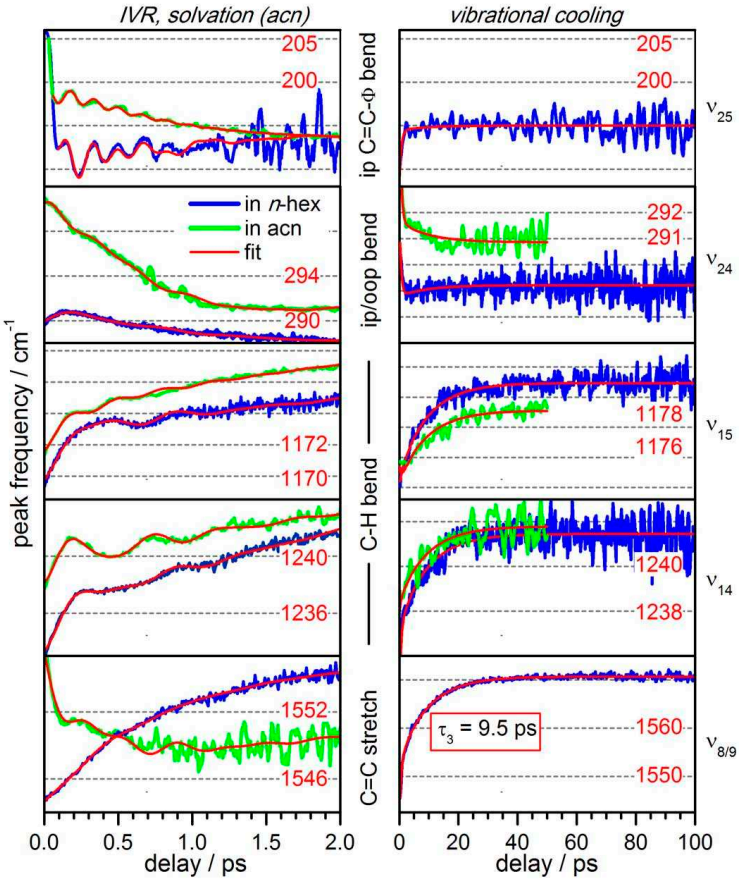

Figure 4.12: Time-dependent shift of representative transient Raman bands of *trans*-stilbene in *n*-hexane (blue) and in acetonitrile (green). For clearer presentation the acetonitile data and the 190 cm^{-1} trace for *n*-hexane solution were smoothed by a Sawitzky-Golay filter. For both solvents the shifts were fitted with three exponential functions (red) which reflect IVR (sub-picosecond) and cooling (9.5 ps), together with two oscillatory terms caused by anharmonic coupling to wavepacket motion.

ure 4.12.[3] It is immediately seen that a polar environment affects individual modes differently. The bands around 1175 cm^{-1} (ν_{15}) and 1240 cm^{-1} (ν_{14}) behave similarly in both solvents and exhibit an upshift with increasing delay. Other behavior is seen for the C=C stretching band ν_8/ν_9 around 1550 cm^{-1}: in *n*-hexane a strong upshift is observed and in acetonitrile a downshift. A similar divergence is found for the 192 and 289 cm^{-1} bending modes (ν_{25} and ν_{24}, respectively). In addition oscillatory modulations

[3] Short and long-time measurements were recorded separately. The calibration precision for the absolute peak positions is estimated 1 cm^{-1}. Fits in spectrally congested regions may show additional jitter for the absolute frequencies of up to 3 cm^{-1}. These errors are systematic and do not affect relative changes within a single measurement. Spectral fits to a well defined band allow to monitor changes which are significantly below the pixel separation of the photodiode array.

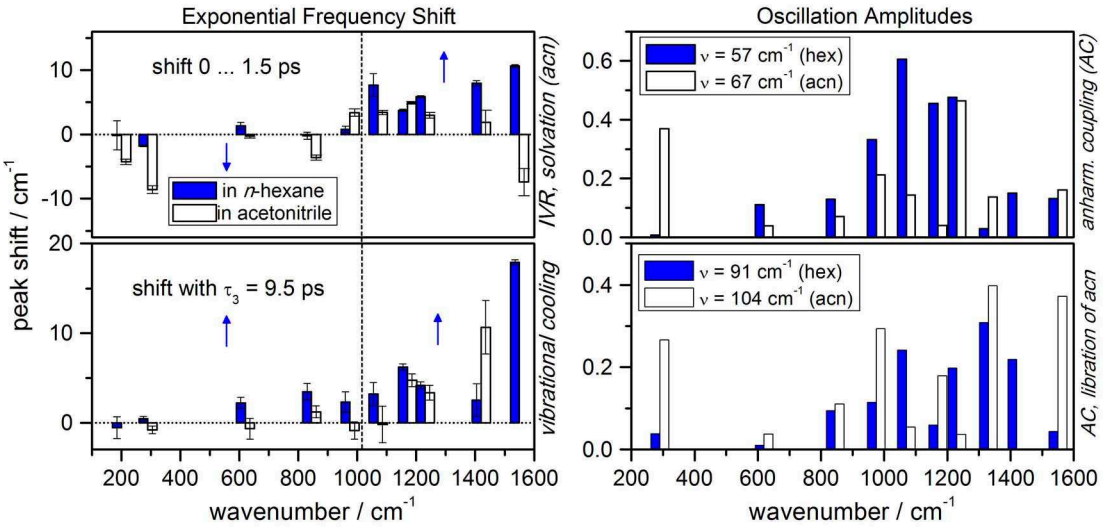

Figure 4.13: Global fitting results for the time dependent peak-shifts of excited *trans*-stilbene (*cf.* Figure 4.12) in *n*-hexane (blue) and acetonitrile (white). *Left*: Oscillation-free shift during the first 1.5 ps (*top*) and long-time evolution (*bottom*, 9.5 ps component). The standard deviation of the residual up to 1.5 ps and 30 ps is given as error bars. The blue arrows illustrate the trends for the high- and low-frequency modes in *n*-hexane. *Right*: Amplitudes of the oscillations.

of the peak frequency are found within the first picoseconds. The shifts are therefore fitted with three exponential functions ($\tau_1 = 0.2$ ps, $\tau_2 = 0.6$ ps, $\tau_3 = 9.5$ ps) and two damped oscillations ($\nu_1 = 57/67$ cm^{-1} and $\nu_2 = 91/104$ cm^{-1} in *n*-hexane/acetonitrile, respectively, with damping time $\gamma = 0.6$ ps). Only the 190 cm^{-1} band oscillates with its own frequency as already described in the analysis of Raman intensities. Here, the previously obtained parameters are applied. Due to the oscillations the sub-picosecond time-constants cannot be well distinguished. They were fixed in approximate agreement with the decay-times of the band integrals. The spectral shifts and oscillation amplitudes are compared in Figure 4.13.

For a discussion of spectral shifts in *n*-hexane, consider relaxation on an anharmonic potential energy surface. On a Morse-like potential, a decline on the vibrational ladder leads to a shift of oscillation frequency to higher values. In the band integral discussion Franck-Condon active modes were located mainly in the spectral region > 1000 cm^{-1}. In accordance with the proposed model, an upshift is observed for these modes during sub-picosecond relaxation. In contrast, the low-frequency modes ($<$1000 cm^{-1}) gain excess vibrational energy during IVR and are expected, accordingly, to show a frequency downshift. Indeed, for some modes like ν_{24} (289 cm^{-1}) such evolution is observed, but the effect is reduced by the large number of non-totally symmetric acceptor modes. Following the discussion of the band integral analysis, redistribution within a vibrational subset and equilibration over the complete vibrational manifold should be distinguishable by the peak shifts as well. The strong oscillations, however, prevent a clear separation

of the two processes, and the full shift during the first 1.5 ps is presented in Figure 4.13, instead. The band position could be further influenced by a gradual evolution along low-frequency modes; quantification of vibrational excitation requires anti-Stokes information from future experiments.

The influence of the polar acetonitrile environment is observed as a frequency downshift of the C=C stretching modes ν_8/ν_9 (1550 cm^{-1} band) and the phenyl bending modes ν_{24} (291 cm^{-1}) and ν_{25} (193 cm^{-1}). This additional relaxation process could indicate dynamic polar solvation. The excited chromophore is initially prepared in the solvation shell of the ground state, after which the solvent molecules reorient to stabilize a more polarized form of S_1 stilbene. Calculations found elongation of the C=C bond lengths and a decrease of the C_{et}=C_{et}-C_Φ angle upon $S_1 \leftarrow S_0$ transition.[119] At early delay time the solvent shell may hinder oscillation along the new equilibrium geometry. Subsequent reorientation of the solvent molecules then allows a gradual relaxation of the potential minimum position for the affected modes. One may therefore conclude that the 0.69 ps component found in the band-integral analysis corresponds to dynamic solvation rather than to a separate IVR process. This component is most obviously identified for the low-frequency modes in Figure 4.12. The special role of the modes ν_{25}, ν_{24} and ν_8/ν_9 is further supported by a strong loss of Raman intensity during the 0.15 ps relaxation (Figure 4.8).

After IVR the molecule is internally equilibrated but still hot. Transfer of energy to the solvent (vibrational cooling) was reported to take place on a 10 ps time scale,[53,102–107] and for the 1570 cm^{-1} mode (ν_8) a linear dependence of peak position and spectral width on temperature was confirmed.[105,131] The 9.5 ps shift in Figure 4.12 is in good agreement with this picture. In *n*-hexane all modes are upshifted in frequency as the full vibrational manifold looses excess energy to the solvent. Let us consider the different situation in acetonitrile. Like in IVR, the shifts of 1179 cm^{-1} and 1240 cm^{-1} bands exhibit analogous behavior in both solvents, while that of the 289 cm^{-1} band seems to be reversed in acetonitrile. Here the position of the 1550 cm^{-1} C=C stretching band cannot be determined with sufficient accuracy during the cooling process. However previous experiments found smaller shifts for this peak on the 10 ps time scale in acetonitrile than in *n*-hexane solution.[132,133] Within the proposed model these differences indicate that mixing with the zwitterionic state during solvation (0.69 ps) leads to a persistent modification of the potential energy surface along the main interacting modes.

Oscillatory frequency modulations are observed for most high-frequency bands even though the band integrals of the modes > 200 cm^{-1} do not show similar variations. Modulation with 91 or 104 cm^{-1} (*n*-hexane or acetonitrile) matches the frequency of the inverse Raman band which was tentatively assigned to a combination mode involving ν_{37} ($2\nu_{37}$ or $\nu_{37} + \nu_{36}$). For this mode wavepacket motion was already directly identified by vibration of Raman intensity in Figure 4.10; here it is observed indirectly by anharmonic coupling to higher frequency modes. The strong anharmonicity of the ν_{37} potential and its mixing to other modes further supports the assignment. Limited by Raman selection rules, the fundamental itself is not observed directly in the Raman spectrum. Following the evolution of the band positions, however, additional oscillations are seen with 57/67 cm^{-1} which correspond well to the expected fundamental frequency of ν_{37}.

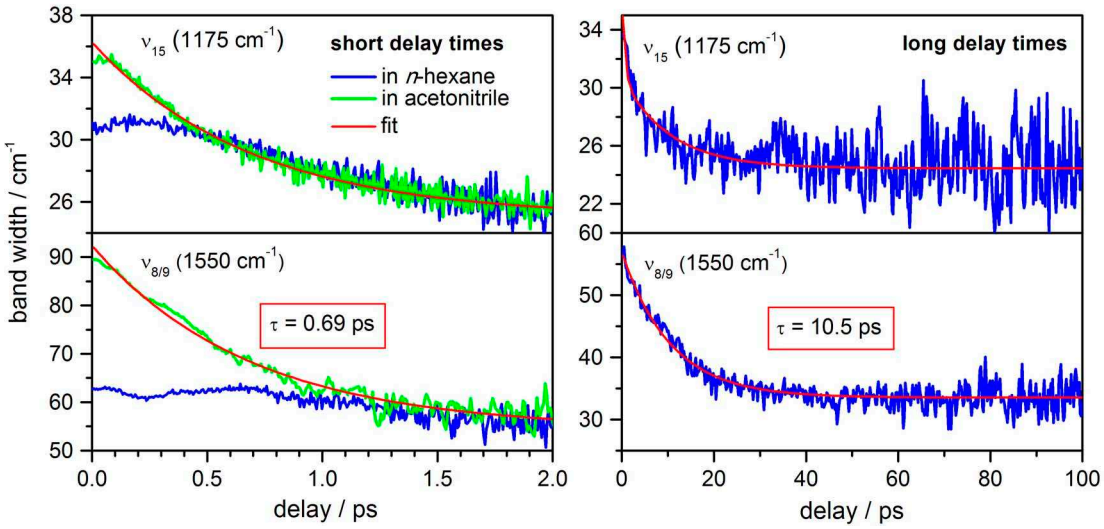

Figure 4.14: Time-dependent spectral width of representative transient Raman bands of *trans*-stilbene in *n*-hexane (blue) and in acetonitrile (green).

The maximum amplitude for the 57 cm^{-1} oscillation is found around 1100 cm^{-1}, in the C-H bending region of the spectrum. The 91 cm^{-1} modulation amplitude instead, appears to be associated with higher modes, where C=C stretching contributions are involved. These differences may result from a contribution of the $\nu_{37} + \nu_{36}$ combination to the 90 cm^{-1} vibration. A more sophisticated interpretation of the coupling strength requires quantum chemical calculations. The ν_{37} and ν_{36} modes describe a mixture of phenyl and ethylene torsion.[119] This motion can alter the electronic delocalization in the molecule and thus affect the curvature of the high-frequency modes. Here the different behavior of the 192 cm^{-1} bending mode ν_{25} should be stressed. For both, the 90 and the 192 cm^{-1} mode, wavepaket motion is observed, but only the 90 cm^{-1} mode couples efficiently to high-frequency vibrations. In this context it seems also unlikely that the 90 cm^{-1} Raman signal is generated by difference frequency formation of ν_{24} and ν_{25}, giving further confidence to the proposed assignment.

In a polar environment the dynamics of the solvent should be taken into account. In transient absorption of a charge-transfer compound a coherent libration with 100 cm^{-1} was found for acetonitrile.[134] The frequency is close to the value of 104 cm^{-1} observed in the present experiment. Indeed, in acetonitrile the corresponding oscillation is significantly enhanced for the 1550 cm^{-1} mode which feels the solvent influence strongest (see above). It may therefore be concluded that the 104 cm^{-1} vibration reflects both coupling to internal low-frequency modes and to external libration of acetonitrile molecules.

Band Widths

The time-dependent widths (full width at half maximum) for the 1175 and 1550 cm^{-1} bands are shown in Figure 4.14. The signal is broad at early delay times and narrows

as the molecule cools down (shown for *n*-hexane solution only). An exponential fit yields a characteristic time-constant of 10.5 ps. The C=C stretching bandwidth at long delay times (34 cm^{-1}) is somewhat higher than values reported in the literature (19–29 cm^{-1}).[106,108] The determined widths depend on the instrumental function and the decomposition of the bands. Therefore the absolute values may be subject to systematic error; the temporal changes, however, reproduce the reported cooling dynamics well.

During the first picosecond, the band-width behavior in *n*-hexane solution is reversed: the bands directly after excitation are narrow and broaden on the time scale of IVR. Due to the limited bandwidth of the pump pulse, at the beginning the energy is concentrated in only few vibrational levels and the ensemble is prepared in a narrow energy distribution. IVR leads to a broader Boltzmann distribution where the energy is equilibrated over the complete vibrational manifold. The process is thus accompanied by inhomogeneous broadening of the bands. In acetonitrile this fast evolution is masked by additional broadening at initial delay times. The 0.69 ps exponential decay of the spectral width is in agreement with the dynamic solvation time. After excitation the random orientation of the polar solvent gives rise to additional inhomogeneous broadening. If during solvation an excited stilbene molecule is stabilized in the polarized state, then this leads to a strong ordering of the solvent shell and a concomitant narrowing of bands.

4.4.2 *cis*-Stilbene

Spectral Evolution

Decomposition of the spectral evolution into underlying spectra is accomplished by a global fit. Each single frequency trace is described by the sum of one exponential function and two oscillations, resulting in the following fit parameters: decay time $\tau = 0.48$ (0.2) ps, oscillation frequencies $\nu_1 = 70$ (70) cm^{-1} and $\nu_2 = 250$ (264) cm^{-1} with damping times $\gamma_1 = 0.07$ (0.07) ps and $\gamma_2 = 0.13$ (0.08) ps in *n*-hexane (acetonitrile). The respective amplitude spectra are shown in Figure 4.15. The strongly damped 70 cm^{-1} oscillation (not presented in the figure) phenomenologically models the ultrafast spectral changes during the first 0.15 ps. The uniform decay thereafter plays out on the same time scale as IVR in *trans*-stilbene. With *cis*-stilbene it is not possible to distinguish two successive relaxation regimes (remember, 0.33 and 0.92 ps for *trans*-stilbene in *n*-hexane), but the 0.48 ps decay time may be interpreted to describe the average IVR behavior corresponding to the correlation time $\langle\tau\rangle$ in Table 4.2. Similarly, the 0.2 ps decay in acetonitrile approximately matches the corresponding time constant in *trans*-stilbene (0.15 ps); the 0.69 ps solvation dynamics is not resolved here. In contrast to *trans*-stilbene, the *cis*-stilbene signal completely vanishes on the time scale of IVR, and no equilibrium spectrum could be obtained. As before, Raman induced population depletion an mechanism for the initial intensity decay, alternative to IVR and solvation. The contribution of this process to the total signal is difficult to estimate on the basis of the current results.

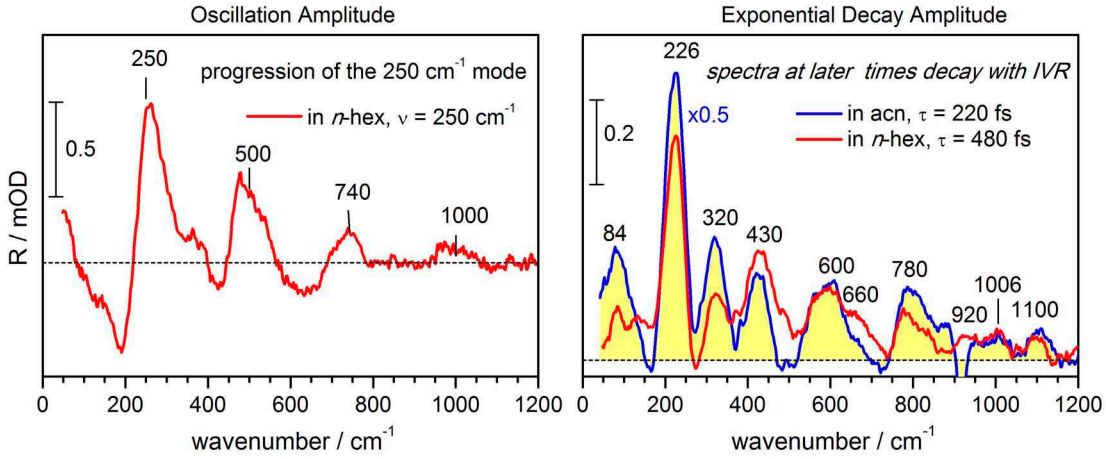

Figure 4.15: Global analysis of the spectral evolution of *cis*-stilbene in acetonitrile (blue) and *n*-hexane (red) after excitation with 280 nm. Each time trace was fitted to one exponential function and two oscillations convoluted with a Gaussian response function. The spectrum associated with the 250 cm^{-1} oscillation is shown to the left, the decay associated spectra are given on the right.

Raman Band Shapes and Resonance Conditions

Resonance conditions need to be taken into account for a discussion of the *cis*-stilbene Raman signal. At 620 nm, the Raman pulse is resonant with both $S_n \leftarrow S_1$ excited state absorption and $S_1 \rightarrow S_0$ stimulated emission. Therefore the FSRR spectra of excited *cis*-stilbene may be affected by all 12 optical processes represented by the diagrams in Figure 2.7, top. The relative contributions of each pathway is determined by the detuning of the Raman pulse from the involved transitions. The simulation of the Raman signal in Section 2.4.2 suggests that sequences with mixed transitions (Figure 2.7, blue/yellow) play only a minor role, so that the discussion is focused here on the influence of pathways involving solely S_n–S_1 (blue in Figure 2.7) or S_1–S_0 (yellow in Figure 2.7) transitions.

In the transient absorption spectrum around 620 nm, the stimulated emission is buried under a much stronger excited state absorption, and one may expect also stimulated Raman spectra to be dominated by S_n–S_1 resonance. In the limit that the influence of transitions to the ground state is negligible, the same situation as in *trans*-stilbene is encountered, *i.e.* emissive Raman bands are observed at the positions of S_1 state vibrational frequencies. In agreement with this expectation, the Raman signal in Figures 4.5 and 4.6 is mainly positive (emissive). Vibrational relaxation does not complete within the measured time window, but at least at later times spectra should be dominated by the R^A_{3e} pathway, whereas directly after excitation also the R^B_{4e} pathway may contribute as well. The shape of Raman signals with a *B*-type interaction sequence is sensitive to the Raman detuning (see Section 2.4.1). In this context a contribution of R^B_{4e} could explain the dispersive shape observed in *n*-hexane at earliest delay times.

For S_1–S_0 resonance the simulation indicates Raman absorption (negative bands) at

the positions of the ground state vibrational frequencies. A clear signature of such ground state Raman features is absent in the transient spetra in Figures 4.5 and 4.6, but a contribution of these pathways can not be completely excluded here. In particular, dispersive band shapes, similar to those observed for *cis*-stilbene in *n*-hexane, were found for bacteriorhodopsin as well, and there assigned to the *hot luminescence* pathways R^B_{5e} and R^A_{6e}.

Changes within the first 0.15 ps

The ultrafast spectral evolution can be characterized by the initial spectrum at 50 fs delay and the decay-associated spectrum ($\tau = 0.48$ or 0.2 ps, respectively). The band positions are compared in Table 4.3 to results obtained from picosecond spontaneous Raman measurements on *cis*-stilbene in *n*-hexane[111]. The spontaneous Raman signal is dominated by the R^A_{3e} process (see Section 2.4.2). Since the experiment has only picosecond time resolution it integrates over the evolution in *cis*-stilbene. Compared with the present measurements, the sponaneous Raman spectrum thus comprises contributions from both, the initial spectrum (at 50 fs) and the spectrum after the early evolution is complete (spectrum associated with $\tau = 0.48$ ps). In particular, the strong bands at 226 and 252 cm^{-1} are, within precision, both found in the literature spectrum. The composition of the spontaneous Raman signal will depend on the temporal structure of the picosecond Raman pulse and its overlap with the pump pulse. Consistently, in a previous publication a spectrum was reported that resembles better the signal observed here at early times.[112] The agreement of results from stimulated and spontaneous Raman scattering corroborates that the R^A_{3e} pathway is the dominant contribution to the signal. The comparison further shows that the ultrafast changes originate from a relaxation process of the excited molecule, and not from coherent $\chi^{(5)}$ interaction of pump, Raman and probe pulses during the cross-correlation time. Note that similar ultrafast changes are observed for the 192 cm^{-1} mode in *trans*-stilbene.

The spectral changes during the first 0.15 ps can be interpreted in two ways: either a shift of the main bands of a single spectrum is observed, as described for the *trans*-stilbene high-frequency modes, or two spectra interconvert, which differ from each other. In the present experiment it is not possible to distinguish between the two variants directly. However the spectrum at late time exhibits only positive bands of approximately Gaussian shape. The absence of dispersive contributions suggests that resonance conditions change during relaxation. Within this model, the existence of two interconverting spectra seems natural; they originate from the same electronic state S_1, but differ in spectral shape and the relative enhancement of vibrational modes.

Raman peak positions can be well correlated to the calculations of ref. 111. The 250 cm^{-1} band (270 cm^{-1} in acetonitrile) is assigned to the ethylenic torsion mode ν_{34}, the 226 cm^{-1} band to the phenylic torsion mode ν_{35} (Table 4.3). In ref. 100 the 252 cm^{-1} band was attributed to ν_{33}, instead. In the present experiment, however, in the decay-associated spectrum also a band at 320 cm^{-1} is resolved and assigned to this mode. In addition for the low-frequency modes at 45-60 cm^{-1} and 84 cm^{-1}, counterparts are found in the calculated spectrum (ν_{37} and ν_{36}, respectively).

Table 4.3: Transient Raman peak positions of *cis*-stilbene in acetonitrile and in *n*-hexane, comparison to ps-measurements, and mode assignment. The spectrum at 50 fs delay, the spectral distribution of the 250 cm^{-1} oscillation and the exponentially decaying component (τ = 0.48 ps, obtained from a global data analysis) are given. The progression of ν_{34} is marked grey. In acetonitrile the decay associated spectrum (τ = 0.2 ps, *cf.* Figure 4.15) is similar to that in *n*-hexane.

Raman band positions / cm^{-1}						**Assignment**[b]	
at t = 50 fs		**250 cm^{-1} osc.**	**τ = 0.48 ps**	**ps-measurement**[a]	**calculated**[b]	**mode**	**motion**
acn	***n*-hex**	***n*-hex**	***n*-hex**	***n*-hex**			
$\sim$ 45	60				48	ν_{37}	C_{et}-C_Φ torsion
			84		71	ν_{36}	C_{et}=C*et* torsion
			226	229	181	ν_{35}	C_{et}-C_Φ torsion
270	252	250		252	255	ν_{34}	C_{et}=C_{et} torsion
			320		325	ν_{33}	C_{et}=C_{et} torsion
			430		418	ν_{32}	
465	480			457	471	ν_{31}	
		500			510	$2\nu_{34}$	
525	525			520	519	ν_{30}	
			600		597	ν_{29}	
680			660		662	ν_{28}	
	724			709	731	ν_{27}	
		740		755	765	$3\nu_{34}$	
783	765		780		756	ν_{26}	
					813	ν_{25}	
875					839	ν_{24}	
			920		900	ν_{23}	
					957	ν_{22}	
1000	1000	1000	1006		1020	$4\nu_{34}$	
			1100				

[a] from ref. 111. Experimental conditions: 267 nm excitation, 630 nm Raman wavelength, spontaneous Raman experiment with ps-resolution. [b] from ref. 111. CIS calculations with a 6-31+G(d) basis set. Harmonics of ν_{34} were calculated as integer multiples of the fundamental frequency.

Intensity Oscillations

The spectral distribution of the 250 cm^{-1} oscillation in *n*-hexane is shown in Figure 4.15 (left). Strikingly, the largest amplitude is observed for the 250 cm^{-1} band itself. In agreement with the upshifted band in acetonitrile, the oscillation is there observed with 264 cm^{-1}. It is concluded that the oscillatory modulation derives from wavepacket motion along the potential of this mode. In time-resolved pump-depletion spectroscopy, a strongly Franck-Condon active mode was seen in the same spectral region and its evolution followed in time.[100] Returning to the observations in the present work, a Raman progression of ν_{34} up to the 4^{th} harmonic is visible in the oscillation spectrum (Figure 4.15) indicating strong displacement in the resonant state. A similar conclusion was drawn from ps-Raman measurements although there definite identification of the features was hindered by congestion with other bands.[111,112] Note also that in the pump-depletion experiment mentioned above, the time-domain vibrational signal was generated by dumping population to the ground state, thereby creating a hole in S_1 which oscillates. As a consequence, the experiment follows the evolution of modes that are Franck-Condon active between S_0 and S_1 states exclusively. In contrast, Raman spectroscopy as presented here is also sensitive to modes that are enhanced by resonance with higher electronic states. The stimulated Raman spectra seem to be dominated by this contribution, at least at later delay times.

Finally for this section it is emphasized that the changes observed here only reflect relaxation towards the local S_1 minimum. The existence of an excited-state barrier is confirmed by the well-defined fluorescence spectrum (Figure 4.2). The motion over the barrier towards isomerization is not seen here.

4.5 Conclusions

The relaxation pathways proposed for *trans*-stilbene are illustrated in Figure 4.16, the observed changes for both isomers are summarizend in Table 4.4. The following points are concluded:

(1) After excitation intramolecular vibrational redistribution (IVR) takes place which is seen as subpicosecond decay of Raman intensity, shift of spectral band position, and broadening of the Raman signal. These changes are observed with a correlation time of 0.5–0.7 ps for both isomers. For *trans*-stilbene a detailed analysis of the intensity decay further allows to distinguish two processes which may be described with a biexponential fit (τ_1 = 0.33 ps, τ_2 = 0.92 ps). It is suggested that at early delay times, vibrational energy is redistributed within a subset of modes which is probably governed by symmetry constraints. Increased intensity loss for individual bands, mainly situated in the spectral region > 1000 cm^{-1} may be assigned to this process. A subsequent uniform decay of the transient spectrum with 0.92 ps is then interpreted as equilibration over the full vibrational manifold. The energy drain from Franck-Condon active modes is observed as an upshift of high-frequency modes > 1000 cm^{-1}. In agreement with the polarization exchange model acetonitrile may facilitate symmetry breakage and accel-

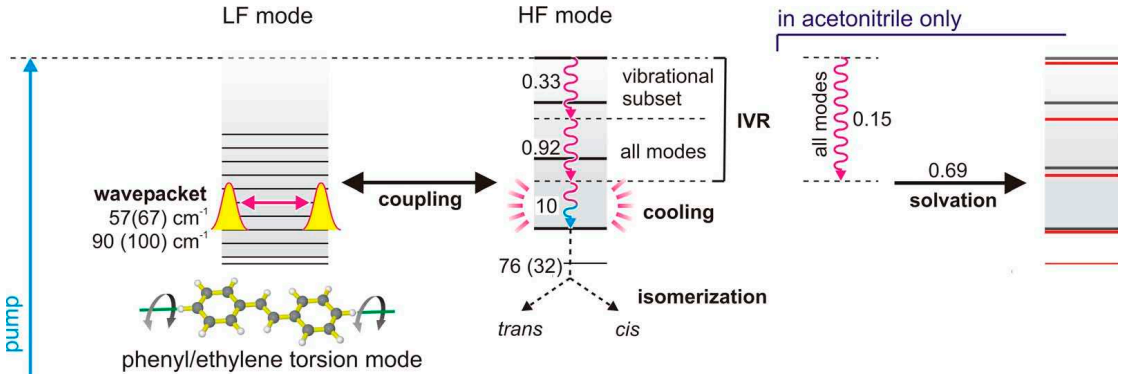

Figure 4.16: *trans*-stilbene relaxation pathways after excitation at 280 nm (blue arrow). Time constants are given in ps. In *n*-hexane, sequential IVR (intramolecular vibrational redistribution) takes place with 0.33 and 0.92 ps. In acetonitrile only one process with 0.15 ps is found. The molecule vibrationally cools with 10 ps and isomerizes with 76 ps (32 ps in acetonitrile). High-frequency modes are coupled to low-frequency phenyl torsion modes and are modulated with their frequency. In acetonitrile dynamic solvation modifies the potential with 0.69 ps.

erates IVR to monoexponential evolution with about 0.15 ps. As an alternative model for early decay of Raman signals in Chapter 6 population loss due to depletion by the Raman pulse is suggested. Raman measurements on flavin indicate a dependence of the initial intensity loss on the measurement parameters, but the peak positions appear to be unaffected. A clear assignment of the observed effects requires further experiments.

(2) Wavepacket motion modulates the amplitude and peak position of low-frequency Raman bands in both isomers. For *trans*-stilbene in *n*-hexane (acetonitrile), the 90(100) cm^{-1} and the 192(193) cm^{-} bands vibrate with their own frequencies. For *cis*-stilbene oscillations with 250(264) cm^{-1} reveal a spectral progression of the corresponding torsional mode up to the fourth harmonic.

(3) Anharmonic coupling, the driving force of IVR, shows up as oscillations of *trans*-stilbene peak frequencies. Wavepacket motion along the 90(100) cm^{-1} and a 57(67) cm^{-1} mode modulate the C-H bending and C=C stretching potentials. These low-frequency modes are assigned to the phenyl/ethylene torsion vibration ν_{37} and its combination modes $2\nu_{37}/\nu_{37} + \nu_{36}$.

(4) Decay and shift of the 90(100) cm^{-1} band during the first 0.25 ps suggests torsional changes during IVR.

(5) Dynamic solvation by acetonitrile gives rise to additional band shift and narrowing in *trans*-stilbene with a time constant of 0.69 ps. Affected are mainly the 1550 cm^{-1} ethylenic stretch ν_8/ν_9 and the 291 cm^{-1} and 193 cm^{-1} bending modes (ν_{24} and ν_{25},

respectively). It is proposed that the adaption of the excited state geometry is hindered along these modes and follows the reorientation of the solvent shell. An increased 100 cm^{-1} oscillatory component for the C=C stretching band in acetonitrile may be attributed with coherent libration of solvent molecules.

(6) Cooling of the vibrationally equilibrated molecules expresses itself in *trans*-stilbene as further shifts in peak position and spectral narrowing on a time scale of 10 ps.

(7) Ultrafast spectral changes on the 0.1 ps time scale are found in the low-frequency regions of *cis*- and *trans*-stilbene. They may either reflect a change of resonance enhancement for different vibrational modes or a strong spectral shift of a single vibration during relaxation. Global analysis allows temporal decomposition of the S_1 spectral evolution.

In future, comparison to anti-Stokes spectra should help quantify the vibrational population flow, thus completing the picture of relaxation at earliest times.[135–137] To avoid abiguity, it is necessary to exclude potential effects from population depletion by the Raman pulse. The present experiment is limited to following the relaxation to the excited state minimum. The involved processes are expected to play a crucial role for the subsequent isomerization. Frequency doubling of the Raman pulses will allow to monitor evolution beyond the isomerization barrier and will provide a unified view of stilbene photophysics. On this basis, shaped pulses could be designed that efficiently drive population through a specific isomerization path.

Table 4.4: Proposed relaxation processes for *cis*- and *trans*-stilbene in *n*-hexane and acetonitrile excited with 280 nm; as derived from observed changes.

Process	**Observed Changes**			**Parameters**	
	Intensity	**frequency**	**width**	**in *n*-hex**	**in acn**
IVR					
trans	——— change of the 192 cm^{-1} band (ν_{25}) ———			$\tau < 0.1$ ps	$\tau < 0.1$ ps
	preferential decay of hf bands	upshift of hf, downshift of lf bands	broadening	$\tau_1 = 0.33$ ps,	
	decay	—	broadening	$\tau_2 = 0.92$ ps	$\tau = 0.15$ ps
cis	——— change of the 250 cm^{-1} band (ν_{34}) ———			$\tau \sim 0.1$ ps	$\tau \sim 0.1$ ps
	decay			$\tau = 0.48$ ps	$\tau = 0.2$ ps
solvation					
trans	decay	downshift of ν (C=C) and C=C-Φ bending modes ν_8, ν_{24} and ν_{25}	narrowing		$\tau = 0.69$ ps
vibr. cooling					
trans		upshift of all bands (in *n*-hexane)	narrowing	$\tau = 10$ ps	$\tau = 10$ ps
wavep. motion					
trans		osc. of hf bands		$\nu = 57$ cm^{-1}	$\nu = 67$ cm^{-1}
	osc. of 90 cm^{-1} band	osc. of hf-bands		$\nu = 90$ cm^{-1}	$\nu = 100$ cm^{-1}
	osc. of 200 cm^{-1} band	osc. of 200 cm^{-1} band		$\nu = 195$ cm^{-1}	$\nu = 206$ cm^{-1}
cis	osc.of ν_{34} progression	osc. of 250 cm^{-1} band (ν_{34})		$\nu = 250$ cm^{-1}	ν=264 cm^{-1}
isomerization					
trans	decay			$\tau = 76$ ps	$\tau = 32$ ps

5 Structural Changes upon Internal Conversion of a "Parent Cyanine"

5.1 Introduction

In the previous chapter the relaxation of stilbene on the excited-state potential energy surface was studied in detail. Due to resonance conditions, however, the isomerization reaction itself could not be followed. In this chapter transient Raman measurements are extended beyond the isomerization barrier for another aromatic dye, 1,1'-diethyl-2,2'-pyrido cyanine iodide (PC), whoose structure is shown as an inset to Figure 5.1. This molecule has not been studied by ultrafast spectroscopy, before, even though it can be regarded as the "parent molecule" for the important family of cyanine dyes.

Previous experiments on thiazole orange[138] and calculations[139] suggested that the photoreaction is initiated by a stretch and conrotatory twisting, followed by an asymmetric distortion. It was proposed that conversion to the ground state occurs from a perpendicular structure, which carries charge-transfer character.

A current application of cyanines is the use as indicator dyes for DNA hybridization: the chromophore is inserted into the helix in place of a nucleobase. Binding to a complementary strand reduces the free volume of the dye and prevents the isomerization. As a consequence, the fluorescence quantum yield increases by orders of magnitude. To draw conclusions about the nature of the pairing event itself, it is crucial to acquire detailed information about the isomerization event.

Here the reaction is studied by a combination of femtosecond absorption, fluorescence and stimulated Raman spectroscopy. Decay and shift of the stimulated emission reports on the relaxation in the excited state. Internal $S_1 \rightarrow S_0$ conversion is identified by a rising signature of the hot ground state. Transient Raman spectroscopy is used to obtain vibrational spectra of the educt, intermediate and product states.

5.2 Materials and Methods

5.2.1 Synthesis and Characterization

Synthesis. 1,1'-diethyl-2,2'-pyrido cyanine iodide (PC) was synthesized and characterized by Matthias Pfaffe in cooperation with Rainer Mahrwald.[1]

Briefly, a concentrated solution of 2-iodopyridine ethiodide and α-picoline ethiodide in *n*-propanol was treated with triethylamine, yielding a deeply colored product[27,140]

[1] Department of Chemistry, Humboldt-Universität zu Berlin, Brook-Taylor-Str. 2, 12489 Berlin, Germany.

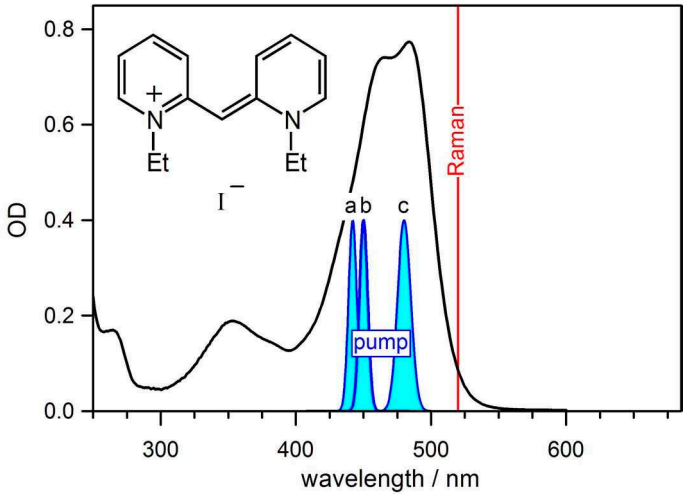

Figure 5.1: Stationary absorption spectrum of 1,1'-diethyl-2,2'-pyrido cyanine iodide (PC) in methanol, at the concentration and optical path length used in the femtosecond transient absorption measurements. The power spectra of the actinic pump pulses are also shown in blue (a – transient absorption, b – fluorescence upconversion, c – FSRS). The red line indicates the wavelength of the Raman pulse.

that was purified by column chromatography (chloroform/ethanol 4:1). The obtained substance was identified as 1,1'-diethyl-2,2'-pyrido cyanine iodide by its optical absorption spectrum and its decomposition into the 2,2'-bispyridinium salt, which could be characterized by X-ray diffraction.

The stationary absorption spectrum of PC in methanol is shown in Figure 5.1 for the concentration and optical pathlength used in the transient-absorption experiments (typically, $OD_{max} = 0.8$ over 350 μm). At such high concentrations, association leads to a 4% deviation from the Lambert-Beer law at the absorption peak. For excitation with $\lambda_{pump} > 440$ nm the contribution of excited associated molecules is negligible. The solvent for all measurements reported here was methanol (Merck UVASOL).

5.2.2 Transient Absorption

Broadband transient absorption spectra were recorded with optical pumping at 442 nm (0.5 μ J, a in Figure 5.1). A broad spectral range was probed with the supercontinuum setup based on the Femtolasers *sPro* system (Chapter 3); the maximal bleach signal was ΔOD_{max} = -0.160. A pump-probe intensity cross-correlation time of 86 fs (fwhm) was determined from the coherent spike in solvent measurements.

5.2.3 Fluorescence Upconversion

Time-dependent fluorescence spectra of PC in methanol were provided by Mohsen Sajadi.[2] Measurements were performed with the broadband fluorescence upconversion setup described in the experimental chapter. The sample solution was excited with 40 fs, 450 nm pulses (0.6 μJ, b in 5.1) The absorbance over 0.4 mm internal path length was adjusted to ~ 0.6 at the absorption peak. Photometric calibration and time correction was performed with several dyes and dye mixtures. As a result, transient fluorescence photon distributions over visible wavelengths were obtained with 132 fs time resolution (fwhm of apparatus function). They were smoothed with a Gaussian filter to a spectral resolution of 4.7 nm (fwhm) and transformed into the corresponding spectra for stimulated emission.

5.2.4 Femtosecond Stimulated Raman Scattering (FSRS)

Time-dependent Stokes-shifted Raman spectra of PC in methanol were obtained with the Raman setup described in Chapter 3. Transient measurements were carried out by exciting the sample at 480 nm with 0.6 μJ (c in 5.1). Narrowband Raman pump pulses at 520 nm (0.5 μJ, red line in Figure 5.1) were generated with the *nb*-OPA from Section 3.5.1. Spectral integration of the background gives a fifth-order intensity correlation function from which a time resolution of 70 fs (fwhm) is inferred.

The spectral resolution is 12 cm^{-1} (fwhm). To cover the full evolution, measurements were recorded in time steps of 6 and 100 fs. For presentation of the transient spectra in Figure 5.7 a 5-point (30 fs/500 fs) moving average filter in time was applied.

As shown in Figure 5.2 the ground-state Raman spectrum of PC in solution contains a methanol contribution (dashed red) with strong bands at 1034, 1109, and 1454 cm^{-1}. The methanol spectrum was measured separately and subtracted to give the pure PC Raman spectrum (Figure 5.2, bottom).

5.2.5 Quantum-chemical Calculations

Quantum-chemical calculations were provided by Fabrizio Santoro,[3] Roberto Improta,[4] and Vincenzo Barone.[5]

As a model for PC, the homologous 1,1'-dimethyl-2,2'-pyridocyanine (Me-PC) was studied on the DFT and TD-DFT (for electronic excited states) levels of theory. Two sets of functionals were used: (i) B3LYP, which gives accurate results for valence transitions without charge-transfer character, and (ii) long-range corrected CAM-B3LYP to treat charge-transfer effects.[141,142] Solvent effects were included through the Polarizable

[2]Department of Chemistry, Humboldt-Universität zu Berlin, Brook-Taylor-Str. 2, 12489 Berlin, Germany.

[3]Instituto di Chimica dei Composti Organo Metallici del Consiglio Nazionale delle Ricerca, Via G. Moruzzi 1, 56125 Pisa, Italy

[4]Dipartimento di Chimica Universitá Federico II, Complesso Universitario di Monte S. Angelo, 80126 Napoli, Italy.

[5]Scuola Normale Superiore, piazza dei Cavalieri 7, 56126 Pisa, Italy.

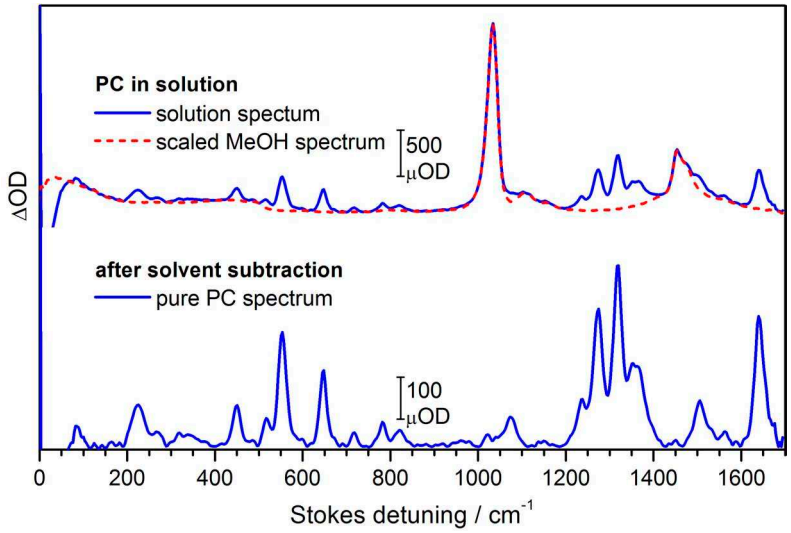

Figure 5.2: Ground-state Raman spectrum of PC in MeOH (blue, top). Removal of the solvent spectral features (dashed red) gives the pure cyanine spectrum (bottom).

Continuum Model (PCM),[143] with both a standard linear response (LR) and a state specific (SS) implementation.[144,145]

For optical absorption and resonance Raman calculations of all isomers Herzberg Teller effects were neglected, and the normal modes and frequencies of S_1 were supposed to be equal to those of S_0. Geometry displacements were obtained from a suitably constrained S_1 optimisation or derived from the S_1 potential energy surface gradient at the equilibrium geometry of S_0. Harmonic frequencies were scaled by a factor of 0.9614.[146–148] Duschinsky effects were included by the recently developed method FCclasses.[149]

5.3 Results and Discussion

5.3.1 Transient Absorption

The spectral evolution of PC in methanol is shown in Figure 5.3. Immediately after excitation at 442 nm (Figure 5.3 a) one observes stimulated emission (SE) in the fluorescence region. The emission band shifts to the red and broadens within $\sim$ 300 fs. During this time the bleach stays constant. From about 300 fs to 1.5 ps (Figure 5.3 b) the SE band disappears, *i.e.* the induced optical density turns positive in the fluorescence region; at the same time the bleach begins to decay. These observations are consistent with internal conversion to a hot electronic ground state for which the absorption lobe around 525 nm is characteristic. The latter grows to a maximum around 5 ps (panel c). Thereafter, slow decay (d) indicates vibrational cooling. At long delay times (black in panel d) an offset spectrum stays, which can be assigned to partial isomerization to the *trans* form.

The dynamics of the evolution is captured by the band integral (see Section 2.2.2)

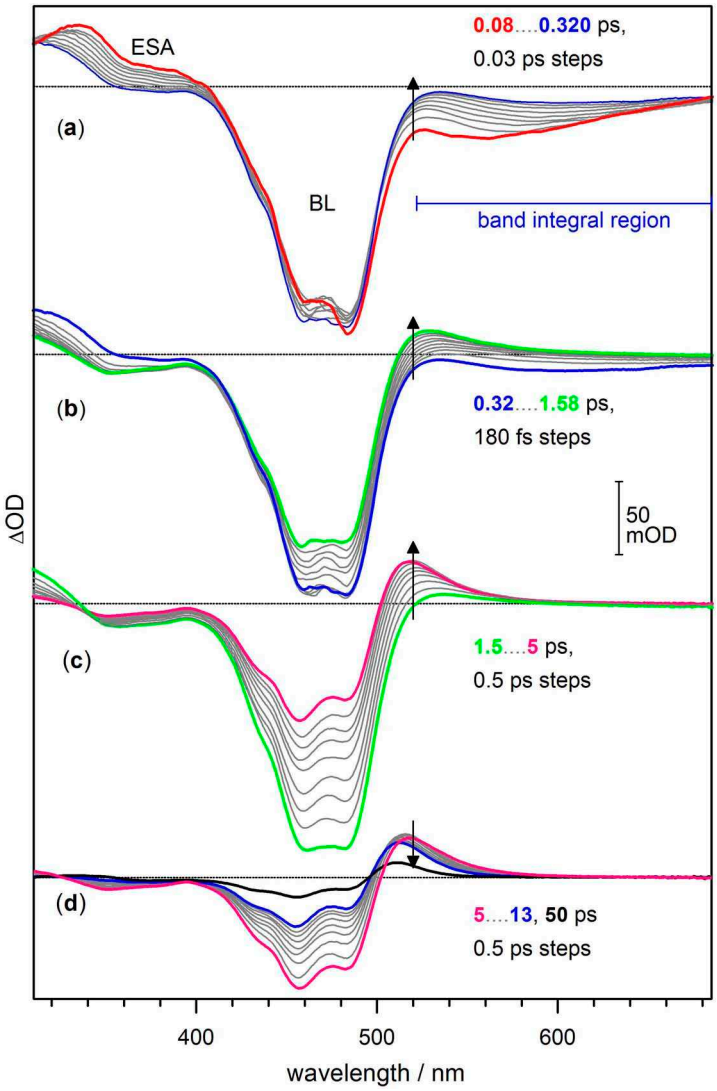

Figure 5.3: Transient absorption (TA) spectra of DP in methanol after excitation at 442 nm (a–d). The time resolution was 86 fs (fwhm of apparatus function) in this case. BL – bleached absorption, SE – stimulated emission, ESA – excited-state absorption. Arrows indicate the spectral evolution, and also the wavelength of the Raman pump in the FSRS experiments.

over the spectral region 522–685 nm; the resulting trace is shown in Figure 5.4. A multi-exponential fit (red, see Section 3.6 for the procedure) finds time constants of 170 fs, 1.3 ps, and 7.9 ps. Note that the band integral does not cover the full stimulated emission, which extends further to the red beyond the measured spectral window. Hence, the short-time rise of the transient absoption band integral reflects both internal conversion to S_0 and a dynamic Stokes of the stimulated emission band. Population transfer to the hot

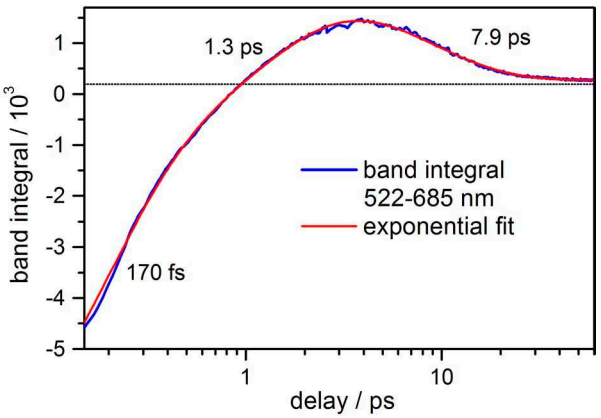

Figure 5.4: Time-dependent band integral of the transient absorpton of PC over the spectral region 522–685 nm (blue bar in Figure 5.3). A multi-exponential fit is given in red; the obtained time constants are indicated.

ground state is seen here as a rise of the band integral above the zero level. Vibrational cooling is reflected by a subsequent decay of the band integral with 7.9 ps. This time constant is close to the 10 ps evolution found in the previous section for the cooling of stilbene.

5.3.2 Transient Fluorescence Upconversion

Time-resolved fluorescence allows to monitor the excited-state evolution, free from contributions of bleach and excited state absorption. Emission spectra for delay times from 80 to 640 fs are shown in Figure 5.5 a. To characterize the decay and spectral shift, all time traces are fitted globally to a sum of exponentials convoluted with the apparatus function. Two time constants of $\tau_1 = 130$ fs and $\tau_2 = 880$ fs are needed for the description. The decay times are slightly shorter than in transient absorption, since the global fit captures not only internal conversion, but also the fluorescence band shift due to relaxation on the excited state potential. The global fit may be recast into a kinetic scheme involving an initial Franck-Condons state FC which relaxes ($\tau_1 = 130$ fs) into an intermediate excited state I, which in turn decays ($\tau_2 = 880$ fs) to zero. Band shape[6] spectra associated with FC and I are compared in Figure 5.5 b to the stationary absorption band shape. Directly after excitation, the emission spectrum is approximately mirror-symmetric to the first absorption band, but it lacks vibrational structure and is slightly broader. With 130 fs the band shifts by 1200 cm^{-1} to the red; the formation of the intermediate I is accompanied by a strong intensity loss ($\sim 88\%$). The transient absorption bleach stays constant on this time scale, indicating that the signal decay is not related to a return of population to the ground state. Similar evolution was seen also for thiazole orange,[138] and there assigned to a loss of oscillator strength for the $S_1 \rightarrow S_0$ transition due to conrotatory distortion of the molecule. Details about the relaxation in

[6] see Section 2.2.2 for the definition of the band shape.

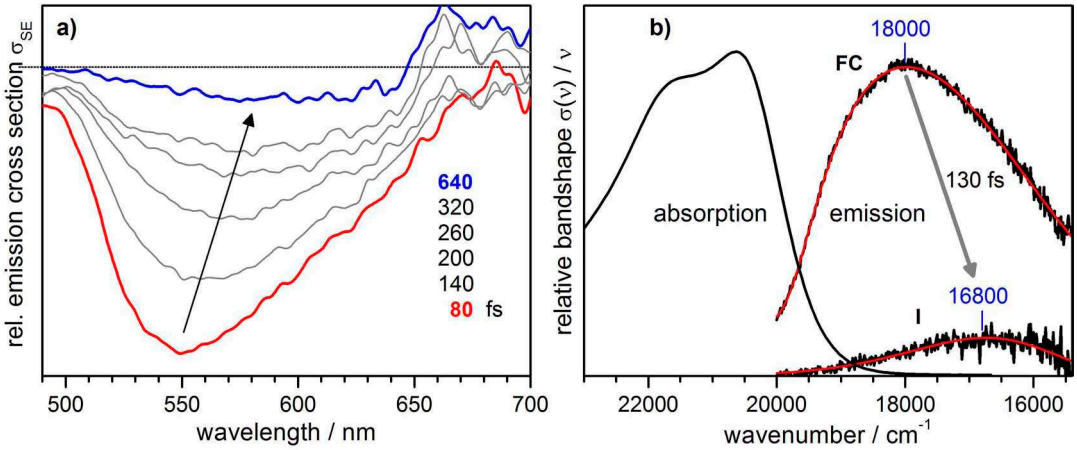

Figure 5.5: a: Time-resolved fluorescence, presented as emission cross-section spectra σ_{SE}. b: band shapes $\sigma(\nu)/\nu$ of the species associated spectra for a virtual kinetic sequence FC→I→0, and comparison to the absorption bandshape. Black: from global analysis, red: fit by lognormal functions.

PC will be revealed by the results from quantum-chemical calculations.

5.3.3 Femtosecond Stimulated Raman Spectroscopy

Resonance Conditions

The Raman pulse was tuned to 520 nm, to the red flank of the ground-state absorption. The hot ground state populated by internal conversion from S_1 has a charcteristic red-shifted absorption, as seen by the lobe around 520 nm in the transient absorption signal (Figure 5.3). The Raman wavelength is thus ideally suited to record resonance-enhanced spectra of the hot intermediate in the electronic ground state.

Additional contributions to the signal need to be considered in stimulated Raman spectroscopy, see Section 2.4.1 for a detailed discussion and simulations. Since the Raman pulse still overlaps with the $S_1 \leftarrow S_0$ absorption, a Raman bleach contributes to the signal as long as the population has not returned to the equilibrated initial ground state S_0. The bleach has the shape of the negative ground state Raman spectrum. A comparison with the transient absorption spectra in Figure 5.3 shows that in the S_1 excited state, before internal conversion to S_0, the Raman pulses are also resonant with stimulated emission, but not with excited state absorption, which is seen only around 340 nm. Hence, the third-order pathways represented by the yellow-shaded ladder diagrams in Figure 2.7 contribute to the Raman signal in the excited state. As shown in the simulations of Section 2.4.2, negative, *i.e.* absorptive bands are expected at the positions of the excited *and* ground state frequencies. In addition, the shape of the signal may be distorted depending on the resonance conditions, as described by the polynomial prefactor in equation (2.98). Especially prone to such distortion are contributions of B-type sequences, here R^B_{5e} and R^B_{8e}. Note that S_0 vibrational signatures from resonance

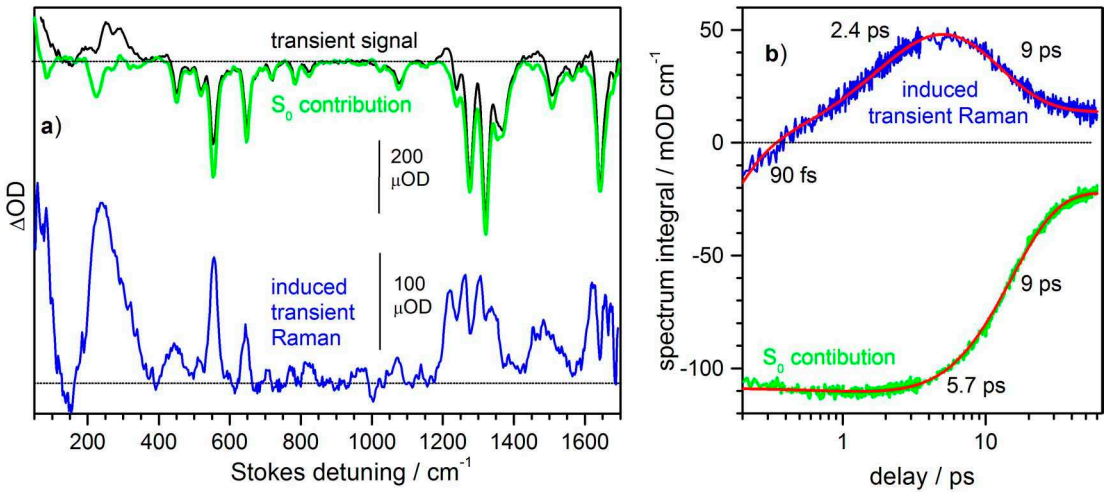

Figure 5.6: a: transient Raman signal of PC in methanol at 5 ps (black, top). The bands are absorptive, generally shown by negative ordinate values. At every delay time the ground-state Raman spectrum of PC at room temperature (S_0 contribution, green) is scaled and subtracted such that $\int(\partial\nu/\partial\nu)^2 d\nu$ is minimal. The optimal residuum (blue) represents the induced transient Raman spectrum which is subsequently discussed. b: time evolution of the S_0 contribution and induced transient Raman spectrum, with time constants from multi-exponential fits (red).

with stimulated emission can be different from the bleach, since they report on the S_0 vibrations, but with the molecule in the excited state geometry.

Decomposition of the Raman Signal

Typical transient signal, recorded 5 ps after the actinic pump, is shown in Figure 5.6 a (black). As expected from the resonance conditions, mostly Raman absorption, *i.e.* negative features are seen. The contribution of the ground state Raman spectrum is now estimated at every delay time (green, from independent measurements). Because sharp structure can be recognized better than background, spectral derivatives are used for the estimate. Thus, a scaled ground-state Raman spectrum is subtracted from the transient signal and $\int(\partial residuum/\partial\nu)^2 d\nu$ calculated. Minimization gives the optimal residuum (blue line in Figure 5.6 a) which is denoted throughout the rest of the Chapter as the "induced transient Raman spectrum".

The amplitudes of the S_0 contribution and induced Raman spectra are shown in Figure 5.6 b as a function of time, together with time constants from multiexponential fits. At longer delay times, after internal $S_1 \rightarrow S_0$ conversion to the hot ground state, the S_0 contribution to the transient Raman spectra corresponds solely to the bleach. In agreement with transient absorption results, the bleach found decays with 9 ps as the molecule cools down. At early delay times, when population is still in S_1, also resonance with stimulated emission occurs and leads to Raman bands at ground state vibrational

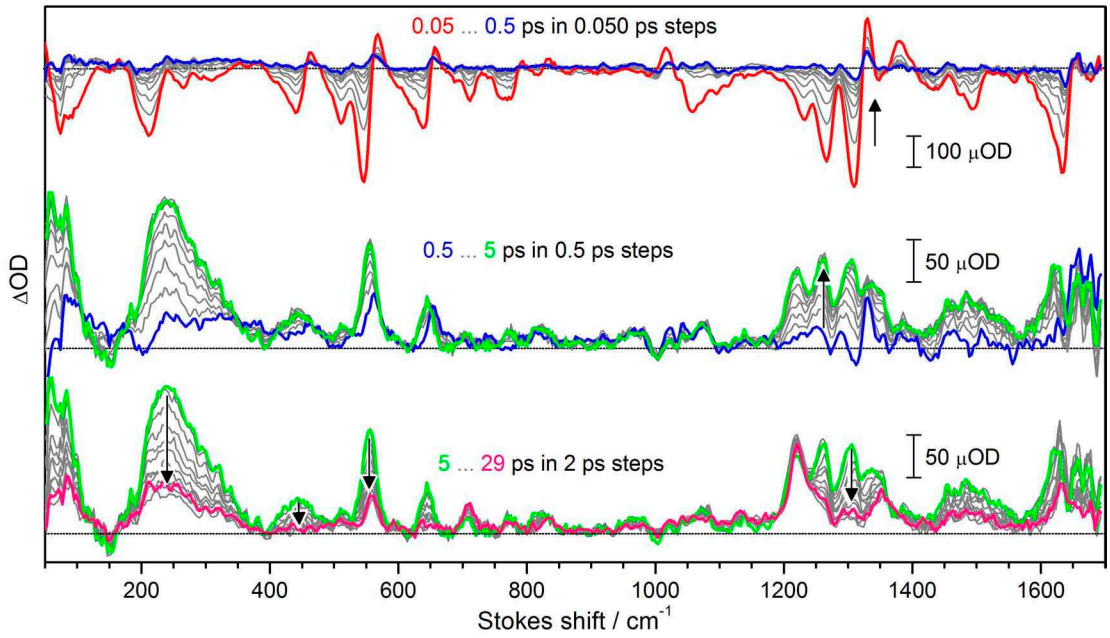

Figure 5.7: Time evolution of the induced transient Raman spectrum (i.e. after the S_0 contribution has been removed) of 1,1'-diethyl-2,2'dipyridocyanine iodide in methanol, after actinic excitation at 480 nm.

frequencies, which in contrast to the bleach may not be reproduced by stationary Raman spectra from S_0. This deviation is seen as an initial plateau of the S_0 contribution in Figure 5.6.

The band integral over the induced Raman absorption monitors also the initial relaxation. It rises with 90 fs and 2.4 ps and reaches a maximum around 5 ps. The ultrafast 90 fs time constant may describe the same relaxation process as the 130 fs time constant in transient fluorescence; however, it is close to the temporal resolution of the Raman spectrometer (70 fs). The 2.4 ps rise is slower than the evolution in transient absorption and fluorescence. This may be an artefact from the incomplete description of the S_0 signal in the excited state. Also depletion of population by the Raman pulse, as proposed in next Chapter, should be considered. After the rise of the hot ground state signal is complete, induced transient Raman evolves consistently with the other spectroscopic results: the band integral decays with the cooling time of 9 ps.

At long delay times, the bleach and the induced transient Raman signal do not approach the baseline, indicating that part of the population stays permanently in a state that is different from the equilibrated ground state of *cis*-PC. It may be concluded that the ground-state minimum of the *trans*-isomer has been populated.

Spectral Evolution

The time evolution of the induced Raman spectrum is shown in Figure 5.7. For the initial period < 0.5 ps the spectrum is mainly absorptive and has dispersive character, indicating the influence of third-order pathways, where the first interaction is with the probe pulse. This initial signature decays ultrafast (90 fs); thereafter Raman emission grows in, to a peak at 5 ps, and then changes gradually to the "final" induced Raman spectrum at 29 ps (magenta).

Global Analysis and Raman Spectra of the involved Species

The time constants obtained in the previous analysis are now used to describe the spectral evolution by a global fit. Applying a model of sequential interconversion the spectra of the intermediate species are obtained. They are shown in 5.8 together with the ground-state Raman spectrum.

Let us follow the relaxation path: The chromophore is excited into the Franck-Condon state FC, characterized by the time-zero Raman spectrum. The shape of the signal is here too complicated to extract the vibrational information about the S_1 state. At this point additional theoretical and experimental work is required to quantify resonance effects on the signal shape.

The signal vanishes with 90 fs almost completely to the baseline (species associated spectrum not shown in Figure 5.8). Assuming that this change correlates with the ultrafast shift and decay of fluorescence, the evolution monitors relaxation on the excited state potential towards a twisted geometry. More insights into underlying processes will be obtained from the quantum-chemical calculations.

With 2.4 ps a new Raman emission spectrum rises; it is assigned to the vibrationally hot ground state after internal conversion. The excess energy is distributed to the surrounding solvent with 9 ps. During this relaxation branching occurs: part of the population returns to the minimum of the *cis* isomer, another part relaxes into the minimum of the *trans* isomer. The long-time offset is therefore assigned to the spectrum of *trans*-PC. Compared to the Raman spectrum of *cis*-PC, mainly the multi-peak structure around 1320 cm^{-1} splits into two bands at 1221 and 1355 cm^{-1}. Also the low-frequncy region differs: The offset spectrum shows a broad band at 230 cm^{-1} with a shoulder around 350 cm^{-1}; sharp bands are found at 560 and 712 cm^{-1}. Strikingly, the spectrum of the hot S_0 state contains spectral features from both isomers. This is consistent with the idea of branching after internal conversion. The hot S_0 spectrum then corresponds either to a still undetermined geometry or to a mixture of hot *cis*- and *trans*-PC.

5.3.4 Mechanistic Conclusions from Quantum-chemical Calculations

Resonance Raman Spectra

Figure 5.9 compares Resonance Raman spectra of *cis*- and *trans*-PC from quantum-chemical calculations (presented as stick spectra) to experimental results from the previous analysis. The optimized ground-state geometries are also shown. The theoretical

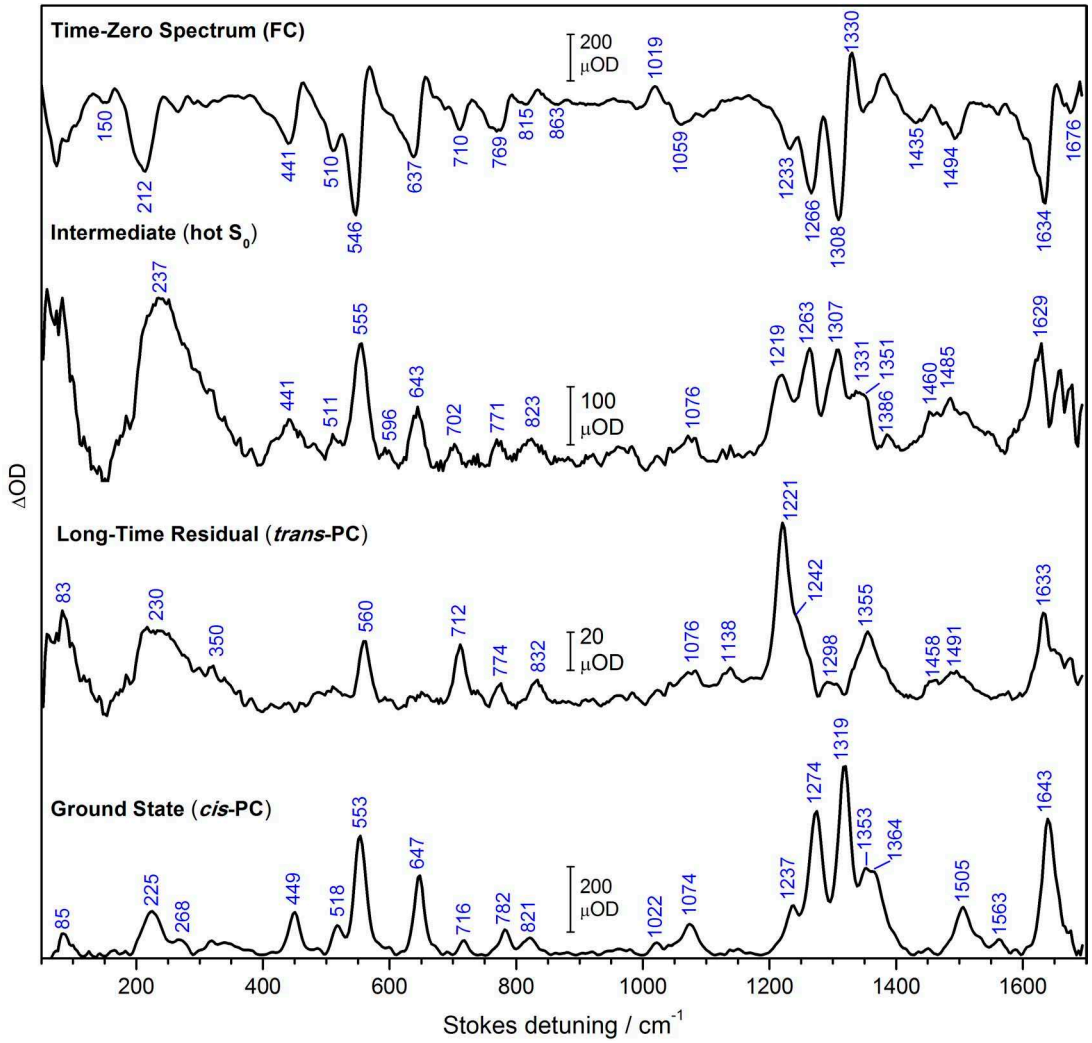

Figure 5.8: Species associated spectra from a global fit of the transient Raman evolution under assumption of sequential interconversion.

spectra reproduce the main spectral pattern for both isomers. In particular, for *trans*-PC, the characteristic bands at 1221, 712, and 560 cm^{-1} are also found by calculation, thus confirming that the *trans*-isomer is formed.

The assignment of the vibrational bands was not yet complete at the time of the submission of this work.

Potential Energy Surfaces and Model

Based on calculations of the minimum energy path, the model in Figure 5.10 gives the most likely explanation of all spectral measurements on PC here. Species, for which Raman spectra were obtained in this work (Figure 5.8) are marked by red dots. The

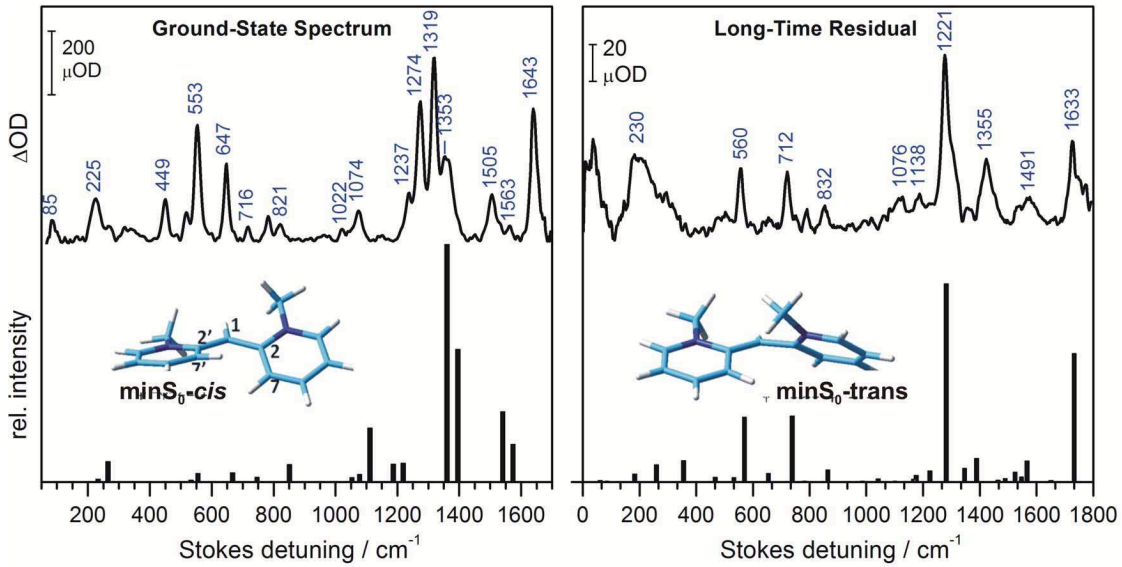

Figure 5.9: Comparison of experimental and calculated Resonance Raman spectra. Calculations were carried by Santoro, Improta, and Barone on the CAM-B3lYP/6-31G(d) level of theory with the VG approximation.

ground-state structure of the cyanine[7] is C_2 symmetric, with the phenyl groups rotated by 22.1° against the central C-H bond (dihedral angles ϕ(7'2'1 2) and ψ(7 2 1 2') are given next to the structures). The excited state potential is very shallow; a local minimum is found for a C_2 symmetric structure with dihedral angles of 30°. Loss of conjugation upon distortion of the molecule could explain the decay and shift of fluorescence (Figure 5.5). Then the ultrafast $\sim$ 130 fs evolution would reflect relaxation towards the C_2 minimum, which is consequently assigned to the intermediate I. Note that for stilbene a different situation was encountered: there calculations found almost planar structures for the minima on the excited state potential; distortion towards a 90° twisted geometry occurs for stilbene after passing the barrier towards the phantom state p (Figure 4.1). Due to resonance conditions the associated spectral evolution could not be followed in that case.

Returning to cyanine, the global minimum on the S_1 potential surface is not the C_2 structure (minS_1-*cis*), but an asymmetric structure with one phenyl group planar and one perpendicular to the central C-H bond (minS_1). Electronically, this structure has charge-transfer character. Since the S_1 potential is shallow, it is not clear whether the global minimum is reached within the residence time in the excited state. The time constant of 880 fs probably describes a combination of relaxation to minS_1 and internal conversion to the hot ground state. Polar solvation progressively stabilizes the S_1 state during relaxation and destabilizes S_0, thus facilitating transition to the ground state. After internal conversion, the molecule is vibrationally hot. It cools down into the

[7] here the dimethyl analogue of PC was calculated.

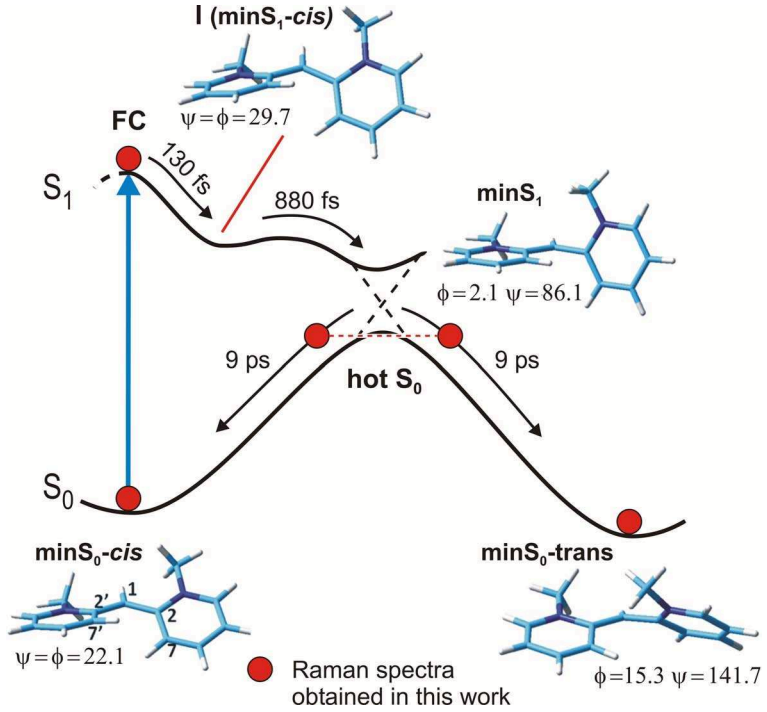

Figure 5.10: Model for the relaxation of excited PC and structures from quantum-chemical calculations. Species, for which Raman spectra were obtained (Figure 5.8 are marked by red dots.

minima of the *cis* and *trans* isomers.

5.4 Conclusions

Photoinduced isomerization of 1,1'-diethyl-2,2'-pyrido cyanine iodide (PC) was traced with femtosecond transient absorption, fluorescence, and stimulated Raman specÅ$\frac{1}{2}$troscopy. The mechannistic interpretation was supported by quantum-chemical calculations.

Upon excitation the stimulated emission band shifts by 1200 cm^{-1} already within 130 fs, accompanied by an intensity decay. The evolution is assigned to the conrotatory motion of the phenyl groups to a dihedral angle of 30°. The ultrafast fluorescence quenching makes PC a promising dye for future DNA intercalation experiments with high contrast. Molecular relaxation on the S_1 potential proceeds with 880 fs towards a 90° twisted structure with charge-tranfer character, until internal conversion to the ground state occurs. The generated hot molecule cools down into the minima of *cis*- and *trans*-PC with 9 ps.

Raman spectra of the Franck-Condon region, the hot ground state, and the *cis* and *trans* isomers could be obtained from a global analysis. Experimental ground-state resonance Raman spectra were reproduced by calculations.

It could be shown that for population on the S_0 potential the bleach can be described by the scaled stationary spectrum, and subtracted from the Raman signal. The resulting contributions can be analyzed separately. In the excited state, when resonant with stimulated emission, the spectrum is complicated; to extract vibrational information, resonance with the $S_1 \rightarrow S_0$ transition should be avoided at the current stage (as in the measurements on *trans*-stilbene).

6 Excited Flavin: A Femtosecond Stimulated Raman Study

6.1 Introduction

Flavin plays a key role in biology as a chromophore of blue-light photoreceptors.[83,150,151] The flavin family is based on the heteroaromatic ring-system of 7,8-dimethyl-isoalloxazine, Figure 6.1. Biologically relevant flavin chromophores derive from riboflavin (RF, vitamin B_2); common derivatives are flavin mononucleotide (FMN) and flavin adenin dinucleotide (FAD). Whereas the primary activation step for other photoactive co-factors like phytochromobilin, retinal, and coumaric acid involves E/Z isomerization, the flavin structure prevents strong conformational changes.[151] Nonetheless, flavin is a tremendously versatile reactant whose specific activation mechanism is determined by the protein environment. In LOV (Light Oxygen Voltage) domains, it is established that formation of the signalling state involves inter-system crossing to the triplet state, followed by covalent addition of a nearby cysteine on the microsecond time scale.[152–156] Flavin photochemistry in other photoreceptors is less well understood. In cryptochromes, one-electron reduction of flavin to its semiquinone form leads to conformational changes of the protein, but the underlying mechanism is still under debate.[157–160] BLUF (Blue Light Using Flavin) photoreceptors show only subtle changes upon illumination. Signalling state formation is accompanied by an approximately 10 nm red-shift of the absorption spectrum.[161–163] Infrared and Raman difference spectroscopy found a concomitant weakening of the C_2-O_2 and C_4-O_4 bonds.[162,164] Femtosecond-resolved transient absorption and infrared studies indicated that signalling state formation occurs on the 100 ps time scale in the singlet state manifold and involves electron and proton transfer.[165–168] It was suggested that these reactions stimulate a rearrangement of the hydrogen bond network around the chromophore.[164–167,169–171] Discussed mechanisms are a 180° rotation of a glutamin residue,[165] and a change in the orientation of a tryptophan residue.[171]

The spectroscopy of blue-light photoreceptors is frequently complicated by conformational heterogeneity in the electronic ground state,[165,167] causing the observed spectral evolution to become multi-exponential. Also light-induced effects are small and different contributions overlap spectrally. Both effects hamper the conclusion of mechanistic details for the early stages of signal transduction. In a complementary approach we concentrate instead on the excited flavin chromophore by itself, free in solution. If its electronic and structural properties were accurately known, including the response to changes in the solvent environment, then this information could be used to deconvolve

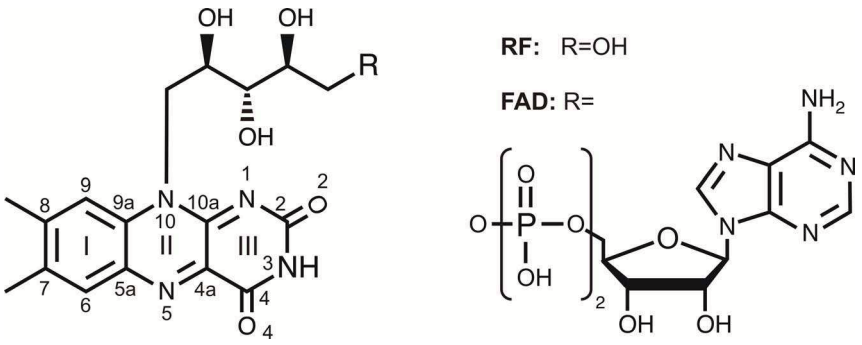

Figure 6.1: Structure of riboflavin (RF) and of flavin adenine dinucleotide (FAD).

the inhomogeneity in proteins, for example. For this purpose flavin is examined by femtosecond stimulated-Raman, absorption, and fluorescence spectroscopies. By correlating the results, electronic and structural changes upon photoexcitation of RF and FAD are quantified.

The photochemistry of flavin depends on its redox state: the oxidized flavoquinone, the semireduced flavosemiquinone, and the fully reduced flavohydroquinone, which may undergo protonation or deprotonation depending on pH.[172] Whereas in the electronic ground state flavoquinone is protonated at N(1), transient absorption experiments on FMN suggest an increased basicity for N(5) in the excited state.[173] In the current experiments, flavin is in the neutral oxidized form that is dominant in the pH range 2 to 8 in polar solvents and constitutes the chromophore in blue-light photoreceptors. Its lowest singlet and triplet states were assigned to $\pi\pi^*$ symmetry, but calculations find a dark state of $n\pi^*$ symmetry in the vicinity of S_1.[174–177] Solvatochromism[178] and Stark effect spectroscopy[179] indicate that the charge-transfer character of the $S_1 \leftarrow S_0$ transition is small. Nonetheless, in femtosecond transient absorption[180] and picosecond fluorescence[181] experiments, signal changes on the time-scale of solvent reorientation were observed. It was proposed that dynamic polar solvation controls vibronic coupling between the S_1 state and the nearby $n\pi^*$ state, and a dependency on the pump wavelength for this process was found.[180] Excited into S_1, RF fluoresces with a lifetime of ~ 5 ns and ~ 20 % quantum yield.[180,182] As a side-reaction, inter-system crossing to the triplet state takes place with 20–30% quantum yield in aqueous solution.[183] Fluorescence is quenched by aromatic amino acids and purines, a finding that was explained by an intermediate reduction of the isoalloxazine ring.[184–189] For FAD in solution, intramolecular electron transfer from the adenine to the flavine was proposed. In polar solvents FAD favors a stacked arrangement of the flavin and adenine moieties.[190–194] The subset of molecules that adapts the π stacked conformation, may return to the ground electronic state via reversible electron transfer. Transient absorption, fluorescence, and infrared spectroscopy find an associated time constant of 5–10 ps.[159,190,195–197] Although this mechanism is commonly accepted, it is still under debate whether the charge-transfer intermediate can be captured by spectroscopy.

Structural changes can be monitored by time-resolved vibrational spectroscopy, *i.e.* by observing changes of normal modes of the chromophore upon photoexcitation. Femtosecond mid-infrared spectroscopy has been applied to flavin derivatives in solution [196,198,199] and embedded in blue-light photoreceptors. [155,165] However the spectral window was limited by the accessible probe frequencies and solvent absorption, and the generation and detection of femtosecond infrared pulses requires significant effort. A general difficulty is presented by ground-state bleaching of IR bands, which – at least for flavins – is superimposed on the photogenerated IR bands, causing dispersive line shapes that are hard to quantify. An alternative approach to measure vibrational spectra with high time resolution is offered by femtosecond stimulated resonance Raman (FSRR) spectroscopy. [8,16,18,19,80] In contrast to infrared spectroscopy, Raman and stimulating probe pulses may be applied in the UV-visible or near-infrared spectral region. Resonance enhancement allows chromophore-selective spectroscopy with minimal disturbance from the bulk environment. This renders the technique particularly valuable for the investigation of biological samples in aqueous media. Most importantly, resonance conditions can be chosen such that Raman bands are observed free of corresponding bleach, as will be shown here. Recently FSRR spectroscopy has been applied to study the primary photochemistry of bacteriorhodopsin, [14] phytochrome, [21] and green fluorescent protein. [23] Spectral oscillations of Raman bands were seen which indicate wavepackets in low-frequency modes. [23,200] This new two-dimensional perspective on photochemical reactivity with flavin chromophores is explored here. Raman spectra in the excited state are provided, and the influence of solvent and resonance conditions on the signal is investigated. Also artefacts that distort the temporal evolution are addressed.

The assignment of vibrations observed in IR or (resonance) Raman spectra is greatly facilitated by quantum chemical calculations. Several previous publications report on the vibrational analysis of flavins in their ground electronic state S_0. [164,198,201–203] Fewer works deal with vibrations in the first excited state S_1. [198,203] In most cases the vibrational assignment was based on normal mode analysis, in some cases IR vibrational spectra (*i.e.*, peak positions and intensities) were calculated. In ref. 203, vibrationally resolved $S_1 \leftarrow S_0$ absorption and $S_1 \rightarrow S_0$ emission spectra were determined for riboflavin. Also from there, information on (some) vibrations is gained, albeit more indirectly. So far no resonance Raman spectra have been computed for RF or FAD to the best of my knowledge. For the current work, a vibrational analysis based on hybrid density functional theory was provided by Bastian Klaumünzer[1] for riboflavin and FAD in the ground state S_0 (normal mode analysis and resonance Raman), and for RF in the first excited state, S_1. Solvent effects of DMSO and water are included, using a polarizable continuum model. For water, in addition a microsolvation environment consisting of four water molecules is considered, to account for hydrogen-bonding at the polar (isoalloxazine) side of flavin.

Electronic transitions are monitored by transient absorption and emission spectrosco-

[1] Bastian Klaumünzer, Department of Chemistry, Universität Potsdam, Karl-Liebknecht-Str. 24/25, 14476 Potsdam-Golm, Germany.

py. The influence of the solvent environment, the excitation wavelength, and the effect of the adenine moiety in FAD on spectral evolution is investigated. A well-known difficulty of the analysis is that transient absorption spectra consist of several overlapping terms which can not be separated uniquely. The pump–induced spectra report simultaneously on the evolution of the excited state via its absorption and stimulated emission properties, and on the population of the ground state via the bleach. Thus, if wavepacket motion is observed by transient absorption, the experiment gives no clue as to whether an oscillating $S_1 \rightarrow S_0$ emission band or an oscillating $S_n \leftarrow S_1$ absorption band is behind the phenomenon, for example. Using a novel fluorescence technique, broadband upconversion, this ambiguity is removed. The rise, spectral change and eventual decay of the flavin emission band is measured with 100–350 fs time resolution (fwhm of the instrumental response function). The photometric accuracy of the femtosecond fluorescence spectra allows quantitative comparison with transient absorption spectra. No evidence is found for an initial fluorescence contribution around 500 nm from the $n\pi^*$ state. Flavin transient absorption is decomposed with the help of fluorescence-upconversion results and present pure excited-state absorption spectra of RF and FAD, allowing to optimize Raman resonance conditions.

6.2 Experimental Details

6.2.1 Transient Absorption Spectroscopy

Transient absorption spectra were recorded with the pump-supercontinuum probe setup that is based on the Femtolasers *sPro* laser system. Pump pulses at 400 nm (40 fs fwhm) were generated by frequency doubling the fundamental. Pulses at 440 nm (50 fs fwhm) were obtained by mixing the 800 nm fundamental with the frequency-doubled output of the *TOPAS* parametric amplifier. The sample was excited with 0.35 μJ of the compressed pulses. The temporal apparatus function is well described by a Gaussian with 50–60 fs width. The spectral range was extended up to 1030 nm by additional measurements with the *CPA 2001* laser system (Clark MXR). For actinic excitation 30 fs NOPA pulses were used, centered at 475 nm.

6.2.2 Transient Fluorescence Spectroscopy

Fluorescence upconversion measurements were recorded with actinic excitation at two different wavelengths: pulses at 400 nm (4 μJ, 40 fs) were generated by frequency-doubling part of the fundamental; pulses at 440–450 nm (0.5 μJ, 50 fs) were provided by a TOPAS (Lightconversion) in combination with frequency mixing (see above). Measured spectra were corrected for instrumental factors such that transient spectra at long delay times match the stationary fluorescence. The apparatus function is described by a Gaussian with the following widths (fwhm): 160 fs (400 nm excitation) and 350 fs (440 nm excitation) for measurements of FAD/H_2O; 100 fs for RF/DMSO with 400 nm excitation and RF/H_2O with 450 nm excitation.

6.2.3 Transient Raman spectroscopy

For Raman excitation at 776 nm, part of the amplifier output was filtered in a monochromator to yield 3.7 μJ pulses with a spectral width of 5.5 cm^{-1}. The stimulating probe pulses were obtained from a noncollinear optical parametric amplifier, centered at 855 nm and broad enough to cover the detection window. The actinic pump was provided by a second noncollinear optical parametric amplifier centered at 467 nm. The compressed output pulses had a duration of $\sim$ 50 fs (fwhm) and a pulse energy of 1 μJ.

Narrowband Raman pulses at 500 and 523 nm were generated in the home-built optical parametric amplifier (see Section 3.5.1), which delivered 1 μJ pulses with a spectral width of 12 cm^{-1} (fwhm) at 500 nm and 20 cm^{-1} at 523 nm.[2] For actinic excitation, NOPA pulses at 475 nm with a duration of 30 fs (fwhm) and a pulse energy of 0.8 μJ were used.

For the presentation of transient spectra at different delay times in Figure 6.6, top, the full spectral evolution, measured in data sets of 660 spectra in 10 and 100 fs time steps, respectively, was filtered by 11-point moving averages in time.

6.2.4 Other Experimental Details.

In all time-resolved experiments the optical density was adjusted to 0.5–0.8 at the maximum of the first absorption band for RF in DMSO and FAD in water, and to 0.2–0.3 for RF in water. The sample was circulated through a flow cell at a speed sufficient to replace the sample after each shot. Experiments were carried out under parallel ($\parallel$) and perpendicular ($\perp$) polarizations of actinic pump and probe or Raman/probe pulses; Raman measurements at short delay times and fluorescence-upconversion measurements on RF in water were only recorded with parallel polarization conditions. The magic angle signal was calculated as $S_{ma} = \left(S_{\parallel} + 2S_{\perp}\right)/3$. The full delay-time window for a transient method was covered by recording individual measurement runs with different time steps. Typically, for given step size and polarization conditions, data from 5–10 runs was averaged. An overview of time-dependent observables was achieved by scaling and combining traces from various measurements. For presentation oscillation traces shown in Figures 6.13 and 6.14 were smoothed by a second-order, 60 fs wide Sawitzky-Golay filter, and the data underlying the contour plot in Figure 6.14 were filterd by a moving average of 30 fs temporal and 15 cm^{-1} spectral width.

6.2.5 Spectral Fits

Spectral fits of time-dependent fluorescence spectra allow to study intensity decay and frequency shift separately (Figure 6.5 c-d). For measurements recorded with 440 nm, the shape of the emission spectrum stays nearly constant during the entire evolution. Therefore each transient spectrum was fitted by a scaled and shifted copy of the stationary emission spectrum. When pumping with 400 nm, the spectral shape at earliest delay times deviates slightly from that of the stationary emission band. In this case the

[2] For the experiment with 523 nm Raman pulses, directly the output of the *nb*-OPA after the amplification was used without additional filtering in a second monochromator.

spectra were fitted by log-normal functions $F(\nu;t)$ instead,[128,204]

$$\sigma_{SE}(\nu;t) = \begin{cases} h\ \exp\left[-\ln(2)(\ln(1+\alpha)/\gamma)^2)\right] & \alpha > -1 \\ 0 & \alpha \leq -1 \end{cases} \tag{6.1}$$

where

$$\alpha \equiv 2\gamma(\nu - \nu_p)/\Delta;$$

the parameters are: amplitude h, peak frequency ν_p, asymmetry γ, and width Δ.

6.2.6 Chemicals

Riboflavin (Sigma Aldrich, 98%) and FAD (Sigma Aldrich, $\geq$ 95%) were used as received. Sample solutions in fluorescence-grade dimethyl sulfoxide (DMSO; Aldrich) or water were freshly prepared before each measurement. Deionized water or deuterium oxide (eurisotop, 99.97 % D) was used for aqueous solutions, except for transient and stationary fluorescence measurements of FAD, in which case 10 mM Tris buffer (FLUKA, pH8) with additional 50 mM NaCl was used. In previous experiments the rate of FAD excited-state deactivation did not change with the pH in the range pH 5–10.[173] Hence, the influence of buffer and salt appears negligible and is not indicated explicitly.

6.3 Quantum Chemical Calculations

Quantum chemical calulations and assignments were provided by Bastian Klaumünzer from the group of Prof. Peter Saalfrank.[3]

6.3.1 Methods and Models

All quantum chemical calculations were performed with hybrid density functional theory on the (TD-)B3LYP[205,206]/TZVP[207] level of theory using the program GAUSSIAN09.[208] Riboflavin was chosen as a model compound for most of the calculations. For comparison also FAD in the ground state S_0 was considered. The chromophore was optimized in S_0, and vertical excitation energies to excited states (S_1, S_2, ...) were determined by TD-B3LYP. For the S_1 state, geometry optimizations were carried out as well. Solvent effects were included first of all using the PCM model.[209,210] Dielectric constants of ϵ = 46.1 for DMSO and ϵ= 80.35 for water were chosen. Since a major effect of the protic solvent is H-bonding to the isoalloxazine ring of flavin, for RF and FAD also microsolvation models with four water molecules in addition to the PCM field were considered. Figure 6.2 shows the optimized ground state geometry for this case and RF, indicating hydrogen bonds in particular to the O_4 and O_2 atoms, and to the N_3-H unit.

[3] see footnote on page 107.

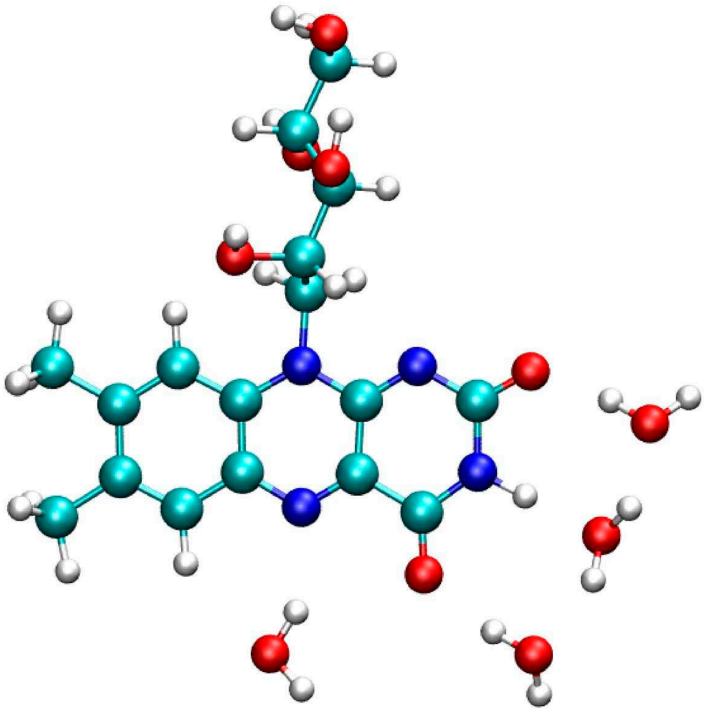

Figure 6.2: Riboflavin in the microsolvation model, i.e. with four water molecules placed around the polar isoalloxazine moiety. The structure was optimized on the B3LYP/TZVP level of theory.

6.3.2 Vibrational Assignment

Ground and excited state vibrations were assigned on the basis of a normal mode analysis in the optimized geometries. To allow for a more unambiguous assignment, also isotope substitution experiments were simulated by calculating vibrations after replacing the four water molecules by heavy water, D_2O, and in addition exchanging the H atom at N_3 with deuterium, D.

Resonance Raman spectra were calculated for the ground state S_0 of RF by resonant transitions to S_1 only. This was done by the time-dependent method of Heller *et al.*,[211–213] as implemented in the ORCA–ASA[214] module of the ORCA 2.8[215] quantum chemistry program suite. In this approach, under the Born-Oppenheimer and Condon approximations the resonance Raman polarizability elements $(\alpha_{\rho\lambda})_{I\to F}$ (with $\rho, \lambda = x, y, z$) for vibrational transitions between vibrational state $I = (i_1, i_2, \ldots, i_N)$ and final state $F = (f_1, f_2, \ldots, f_N)$ on the ground state surface S_0 (N is the number of

vibrational modes in the molecule), are given as

$$(\alpha_{\rho\lambda})_{I\to F} = \frac{i}{\hbar}\,\mu_{01,\rho}\mu_{01,\lambda}\int_0^\infty \langle\phi_F|\phi_I(t)\rangle e^{i(\omega_L+\omega_{I0}+i\Gamma_1)t}dt \quad . \tag{6.2}$$

Here, ϕ_F is the ground state vibrational wavefunction corresponding to index F, $\phi_I(t) = \exp(-i\mathcal{H}_1 t/\hbar)\,\phi_I$ the ground state vibrational wave function ϕ_I when propagated under the influence of the excited state nuclear Hamiltonian $\mathcal{H}_1$, $\mu_{01,\rho}$ is the ρ-th component of the transition dipole moment $\underline{\mu}_{01} = \langle\Psi_0|\underline{\hat{\mu}}|\Psi_1\rangle$ (with Ψ_0 and Ψ_1 being electronic wavefunctions for states S_0 and S_1 and $\underline{\hat{\mu}}$ the dipole operator), ω_L is the frequency of the exciting laser, ω_{I0} the vibrational frequency of the initial vibrational state, and, finally, Γ_1 a homogeneous lifetime parameter for the S_1 state. The correlation function $\langle\phi_F|\phi_I(t)\rangle$ can be evaluated analytically if both ground and excited state potentials are assumed to be harmonic.[211] In particular, under the independent mode, displaced harmonic oscillator (IMDHO) model used here it is further assumed that there is only a displacement of the excited state S_1 potential, but no frequency and/or normal mode changes, relative to S_0, *i.e.*, frequency shifts and Duschinsky rotation are neglected. As a consequence, the resonance Raman signals are obtained from ground state normal modes and frequencies, and the displacement of the excited state, where the latter can be calculated locally using the gradients of S_1 at the Franck-Condon point as outlined elsewhere.[214,216] All resonance Raman signals were computed for an excitation energy of $\hbar\omega_L = 23000$ cm^{-1} (435 nm) (the computed, vertical S_0–S_1 energy difference is 23600 cm^{-1} (423 nm) for RF/DMSO, see below), and homogeneously broadened with a width parameter $\hbar\Gamma_1 = 10$ cm^{-1}. The resonance Raman intensity for a $I \to F$ transition is proportional to the spatially averaged, and squared polarizabilities.[211,214] All quantum chemical calculations will be presented together with discussion in Section 6.5.1.

6.4 Experimental Results

6.4.1 Resonance Conditions.

Stationary and transient absorption spectra of flavin are compared in Figure 6.3 for three different conditions: RF in the polar aprotic solvent DMSO (black), RF in polar protic water (dashed blue), and FAD in water (green). The spectral shape appears to be mainly controlled by the solvent environment. While the $S_1 \leftarrow S_0$ absorption band is insensitive to the flavin surrounding and peaks uniformly around 450 nm, the maximum of the $S_2 \leftarrow S_0$ transition is red-shifted in water by approximately 1900 cm^{-1}. This effect has been attributed to the electronic influence of hydrogen-bond changes.[217] A similar trend is observed for the $S_1 \rightarrow S_0$ emission: when changing from DMSO to water solution, the stationary emission spectrum red-shifts by ~ 400 cm^{-1}.

Most transient absorption and fluorescence-upconversion measurements were carried out with actinic excitation at 440 nm, near the maximum of the first absorption band. In order to evaluate the dependence of excited state relaxation on the pump photon energy, some experiments were performed with 400 nm excitation. In aqueous solution

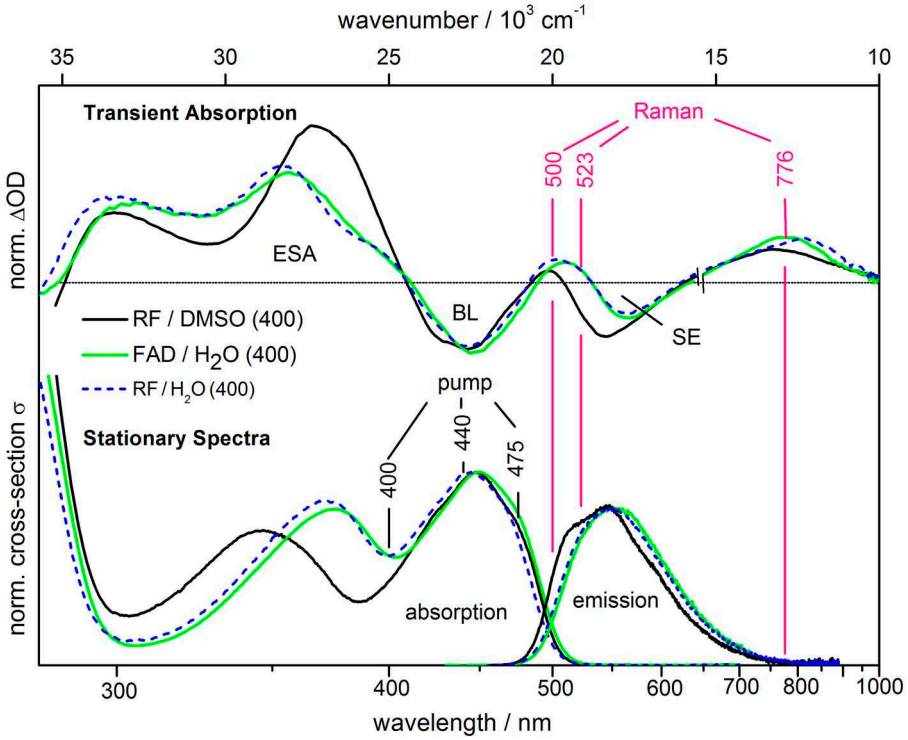

Figure 6.3: Transient absorption at 0.4 ps delay *(top; magic angle conditions)* compared to stationary absorption and emission *(bottom)*. Induced absorption spectra have been normalized at the minimum of the bleach band, and stationary spectra were set to equal oscillator strengths for the $S_1 \leftarrow S_0$ and $S_1 \rightarrow S_0$ bands. Vertical lines indicate the "actinic" pump and Raman wavelengths of this work. (Note that the range 645–1000 nm was observed separately following excitation at 475 nm.)

the $S_1 \leftarrow S_0$ and $S_2 \leftarrow S_0$ absorption bands overlap at this wavelength. In DMSO this overlap is small, and transition to the S_1 state dominates upon excitation with ≥ 400 nm.

Typical transient absorption spectra are shown in the upper panel of Figure 6.3, for 0.4 ps delay. Positive signals indicate excited state absorption (ESA), whereas negative features to the red of the ground-state absorption indicate stimulated $S_1 \rightarrow S_0$ emission (SE). The bleach of the S_0 population (BL) causes an additional negative contribution of the ground-state absorption spectrum. As in stationary spectroscopy, the shape of the transient signal depends on the solvent. In DMSO, BL and SE bands have similar induced optical density, while in water the minimum of the SE band is significantly red-shifted and shows a decreased amplitude.[180] In addition the ESA band peaking at 366 nm in DMSO blue-shifts to 354 nm in water.

Time-resolved Raman spectra were collected after actinic excitation at 467–475 nm, on the red side of the first absorption band. The effect of different resonance conditions on the transient signal was explored by performing experiments with Raman excitation at

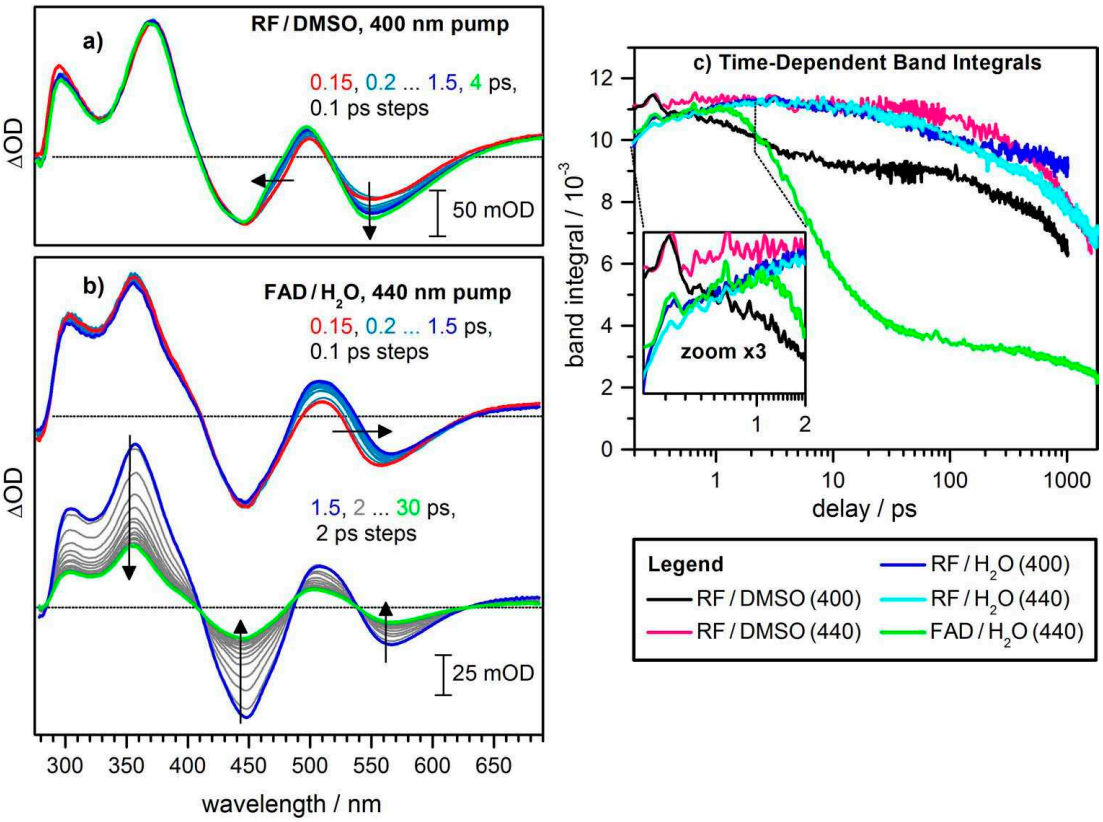

Figure 6.4: Transient absorption of the flavin chromophore (a,b) and band integrals $BI(t)$ (c) over the induced spectra. Solvents and excitation wavelengths are generally given as inset. For better comparison, the black, magenta, blue and cyan time traces were scaled by factors of 0.6, 1.3, 2.6, 3.4 respectively.

500, 523, and 776 nm. At 776 nm the Raman pulse is resonant only with the excited-state absorption band in the near infrared. In contrast, at 500 nm several electronic transitions are accessed: the Raman pulse not only overlaps with the excited-state absorption in this region, but also with ground-state absorption and $S_1 \rightarrow S_0$ emission. Therefore, for this experiment, at least three electronic levels have to be considered to describe the resonance Raman signal: the ground state S_0, the first excited state S_1, and a higher excited state S_n. In a third experiment the Raman pulse was tuned to 523 nm, now still resonant with excited-state absorption and stimulated emission, but only preresonant with ground-state absorption.

6.4.2 Evolution of Induced Absorption Spectra

Transient absorption spectra of RF in DMSO upon excitation with 400 nm are shown in Figure 6.4 a. During the first picoseconds the stimulated emission band rises, accompa-

nied by small changes of the excited state absorption band around 500 nm. This rise is not observed when exciting with 440 nm, see the Supporting Material. The fluorescence lifetime of flavin in the absence of quenching is 3–6 ns depending on the solvent.[180,184] In agreement with these values, in all transient absorption experiments nanosecond decay of the induced spectrum is found. A long-time spectral offset corresponds to the flavin triplet.

Transient absorption spectra of FAD in water at different delay times are shown in Figure 6.4 b. During the first 1.5 ps the bleach and most of the excited-state absorption stay unchanged: the molecule is still excited and does not return to the electronic ground state on this time-scale. Relaxation on the excited-state potential energy surface is observed as an increase of transient signal between 480 and 580 nm. At this point it can not be distinguished whether the changes originate from a shift of the stimulated emission or from a rise of ESA around 510 nm; details will be obtained from a comparison with time-resolved fluorescence measurements. The subsequent evolution up to 30 ps is for FAD dominated by uniform decay of the transient spectra indicating internal conversion to the ground state. The residual spectrum continues to decay on the nanosecond time-scale (not shown), leaving a long-time offset which resembles the flavin triplet spectrum.[152,218]

The integral signal evolution is studied next, by forming the band integral over the full transient spectra,

$$BI(t) = \int_{290nm}^{690nm} d\lambda \; \sigma(t,\lambda)/\lambda, \tag{6.3}$$

where $\sigma(t,\lambda)/\lambda$ is the band-shape function (see Section 2.2.2). In order to systematically evaluate the influence of the adenine moiety, the surrounding solvent shell, and pump photon energy, transient absorption measurements were performed under the following conditions: RF in water with excitation at 400 nm (blue) and 440 nm (cyan), FAD/water with excitation at 440 nm (green), RF/DMSO with excitation at 400 (black) and 440 nm (magenta). All results are compared in Figure 6.4 c. The simplest evolution is observed after exciting RF in DMSO at 440 nm (magenta). In this case the band integral does not change within the first 100 ps and finally decays in the nanosecond regime. Upon excitation with 400 nm (black), 20% of the band integral decays on the picosecond time-scale, reflecting the rise of the stimulated emission band in Figure 6.4 a.

Unlike in DMSO, in water (blue and cyan) a sub-picosecond rise is identified for RF. The initial rise describes the spectral changes in Figure 6.4 b and is reproduced by the FAD trace (green, see also the inset in Figure 6.4 c). Therefore this effect has to be assigned to the dynamic influence of the water surrounding. Additional signal decay is found on the 100 ps time scale. As already demonstrated in a previous publication,[180] this component depends on the excitation wavelength and derives from small changes in the region < 500 nm, see also the Supporting Material.

In the case of FAD (green), recovery of the ground state is observed as a decay on

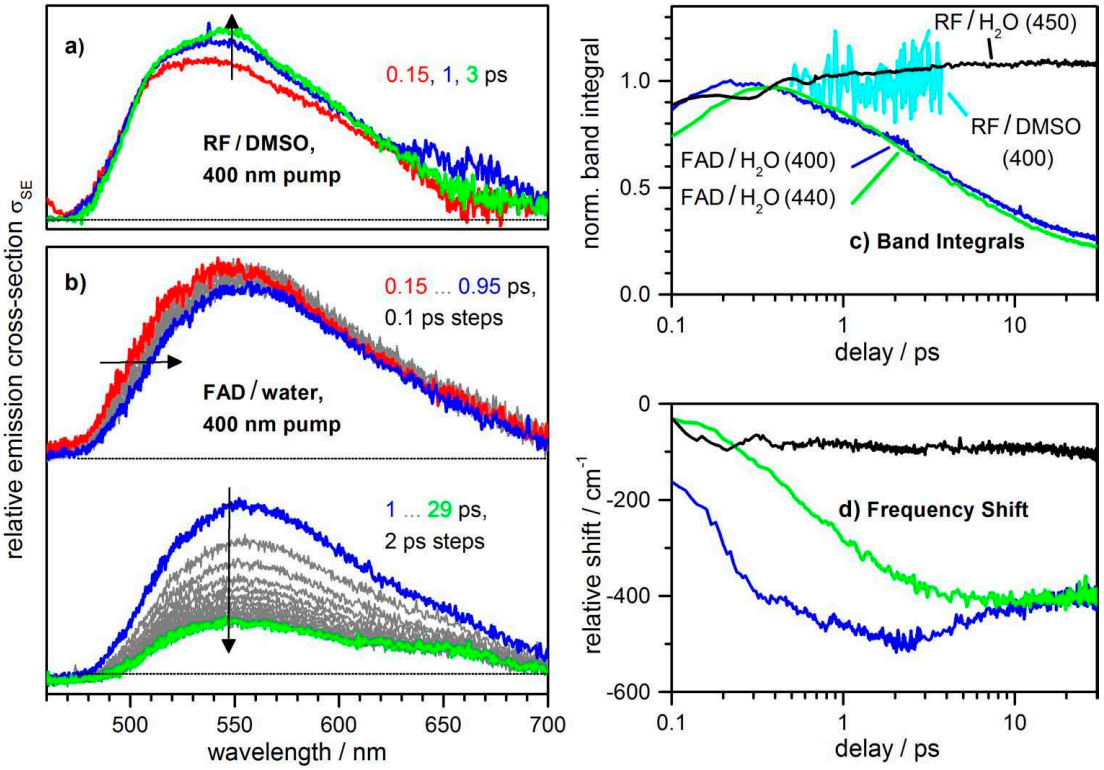

Figure 6.5: (a,b) Transient fluorescence of the flavin chromophore under different conditions, shown as inset, with magic-angle detection. Fluorescence spectra are generally expressed as cross-sections $\sigma_{SE}(\nu)$ for stimulated emission. (c) Normalized fluorescence band integrals $BI(t)$. (d) Frequency of the fluorescence peak relative to that of the initial spectrum.

the 5–10 ps time scale, amounting to $\sim$ 65% signal loss. It will later be assigned to quenching by adenine.

Wavepacket motion shows up as oscillation of the transient absorption signal. In the band integral traces this is most clearly observed as a hump at $\sim$ 300 fs delay. This feature originates from a $\sim$ 290 cm^{-1} in-plane deformation mode that was reported before.[180] Fourier analysis of the time-domain signal provides an alternative approach to low-frequency vibrational spectra of the excited state, as will be shown further below.

6.4.3 Evolution of Fluorescence Spectra

FAD in water: the spectral evolution of the emission cross section after 400 nm excitation is shown in Figure 6.5 b. During the first picosecond a dynamic red-shift is observed, accompanied by slight intensity decay. As in transient absorption, on the 10 ps time-scale strong decay of the signal takes place, indicating population drain from the S_1

state. Time-dependent emission band integrals are compared in Figure 6.5 c. Around zero delay time the signal rises according to the apparatus function (~ 0.16 ps with 400 nm pump and ~ 0.35 ps with 440 nm pump wavelength). Otherwise the traces for both excitation wavelengths (blue and green) are indistinguishable.

The time-dependent shift of the peak frequency provides complementary information on the excited state dynamics, Figure 6.5 d. For 440 nm excitation (green), no significant band shift is observed on the 10 ps time scale. Early relaxation becomes apparent as a continuous shift to longer wavelengths during the first 2 ps; the total shift is 410 cm^{-1}. When pumping at 400 nm (blue), an additional ultrafast red-shift within the first 0.2 ps contributes. On the 5–10 ps time scale the frequency-shift reverts in this case, and the emission peak position approaches the long-time offset from below.

RF in water: due to low solubility, the fluorescence-upconversion signal is small (see Supporting Information) and the first 0.5 ps is obscured by a coherent contribution. Thereafter the band integral (cyan) stays unchanged within precision. As with FAD, the dynamic Stokes shift is small on the time scale 0.5–3 ps; the signal/noise ratio prevents a detailed analysis of the band position.

RF in DMSO: transient emission spectra after excitation at 400 nm are shown in Figure 6.5 a. In contrast to FAD/water, no spectral shift is observed. The spectrum at longer times (green) resembles the mirror image of the first absorption band, and the vibrational structure is reproduced. At early delay times (red) the spectrum lacks the vibrational structure and has decreased amplitude in the range 526–620 nm. During the first picosecond, fluorescence intensity rises in this region, but the spectrum (blue) is still void of structure. The characteristic hump at 545 nm then builds up during several picoseconds. The rise of the band integral, shown in Figure 6.5 c (black), resembles the decay kinetics of the transient absorption signal discussed before. Following the evolution of the emission spectrum with a log-normal fit, the asymmetric rise of the signal is reflected by a 25 cm^{-1} red-shift of the peak maximum, although the band itself does not appear to shift overall, Figure 6.5 d. Both band integral and peak frequency do not evolve monotonically, but are modulated by an oscillation with a frequency of ~ 100 cm^{-1} (see also Figure 6.18).

Generally, fluorescence appears as a single emission band at all delay times; no evidence is found for additional early emission around 500 nm.

6.4.4 Femtosecond Stimulated Raman Spectra

Transient spectra $R(\nu)$ upon 776 nm Raman excitation are shown in Figures 6.6 a,b for RF/DMSO and FAD/H_2O. In both cases well-resolved, emissive, vibrational bands are seen, which decay with only minor spectral changes. The appearance of new bands is not observed. The time behavior is shown in Figure 6.6 c where the integral over the range 1100–1650 cm^{-1} is considered. It is fitted by a sum of exponential functions; optimal decay times and relative amplitudes are summarized in Table 6.1. It is noted

Table 6.1: Time constants from multi-exponential fits of the transient Raman evolution under different experimental conditions.[a]

RF (DMSO)	**FAD (H_2O)**
Raman excitation at 500 nm, 1.2 ps, 1 μJ	
0.15 (0.34)	0.15* (0.32)
1.2 (0.16)	1.2* (0.15)
	6.8 (0.37)
	68 (0.05)
2000* (0.27)	2900* (0.08)
offset (0.23)	offset (0.03)
Raman excitation at 523 nm, 0.73 ps, 1 μJ	
	0.33 (0.16)
	6.8 * (0.69)
	offset (0.15)
Raman excitation at 776 nm, 2.7 ps, 3.7 μJ	
0.84 (0.42)	1.2 (0.69)
	7.8 (0.19)
offset (0.58)	offset (0.12)

[a] integrated over the range 1100–1650 cm^{-1}. Time constants in ps, with the relative exponential amplitudes in brackets. Asterisks mark time constants that were fixed during the fit. Underlayed grey: evolution attributed to depletion by the Raman pulse. Raman pulse durations are given for transform-limited Gaussian pulses.

here already that the initial decay, until $\sim$ 3 ps, is probably related to depletion of the S_1 state by the ps Raman pulse, as will be argued later.

Small spectral changes have molecular significance, though. Raman peaks shift slightly to lower frequencies on a 3 ps time scale, by $\sim$ 1 cm^{-1} for RF/DMSO and $\sim$ 2.5 cm^{-1} for FAD/water. A larger downshift is seen only for the 1579 cm^{-1} band of FAD, albeit at low signal/noise. The shifts are accompanied by narrowing of the Raman bands, leading to better resolved spectra at longer delay times. For FAD/water this allows to identify peaks at 1328, 1377, 1406, and 1453 cm^{-1}, which are only recognized as shoulders in initial spectra.

Spectral comparison of different experiments (sample, solvents, actinic excitation wavelength) is best done at t=0, before each system relaxes along different pathways. To generate the time-zero Raman spectrum global exponential analysis of the spectral evolution is employed. Two or three exponential functions were included, and the parameters varied freely to obtain the best fit of the time-dependent spectra.

Time-zero spectra for measurements with 776 nm Raman excitation are shown in Figure 6.7. Compared to RF/DMSO (black), the bands of FAD/H_2O (green) are observed

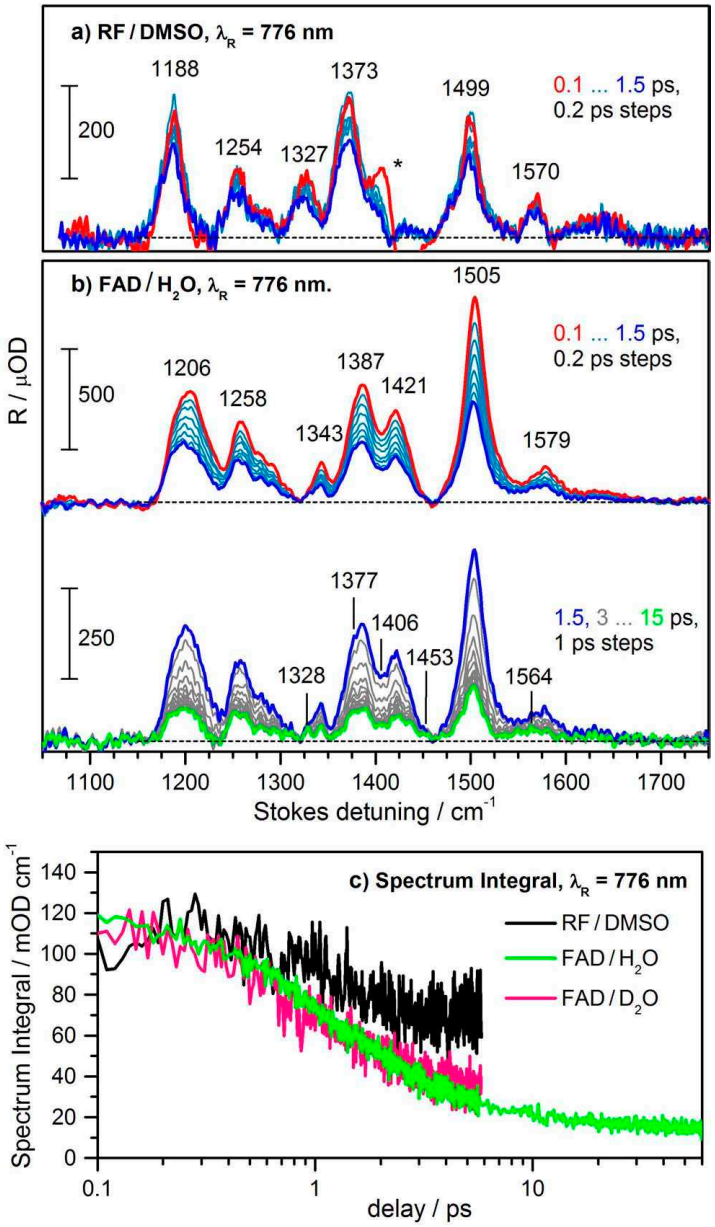

Figure 6.6: (a,b) Excited-state stimulated Raman spectra $R(\nu)$ of flavin, from Raman pulses at 776 nm that are resonant with excited-state absorption only. (c) Time-traces of $\int R(\nu)d\nu$ integrated over the range 1100–1650 cm^{-1}. Spectra were recorded with parallel polarizations, and nonresonant solvent signal has been subtracted. The asterisk in (a) indicates a dispersive solvent residuum at earliest delay times.

at higher frequencies by up to 21 cm^{-1}. Smaller shifts are observed for the bands at 1254 cm^{-1}, with a shoulder around 1280 and 1499 cm^{-1}. These changes are accompanied by a decrease in relative intensity for the bands at 1188, 1327, 1373, 1570, and 1637 cm^{-1}.

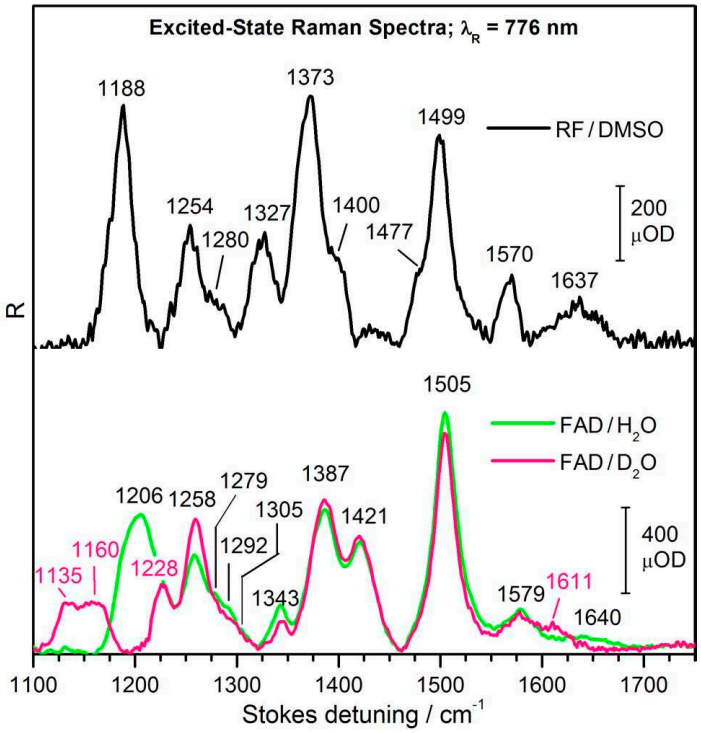

Figure 6.7: Excited-state stimulated Raman spectra $R(\nu)$ at zero delay time, from Raman pulses at 776 nm, as in Figure 6.6 a,b. Shown are extrapolations to $t = 0$ from a global multi-exponential fit of each evolution.

In heavy water (magenta) most of the FAD Raman signals are reproduced in position and relative amplitude. The strongest isotope effect is found for the 1206 cm^{-1} band: it splits in D_2O, giving rise to a weaker band with two maxima at 1135 and 1160 cm^{-1} and a band at 1228 cm^{-1}. The position of the 1258 cm^{-1} band is not affected by isotope substitution, but the band has slightly increased intensity in D_2O. Another change is found for the broad low-intensity band at 1640 cm^{-1}, which shifts to 1611 cm^{-1} in D_2O.

Ground-state spectra $G(\nu)$ upon 500 nm Raman excitation are shown in Figure 6.8 b. Here Raman resonance with the first absorption band is used. Similar spectra are obtained upon pre-resonance at 523 nm (not shown). Compared to RF/DMSO (black), FAD/water (green) generally shows slightly up-shifted peak frequencies. Strong differences are observed between 1100 and 1300 cm^{-1}: for FAD, bands around 1180 and 1230 cm^{-1} have decreased intensity, and additional bands are found at 1256 and 1283 cm^{-1}.

Transient spectra $R(\nu)$ upon 500–523 nm Raman excitation also decay uniformly with only minor spectral changes, similar to what was observed above. Time-zero spectra are compared in Figure 6.8 a. They are dominated by negative features which resemble the ground-state Raman signal, and thus differ seriously from those which were observed in

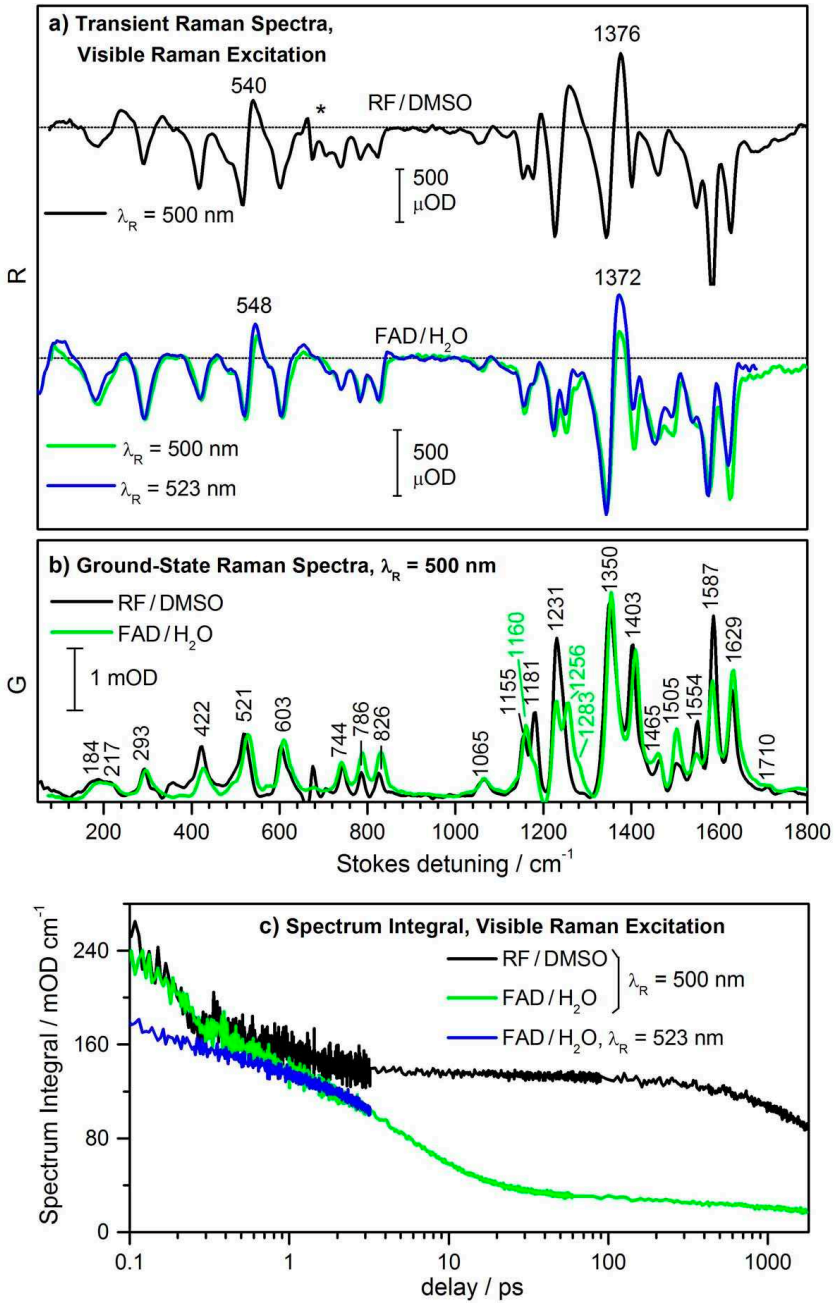

Figure 6.8: (a) Transient stimulated Raman spectra $R(\nu)$ of flavin after optical excitation, from Raman pulses at 500 and 523 nm. Now resonance originating from the S_1 state involves not only excited-state absorption but also stimulated emission. Shown are extrapolations to t=0 from a global multi-exponential fit of each evolution. Negative signal is largely due to the bleached S_0 state. (b) Ground-state resonance Raman spectra $G(\nu)$. (c) Time-traces of $\int |R(\nu)|d\nu$ integrated over the range 1100-1650 cm^{-1}. Results for 523 nm Raman resonance have been scaled for better comparison.

the near-infrared. Positive (= emissive) contributions are found mainly around 540 cm^{-1} and 1370 cm^{-1}. In contrast to excitation at 500 nm, the 523 nm Raman pulse is only pre-resonant with the $S_1 \leftarrow S_0$ transition. Spectra for FAD/H_2O under both resonance conditions are compared in Figure 6.8 a, and found to be identical within precision. The influence of various electronic transitions on the Raman signal was modelled in Section 2.4.2.

Time-dependent integrals are shown in Figure 6.8 c. Since $R(\nu)$ now comprises positive and negative parts, the absolute values $|R(\nu)|$ are integregrated, as before over the range 1100–1650 cm^{-1}. For $t \geq 3$ ps the results from transient absorption spectroscopy (Figure 6.4) are well reproduced. For example, with RF/DMSO only nanosecond decay of Raman intensity is found, whereas FAD exhibits again an additional loss on the 5–10 ps time scale.

6.5 Discussion

6.5.1 Assignment of FSRS Bands Based on Quantum Chemistry

Ground state vibrations

Experimental and theoretical resonance Raman peak positions for the ground electronic state S_0 are compared in Table 6.2. The experimental spectra of Figure 6.8 b for RF/DMSO, RF/H_2O, and FAD/H_2O have their theoretical analogue in Figure 6.9. The theoretical spectra were calculated by the IMDHO model as outlined above, with microsolvation (plus PCM) in the case of water, and only PCM for DMSO.

The resonance Raman spectra compare well to reports in the literature.[219–224] Band positions and intensities were found to be largely independent of the residue at N_{10} (RF *vs.* FAD), but are sensitive to the proton donating properties of the solvent (DMSO *vs.* water).[224] The spectra are characterized by a high-frequency region above > 1000 cm^{-1} with characteristic high-intensity modes, and a low-frequency, low-intensity region < 1000 cm^{-1}. The latter contains in- and out-of plane vibrations of the ribityl chain or the flavin ring system, which are not analyzed in this section. Focusing on the > 1000 cm^{-1} fingerprint region and RF/DMSO first, dominant peaks are found at 1629, 1587, 1554, 1403, 1350, 1231, 1181, and 1155 cm^{-1} in the experimental spectrum, Figure 6.8 b. In the theoretical spectrum strong bands are found at 1675, 1664, 1597, 1550, 1409, 1361, 1235, 1191, and 1163 cm^{-1}.

The band assignment in Table 6.2 is consistent with the assignment of refs. 198,201, 203. For RF/DMSO the theoretical 1675 cm^{-1} peak, for example, is assigned to the C_2-O_2 stretching vibration. In the experiment no peak can be found in this region, probably because it is hidden under the broad 1629 cm^{-1} band. Note that in the resonance Raman spectra the signals of the C-O stretch modes are weak – in contrast to IR signals, which are sensitive to the change of dipole moment upon vibration. For the calculations a small homogeneous bandwidth of 10 cm^{-1} was chosen so that the peak is resolved, despite being weak.

The experimental 1629 cm^{-1} band belongs to the C_6-C_7, C_8-C_9, N_5-C_{4a} stretching

mode, which is blue shifted to 1664 cm^{-1} in theory. The experimental band at 1587 cm^{-1} corresponds to the 1597 cm^{-1} theoretical peak and belongs to the C_8-C_9, N_5-C_{4a}, C_{9a}-C_{5a} stretching vibration. The experimental 1554 cm^{-1} peak is related mainly to the C_{10a}-N_1 and N_{10}-C_{10a} stretching vibration, and appears at 1550 cm^{-1} in theory. Further, the C_4-N_3 and C_{10a} -C_{4a} stretching is found at 1403 cm^{-1} experimentally, and at 1409 cm^{-1} according to theory. Isoalloxazine framework vibrations are found at 1350 cm^{-1} experimentally and 1361 cm^{-1} theoretically for RF/DMSO. At 1231 cm^{-1} (experiment) and 1235 cm^{-1} (theory) the C_6-H bending is found, C_7-C_8, C_{4a}-C_{10a}, and C_2-N_3 stretching vibrations. The C_{4a}-C_{10a} and C_4-N_3 stretching vibrations are assigned to the 1181 cm^{-1} band experimentally, which appears at 1191 cm^{-1} in theory. Further assignments can be found in Table 6.2.

The experimental resonance Raman spectrum changes when replacing DMSO by water, according to Table 6.2, in agreement with ref. 221 and ref. 225:

(i) The band at 1154 cm^{-1} shifts up to 1161 cm^{-1};

(ii) a weak 1285 cm^{-1} band becomes more intense, shifting at the same time to 1283 cm^{-1} (FAD);

(iii) a new peak at 1258 cm^{-1} appears, and the 1231 cm^{-1} signal shifts to 1229 cm^{-1} with its intensity decreasing;

(iv) the intensity of the 1505 cm^{-1} band increases, while that of the 1554 cm^{-1} band decreases;

(v) the band at 1587 cm^{-1} downshifts slightly to 1586 cm^{-1} and decreases in intensity.

The calculated resonance Raman spectra reproduce well the experimental trends, see Figure 6.9. The following analogous changes are found in the theoretical spectrum when replacing DMSO by water as a solvent:

(i) the 1163 cm^{-1} band shifts up to 1166 cm^{-1};

(ii) a new band at 1293 cm^{-1} appears in the theoretical RF / water spectrum;

(iii) the band at 1235 cm^{-1} decreases in intensity and shifts to 1233 cm^{-1}, where it is hidden under the peak at 1252 cm^{-1}, which appears as a new signal;

(iv) the 1550 cm^{-1} band decreases in intensity, the two bands at 1518 and 1530 cm^{-1} merge into a single band at 1525 cm^{-1};

(v) the band at 1597 cm^{-1} downshifts to 1593 cm^{-1}.

Table 6.2: Ground state (S_0) Raman bands from 500 nm resonance of flavins in DMSO and water (in cm^-). Assignment based on B3LYP/TZVP calculation using resonance Raman signals obtained from the IMDHO model.

Experimental			**Calculated**			**Mode Assignment**[a]
RF/ DMSO[b]	**RF/ H_2O**[c]	**FAD/ H_2O**	**RF/ DMSO**[d]	**RF/ H_2O**[e]	**FAD/ H_2O**[e]	
1760	–	1781	1776	1784	1774	comb. band: 179+1597 (DMSO), 191+1593 (water)
1710	1714	1717	1718	1717	1715	C_4-O_4 str
under 1629[f]	under 1632	–	1675	1675	–	C_2-O_2 str
1629	1632	1632	1664	1664	1663	C_6-C_7 str, C_8-C_9 str, N_5-C_{4a} str
1587	1586	1584	1597	1593	1595	C_8-C_9 str, N_5-C_{4a} str, C_{9a}-C_{5a} str
1554	1550	1548	1550	1550	1550	C_{10a}-N_1 str, N_{10}-C_{10a} str, C_7-C_8 str, C_{5a}-C9a str, N_3-H (wag) (water)
1505	1503	1503	1518	1517	1506	C_9-C_{9a} str, N_5-C_{5a} str, N_{10}-C_{10a} str, HCH(CH_3) bend
1465	1466	1462	1489	1488	1477	C_{4a}-N_5 str, N_1-C_{10a} str, C_9-C_{9a} str, C_6-C_7 str, H-C-H (CH_3) bend
1403	1412	1409	1409	1430	1431	C_4-N_3 str, C_{10a} -C_{4a} str
1350	1355	1354	1361	1362	1369	isoalloxazine framework vibs., H-CH bend
			1315	1320	1330	from modes 1312/1319 (DMSO) and 1310/1324 (water), N_{10}-C_I str, N_5-C_{5a} str, C6-H bend, C_9-H bend, CHR[g] bend
1285	–	1283	–	1293	1301	N_1-C_2 str, C_2-N_3, $N_1$0-C_{10a}, C_6-H ben, C_9-H bend, CHR bend
–	1258	1256	–	1252	1263	C_2-N_3 str

... continued on next page

... **Table** 6.2 continued.

Experimental			**Calculated**			**Mode Assignment**[a]
RF/ DMSO[b]	**RF/ H_2O**[c]	**FAD/ H_2O**	**RF/ DMSO**[d]	**RF/ H_2O**[e]	**FAD/ H_2O**[e]	
1231	1229	1230	1235	under 1252	1228	C_6-H bend, C_7-C_8 str, C_{4a}-C_{10a} str, C_2-N_3 str (only DMSO), C_9-H bend, N_1-C_2 str, CHR bend, O-H bend (ribityl chain)
1181	1183	1182	1191	1205	1209	C_6-H ben, C_9-H bend, C_{4a}-C_{10a} str, C_4-N_3 str, C_{5a}-N_4 str, C_{9a}-N_{10} str
1154	1161	1160	1163	1166	1177	N_1-C_2 str, C_I-N_{10} str, N_1-C_{10a} str, C_{4a}-C_3 str, C_8-CH_3-str
1065	–	1066	1094	1069	1066	CHR bend

a str=stretch, wag=wagging, bend=bending, comb.=combination.
b stimulated resonance Raman of RF in DMSO, Raman pulse at 500 nm.
c from ref. 225.
d Polarizable Continuum Model (PCM) only.
e microsolvation by water molecules plus PCM.
f peaks hidden "under" the corresponding band.
g CHR=CH ribityl chain bending vibrations.

Table 6.3: Excited state (S_1) Raman bands from 776 nm resonance of flavins in DMSO, water, and heavy water (in cm^{-1}). Assignment based on TD-B3LYP/TZVP normal mode analysis.

Experimental		**Calculated**		**Mode Assignment**[a]
RF/ DMSO[b]	**FAD/ H_2O/D_2O**[c]	**RF/ DMSO**[b]	**RF/ H_2O/D_2O**[c]	
–	–	1674	1691/1641	C_4-O_4 str
1637	1640/1611	1658	1668/1635	C_2-O_2 str
1637		1621		C_6-C_7 str, C_8-C_9 str
	1579 (broad)		1634/1539	C_{5a}-C_6 str, C_8-C_9 str
1570		1534		C_{10a}-N_1 str, C_7-C_8 str, C_{4a}-C_{10a} str, C_{5a}-C_6 str, C_9-C_{9a} str
1499	1505	1505	1512/1509	C_{4a}-C_{10a} str, C_{5a}-C_{9a} str, C_7-C_8-str, C_{10a}-N_1 str
1477	1505	1499	1490/1498	CHR bend, C_9-C_{9a} str, C_{5a}-C_6 str, C_6-C_7 str,
1477	1505	1484	1483	CHR bend, C_7-C_8 str, C_{5a}-C_{9a} str, C_9-C_{9a} str, C_{10a}-N_1 str
1477	1505	1479	1477	CHR bend, C_{10a}-N_1 str, C_{9a}-N_{10} str, N_5-C_{4a} str,
1400	1421	1429	1430	CHR bend, C_4-C_{4a} str, C_{4a}-N_5 str, C_8-C_9 str
1400	1421	1407	1409	C_6-H wag, N_1-C_2 str, CHR wag
1400	1421	1394	1397	C_{10a}-N_1, CHR
1373	1387	1374	1377	C_{4a}-C_{10a} str, C_{5a}-C_{9a} str, C_6-C_7 str, N_1-C_2 str
1327	1343	1354	1363	f.v.
1327	1343	1338	1342	f.v.
1327	1305	1301	1316	f.v., N_3-H wag, C_6-H wag, C_9-H wag
1254	1291	1284	1291/1292	N_{10}-C_{10a}, C_9 -H wag,
1254	1258	1272	1275/1276	N_5-C_{5a}, N_3-C_4, ring I open, in D_2O: N_3-H wag
–	–	–	1249/1238	CH-ribityl chain
–	–	–	1226/1228	CH-ribityl chain, (D_2O bending)

...continued on next page

... **Table** 6.3 continued.

Experimental		**Calculated**		**Mode Assignment**[a]
RF/ DMSO[b]	**FAD/ H_2O/D_2O**[c]	**RF/ DMSO**[b]	**RF/ H_2O/D_2O**[c]	
1188	1206/1228	1184	1208/1203+1266	C_2-N_3, C_{4a}-C_{10a}, N_5-C_{5a}, $C_{6/9}$-H wag, in D_2O: N_3-H wag
under[d] 1188	under 1206	1184	1200/1176	C_2-N_3, C_{5a}-N_5, C_6-C_7, in D_2O: N_3-H wag
under 1188	under 1206/1160	1156	1161/1151	N_1-C_2 (in D_2O), N_3-C_4 (in H_2O), N_{10}-C_I, CH_3-C_8 str, N_5-C_{5a}, in D_2O: N_3-H wag
under 1188	under 1206/1135	1140	1144/1136	N_3-C_4 str, N_5-C_{5a} str, CH_3-C_8 str, N_{10}-C_{10a}, in D_2O: N_3-H wag
1188		1220		f.v.
1188		1197		C_6-C_7, C_6 -H wag, C_2 -N_1 str

[a] str=stretch, wag=wagging, bend=bending, comb.=combination, f.v.=framework vibrations.
[b] Polarizable Continuum Model (PCM) only.
[c] microsolvation by water molecules plus PCM.
[d] peaks hidden "under" the corresponding band.

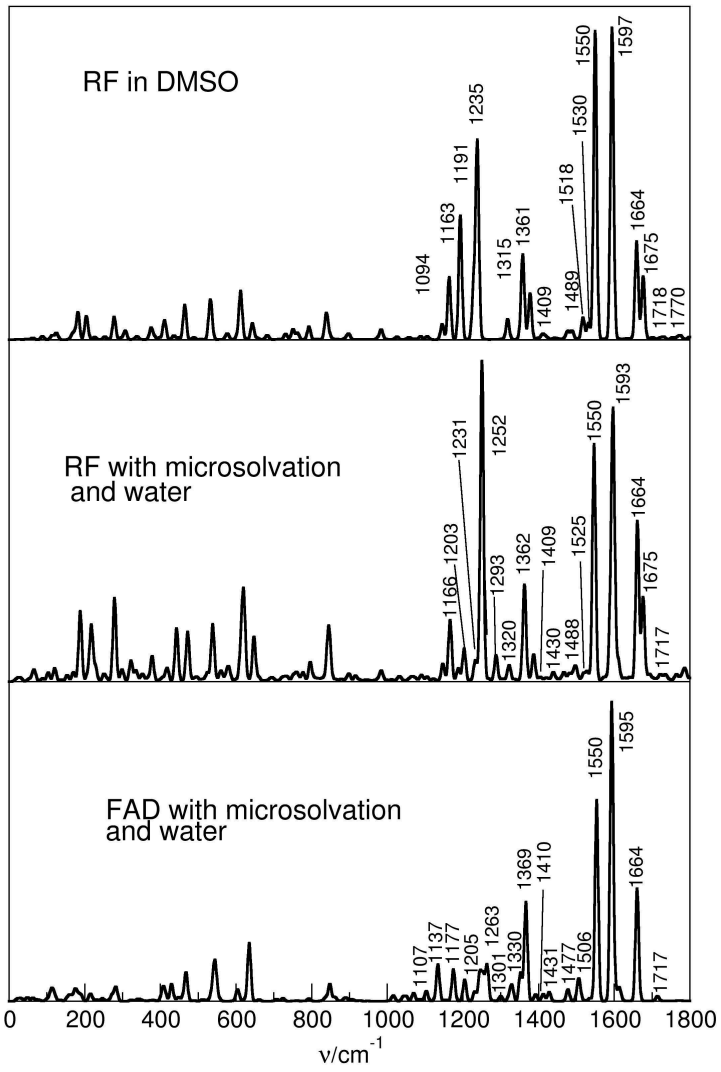

Figure 6.9: Calculated resonance Raman spectra of the flavin ground state S_0. Theory was on the B3LYP/TZVP/IMDHO level, and excited-state broadening of $\hbar\Gamma_1 = 10\,\mathrm{cm}^{-1}$ has been applied.

The following explanations for the observed changes can be given, based on the calculations.

(i) The 1161 cm^{-1} band in the RF / H_2O spectrum is assigned to framework vibrations of the polar moiety of the isoalloxazine unit, mainly N_1-C_2, N_1-C_{10a}, and C_{4a}-C_3 stretching vibrations. Due to the influence of the hydrogen-bonds on the polar side of the ring system, these vibrations, which are also located at the polar side but not directly involved in H-bonds, are more restricted and hence the frequency is blue shifted when replacing DMSO by water.

(ii) In the calculated spectrum for RF/DMSO a band in the 1285 cm^{-1} region is not observed. In water a band is found at 1293 cm^{-1} that belongs mainly to the N_1-C_2, C_2-N_3, N_{10}-C_{10a} stretching vibrations. Due to the hydrogen bonds, these vibrations become more intense. It may be speculated that this has to do with a higher Raman polarizability of the larger, H-bonded system for this transition.

(iii) The band at 1252 cm^{-1} of RF/water is assigned to the C_2-N_3 stretching vibration. Here also the argument comes into play: due to the hydrogen bond the C_2-N_3 bond is more restricted, hence the frequency shifts upward. This assignment is supported by isotope labeling experiments. In ref. 222, exchanging the hydrogen in the N_3-H bond by deuterium, the 1256 cm^{-1} band of FAD/water was found to shift upward by 43 cm^{-1} to 1295 cm^{-1}. When replacing (for RF/DMSO) the N_3-H group by N_3-D (and also the four water molecules by D_2O), according to our calculations this mode shifts by a comparable 52 cm^{-1} from 1252 to 1304 cm^{-1}. In the RF/DMSO spectrum this stretching vibration is spread over three (calculated) modes at 1235, 1228, and 1191 cm^{-1}. So the C_2-N_3 stretching vibration is in the DMSO spectrum part of the 1235 cm^{-1} mode. Therefore the intensity increases when changing the solvent from water to DMSO.

(iv) At the moment no suitable explanation can be given why the experimental 1505 cm^{-1} peak rises and the 1554 cm^{-1} decreases.

In summary, major changes in the S_0 resonance Raman spectrum are due to hydrogen-bonding which causes either more restricted or more intense vibrations at the polar side of the isoalloxazine moiety. The experimental and theoretical spectra match well, but the latter are slightly blue shifted, probably because of the harmonic approximation. Peak intensities are also well represented, with a few exceptions. For example the intense experimental peak at 1403 cm^{-1} is weak (and shifted to 1409 cm^{-1}) according to theory. One may have to go beyond the IMDHO model to improve on that. — The adenine moiety in FAD has less influence on the resonance Raman spectrum. Indeed, the resonance Raman spectra of RF/water and FAD/H_2O are rather similar, both according to Tables 6.2 and 6.9 (see also Figure 6.8 b). Differences are slightly larger in theory compared to experiment, on the order of a few wavenumbers.

Excited state vibrations

An analogous band assignment for the S_1 state is presented in Table 6.3. Listed are the main experimental peak positions of RF/DMSO and FAD/water from resonance at 776 nm, and they are compared to the theoretical values for RF/DMSO and RF/water. It should be mentioned here that the transient Raman spectra of Figure 6.7 provide (to the best of our knowledge) the first direct view of vibrational structure in S_1, *i.e.* not superimposed by ground-state bleaching effects. — FAD is expected to behave similar to RF. In calculations for water solutions, isotope labeling was considered by replacing H_2O with D_2O and N_3-H with N_3-D. The assignment of excited–state vibrations is based on normal mode analysis of the TD-B3LYP/TZVP geometry–optimized S_1 state as outlined earlier.

Let us focus on the effects of isotope labeling – a more general discussion of excited state vibrations of flavins can be found elsewhere.[203] In the experimental spectrum of FAD in (heavy) water as shown in Figure 6.7 and reported in Table 6.3, the most obvious changes in the region around 1200 cm^{-1} are the blue shift of a broad 1206 cm^{-1} band to 1228 cm^{-1}, and the appearance of new peaks at 1160 cm^{-1} and 1135 cm^{-1}. According to our calculations for RF/H_2O, the experimental 1206 cm^{-1} band corresponds to several modes at 1208 cm^{-1}, 1200 cm^{-1} (C_2-N_3 stretch), 1161 cm^{-1}, and 1144 cm^{-1} (N_{10}-C_{9a}, CH_3-C_8, N_5-C_{5a}, C_4-C_{4a} stretch). In theory upon changing the solvent from water to heavy water the C_2-N_3 stretching mode (1208 cm^{-1}) splits into 1203 and 1266 cm^{-1}, and the 1200 cm^{-1} shifts to 1176 cm^{-1}. So in the D_2O spectrum the experimental, blue shifted 1228 cm^{-1} band and parts of the experimental 1160 cm^{-1} signal are assigned to the C_2-N_3 stretching vibration. In D_2O, the theoretical 1161 cm^{-1} and 1144 cm^{-1} peaks are downshifted to 1151 and 1136 cm^{-1}, respectively. Moreover, in D_2O the theoretical modes at 1176, 1151 and 1136 cm^{-1} are strongly coupled to N_3-H (N_3-D) wagging. The appearance of the new 1160 and 1135 cm^{-1} peaks in experiments is explained by the strong coupling of the isoalloxazine framework vibrations to the N_3-H (N_3-D) wagging mode, which causes a rise in intensity, and the downshift. In aprotic DMSO the C_2-N_3 stretching vibration is found at 1184 cm^{-1} by theory and at 1188 cm^{-1} by experiment.

In the energetically higher region, the experimental 1640 cm^{-1} band for FAD/H_2O is red-shifted by 29 cm^{-1} to 1611 cm^{-1} in D_2O. This band is assigned to the C_2-O_2 stretching vibration. According to calculations, the band shifts from 1668 cm^{-1} in water to 1635 cm^{-1} in heavy water, by 33 cm^{-1}. In DMSO, the corresponding signal is at 1658 cm^{-1}, indicating that in the S_1 state H-bridges can cause red- or blue-shifts of the carbonyl stretch, depending on whether H_2O (blue) or D_2O (red) is considered. Similar observations are made, from the theory side at least, for the C_4-O_4 stretching vibration. In contrast, the C_4-O_4 vibration in the ground state is red-shifted already in H_2O, due to the weakening of the carbonyl bond by the hydrogen bond. This is seen more clearly in theory than in experiment, because the resonance Raman signals of the C-O stretch modes are weak as mentioned above.

As a final observation for this section it is noted that in the experimental spectrum (Figure 6.7) the intensity of the 1258 cm^{-1} band of FAD/H_2O increases in intensity in D_2O, without changing position. In DMSO this band appears at 1254 cm^{-1}, and it is assigned it to N_5-C_{5a}, N_3-C_4 and ring I contraction vibrations. In heavy water this mode is coupled to N_3-H (N_3-D) wagging. In theory, it shifts from 1272 cm^{-1} in DMSO to 1275 cm^{-1} in water and 1276 cm^{-1} in D_2O.

6.5.2 Raman Band Shapes

The shape of the femtosecond stimulated Raman signal strongly depends on the resonance conditions. For Raman excitation at 776 nm only $S_n \leftarrow S_1$ transitions play a role, and the conditions resemble those encountered for *trans*-stilbene (see Chapter 4). Like in that case, only the blue-shaded pathways in Figure 2.7 have to be considered. The number of contributing optical processes is further reduced, because the higher excited states S_n are expected to be depopulated in less than 0.1 ps (see also Section 6.5.4). As

a consequence, only pathways in which an intermediate coherence is generated in the first excited state S_1 give contributions to the signal that are spectrally narrow enough to be distinguished from the background (*cf.* the simulation in Figure 2.8, left). Thus, the transient Raman signal at 776 nm is dominated by the R_{3e}^A response, but at early delay times, when the system is vibrationally excited, also the pathway R_{4e}^B may play a role. Hence, the measured signal resembles the spectra that would be obtained in a spontaneous Raman experiment on the S_1 state (although the time resolution in the present experiment is better). The absence of ground-state signals and of band distortion is the reason why the Raman spectra recorded at 776 nm can be compared directly to the quantum-chemical calculations.

For visible Raman pulses, the signal is more complicated. At 523 nm the Rama pulse is resonant with the $S_n \leftarrow S_1$ and the $S_1 \rightarrow S_0$ transition. In contrast to the *cis*-stilbene measurements in Section 4.4.2, where the influence of the stimulated emission was small, its contribution to the early transient absorption signal of flavin amounts to 25% at 523 nm, as deduced from the decomposition of the transient absorption spectra in Section 6.5.5. Simulations suggest, that $S_1 \rightarrow S_0$ resonance gives rise to negative Raman bands at the positions of the ground state frequencies (Figure 2.8, right, and the associated discussion), in agreement with the strong negative signals observed experimentally.

With 500 nm Raman excitation also the ground state bleach should give additional negative contributions to the signal. However, a difference in signal shape between Raman resonance at 500 and 523 nm is not found. It follows that either the bleach does not play a role or else contributions from $S_1 \leftarrow S_0$ and $S_1 \rightarrow S_0$ resonance can not be distinguished. Therefore a quantitative analysis of spectra as in Figure 6.8 a is not reasonable at present; what remains is an empirical view of integrated resonance Raman signal strength in this case. In future work, dominant $S_1 \rightarrow S_0$ resonance should be sought at 570 nm (see Section 5.6), in addition to the useful spectra generated at 776 nm, Figure 6.6.

6.5.3 Vibrational Spectroscopy in Time

The decay of Raman intensities was already shown in Figures 6.6 c and 6.8 c; a multiexponential description gave the time constants and relative amplitudes of Table 6.1. After ~ 3 ps the decay of Raman intensity is comparable to that of transient absorption and fluorescence. This is best seen for measurements with 500 nm Raman excitation, which span the same time range as transient absorption. For both FAD/water and RF/DMSO the nanosecond decay is reproduced. Quenching of S_1 FAD via a putative electron-transfer pathway (see below) is found as decay with $\tau = 7$–8 ps. A small additional decay with 68 ps (5%) matches, within the experimental error, the 84 ps component seen by transient absorption (Figure 6.4 c).

Differences in decay behavior are found within the first 3 ps. Here the transient Raman signal shows additional fast components which are absent in absorption and fluorescence experiments. They are similar in all investigated cases but depend on Raman conditions. The largest initial loss, 40–70 %, is found with 776 nm excitation. Smaller loss is observed with 500 nm excitation and the evolution is faster. In measurements with 523 nm Raman

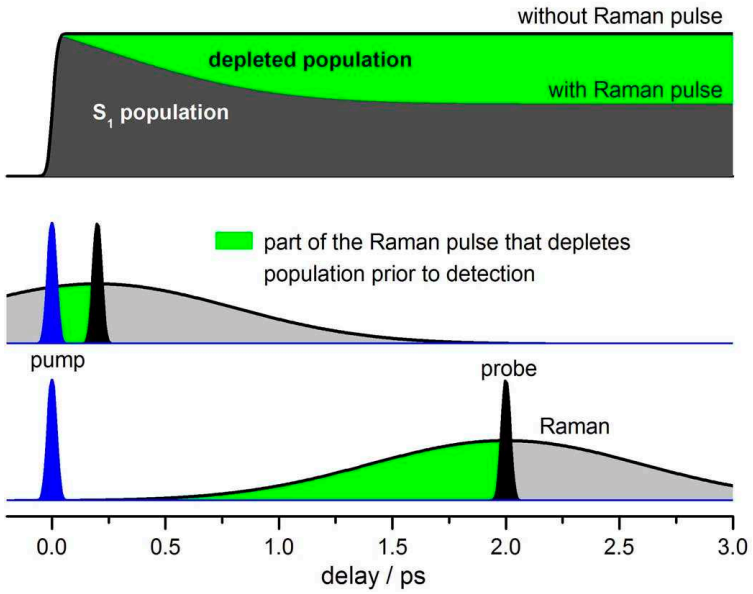

Figure 6.10: Explanation of the initial decay of the Raman signal by population depletion.

excitation only 16 % of the signal decays on the sub-picosecond time scale.

An initial drop of Raman intensity was also reported in Chapter 4 for excited stilbene and attributed loosely to IVR and dynamic solvation. In the present work the initial decay does not depend on the solvent. On the other hand, the Raman pulse parameters are varied here as shown in Table 6.1. Strong loss for 776 nm Raman excitation goes together with a high pulse energy of 3.3 μJ, suggesting that population depletion may play a role. Comparison shows that the early decay lasts approximately half the Raman pulse duration, which is also given in Table 6.1 . On this basis the depletion model of Figure 6.10 is proposed. Population is pumped to the S_1 state by the actinic pulse, and its relaxation and decay is monitored by stimulated Raman scattering with the delayed probe pulse. Let the Raman and probe pulses overlap in their maximum; then the first half of the Raman pulse preceeds the scattering event and may deplete population prior to detection, leading to a loss of Raman intensity. At short delay times the depleted population depends on the convolution of the preceeding part of the Raman pulse with the unperturbed population dynamics. This effect leaves a temporal signature which is not related to molecular relaxation processes but reflects the Raman pulse characteristics. As in the present work, commonly Raman pulses are applied that have energies comparable to the actinic pump pulse.[12,14,16,19,21,23] Under such conditions, depletion should be taken into account. Mixed actinic pump/Raman/probe pathways cause further coherent contributions to the signal when the Raman and actinic pulses overlap.

Spectral shift and narrowing of Raman bands should not be affected by Raman pumping as described above, even though they occur on a similar time scale. For example,

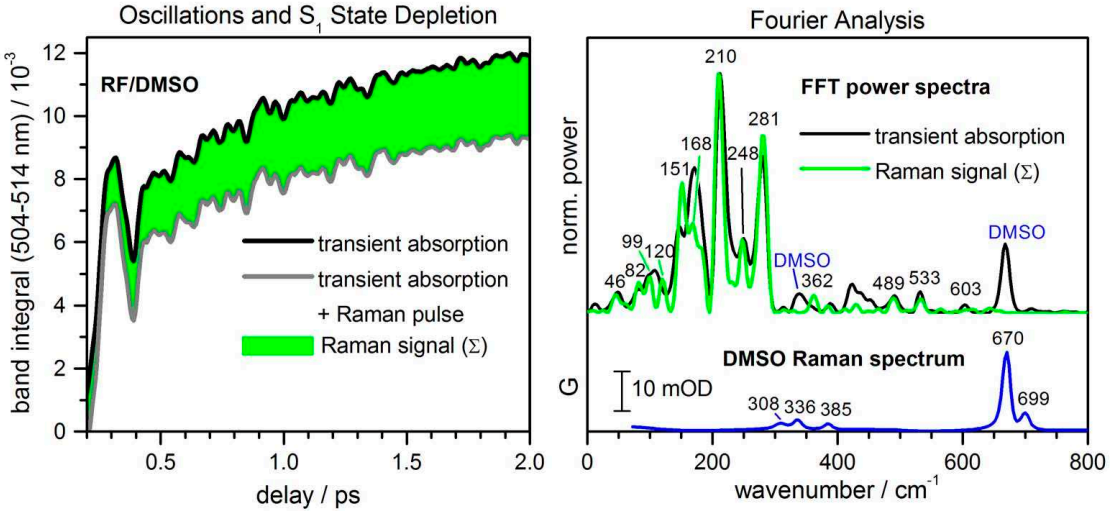

Figure 6.11: Marking chromophore wavepackets, with RF/DMSO as example. Left: Transient absorption averaged over the region 504-514 nm, without picosecond Raman pulses (TAS, black) and with the Raman pulses turned on (grey). The difference (green) is the raw Raman signal Σ. Right: Fourier power spectra (top) of the oscillations in TAS (black) and Σ (green) of the left panel. Below, the non-resonant stimulated Raman spectrum of pure DMSO is shown for comparison.

with 776 nm Raman pulses a $S_n \leftarrow S_1$ transition is pumped. Assuming a short lifetime for S_n, the newly induced Raman signal must be spectrally broad and therefore does not disturb the well-defined S_1 Raman bands. If the population returns to S_1 before the probe pulse arrives, the transient Raman spectrum will carry bands from population in high-lying S_1 vibrational states. This should lead to broadening of the signal, in contradiction with experiment. It is concluded that the spectral shape is not altered significantly by interaction with the Raman pulse. The observed changes could be related to solvation dynamics instead that are discussed later.

Up to now, population transfer by the picosecond Raman pulse was considered an artefact. In the following two sections it is shown that the effect can be used to mark S_1 wavepackets.

Oscillations in Transient Absorption. Femtosecond experiments allow to follow nuclear motion of a molecule in time,[226–229] thus providing an approach to vibrational spectroscopy that is complementary to the frequency-resolved Raman approach presented so far. The short actinic pump pulse has inherent spectral width, so that the first two electric field interactions in Figure 2.7 may prepare a coherent superposition of vibrational levels in the ground or excited state. This wavepacket evolves in time with the pertinent normal–mode frequency, thereby modulating the spectral properties of S_0 or S_1. The transient absorption band integral of RF/water over the region 504–514 nm, shown in Figure 6.11, left (black), exhibits low-frequency oscillations. As

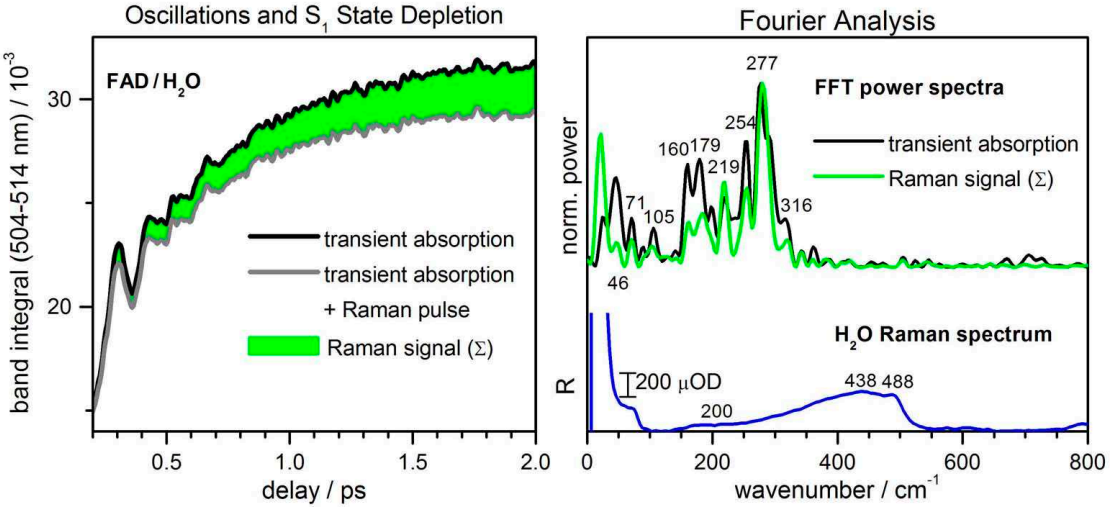

Figure 6.12: Wavepackets motion for FAD/H_2O. Left: Transient absorption averaged over the region 510-519 nm, without picosecond Raman pulses (TAS, black) and with the Raman pulses turned on (grey). The difference (green) is the raw Raman signal Σ. Right: Fourier power spectra (top) of the oscillations in TAS (black) and Σ (green) of the left panel. Below, the non-resonant stimulated Raman spectrum of pure H_2O is shown for comparison.

shown in Figure 6.12. Similar results are obtained for FAD/water. The signal was fitted by a sum of exponential functions and a Fourier transform was performed on the residual. The power spectrum, given in Figure 6.11, right, comprises several vibrational bands. In this experiment the probe pulse is resonant with flavin excited-state absorption and stimulated emission but does not overlap with ground-state absorption (Figure 6.3). Therefore specifically vibrations on the S_1 electronic state are monitored. Only those flavin vibrations contribute that are excited by Franck-Condon transitions from the ground state. The relative signal intensity then depends on the $S_n \leftarrow S_1$ (ESA) and $S_1 \rightarrow S_0$ (SE) Franck-Condon overlap and the system temporal apparatus function (here $\sim$ 50 fs fwhm). Note the difference to the FSRR experiment, where vibrational signals are not limited to impulsively excited modes.

Strongest bands in the power spectrum are found at 170, 210, 280 cm^{-1}, in agreement with previous experiments.[180] Whereas the low-frequency vibrations > 120 cm^{-1} mainly describe in-plane deformation, modes around 100 cm^{-1} (82, 99, and 120 cm^{-1}) were assigned to out-of-plane deformations of the isoalloxazine ring. In pure C_S symmetry, these modes should not be optically active for the $S_1 \leftarrow S_0$ transition. Recent calculations, however, demonstrated that flavin is sufficiently distorted by the ribose chain to render these modes Franck-Condon active.[203] Wavepacket motion with ~ 100 cm^{-1} is observed clearest for the transient absorption and fluorescence signal of RF/DMSO (see also Figures 6.5 and 6.18), but similar signal modulations are also found in aqueous solution.

Marking S_1 wavepackets. Solvent nuclear oscillations contribute to the transient absorption signal as well. But since the actinic pump does not reach electronic transitions of the solvent, wavepackets are only prepared in the electronic ground state by non-resonant impulsive Raman scattering. Due to the high molecular abundance, a significant solvent contribution may be observed. By comparing the Fourier power spectrum in Figure 6.11 with the Raman spectrum of DMSO bands at 336 and 670 cm^{-1} are identified as originating from solvent wavepackets.

Population depletion by the picosecond (Raman) pulse was discussed before. It leads to a decreased transient absorption signal shown for 500 nm Raman excitation in Figure 6.11, left (grey). The induced difference Σ, marked green, is dominated by a broad "sequential" background B and a smaller coherent contribution R, discussed previously. The population depletion which causes B depends on the availability of resonant electronic states. Fourier analysis of Σ, shown in Figure 6.11, right (green), reveals the same flavin oscillations as the original transient–absorption signal. However, since solvent electronic transitions are not accessible for population transfer by the picosecond pulse, the Fourier spectrum of Σ completely lacks DMSO bands. Thus, Fourier analysis of the background B (here for simplicity the complete signal Σ is used) provides an elegant way to obtain excited-state vibrational spectra which are free from solvent contributions. Compared to depletion experiments with femtosecond dump pulses,[100,226] the narrow bandwidth of the picosecond "marker" pulse prevents a formation of wavepackets which may contaminate the signal. As a price, information on the ultrafast temporal evolution of vibrations is of course no longer provided.

Also for FAD in water wavepacket motion is seen as oscillations of the transient absorption and Raman background signals, as shown in Figure Figure 6.12 for the band integral over the range 510–519 nm. Water is a poor Raman scatterer; this can be seen from a comparison of the scales for the stimulated Raman signal in Figure 6.12 and Figure 6.11. A water contribution can not be identified clearly in the Fourier power spectrum of the transient absorption oscillations. The deviation of the black spectrum from the green one in the regions < 100 cm^{-1} and around 200 cm^{-1} may originate from solvent contributions, but could also result from differences in the subtraction of the non-oscillatory background.

Oscillations of Raman Bands. Whereas the previous paragraph focused on an analysis of the Raman background B, in Figures 6.13 and 6.14 oscillations of Raman bands themselves are presented. In measurements of RF/DMSO with a Raman wavelength of 500 nm, oscillations of the background-corrected signal $R(\nu)$ are found around 90, 170, 210, and 420 cm^{-1}. For FAD/water, oscillations of the Raman signal are mainly observed around 300 cm^{-1} (see also Figure 6.14). As shown in Figure 6.13 for FAD/water, the signal evolution is comparable for 500 (black) and 523 nm (green) Raman excitation. Fourier analysis of the traces reveals that the signal oscillates with the pertinent frequency. Similar low-frequency oscillations were found for Raman bands of stilbene (Chapter 4), but also for green fluorescent protein,[23] and were assigned to wavepacket motion along the corresponding normal modes. Note that such oscillations can not be

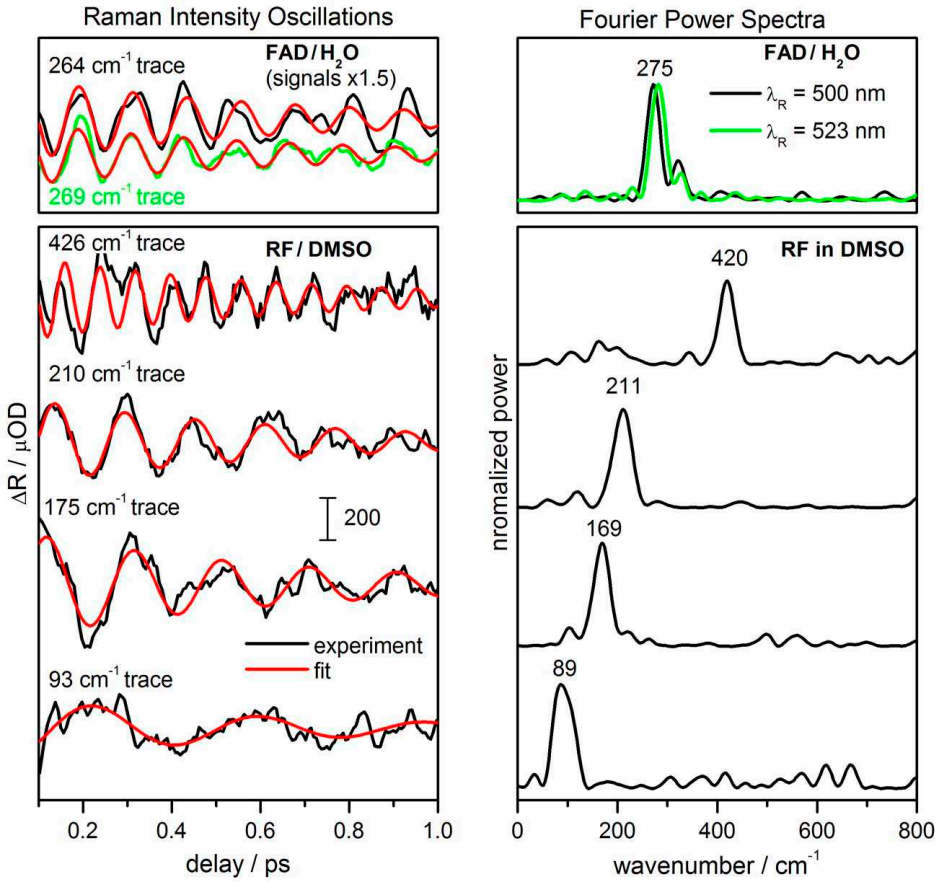

Figure 6.13: Left: Oscillations of background corrected Raman signals of FAD/water and RF/DMSO at the the indicated frequencies measured with 500 nm (black) and 523 nm (green) Raman excitation; the traces were smoothed by a Sawitzky-Golay filter. A fit with a single oscillation, exponentially damped with $\gamma = 0.6$ ps, is shown in red. Right: Fourier power spectra of the traces.

related to depletion artefacts from the narrowband Raman pulse. It is pointed out that wavepacket motion affects transient absorption and Raman signals differently: in transient absorption broad vibronic bands are modulated, resulting in gradual changes of the Fourier components over the spectrum; in contrast, Raman signals show modulation of sharp vibrational bands, and different frequencies are found for adjacent bands.

Figure 6.14 shows a contour plot of the oscillations found in the FAD Raman signal. The oscillatory modulation is clearly restricted to an ~ 100 cm^{-1} wide spectral region around 300 cm^{-1}, over which the phase shifts by 180°. This behaviour is compatible with the idea that wavepacket motion induces changes in the polynomial prefactor in equation (2.99), thus leading to oscillatory distortion of the corresponding Raman band. Under the current resonance conditions the Raman shapes are too complicated to allow a clear assignment of the oscillations to specific bands. Moreover, the Raman spectra at

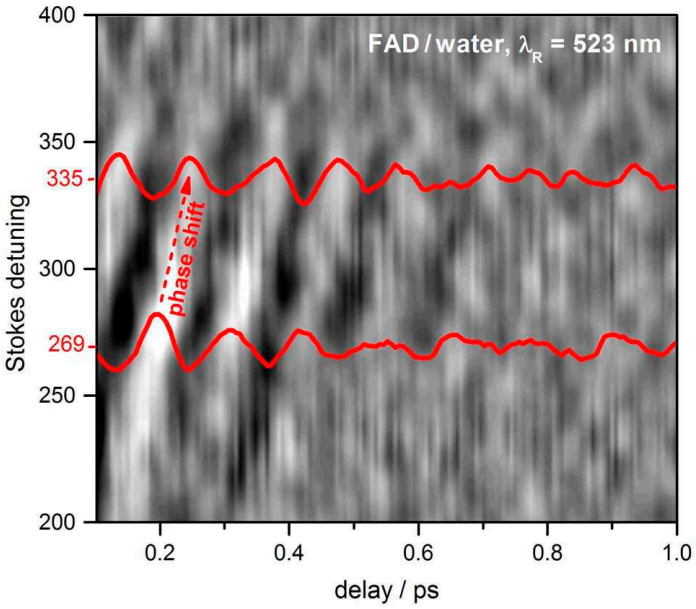

Figure 6.14: Oscillations of the transient Raman signal from FAD/water, measured with 523 nm Raman excitation: contour plot and selected traces.

500 nm excitation comprise contributions from both the ground and excited state. Thus, from the Raman signal a distinction between wavepackets on the S_0 and S_1 potential energy surface is not possible with the present data. Nonetheless, Figures 6.13 and 6.14 demonstrate the feasibility of simultaneous time- and frequency-domain Raman spectroscopy in the presence of an oscillating background from transient absorption.

6.5.4 Relaxation of Excited Flavin Seen by Transient Absorption and Fluorescence

Fluorescence spectral evolution and bandshapes. Different aspects of the relaxation dynamics are seen by fluorescence frequency shifts and transient absorption/emission band integrals (Figure 6.4 and Figure 6.5). All time traces are fitted with exponential functions convoluted with the apparatus function. The results of the exponential analysis are summarized in Tables 6.4 and 6.5. To facilitate the discussion the fluorescence evolution is studied with global analysis: all individual time traces are fitted with a common set of exponential functions. For a consistent picture, decay times are carried over from the previous analysis of band integrals and shifts, *i.e.* the following values are used to describe the evolution up to 3 ps: $\tau_1 = 0.22$ ps, $\tau_2 = 2.6$ ps for RF/DMSO with 400 nm excitation; $\tau_1 = 0.79$ ps, $\tau_2 = 1.6$ ps for FAD/water with 440 nm excitation. Such a description cannot truly mimick a continuous shift of a band, but here shifts are small

Table 6.4: Time constants[a] from a multi-exponential analysis of transient absorption band integrals.

RF/DMSO 400 nm	**RF/DMSO 440 nm**	**RF/H_2O 400 nm**	**RF/H_2O 440 nm**	**FAD/H_2O 440 nm**
		0.55 (-0.10)	0.6 (-0.12)	0.6 (-0.26)
2.9 (0.18)				
				6.5 (0.84)
		52 (0.13)	84 (0.14)	84* (0.08)
2000 (0.60)	2000 (0.72)	2900* (0.28)	2900 (0.67)	2900* (0.20)
offset (0.22)	offset (0.28)	offset (0.69)	offset (0.31)	offset (0.13)

[a] Time constants are given in ps; the contribution of the corresponding exponential functions to the total signal is given in brackets; asterisks mark time constants that were fixed during the fit.

Table 6.5: Time constants[a] from a multi-exponential analysis of band integrals over the emission cross sections, and of frequency shifts.

Band Integral		**Frequency Shift**		
RF/DMSO 400 nm	**FAD/H_2O 400, 440 nm**	**RF/DMSO 400 nm**	**FAD/H_2O 400 nm**	**FAD/H_2O 440 nm**
			0.09 (0.91)	
0.22 (-0.36)		0.22* (0.86)	0.79* (0.30)	0.79 (0.98)
2.6 (-0.11)	1.6 ps (0.32)	2.6* (0.14)		
	8.0 ps (0.46)		5.5 (-0.21)	5.5* (0.02)
offset (1.47)	offset (0.22)			

[a] Time constants are given in ps; the contribution of the corresponding exponential functions to the total signal is given in brackets; asterisks mark time constants that were fixed during the fit.

enough so that two exponential functions suffice to describe FAD/water fluorescence, at all observation wavelengths, down to noise level. For RF/DMSO a damped oscillation with $\nu = 102$ cm^{-1} (damping time 0.5 ps) must be added for a description of the signal.

A formal model with sequential interconversion of three species is then used, shown in the inset to Figure 6.15. The emission cross section is represented by

$$\sigma_{SE}(\nu, t) = a_1(t)f_1(\nu) + a_2(t)f_2(\nu) + a_3(t)f_3(\nu). \tag{6.4}$$

The spectra f_i of the virtual states and their population dynamics a_i are derived from the results of the global exponential fit.[76] f_1 corresponds to the fluorescence spectrum

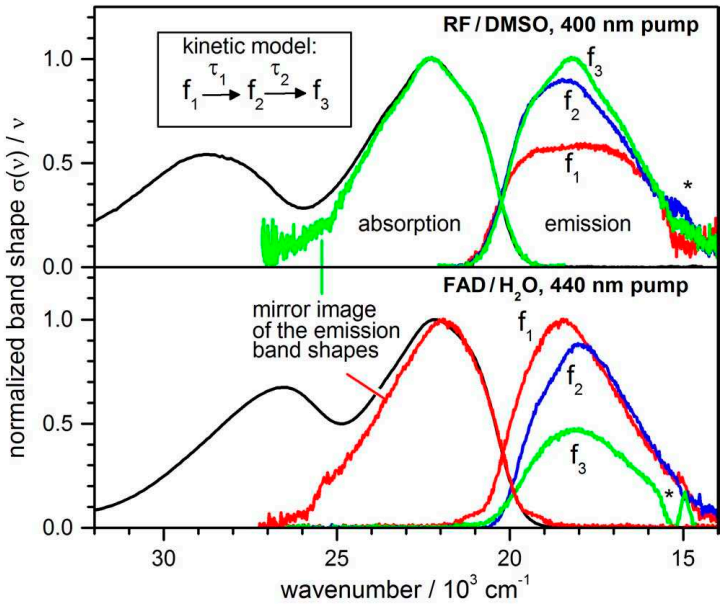

Figure 6.15: Comparison of bandshape of stationary absorption σ/ν (black) and fluorescence f_1/ν (red), f_2/ν (blue), and f_3/ν (green) up to ~ 3 ps. The latter were obtained from the time-resolved spontaneous fluorescence spectra with the formal kinetic model shown as inset. Top: RF/DMSO upon excitation with 400 nm; $\tau_1 = 0.22$ ps, $\tau_2 = 2.6$ ps. Bottom: FAD/water upon excitation with 440 nm; $\tau_1 = 0.79$ ps, $\tau_2 = 1.6$ ps. Asterisks mark contamination by the third harmonic of the gate pulse.

at zero delay time, f_2 is an intermediate spectrum that rises with τ_1 and decays with τ_2, and f_3 is the spectrum at 3 ps. In the figure the corresponding bandshapes $f(\nu)/\nu$ are shown. The reason for using bandshapes is that they reflect the distribution of Franck-Condon factors, or oscillator strength, for quantitative comparison with the ground-state absorption which is also shown in this form. The correponding band integrals are frequently used here as measures of electronic change.

Mirror symmetry between the $S_1 \leftarrow S_0$ absorption and $S_1 \rightarrow S_0$ fluorescence bandshapes is expected at earliest delay times. This situation is found for FAD/water at t = 0 (red). The fluorescence then shifts and slightly decays with $\tau_1 = 0.79$ ps to f_2 (blue); thereafter it decays to f_3 (green) without further shift. In contrast, the fluorescence of RF/DMSO upon 400 nm excitation is weaker at earliest delay times (red) and not mirror-symmetric to the first absorption band. This suggests that in addition to S_0 and S_1, a third state should be taken into account to explain the fluorescence in this case. It is either directly excited by the pump pulse, or it couples to the S_1 state after optical pumping but within the temporal apparatus function.[180] With increasing delay time, the fluorescence rises with 0.22 and 2.6 ps and the vibrational structure of the stationary fluorescence appears. Only after this relaxation is complete (f_3, green) does the mirrored fluorescence bandshape match the first absorption bandshape. Also by transient absorption, the stimulated emission is seen to be rising well resolved when

Table 6.6: Energies (in eV) for the lowest $\pi\pi^*$ and $n\pi^*$ singlet transitions of RF in different solvent environments, and oscillator strengths f.

Transition	**RF (g)[f]**[a]	**RF (DMSO)[f]**[b]	**RF (aq)[f]**[b]	**RF (aq)[f]**[c]
$S_1 \leftarrow S_0$	3.04 [0.1749]	2.93 [0.2225]	2.94 [0.2091]	2.86 [0.2037]
$n\pi^* \leftarrow S_0$	3.22 [0.0025]	3.64 [0.0003]	3.64 [0.0003]	3.73 [0.0002]
$S_2 \leftarrow S_0$	3.76 [0.1620]	3.52 [0.2776]	3.53 [0.2681]	3.43 [0.2876]

calculated *a* with TD-B3LYP/TZVP , *b* with TD-B3LYP/TZVP/PCM , *c* for the micro-solvation model with TD-B3LYP/TZVP/PCM.

exciting at 400 nm (Figure 6.4 a), whereas 440 nm excitation causes its immediate appearance (see Supporting Material). This behaviour will be discussed further below.

Let us return to the absorption side of Figure 6.15. Comparing with the "mirrored" fluorescence shapes, no compelling evidence is found for an *absorption* band that could be attributed to the weak $n\pi^* \leftarrow S_0$ transition. In water the bright $S_2 \leftarrow S_0$ transition was calculated (Table 6.6) to overlap with the blue tail of the $S_1 \leftarrow S_0$ band. With excitation at 440 nm the fraction of population pumped to the S_2 state is estimated to be small. In DMSO the $S_2 \leftarrow S_0$ absorption is prediced further to the blue so that its contribution at 440 nm can be neglected. But when exciting at 400 nm as in the transient fluorescence experiment, some population is expected in S_2 initially.

The intersection of the $S_1 \leftarrow S_0$ absorption bandshape with the corresponding $S_1 \rightarrow S_0$ fluorescence shape, $f_1(\nu)/\nu$ for FAD/water and $f_3(\nu)/\nu$ for RF/DMSO, provides an estimate for the position of the 0-0 vibronic transition, or electronic origin. (For RF/DMSO this is valid only in the absence of a dynamic Stokes shift, see below.) The electronic origin is located at 20200 cm^{-1} (495 nm) for FAD/water and 20240 cm^{-1} (494 nm) for RF/DMSO. Previous quantum-chemical calculations, with the same methods as in this work, explained the bandshapes of RF.[203] The relative position of the 0-0 transition determined here agrees with these calculations. The excess energy deposited in the system by "vertical" excitation can now be estimated: 4800 cm^{-1} for 400 nm, 2500 cm^{-1} for 440 nm, and 850 cm^{-1} for 475 nm excitation. In the remainder of this section the processes are discussed that underlie changes of the transient absorption and fluorescence signals.

Vibrational relaxation of the excited molecule starts with intramolecular vibrational redistribution (IVR). The pump pulse moves population into the Franck-Condon active modes with excess vibrational energy. Anharmonic coupling then spreads the energy over the full vibrational manifold, resulting in an internally equilibrated hot molecule. This process typically takes place on the sub-picosecond time scale.[113] With purely optical means only the relaxation of an average potential energy gap is seen, as shift and narrowing of vibronic band envelopes.[53] By transient fluorescence an initial red-shift is observed before 0.2 ps, when increasing the excess vibrational energy from 2500 cm^{-1} (440 nm excitation) to 4800 cm^{-1} (400 nm). Exponential analysis finds an associated time constant of 0.09 ps, well within the temporal resolution of 0.16 ps. This shift

is treated as part of the apparatus response and it is assumed that the fluorescence spectrum is created, partly red-shifted already, at zero delay time. Differences between the initial fluorescence spectra, as the pump photon energy is varied, reflect changes in Franck-Condon overlap for the initial $S_1 \rightarrow S_0$ transition; similar effects were found for *cis*-stilbene.[64] The effective non-equilibrium distribution at $t = 0$ subsequently relaxes by the resolved part of IVR which, however, can not be distinguished from solvation (see below).

Vibrational cooling, the transfer of excess energy from the chromophore to the solvent shell, was reported to occur on the 5–10 ps time scale for various molecules.[19,53,104,107,200,230] In agreement with these findings, after excitation at 400 nm a blue-shift of the fluorescence is observed with 5.5 ps, approaching the position of the stationary spectrum (Figure 6.5 d). Infrared experiments found similar time constants of 4.0–4.8 ps for the cooling of RF in DMSO.[198]

In contrast to a band position, the corresponding band integral should be insensitive to IVR and cooling[53] if the electronic characters of the initial and final states are maintained. For example, the transient absorption band integral of RF/DMSO upon excitation with 440 nm (Figure 6.4 c) does not change on the pertinent time scale. Note here that our integration (280-690 nm) misses part of the stimulated emission and near-infrared excited state absorption. This is irrelevant for changes during vibrational relaxation but should be remembered when different band integrals are compared. In this context it is instructive to compare the fluorescence band integrals of FAD/water upon excitation with 400 and 440 nm in Figure 6.5: despite the difference of excess vibrational energy, the integrals show the same decay behaviour. The observed decay therefore has to be assigned solely to adenine quenching, not to vibrational relaxation.

$S_2 \rightarrow S_1$ internal conversion. By illuminating FAD with 400 nm, some population is placed in the S_2 electronic state according to the previous discussion. Since fluorescence from the S_1 state rises with the temporal apparatus function, the characteristic time for $S_2 \rightarrow S_1$ internal conversion must be less then 0.1 ps. Equally in transient absorption (Figure 6.4 b, top) the rise of S_1 stimulated emission is not resolved. The time scale for $S_2 \rightarrow S_1$ conversion agrees with previous transient absorption experiments[190] and may be assumed to apply to water as well.

Dynamic polar solvation is another process that affects the sub-picosecond evolution.[128,231] Directly after excitation the molecule is still surrounded by the equilibrium solvent shell of the ground state. Solvent molecules then rearrange and adapt to the new charge distribution, causing a red-shift of the emission spectrum.[63,128,232] Here the 0.8 ps shift of the fluorescence band of FAD/water (440 nm excitation; green in Figure 6.5 d) is assigned to dynamic solvation. In agreement with our results, a decay component of 0.8 ps was previously found by global analysis of fluorescence traces at various frequencies[195], while measurements of the dynamic Stokes shift with different solvatochromic compounds yielded an average solvation time of $\langle\tau\rangle = 0.6$ ps.[130,180]

Of concern are the curves for the total band integral of transient absorption by RF

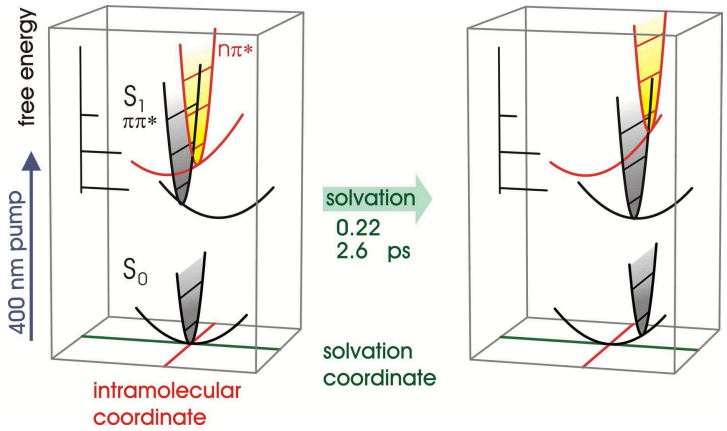

Figure 6.16: Vibronic coupling of the $\pi\pi^*$ to the $n\pi^*$ state in DMSO: the $n\pi^*$ state is only accessible after excitation with 400 nm. Dynamic polar solvation by DMSO shifts the energetic position of the $n\pi^*$ state.

and FAD in water (Figure 6.4 c, inset) which register a 0.6 ps rise, on the same time scale as the fluorescence shift. This must be contrasted with the corresponding fluorescence band integrals (Figure 6.5 b) and the *amplitude* of the stimulated emission in transient absorption measurements (Figure 6.4 b, top), which all show that the S_1 population and the oscillator strength for the $S_1 \rightarrow S_0$ transition are *not* influenced by water solvation. We believe that the observed rise of total band integral is an artifact from incomplete integration. The similarity of the initial changes suggests that dynamic solvation of flavin by water is not affected by the adenine moiety and does not depend on excitation wavelength. An additional decay with τ = 52–84 ps is identified in the transient absorption band integral of RF in water (Figure 6.4 c). This component depends on the pump wavelength; its assignment requires further experimental work. The evolution may be related to hydrogen-bond interactions, where water and the ribityl chain may act as donors.

Coupling to the $n\pi^*$ state. Excitation conditions affect the emission from excited RF in DMSO. With the pump wavelength at 440 nm, the transient absorption band integral appears constant at least until 50 ps (magenta line in Figure 6.4 c): there is no obvious electronic change in this time range. Excitation at 400 nm, however, causes intensity changes at early times. By fluorescence two rising components with τ_1 = 0.22 ps and τ_2 = 2.6 ps are observed which were described here already. By transient absorption the stimulated-emission band rising is seen, reflected by a 2.8 ps decay of the total band integral. Such time constants can not be associated with internal conversion $S_2 \rightarrow S_1$, as explained before. They are typical for IVR and cooling, but these processes do not directly affect overall intensities or oscillator strengths. Thus IVR by itself is ruled out as possible cause for early emission rise of RF/DMSO upon 400 nm excitation. The involvement of another electronic state was already concluded. Dynamic solvation, unlike IVR, can influence the electronic structure of the chromophore and thus modify

the oscillator strength of a transition. Polar solvation in DMSO has been characterized by the time-dependent fluorescence Stokes shift of a solvatochromic probe,[128] and time constants of 0.21 ps and 2.3 ps were reported. Their similarity to the values above suggests that the early emission intensity of RF/DMSO is coupled to polar solvation.

A possible scenario is shown in Figure 6.16. It is proposed that following 400 nm excitation, coupling between the S_1 ($\pi\pi^*$) state and the $n\pi^*$ state, above, builds up unresolvably fast. In the present work, time-resolved fluorescence did not detect a radiative $n\pi^* \rightarrow S_0$ transition at earliest delay times, in agreement with quantum-chemical calculations which predict a low oscillator strength. State mixing between $\pi\pi^*$ and $n\pi^*$ states would dilute the $S_1 \rightarrow S_0$ transition, reducing its radiative rate. As solvation proceeds, the energy gap between the two electronic states increases, while IVR occurs simultaneously. In the course of both processes, mixing is diminished and the full fluorescence strength is restored. (Note that oscillations of the transient absorption signal around 500 nm, previously assigned to stimulated emission $n\pi^* \rightarrow S_0$,[180] are now seen to belong to ESA.)

The calculated term values depending on the environment, Figure 6.6, support this idea. Solvation by either DMSO or water stabilizes S_1 and S_2 but destabilizes the $n\pi^*$ state. Thus the energy gap between the $S_1(\pi\pi^*)$ and $n\pi^*$ states is smallest in the gas phase, 1500 cm^{-1}, and rises to 5700 cm^{-1} in DMSO (PCM), and to 7000 cm^{-1} in water (microsolvation model). As shown in ref. 216, the solvent shifts can be explained by analyzing the dominant orbitals involved in the pertinent excitations of S_0 . For example, a polar solvent shifts the S_2—S_0 transition more to the red than S_1—S_0 because the former has stronger contributions from orbitals below the HOMO (highest occupied molecular orbital). The contributing orbitals are localized at the non-polar end of the flavin and therefore destabilized upon increasing solvent polarization. Further, in ref. 216 it has been found as here (albeit for lumiflavin) that the $n\pi^*$-S_1 gap is smallest in the gas phase and increases in polar solvents. Similar to the water microsolvation model of Figure 6.2, hydrogen bonds to O_2, O_4 and N_3 were also introduced in ref. 216, in this case to model a protein environment. In both cases the H-bonds lead to red-shifts of the S_1 and S_2 signals, by stabilizing unoccupied π^* orbitals with significant localization at the polar end of the flavin unit. At variance with our findings in Table 6.6, in ref. 216 the protein environment was shown to produce smaller $n\pi^*$-S_1 gaps again, which are still larger than in the gas phase, though.

In aqueous solution dynamic solvation does not affect the fluorescence band integral. Nonetheless, $\pi\pi^*$-$n\pi^*$ coupling may also play a role in water, and the smaller amplitude of the transient absorption signal in the stimulated emission region was taken as an indication for this.[180] On the other hand, the formation of hydrogen bonds should facilitate a location of electron density at the oxygen atoms and thus destabilize the $n\pi^*$ state, in agreement with the calculated energies in Table 6.6. Hence, in water the $n\pi^*$ state may be energetically too high for coupling.

Deactivation by adenine. The adenine moiety provides an additional reaction channel for excited flavin: transient fluorescence and absorption band integrals of FAD show a

decay with 6.5–8 ps, which is absent for RF in aqueous solution. This result agrees with previous publications.[159,190,195–197] Compared to transient absorption, results of the fluorescence band integral analysis on FAD/water are less clear. In transient fluorescence, a bi-exponential function with 1.6 ps (32 %) and 8.0 ps (46 %) is needed to describe the intensity decay. The origin of the 1.6 ps time constant is not evident; additional solvation effects or reaction with the adenine moiety could be involved. Note that in none of the experiments in this work a spectral change was observed that could be associated with a formation of the charge-transfer state. It is concluded that flavin→adenine electron transfer is the rate-limiting step, and that back-transfer is faster so that the intermediate does not accumulate.

6.5.5 Decomposition of Transient Absorption Spectra

A decomposition of the transient absorption signal for RF in DMSO and FAD in water (400 and 440 nm excitation, respectively) into excited-state absorption (ESA), bleach (BL), and stimulated emission (SE) is achieved with the information from fluorescence upconversion measurements; results are shown in Figure 6.17.The following assumptions are made:

(i) The evolution of the bleach can be monitored best at the transient absorption minimum (446 nm for FAD in water and 440 nm for RF in DMSO); normalized time traces are shown in Figure 6.17, right. Smooth curves without oscillations and coherent contribution are obtained from multi-exponential fits. Bleach spectra are modelled by multiplying the ground-state absorption spectrum with the amplitude of the previously fitted trace at each delay time.

(ii) Stimulated emission spectra σ_{SE} are taken from corresponding fluorescence upconversion measurements. Figure 6.18 demonstrates that the fluorescence upconversion traces reproduce the changes of induced absorption at wavelengths where ESA is small. Note that for RF in DMSO even the wavepacket oscillation with ~ 100 cm^{-1} is observed in both experiments. The evolution of the stimulated emission signal is approximated by a global exponential fit of all individual time traces. For RF in DMSO a damped oscillation with $\nu = 102$ cm^{-1} and a damping time $\gamma = 0.5$ ps is included, see Figure 6.18. For FAD in water, the apparatus function was significantly longer for fluorescence upconversion (0.35 ps fwhm) compared to transient absorption (0.05 ps). In order to correct for this difference, the obtained fit was re-convoluted with a Gaussian of 0.05 ps width (fwhm), Figure 6.18, dashed red. The fit of the evolution was then used to correct transient absorption for the contribution of stimulated emission, apropriately scaled according to the assumptions in (iv).

(iii) Coupling of the nπ^* state to the $S_1(\pi\pi^*)$ state is assumed to be negligible for FAD in water (see Figure 6.15 and the associated discussion). Then, the oscillator strengths for $S_1 \leftarrow S_0$ absorption and $S_1 \rightarrow S_0$ emission are the same at zero delay time. The total transition probability is proportional to the band integral, *i.e.*

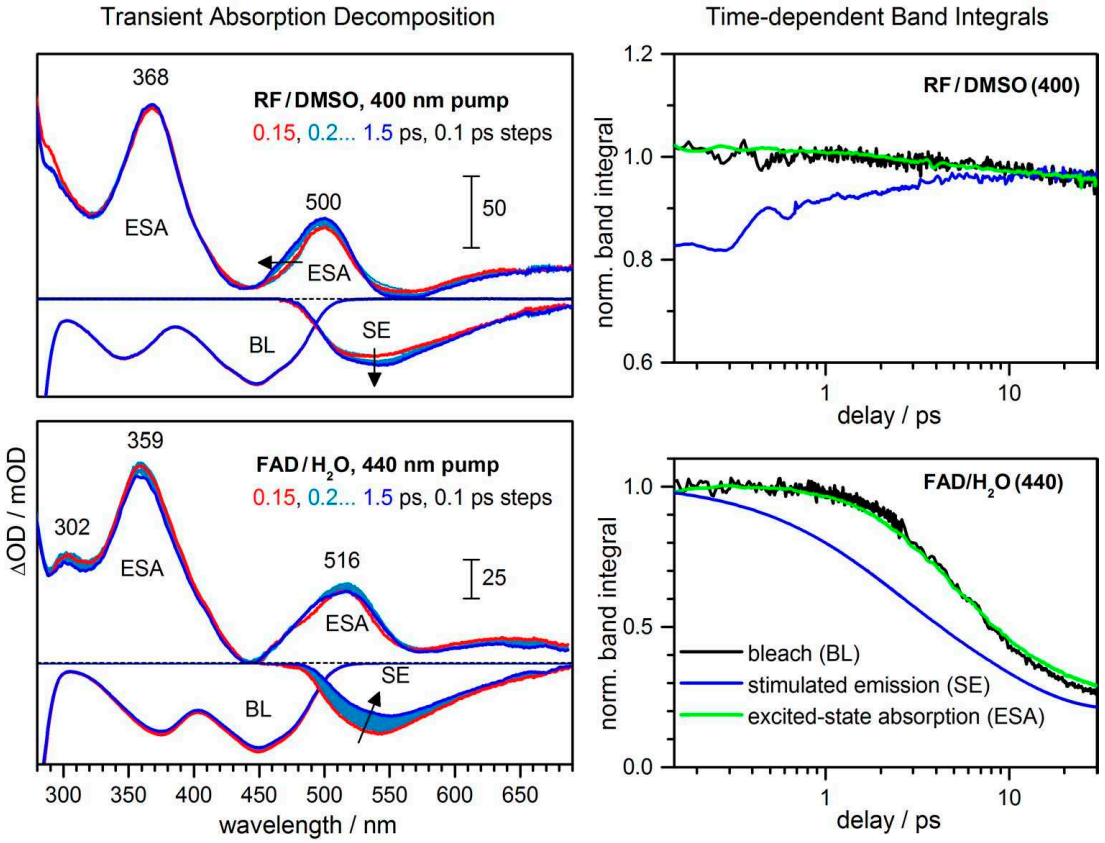

Figure 6.17: Left: Decomposition of the transient absorption spectra of Figure 6.4 into bleach BL, stimulated emission SE, and excited-state absorption ESA. Right: Band integrals separated for BL (black), SE (blue), and ESA (green) (normalized) from the panels to the left.

the integrated band-shape function $\sigma(\nu)/\nu$. Since S_0–S_1 absorption and initial fluorescence have approximately mirror symmetry, bleach and stimulated emission are scaled to equal peak band-shape values at zero delay time. For RF in DMSO, the influence of solvation on the oscillator strength should be taken into account. According to the model suggested in Figure 6.16, $\pi\pi^*$–$n\pi^*$ coupling occurs at early delay times but diminishes due to solvation with $\tau_1 = 0.22$ and $\tau_2 = 2.7$ ps. It is proposed that the excited-state population does not change during this evolution. This assumption is supported by the bleach trace in Figure 6.17. Consequently, for RF in DMSO, the fluorescence evolution is scaled such that stimulated emission and bleach bandshapes are of equal amplitude after solvation has completed. The relative scaling of bleach and stimulated emission thus corresponds to the situation shown in Figure 6.15.

(iv) The pure ESA at each delay time is obtained by subtracting the set of bleach and stimulated-emission spectra from the previous steps, scaled by a constant factor.

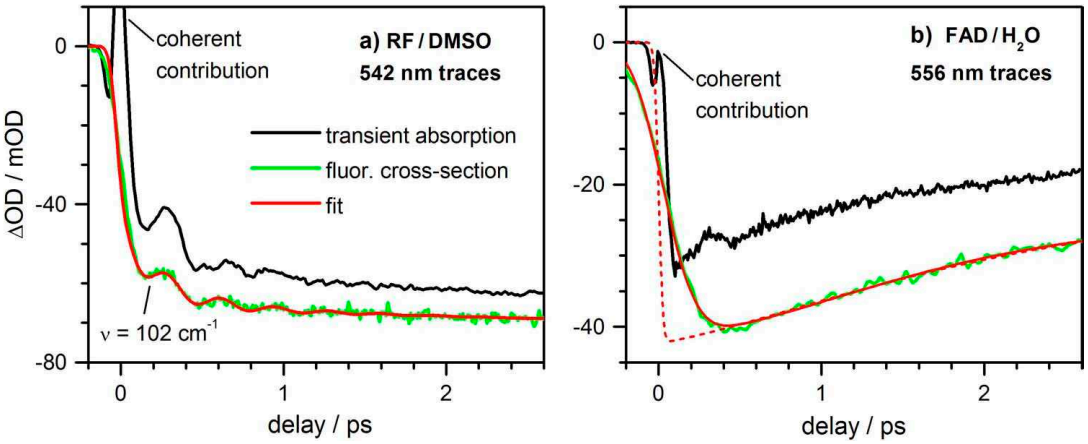

Figure 6.18: a and b: time-dependent transient absorption (black) and scaled fluorescence cross-section (green) signals at single wavelengths. In red: multi-exponential fit to the fluorescence. Dashed red in b: the exponential sum from the fit of the FAD fluorescence, convoluted with a Gaussian of 0.05 ps width to match the apparatus function of the transient absorption experiment.

The absolute scaling is adjusted to the minimum factor that assures non-negative ESA signals at all delay times.

Comparing the transient absorption spectra of RF and FAD in water, it is found that the adenine moiety only causes an overall red-shift of 200 cm^{-1}. When the solvent is changed from water to DMSO, the UV absorption band shifts to the red from 359 to 368 nm, whereas the visible band blue-shifts from 516 to 500 nm. A hump at 302 nm is only observed with RF/DMSO. Additional measurements with excitation at 475 nm show an ESA band around 780 nm, Figure 6.3. For future use the excited-state absorption spectra at 1 ps delay are fitted with lognormal functions, equation (6.1); the optimal parameters are collected in Table 6.7. Spectra are scaled so that the bleach contribution has -0.058 optical density at the first absorption peak (this information may be used to estimate the ESA extinction scale).

Band integrals revisited. Now integration over the range 290–690 can be performed separately for the ESA, bleach and stimulated emission spectra; normalized results are compared in 6.17 c. For RF/DMSO the bleach integral (black) shows only minor change during the first 30 ps. Therefore, the decay of the transient absorption band integral in 6.4 (black) should not be associated with population return to the electronic ground state (in contrast to FAD). The ESA band integral, green in Figure 6.17, reproduces the temporal evolution of the bleach trace. This supports the previous view that the population in the excited state does not change on the time scale of solvation. Moreover it is concluded that dynamic solvation and initial $\pi\pi^*$-$n\pi^*$ coupling do not affect the total oscillator strength of the excited state absorption in the range investigated, although bands may shift. The decay of the transient absorption band integral with 2.9 ps is

Table 6.7: Log-Normal fit to the ESA spectra from the decomposition of the transient absorption spectra of RF/DMSO (400 nm) and FAD/water (440 nm) at 1 ps delay.[a,b]

(a) RF/DMSO, 400 nm pump

ν_p	γ	Δ	h
(36768	0.275	2109	99.98)
34983	-0.626	6000	86.16
27189	0.042	3798	109.16
20028	0.221	2041	50.16
15383	-0.659	3678	13.87
12991	-0.056	3220	17.2

(b) FAD/water, 440 nm pump

ν_p	γ	Δ	h
(36575	-0.066	2870	117.38)
32613	-0.706	4927	66.35
27599	-0.191	4313	103.71
20564	0.994	3718	-23.5
19880	0.093	2689	62.88
15353	-0.724	4379	12.62
12881	0.064	2635	27.33

[a] ν_p – peak frequency in cm^{-1}, γ – asymmetry, Δ – width in cm^{-1}, h – amplitude in mOD. [b] Spectra were scaled to equal amplitude of the bleach contribution (-58.3 mOD for the maximum of the first absorption band). The log-normal descriptions are valid strictly only in the spectral region 287–690 nm, corresponding to the spectra in Figure 6.17. The range was extended to 1000 nm with excitation at 475 nm. Brackets indicate bands which are centered outside the observation window.

therefore ascribed solely to the solvent-induced rise of the stimulated emission (blue), as discussed in the previous section.

For FAD/water, Figure 6.17 c shows a drop of the stimulated-emission band integral below the traces for bleach and ESA on the 1 ps timescale; this evolution is associated with the 1.6 ps time constant from the previous analysis. Stimulated emission is sensitive to the drain of population from the S_1 state and to electronic changes, whereas the bleach reports on the return of population to the room-temperature equilibrium in S_0. A difference between the two band integral traces suggests the existence of additional evolution after actinic excitation. The following processes should be considered: dynamic solvation, electron-transfer, back-electron-transfer with recovery of the ground state, and vibrational cooling of the hot ground state. The signal may also be affected by intersystem crossing to the triplet state. Previous infrared experiments found a 1 ps rise and 9 ps decay in the spectral region of adenine ring vibrations, which were assigned to electron-transfer and back-transfer.[196] Characteristic changes of excited-state absorption are not observed; an involvement of electronic transitions like electron transfer or triplet formation is therefore not apparent. This suggests that states may be involved that are dark with respect to the $S_1 \rightarrow S_0$ transition. Evidence for $\pi\pi^*$-$n\pi^*$ vibronic coupling is not found in water, but dynamic changes of the adenine moiety may also influence the electronic structure of the isoalloxazine ring.

6.6 Outlook

The optimum Raman wavelength for monitoring the first excited singlet state S_1 of flavin should be sought around 780 nm, in pure resonance with the $S_n \leftarrow S_1$ transition. Here well-defined emissive bands are observed by femtosecond stimulated Raman scattering (FSRS), as $S_1 \rightarrow S_0$ resonance and ground-state bleaching are avoided. Modes $>$ 1000 cm^{-1}, more intense compared to the low-frequency region, were all assigned with the help of quantum-chemical calculations, including shifts upon exchanging the solvent water for heavy water. Thus a first direct view of vibrational structure in S_1 was obtained, not superimposed by ground-state bleaching effects. This will be useful when photochemical change in a protein environment is followed. For quantitative analysis of the temporal evolution, depletion by the Raman pulse should be avoided by decreasing the pulse energy to the order of the probe pulse ($\sim 0.1\ \mu J$). Here methodical development is needed to increase the sensitivity of FSRS.

Resonance conditions strongly affect the shape of the Raman signal. Experimentally, absorptive contributions from ground state vibrations are observed, if the Raman pulses overlap with the bleach or stimulated emission band. Typical band shapes are modelled with the third-order response-function formalism, and a compact formula is given.

Vibrational spectra can be recorded in time domain as well, and contributions from wavepackets in the excited state can be marked by population depletion with the picosecond (Raman) pulse. It is further demonstrate that oscillations of the Raman signal can be separated from the sequential background; this provides the perspective for future devolopment of 2D Raman spectroscopy. In the current experiments, the oscillation frequency appears to be identical to that of the detection band. How wavepackets in any of the participating electronic states affect the FSRS signal needs further experimental and theoretical work.

Excited-state absorption spectra are obtained from a quantitative comparison of broadband transient fluorescence and absorption. This approach could help to disentangle the complex photochemistry of flavin in biological environments. Early emission spectra depend on excitation wavelength and solvent. This is explained as evidence for the $n\pi^*$ state, which may influence the emission oscillator strength during solvation. S_1 quenching by adenine is seen with all methods in terms of dynamics, not by spectral intermediates.

6.7 Supporting Material

6.7.1 Transient Absorption

RF/DMSO: Transient absorption spectra of RF/DMSO upon excitation with 400 and 440 nm are compared in Figure 6.19. (Note that the results for 440 nm excitation cover delay times up to 1600 ps (yellow), whereas measurements at 400 nm were recorded only up to 1000 ps (orange).) The spectral evolution is similar at longer delay times, as also seen in Figure 6.4 of the main article. Within the first picoseconds the rise of the stimulation emission band (SE) upon excitation with 400 nm is clearly visible, accompanied by a small blue shift of the excited state absorption (ESA) around 500 nm, which is apparent also after spectral decomposition (Figure 6.24). Meanwhile, the rest of the spectrum stays unchanged. When exciting RF/DMSO with less excess energy, at 440 nm, a stimulated emission rise is absent. Spectral changes in the SE and ESA region

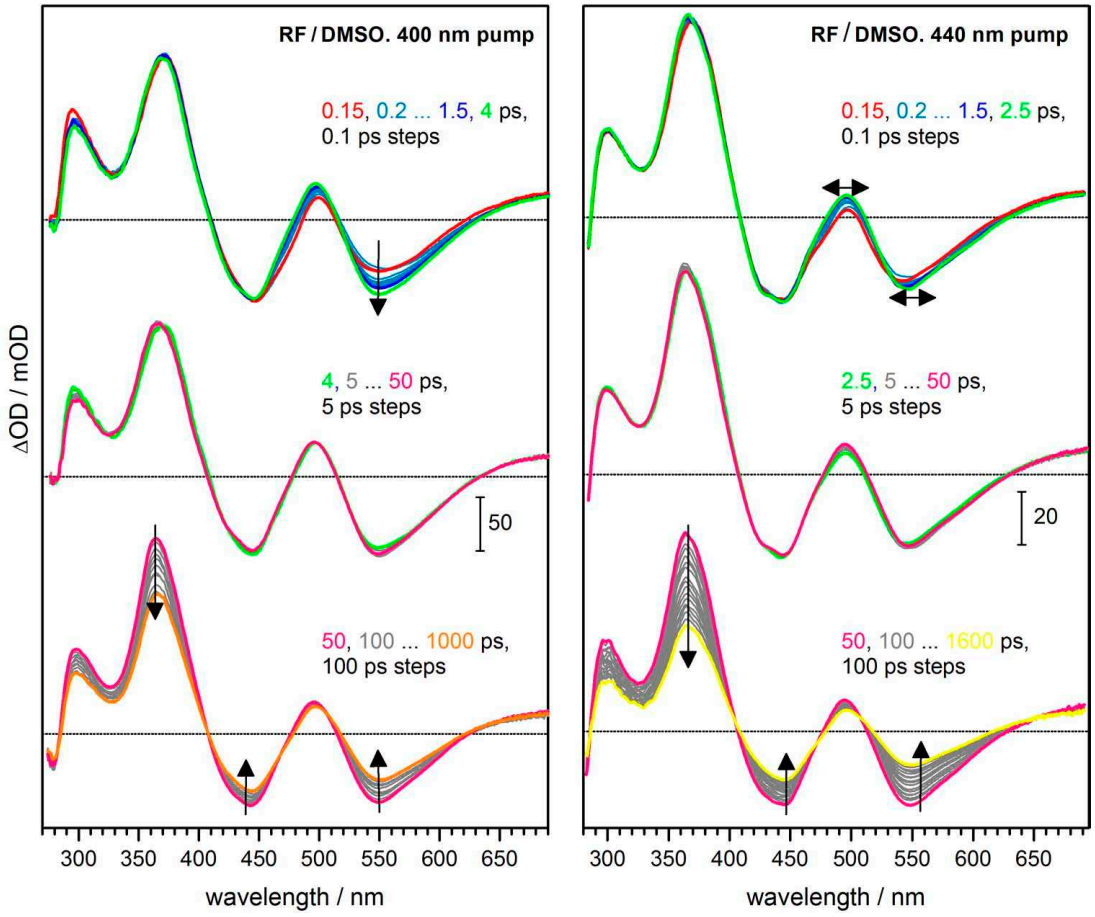

Figure 6.19: Transient-absorption spectra of RF/DMSO upon excitation with 400 nm (left) and 440 nm (right) under magic-angle conditions. Note that for 440 nm excitation spectra are shown up to 1600 ps, but for 400 nm only up to 1000 ps.

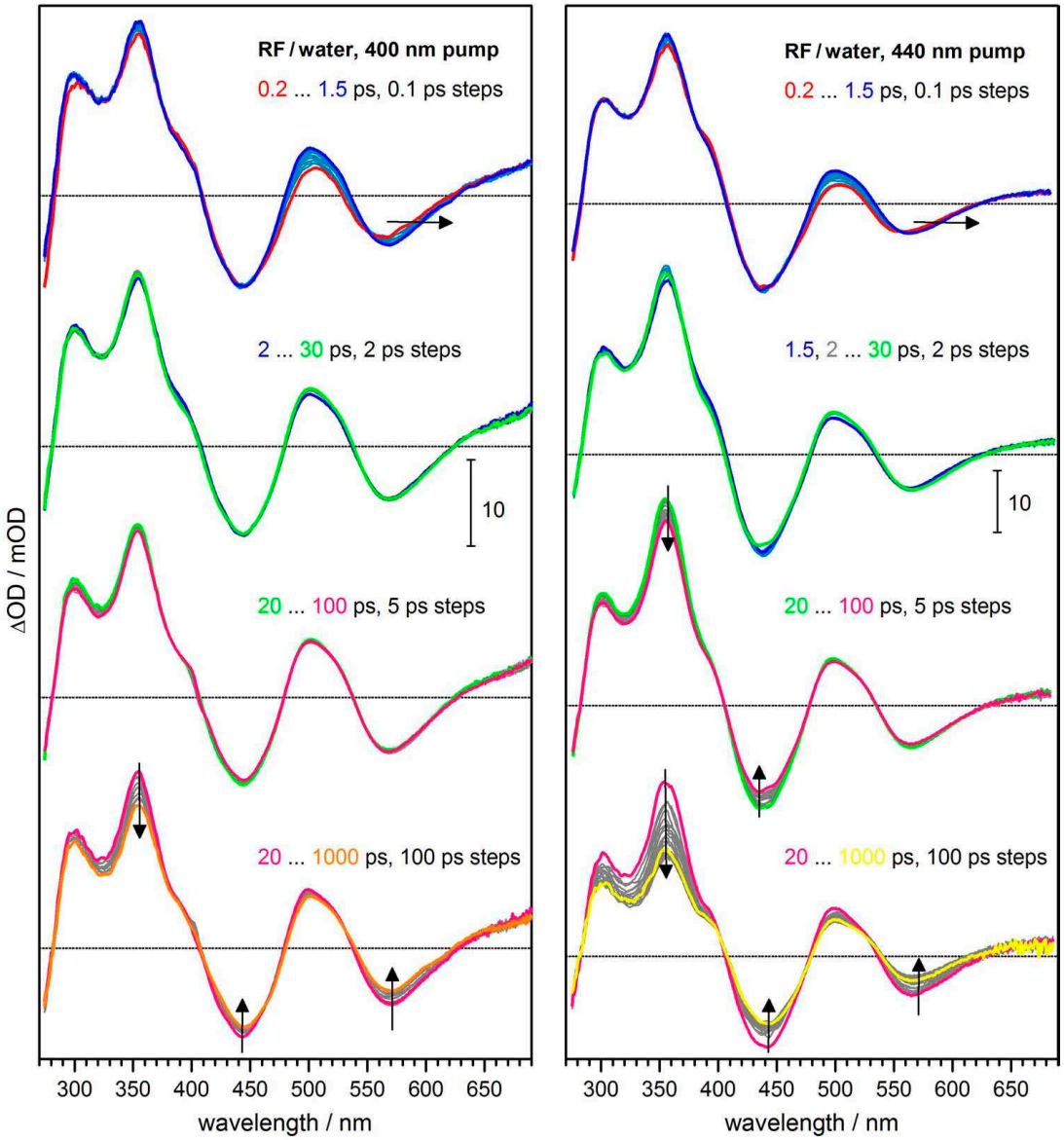

Figure 6.20: Transient-absorption spectra of RF/H_2O upon excitation with 400 nm (left) and 440 nm (right) under magic-angle conditions. Note that for 440 nm excitation spectra are shown up to 1800 ps, but for 400 nm only up to 1000 ps.

in Figure 6.19 mainly originate from wavepacket oscillations (see also Figure 6.18).

RF/H_2O: Transient absorption spectra of RF/H_2O upon excitation with 400 and 440 nm are compared in Figure 6.20. (Note again the difference in the maximum delay time between the orange (1000 ps) and the yellow (1600 ps) spectrum.) Within the first picosecond the stimulated emission shifts to the red without strong changes of the

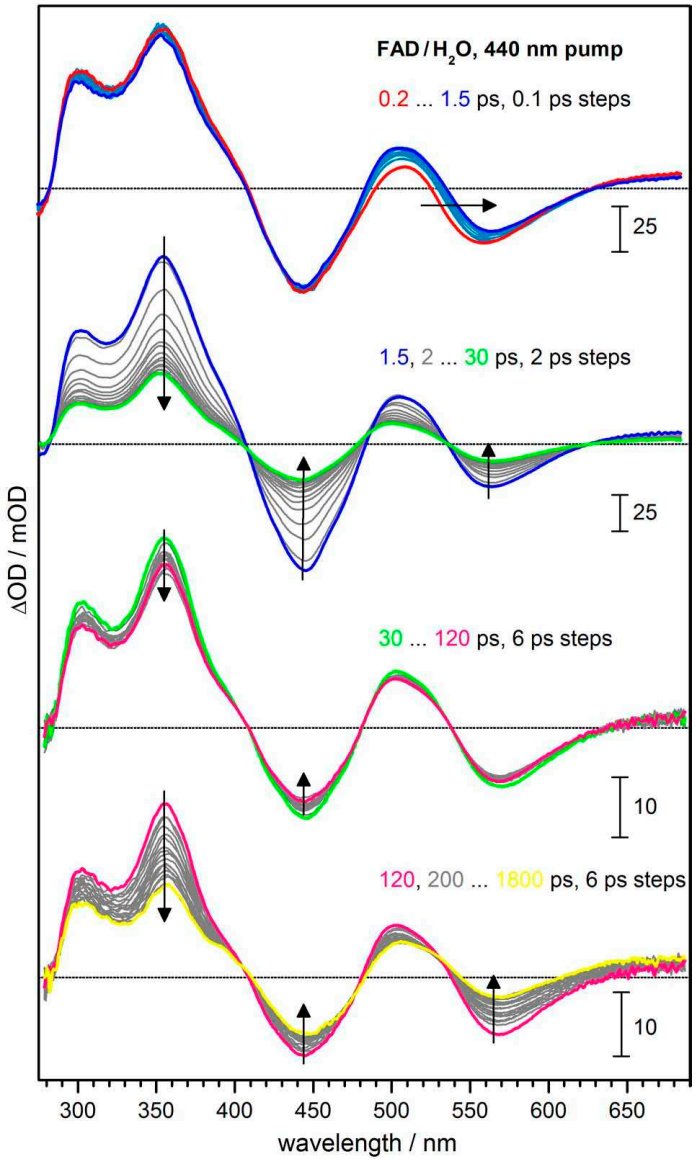

Figure 6.21: Transient-absorption spectra of FAD/H_2O upon excitation with 440 nm under magic-angle conditions.

oscillator strength. The spectra decay within several nanoseconds. In between, small changes are seen in the spectral range < 480 nm on the 100 ps time scale. A quantification of the effect is difficult, but a dependence on the excitation wavelenght appears to be present.

FAD/H_2O: The transient absorption results of FAD/H_2O upon excitation with 440 nm was already described in the main article. In Figure 6.21 transient spectra up to

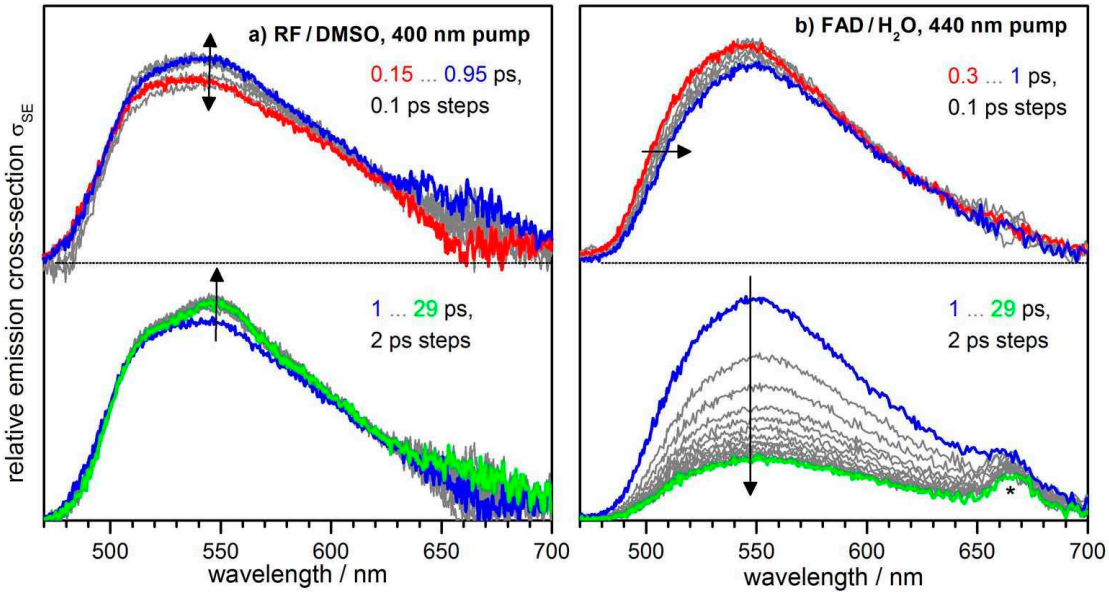

Figure 6.22: Transient fluorescence spectra of a: RF/DMSO upon excitation with 400 nm; b: FAD/H_2O upon excitation with 440 nm. All spectra were measured under magic-angle polarization conditions and are presented as cross-section spectra for stimulated emission, σ_{SE}. The asterisk marks contamination by the third harmonic of the gate pulse.

1800 ps are given to show also the nanosecond decay. Apart from the adenine-induced decay with $\tau = 6.5$ ps the evolution resembles strongly the behaviour of RF/H_2O. In particular, the initial SE shift is reproduced, proving that this is a solvation effect by H_2O and not the influence of the adenine moiety.

6.7.2 Fluorescence Upconversion

RF/DMSO: The full fluorescence spectral evolution of RF/DMSO upon excitation with 400 nm is shown in Figure 6.22 a. The rise of the fluorescence structure around 550 nm within the first picoseconds is apparent. At early delay times also an oscillation of the fluorescence band with 102 cm^{-1} is observed. This frequency corresponds to an out-of-plane vibration of the isoalloxazine ring.[203] Figure 6.18 a demonstrates that the fluorescence changes reproduce the evolution of the SE band seen by transient absorption spectroscopy.

RF/H_2O: Transient fluorescence spectra of RF/H_2O upon excitation with 450 nm are shown in Figure 6.23. Note that due the noise level, spectra were not converted to cross sections; instead the corrected photon count distributions are presented directly. At delay times up to 0.5 ps a coherent contribution from spontaneous Raman scattering (marked by the asterisk) overwhelms the weak signal.

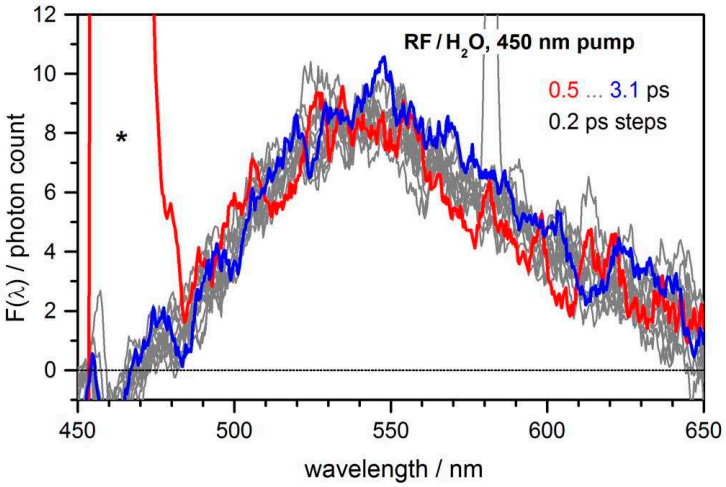

Figure 6.23: Transient fluorescence spectra of RF/H_2O upon excitation with 450 nm under parallel polarization conditions. For presentation the evolution was smoothed by a 60 fs temporal and 4.6 nm spectral moving average. The asterisk indicates spectral distortion by the coherent contribution. The spectra are represented as the corrected photon count distribution $F(\lambda)$.

FAD/H_2O: Transient fluorescence spectra of FAD/H_2O upon 440 nm excition are shown in Figure 6.22 b. The evolution resembels that of FAD/H_2O pumped at 400 nm, which was already presented in the in Figure 6.5. Briefly, the fluorescence spectrum shifts to the red within the first picoseconds and decays with 1.6 and 8 ps as a result from adenine-induced return to the ground state and eventual intermediate steps (see main text).

6.7.3 Excited State Absorption Spectra

RF/DMSO: The evolution of the RF excited state absorption spectrum upon excitation at 400 nm is shown in Figure 6.24, left, up to 30 ps; decomposition of the transient absorption was accomplished with the procedure outlined in Section 6.5.5. After a small initial blue shift of the 500 nm band, the spectrum stays unchanged from 1.5 to 30 ps, demonstrating that the population remains in the excited state.

FAD/H_2O: The evolution of the excited state absorption of FAD/H_2O upon excitation at 440 nm is shown in Figure 6.24, right, up to 30 ps. On the longer time scale the adenine-induced decay is apparent. This is accompanied by a small change in the shape of the 516 nm ESA band; otherwise the spectrum decays uniformly.

6.7.4 Femtosecond Stimulated Resonance Raman Spectroscopy

Transient stimulated Raman spectra of FAD/H_2O and RF/DMSO with Raman wavelengths of 500 nm and 523 nm (only FAD) are compared in Figure 6.25. The spectral

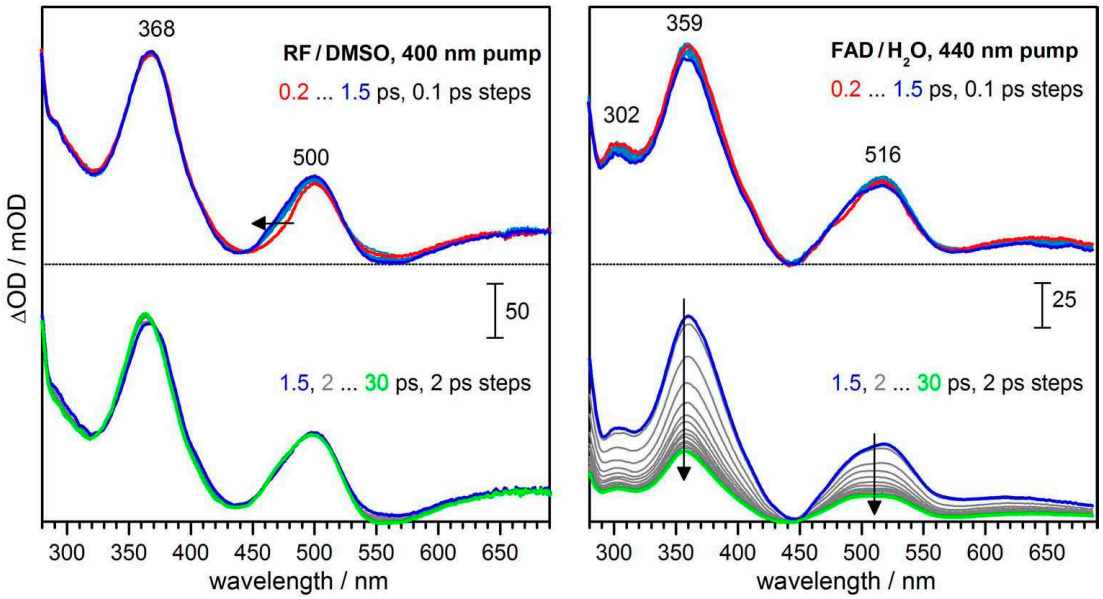

Figure 6.24: Excited-state absorption spectra of RF/DMSO excited at 400 nm (left) and FAD in water excited at 440 nm (right) under magic-angle conditions. The spectra are the result of a decomposition of the transient-absorption spectra as described in Section 6.5.5.

shape was already described before. It is similar for all measurements with visible Raman pulses, and is dominated by negative features at the positions of the ground-state bands. At longer delay times the spectra decay according to the population dynamics, which were observed already in transient absorption and fluorescence upconversion. Within the first picoseconds additional decay is seen, which probably originates from population depletion by the Raman pulse (see Figure 6.10 and the associated discussion). The spectral shape stays similar throughout the evolution although the relative intensities may exhibit minor changes. On account of the complicated signal I refrain from a deeper discussion.

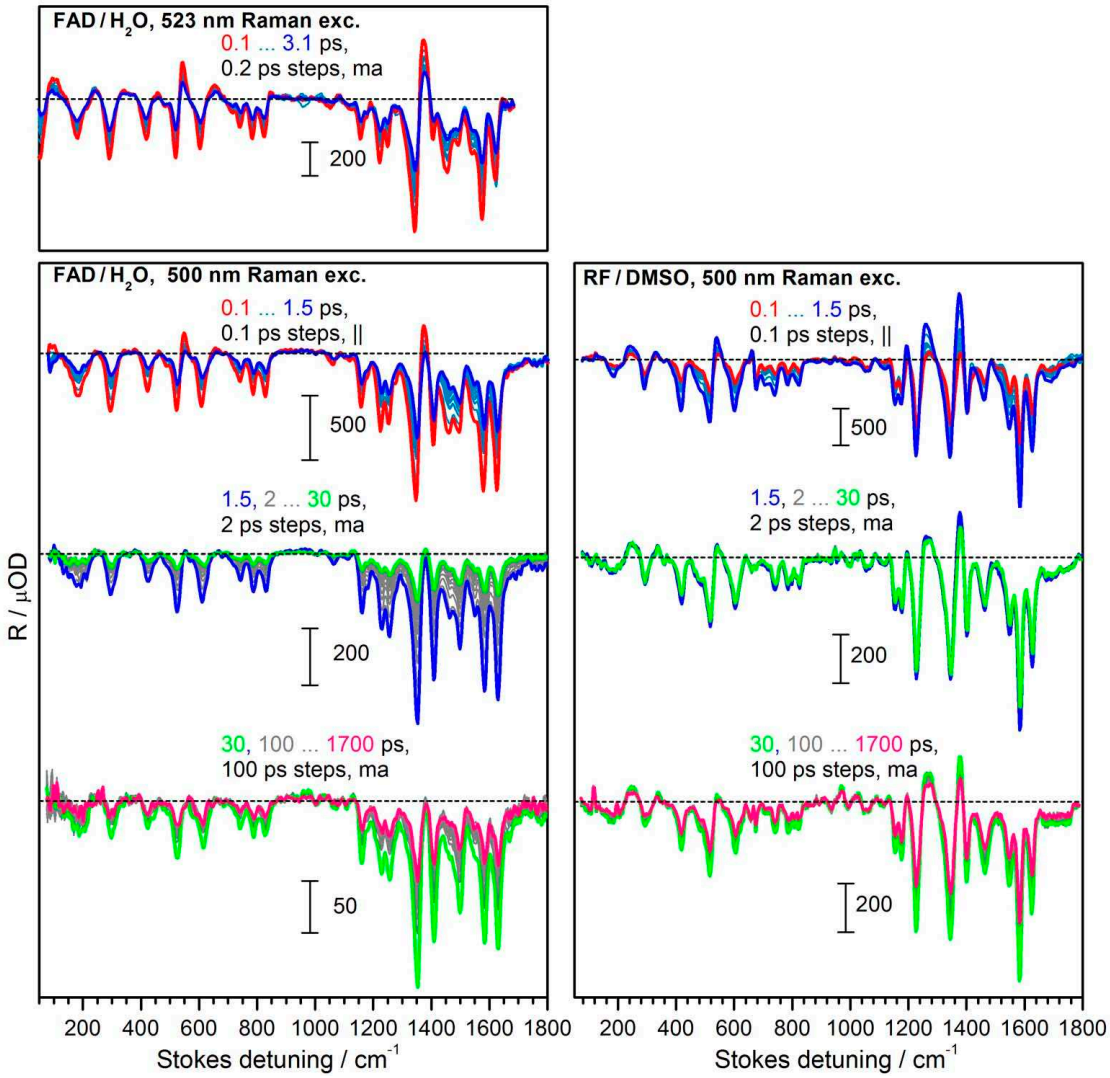

Figure 6.25: Transient stimulated resonance Raman spectra of FAD/H_2O (left) and RF in DMSO (right) recorded with 500 nm and 523 nm Raman pulses. The sample was actinically excited at 475 nm; polarization conditions are indicated as || (parallel) and *ma* (magic angle). Transient spectra at different time scales were acquired in separate measurements in time steps of 6 fs, 100 or 150 fs, and 3 or 6 ps, respectively. For presentation, the transient evolution with 500 nm Raman excitation was smoothed by a 5 point moving-average in time.

7 Light-Induced Changes in BLUF Photoreceptors

7.1 Introduction

Among the various flavoproteins, photoreceptors that contain BLUF (*Blue Light Using FAD*) domains have attracted considerable attention in recent years.[83,168,233–235] This is because upon blue-light excitation, the signaling state is formed already within several hundreds of picoseconds. Spectroscopically only a small (10–15 nm) shift of the absorption spectrum is observed (Figure 7.1), accompanied by subtle changes in vibrational spectra.[161–163,171,236] Surprisingly, the formed light-adapted state which carries these spectra is stable for seconds to minutes.

The biological function of such receptors is highly diverse and still not completely understood. It is known that the protein AppA from the phototropic bacteria *Rhodobacter sphaeroides* regulates the photosynthetic gene expression.[237,238] Another example for this class of receptors are the PAC (*photoactivated adenyl cyclase*) proteins from the flag-

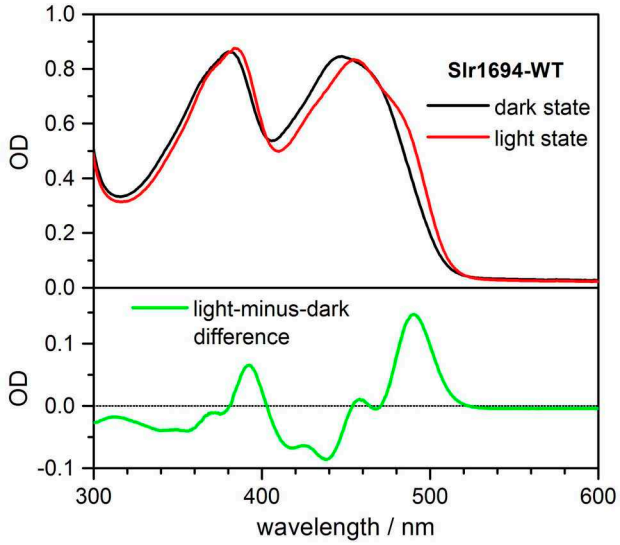

Figure 7.1: Dark- and light-adapted state of the wild-type BLUF photoreceptor Slr1694 (top), and light-minus-dark difference spectrum (bottom). The spectra were kindly provided by Tilo Mathes (see footnote on page 161 for contact details).

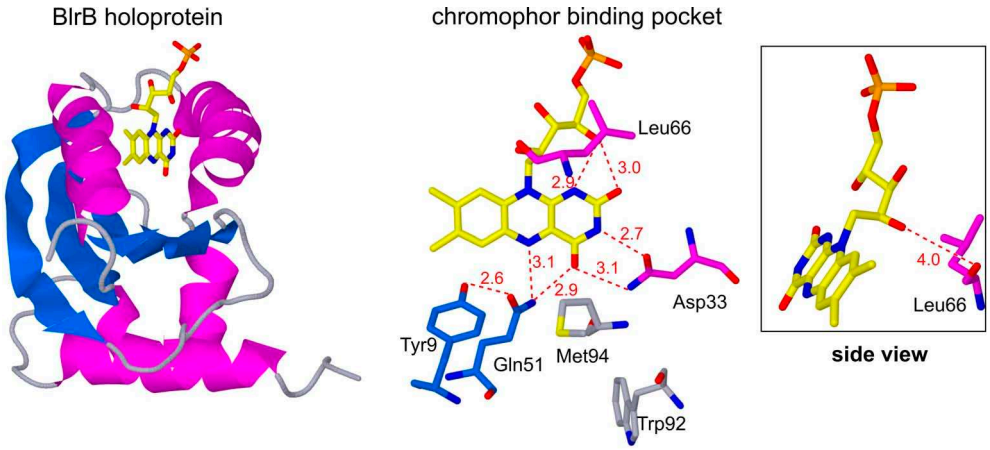

Figure 7.2: The wild-type BlrB photoreceptor. Left: holoprotein. Middle and right: chromophore binding site with the residues around the isoalloxazine ring and leucine 66. Structure from the RCSB protein database, ref. 241.

ella *Euglena gracilis*, which are responsible for a photophobic reaction upon blue-light illumination.[239] Recently also a photoactivated adenyl cyclase from the bacterium *Beggiatoa* was characterized. Another protein, BlrP1 from *Klebsiella pneumoniae* controls motility, virulence and antibiotic resistence in the bacteria.[240]

The protein structure of several BLUF domains was solved by X-ray crystallography.[162,171,240–244] Figures 7.2 and 7.3 show the structures of the holoprotein and the flavin binding site for BlrB from *Rhodobacter sphaeroides* and Slr1694 from the cyanobacterium *Synechocystis* sp. PCC6803.[171,241] These short proteins consist mainly of the BLUF domain itself with a C-terminal extension of unknown function.[171,241] The tertiary structure shows a ferredoxin-like fold, consisting of a five-stranded mixed β-sheet with two parallel α-helices on one side and a helix-turn-helix motif on the other. The flavin is bound noncovalently to two of the α-helices, while the ribityl chain extends to the surface of the protein and the adenosine diphosphate moiety is exposed to the solvent. The adenine is not crucial for the formation of the light-adapted state,[163,241] but it may serve as a recognition site for effector domains of other proteins.[241] The binding site of the isoalloxazine ring is heterogeneous: whereas the dimethyl benzene ring is in a non-polar environment, the pyrimidine part interacts with polar residues and forms several hydrogen bonds with the protein backbone. Involvement in the formation of the signaling state was discussed for the conserved amino acids tyrosin-8, glutamine-50, and the semi-conserved tryptophan-91 (from here on, the notation for Slr1694 is adopted).

The arrangement of the binding site in the dark- and light-adapted state is subject to controversial discussion. For glutamine-50 different orientations were suggested by X-ray and NMR experiments:[243–245] the amino group may be either either hydrogen-bonded to tyrosine-8, or else to the FAD C(4)=O. On this basis it was suggested that

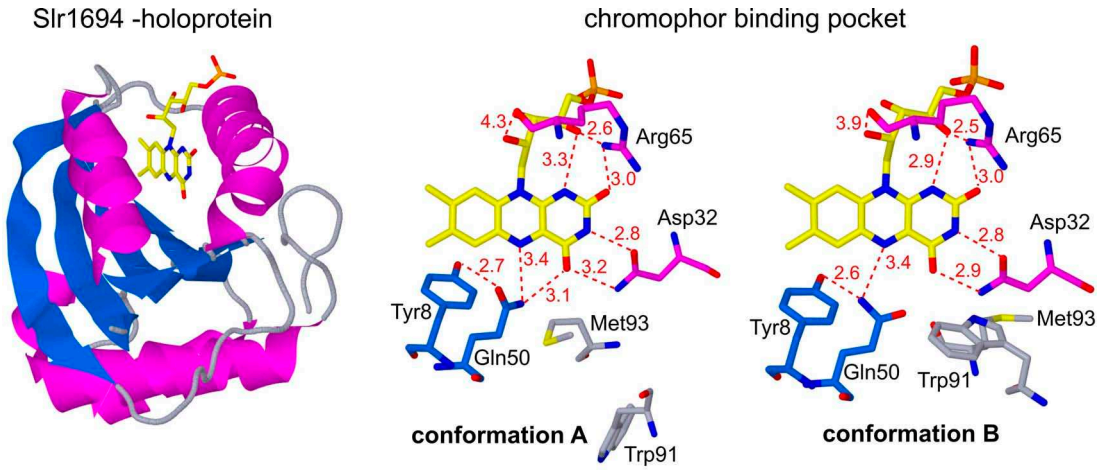

Figure 7.3: The wild-type Slr1694 photoreceptor. Left: holoprotein. Right: two different conformations of the chromophore binding site. The structure was taken from the RCSB protein database, ref. 171.

signaling state formation involves a $\sim 180°$ rotation of the conserved glutamine with a concomitant change of the hydrogen-bond network.[165,243,244] This agrees with results from infrared- and Raman-difference spectroscopy, which found a weakening of the C(4)=O and C(2)=O bonds and a strengthening of the N(1)C(10a) and/or C(4a)N(5) bonds upon formation of the light-adapted state.[161,162,236] Mutation of the glutamine abolishes the ability of the protein to undergo the photocycle.[246]

Tyrosine-8 is another conserved amino acid that is crucial for the formation of the signaling state.[166,236,242,246–249] Early NMR studies on the AppA BLUF domain suggested that an increase of π stacking between the isoalloxazine ring and the conserved tyrosine is responsible for the absorption red-shift.[248] The geometry of the binding site, however, is unfavorable for such interaction,[241,244] and more recent publications explain the role of the tyrosine by its influence on the orientation of glutamine-50 and its ability to act as an electron donor for an intermediate reduction of the flavin chromophore.[165,166,246]

Tryptophan-91 is found in the majority of BLUF domains, but it not essential for signaling state formation. Mutatants, in which Trp-91 is replaced by alanine or phenylalanine, still show the characteristic ~ 10 nm red-shift of the absorption spectrum upon illumination, but with a slightly increased rate for the dark-state recovery.[171,246] As an aromatic amino acid, tryptophan-91 can act as an alternative electron donor for a light-induced reduction of flavin.[166,246] In crystal structures, tryptophan-91 was found in different orientations, see Figure 7.3 (middle and right).[171] It adopted either a solvent-exposed conformation (conformation A), or was buried inside the protein and in contact with FAD (conformation B). The orientation of tryptophan-91 is connected to the position of Methionin-93, which is highly conserved.[249] It was suggested that tryptophan-91 changes its orientation upon formation of the signaling state and acts as a switch that couples the initial glutamine motion to the protein backbone.[166,171,243,250]

Amino acid residues around the ribityl and phosphate chain are not essential for the photocycle. A mutation of leucine-66 in BlrB to phenylalanine (see Figure 7.2), for example, does not impede the formation of the signaling state.[249] Nonetheless, subtle changes of the protein backbone upon mutation lead to a 6× faster return to the dark-adapted form, already within 1.3 s.[249] In this work, the acceleration of dark-state recovery for BlrB-L66F is utilized to avoid accumulation of the light-adapted state during transient absorption measurements. Femtosecond absorption spectroscopy is only sensitive to fast changes around the isoalloxazine ring, so that the measured evolution should not observe effects from the the L66 mutation. The discussed leucine is not conserved among the BLUF domains of different proteins; in Slr1694, for instance, an arginine is found in this position (Arg-65, see Figure 7.3).

The ultrafast evolution upon excitation has been studied for several BLUF photoreceptors by transient absorption, fluorescence, and infrared spectroscopy,[165–169,246,251,252] leading to the following idea about the formation of the BLUF signaling state: The excited chromophore is reduced by electron transfer from the conserved tyrosine within several picoseconds. The generated flavin radical anion ($FAD^{-\bullet}$) is then protonated by tyrosine-8 to the neutral flavin radical ($FADH^{\bullet}$). The concomitant changes in the charge distribution may induce a rotation of glutamine-50. Subsequent hydrogen back-transfer on the 100 ps time scale recovers the oxidized flavin, but embedded into a modified hydrogen-bond network with an $\sim 180^{\circ}$ rotated glutamine. Evidence for the radical intermediates was found for the slr1694 protein[165,167] and several mutants of BLUF domains,[166,246] but they did not accumulate in transient absorption experiments on the AppA protein.[251] A general observation in transient experiments on BLUF domains is the multi-exponential character of the measured dynamics, which has been assigned to a conformational heterogeneity of the chromophore binding site.

The interpretation of previous transient absorption measurements was hampered by two limitations: (i) the sample was excited at 400 nm, thereby populating a mixture of S_1 and the S_2 states. By pumping specifically the $S_1 \leftarrow S_0$ transition, one should be able to reduce the complexity of the measured dynamics. (ii) The spectral window for probing was limited to wavelengths > 400 nm, so that generated intermediates were identified solely by their absorption in the visible, overlapping at early delay times with the stimulated emission. To increase the available information, it is desirable to extend the spectral range to the UV region.

In this work, broadband transient absorption is applied to investigate light-induced changes in the BlrB-L66F mutant over a spectral range from 330 to 1000 nm. Information on the role of the tryptophane-91 as a potential electron donor is obtained from measurements on the Slr1694-Y8F mutant. Selective excitation is assured by using pump pulses at 440–480 nm.

7.2 Experimental Details

7.2.1 Transient Absorption

The transient spectral evolution, presented here, is the average of several measurement runs. Within precision, the transient absorption did not change between consecutive measurements, and product accumulation was not observed.

Transient absorption spectra of BlrB-L66F were recorded with the pump-supercontinuum probe (PSCP) setup based on the CLARK MXR *CPA 2001* laser system. The photoreceptor was excited with 30 fs NOPA pulses at 480 nm (0.5 μJ). Measurements were carried out under parallel polarization conditions. From NMR spectroscopy a rotational correlation time of 8.2 ns was deduced for the monomeric protein,[249] so that the effect of rotational diffusion is considered to be negligible for the present experiment. Replacement of the sample after each shot was assured by circulating the sample through a flow cell. For the presentation in Figure 7.5, spectra up to 5 ps and $>$ 50 ps were smoothed by 50 fs and 11 ps moving averages in time, respectively.

Transient absorption spectra of Slr1694-Y8F were recorded with the pump-supercontinuum probe setup based on the FEMTOLASERS *sPro* laser system. Pump pulses at 440 nm (50 fs fwhm, 0.5 μJ) were obtained by mixing the 800 nm fundamental with the frequency-doubled output of the *TOPAS* parametric amplifier. Measurements were carried under parallel and perpendicular polarization conditions, and the magic angle signal was calculated as $\Delta OD_{ma} = \left(\Delta OD_{||} + 2\Delta OD_{\perp}\right)/3$. The sample was replaced between consecutive laser shots by laterally moving the sample cell by $\sim$ 0.5 cm with an oscillation frequency of 10 Hz, and slowly varying the vertical position of the cell.

7.2.2 Biological Samples

The photoreceptors were provided by Tilo Mathes from the group of Peter Hegemann.[1] BlrB-L66F was dissolved in 10 mM phosphate buffer at pH 8 with additional 10 mM NaCl. Slr1694-Y8F was obtained as a solution of 10 mM Tris buffer at pH 8 with 50 mM NaCl. The samples were measured at optical densities of 0.5–0.8 on a pathlength of 0.5 mm.

7.2.3 Resonance Conditions

In Figure 7.4 ground-state absorption spectra of dark-adapted BlrB-L66F (black) and Slr1694-Y8F (green) in sodium phosphate buffer are compared to FAD in pure water (grey). The first two absorption bands are similar in all samples, but vibrational structure is resolved for the chromophore in protein environment. This suggests that the protein cleft is well-defined, so that inhomogeneous broadening is smaller than in water. The absorption spectrum is slightly blue-shifted for flavin bound to the protein: for

[1] Institute of Biology, Humboldt-Universität zu Berlin, Invalidenstr. 42, 10115 Berlin, Germany.

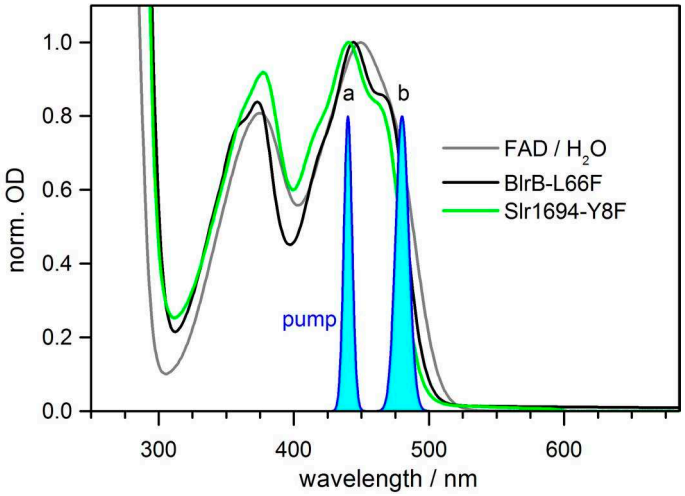

Figure 7.4: Stationary absorption spectra of the BLUF photoreceptors BlrB-L66F (black) and Slr1694-Y8F (green) in phosphate buffer, and of the pure chromophore FAD in de-ionized water. The power spectra of the actinic pump pulses are also shown in blue (a – Slr1694-Y8F measurement, b – BlrB-L66F measurement).

BlrB the first absorption band peaks at 444 nm, for Slr1694-Y8F at 440 nm. The pump pulse spectra are also sketched in blue. BlrB-L66F is excited at 480 nm (b) to the red side of the $S_1 \leftarrow S_0$ absorption band, and Slr1694-Y8F at 440 nm (a), directly in the maximum of the first absorption band. The contribution of $S_2 \leftarrow S_0$ may be considered to be negligible at the chosen pump wavelengths.

7.3 BlrB-L66F: Formation of the Signaling State without Detectable Intermediates

7.3.1 Results

Transient absorption spectra of the BlrB–L66F mutant at different delay times are shown in Figure 7.5 a. Directly after excitation, at 0.2 ps delay (red), the spectrum shows the typical shape of flavin in the S_1 state. Excited state absorption (ESA) is observed at 365 nm with a shoulder at 386 nm, at 512 nm, and at 850 nm. Band positions in the protein resemble those in solution; only the near-infrared band is considerably red-shifted (this band peaks at 780 nm for FAD/H_2O). Below 360 nm the transient absorption signal of BlrB-L66F tails off. This effect is an artefact from reduced UV-light transmission through the prism spectrograph. The bleach of the biological sample reproduces the vibrational structure of the ground-state absorption, indicating that predominantly protein-bound flavin is excited in the measurement. Moreover, the bleach reproduces the spectral position of the first absorption band of the photoreceptor in the dark. This demonstrates that the sample is replaced between successive laser shots, and that the current measurements monitor the photochemical behavior of the dark state alone.

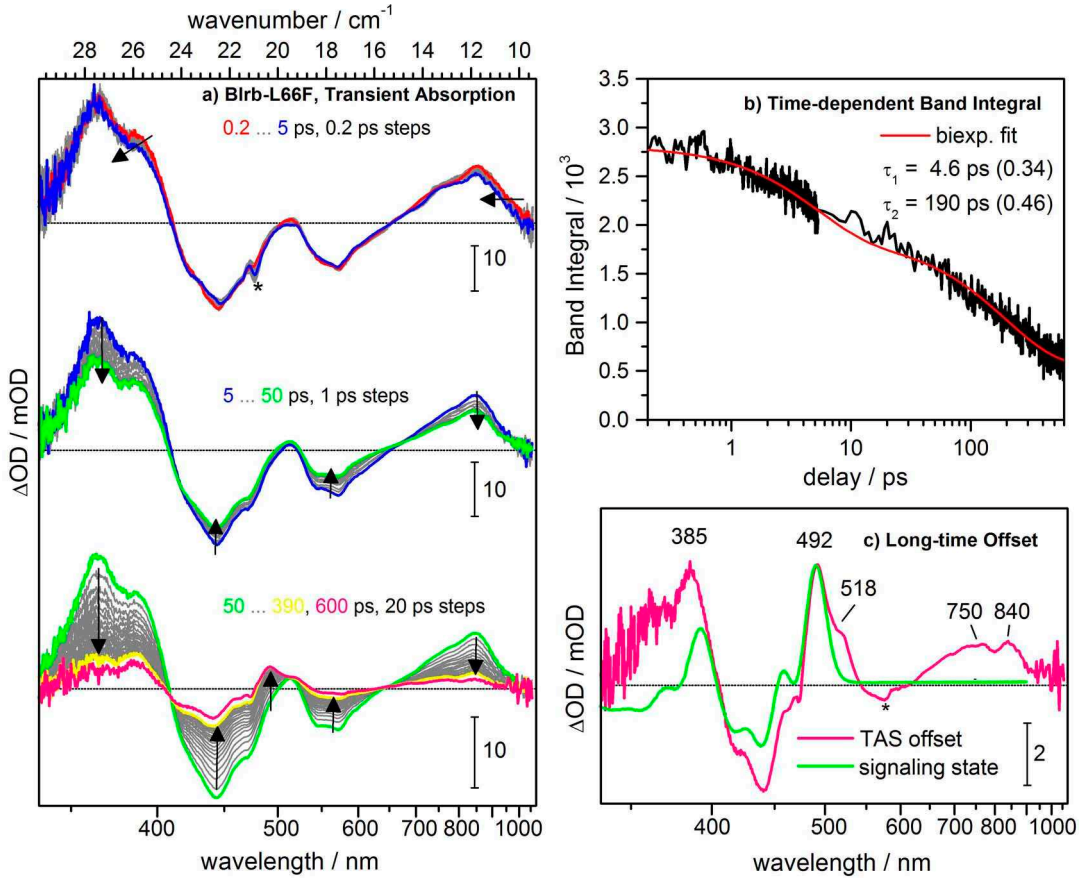

Figure 7.5: Transient absorption on the L66F mutant of the BlrB photoreceptor, upon excitation with 480 nm. a) Transient absorption spectra. The asterisk in the top panel marks spectral residua from pump-pulse stray light. b) Time-dependent band integral over the full transient absorption spectra and bi-exponential fit. c) Long-time offset from a global exponential fit with $\tau_1 = 4$ ps, $\tau_2 = 25$ ps, and $\tau_3 = 190$ ps. The light-minus-dark difference spectrum of the Slr1694 photoreceptor is shown in green for comparison.

Within the first 5 ps, only small variations of the transient spectra are observed. In particular, bleach and stimulated emission do not change on this time scale, suggesting that the population resides in the S_1 state. Nonetheless, a small blue-shift of the near-infrared ESA and subtle changes of the ESA around 400 nm take place. Thereafter, with increasing delay, the transient absorption spectrum decays, and a new band around 492 nm rises, whereas the stimulated emission vanishes almost completely. Most of this evolution takes place until 390 ps (yellow). No intermediate species are apparent in the transient absorption spectra. The stimulated emission band reports on the population in the S_1 state; it would be extinguished by processes like electron transfer. Instead, stimulated emission decays gradually together with the rest of the transient absorption spectrum, evidencing population in the S_1 state over the full time span. The long-

time offset, obtained from global anlysis (see Discussion), is shown in Figure 7.5 c. For comparison, the light-minus-dark difference spectrum of the photoreceptor Slr1694 (wild type) is shown in green.[2] The similarity of the features up to 550 nm indicate formation of the signaling state. The spectrum of the light-adapted state is overlayed by a second spectrum with a broad absorption band around 800 nm and a shoulder at 518 nm, which resembles the triplet spectrum.

The band integral over the full transient-absorption spectra is shown Figure 7.5 b. Decay within the first picoseconds reflects the small spectral changes on this time scale. The positive and negative bands of the transient-absorption spectrum partly compensate upon formation of the band integral. Since the short-time evolution mainly affects ESA bands, it has a pronounced effect on the band integral, leading to a decay of $\sim 30\%$. The subsequent evolution up to 600 ps is seen as a gradual change of the band integral. As the spectral evolution, also the temporal profile does not indicate the formation of intermediate species.

7.3.2 Discussion

Temporal Characterization

The bandintegral trace in Figure 7.5 b is fitted by a bi-exponential decay and a non-decaying offset; the fit is shown as the smooth red line. Time constants of $\tau_1 = 4.6$ ps (34 %) and $\tau_2 = 190$ ps (46 %) were obtained.

The 4.6 ps decay captures the initial blue-shift of the near-infrared ESA and the changes of the ESA around 400 nm. Meanwhile, the bleach stays constant, indicating that population does not return to the ground state. This observation excludes that the evolution is caused by adenine, through quenching of free flavin in solution, which also occurs on the 5–10 ps time scale. It further implicates that the concentration of unbound flavin molecules is negligible in the current measurements. The bleach only indicates the absence of ground state recovery, but does not specify, in which other electronic state the population resides. Such information is given by the stimulated emission: it stays unchanged during initial evolution, thereby showing that the population does not leave the S_1 potential energy surface. It is therefore concluded that the 4.6 ps evolution characterizes a relaxation process of the molecule in the S_1 excited state.

Relaxation in an electronic state can be divided into two categories: vibrational relaxation and dynamic solvation. Intramolecular vibrational redistribution mostly completes already within the first picosecond (see section 4 and refs. 53,113). Vibrational cooling, i.e. the distribution of excess energy to the environment, was shown to take place with 5.5 ps for FAD in solution (see section 6), close to the time constant found here. The band integral,however, should not be sensitive to vibrational relaxation (see Section 2.2.2). In addition, the 475 nm pump beam prepares the system with only little excess

[2] Spectra of the light-adapted state of Slr1694 were provided by Tilo Mathes, see footnote on page 161 for contact details.

energy; considering the results of flavin in solution, one expects that the chromophore is excited only ~ 600 cm^{-1} above the 0-0 transition.

Dynamic solvation is another process that may induce shifts of electronic bands.[128,130] In the case of a photoreceptor, the solvent shell is defined by the chromophore binding site of the protein. Dynamic reorientation upon electronic excitation then corresponds directly to a conformational change of the protein on the way to the signaling state. Depending on the induced motion, the process may take between tens of femtoseconds (O-H rotation) and microseconds (partial protein refolding). Therefore, changes with 4.6 ps are compatible with a reorientation of the protein environment.

The 190 ps decay of the band integral characterizes the formation of the signaling state. Additional exponential terms are not needed to describe the band integral trace, and the spectral evolution does not show any intermediates. Nonetheless, formation of the signaling state requires a return of the population to the ground state with a new conformation of the protein binding site. Electron transfer from aromatic residues was already observed in femtosecond experiments on the Slr1694 BLUF protein,[165,167] and was also used to explain the quenching of free FAD in solution.[184–189] Following this mechanism, the lack of detectable intermediates in the current experiment suggests that for BlrB-L66F, electron transfer to the isoalloxazine ring is the rate-limiting step and takes $\sim$ 190 ps. For the corresponding process in Slr1694 a similar time constant of 180 ps was proposed.[167] In contrast to the results presented here, *Gauden et al.* found for Slr1695 additional evolution on the shorter time scale, which they assigned to different conformations of the protein binding site. For the BlrB-L66F mutant, it is not necessary to assume an effect of conformational heterogeneity. A different situation will be encountered for the Slr1694-Y8F mutant.

A global exponential fit is now performed on time traces at all detection wavelengths. The time constants of 4.6 ps and 190 ps from the band integral analysis were fixed during optimization. For the complete description a third exponential with $\tau = 25$ ps had to be included. As already discussed, a formation of intermediates is neither observed in the transient absorption spectra nor the evolution of the band integral. Instead, the 25 ps time constant describes subtle spectral changes on the way to signaling state. It appears reasonable to assign these effects to a dynamic reorientation of the flavin binding site. Further insights require the application of structure-sensitive methods like femtosecond stimulated Raman spectroscopy.

The long-time offset obtained from the global fit is presented in Figure 7.5 c. It shows the transient signature of the light-adapted state and additional absorption around 800 nm. Together with the shoulder at 518 nm the latter part of the spectrum resembles that of the triplet state, which was reported , for example, by *Kottke et al.* for flavin in the LOV1 domain.[152] There, however the near-infrared band appears more to the blue, with two humps at 648 and 715 nm. Similar differences in band position were found already for S_1 state spectra of free and bound FAD.

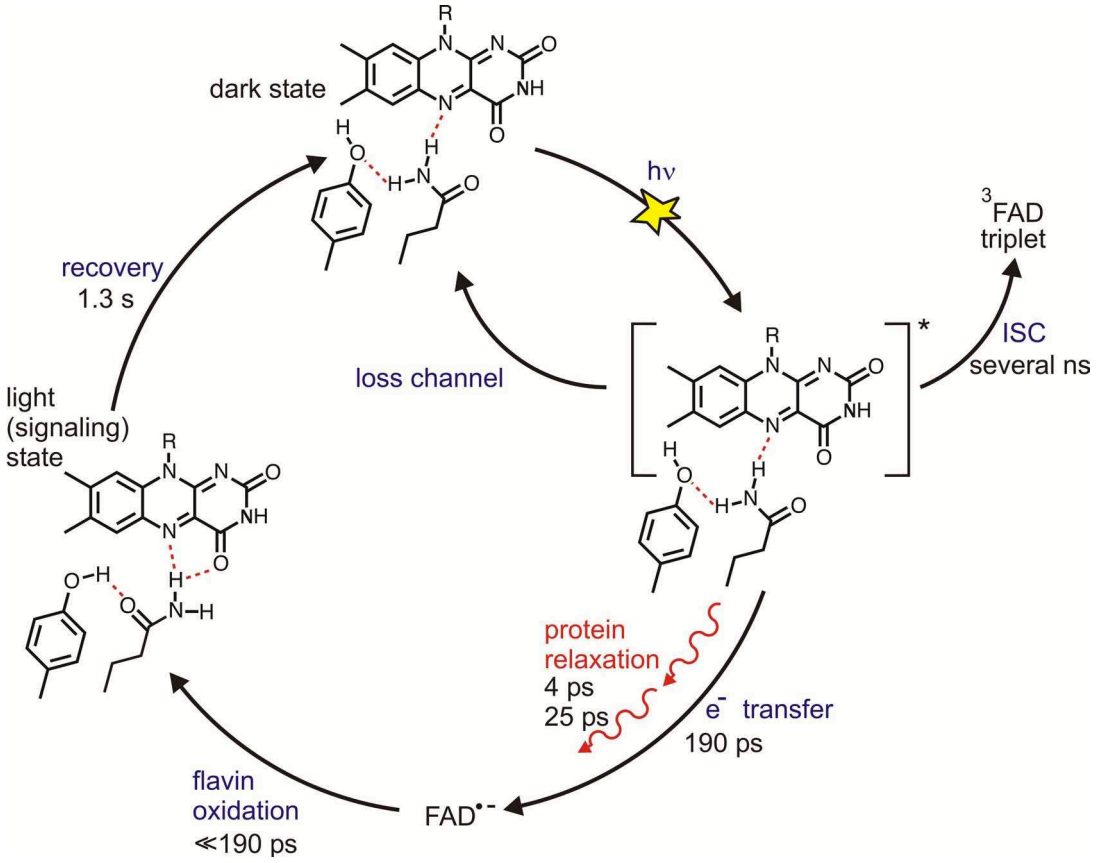

Figure 7.6: Proposed mechanism for the photocycle of BlrB-L66F, as deduced from transient absorption.

Mechanism of the BlrB-L66F Photocycle

A mechanistic picture of the photocycle of the BlrB-L66F mutant is given in Figure 7.6, based on the previous discussion. Illumination at 480 nm promotes the flavin chromophore to the S_1 excited state with ~ 600 cm^{-1} excess energy. The rate-limiting step on the way to the signaling state is electron transfer from an aromatic residue, most probably tyrosine-9, to the isoalloxazine ring. This process occurs with an effective time constant of 190 ps. Additional pathways are the internal conversion to the ground state, which may occur directly or by charge recombination after electron transfer, and inter-system crossing to the triplet state. At this point, a clear separation of these competing processes is not possible. For flavin in solution and in the LOV1 domain, $S_1 \rightarrow S_0$ conversion and formation of the triplet state takes 10–20 ns.[183]

Re-oxidation of FAD$^{\bullet -}$ leads to the formation of the signaling state. The involved reaction steps are faster than the electron transfer, so that intermediates do not accumulate. On the way to the signaling state, additional evolution with 4 and 25 ps describes reorientation of the chromophore binding site. The red-shifted absorption band of the

light state can be explained by changes of the hydrogen bond network, involving, for example, a flip of Gln51. Whereas the largest rearrangements should follow electron transfer, an evolution with 4 and 25 ps may describe the initial response of the protein environment to flavin excitation.

Return of the system from the light to the dark state takes ~ 1.3 s. This process does not require light activation, and the involved reaction steps are still obscure.

7.4 Slr1694-Y8F: Reduction of Flavin by a Tryptophan Residue

7.4.1 Results

Transient Absorption Spectra. Figure 7.7 a shows transient absorption spectra of the BLUF mutant Slr1694-Y8F. Directly after excitation (red) the spectrum has again the typical shape observed for flavin in the S_1 excited state: characteristic excited state absorption bands are seen at 300, 365, and 509 nm, and in the near infrared, peaking outside the spectral range. The bleach and stimulated emission have minima at 440 and 545 nm.

Within the first picoseconds the bleach stays approximately constant (similar to the previous case), indicating that the population does not return to the equilibrated ground state. In contrary, the stimulated emission decays partly on this time scale, accompanied by small changes in the UV < 410 nm. The initial relaxation has only little effect on the positions of the bands. In particular, a dynamic Stokes shift of the stimulated emission band is not apparent.

Following the evolution up to 20 ps, decay of the spectrum over the full detection window is found. From the first view, the evolution appears to be spectrally uniform, but a global analysis in the discussion section will reveal details. Here the attention is directed to the bleach band, which decays as well, a sign for the return of population to the ground electronic state.

Within the next several hundred picoseconds, the decay proceeds, but the spectrum does not approach the baseline. In contrast, in the former stimulated emission region an absorption band rises. Meanwhile, in the UV, the relative contribution of the 365 nm band decreases, so that a band around 388 nm can be distinguished.

On the nanosecond time scale further decay is observed, mainly in the bleach and UV excited state absorption. In the visible, in the region of the S_1 state stimulated emission, only minor changes take place. This shows that the return to the ground state does not occur from the first excited singlet state, but from another state that does not fluoresce. A long-time offset remains with a broad absorption in the visible. The narrow absorption around 490 nm that would indicate signaling state formation (see Figure 7.5, green) is completely absent, in agreement with the inability of the Y8F mutant to undergo the biological photocycle.

The temporal evolution is studied first by performing the band integral over the full transient absorption spectra (295–680 nm); the resulting time trace is shown in Figure 7.7 b. Most clearly visible is a strong signal loss on the 20 ps time scale, followed by a slower decay within the next several hundred picoseconds. Spectral changes within the first picoseconds are not captured by this analysis, because both the UV excited state absorption and the stimulated emission band decrease in amplitude, so that the changes cancel upon integration.

More details are revealed by analyzing different parts of the spectrum separately. Figure 7.7 c compares the evolution of the bleach, represented by the time trace at 440 nm with the band integral over the stimulated emission region, marked by the grey box

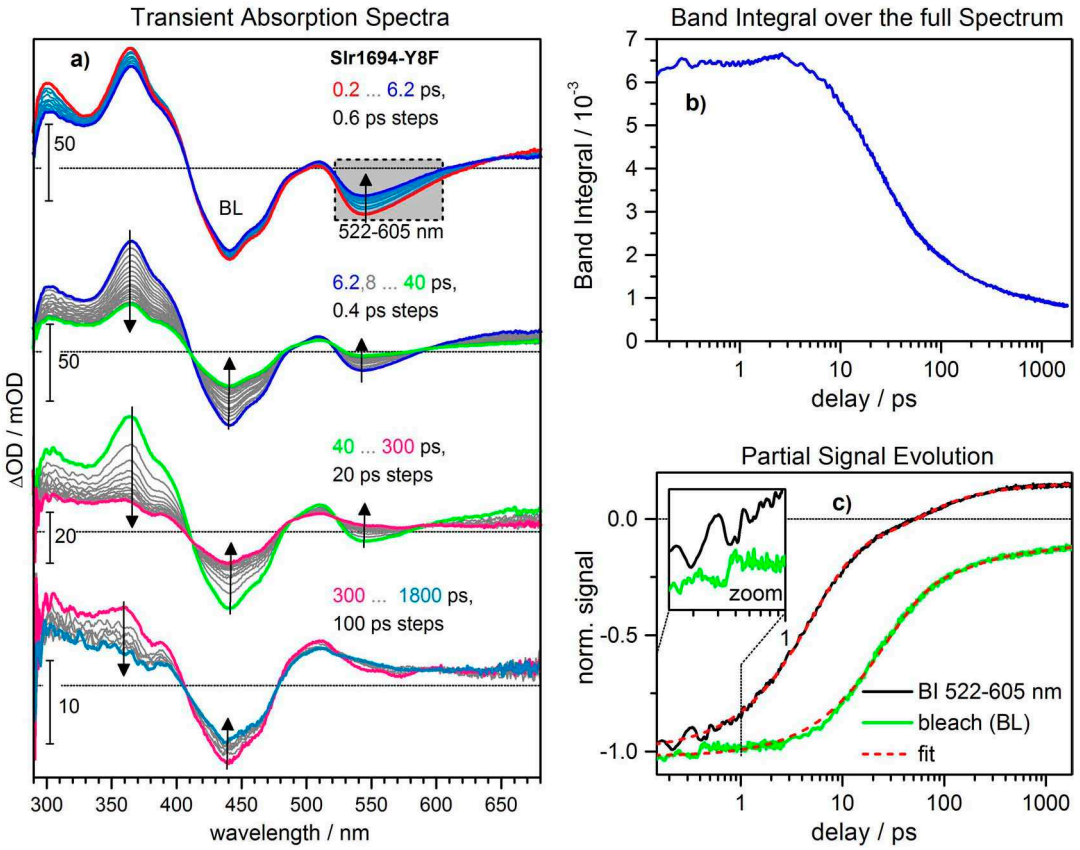

Figure 7.7: Transient absorption of the BLUF mutant Slr1694-Y8F after excitation at 440 nm under magic-angle conditions. a: transient absorption spectra. b: time-dependent band integral over the full spectrum (295–680 nm). c: comparison of the bleach trace at 440 nm and the band integral over the stimulated emission region 522–605 nm (marked grey in panel a).

in Figure 7.7 a (522–605 nm). The difference in the short time behaviour is apparent: whereas the bleach stays initially constant and only decays on the time scale of 20 ps, the stimulated emission band integral changes already within the first picoseconds. After 50 ps, the band integral becomes positive, indicating the rise of excited state absorption in this spectral region. The inset demonstrates also that wavepacket motion is observed in the photoreceptor. Bleach and stimulated emission oscillate 180° out of phase.

7.4.2 Discussion

The temporal evolution is quantified by multi-exponential analysis, and the analysis follows a path towards increasing complexity.

Table 7.1: Results from a multiexponential analysis of transient absorption traces from Slr1694-Y8F,[a] and comparison to results for other photoreceptors.

Slr1694-Y8F		**Slr1694-WT**[b]	**Slr1694-Y8W**[c]	**Blrb-L66F**[d]
bleach	**BI 522–605 nm**			
	4.8 (0.78)	0.9 7	1 11	4.6
25 (0.69)	25 (0.20)	22	76	25
160 (0.16)	160 (0.16)	123		190
2900 (0.08)	2900 (0.01)			
offset (0.07)	offset (-0.15)	offset	offset	offset

[a] time constants are given in ps, with the contribution of corresponding exponential in brackets, [b] from ref. 167, [c] from ref. 246, [d] see Section 7.3.1.

Temporal Characterization

The bleach monitors only the population that returns to the ground state, but it is insensitive to changes in other electronic states. The trace in Figure 7.7 c can be described by the sum of three exponential functions and an offset (dashed red line); time constants of 25, 160, and 2900 ps are obtained. Since the maximum delay is limited by the length of the delay line to 1800 ps, the nanosecond decay is only partly captured, and the associated decay time should be considered an estimate. Multi-exponential photo-dynamics were reported for the Slr1694 photoreceptor before[165,167,246] and assigned to conformational heterogeneity of the flavin binding site. Also here, it appears reasonable to ascribe the three time constants for ground state recovery to subpopulations of excited flavin in slightly different protein environments.

The evolution of the band integral over the stimulated emission region (black in Figure 7.7 c) can only be described by including another exponential. When keeping the time constants from the bleach analysis, a decay time of 4.8 ps is obtained for the additional component. Optimized parameters are summarized in Table 7.1 and compared to results from transient absorption on other photoreceptors.[167,246] Note that multi-exponential analysis is not unique, so that —depending on the noise level— two exponentials may describe in one experiment the same evolution that is characterized in another experiment by a single exponential with an intermediate decay time. In addition, measurements on the Slr1694 wild type (WT) and on the mutant Slr1694-Y8W were recorded with 400 nm excitation. Internal conversion from the S_2 state, which should also be partly excited under these conditions, and vibrational relaxation of the excess energy should contribute to the fast ~ 1 ps time constant in these measurements. With this in mind, the time constants are strikingly similar, suggesting that the different conformations of the flavin binding site are well defined and reflect an inherent ambiguity in the orientation of residues in the chromophore cleft. Note that the spectral evolution associated with the time constants is not unique. In the Blrb-L66F measurements, for example,

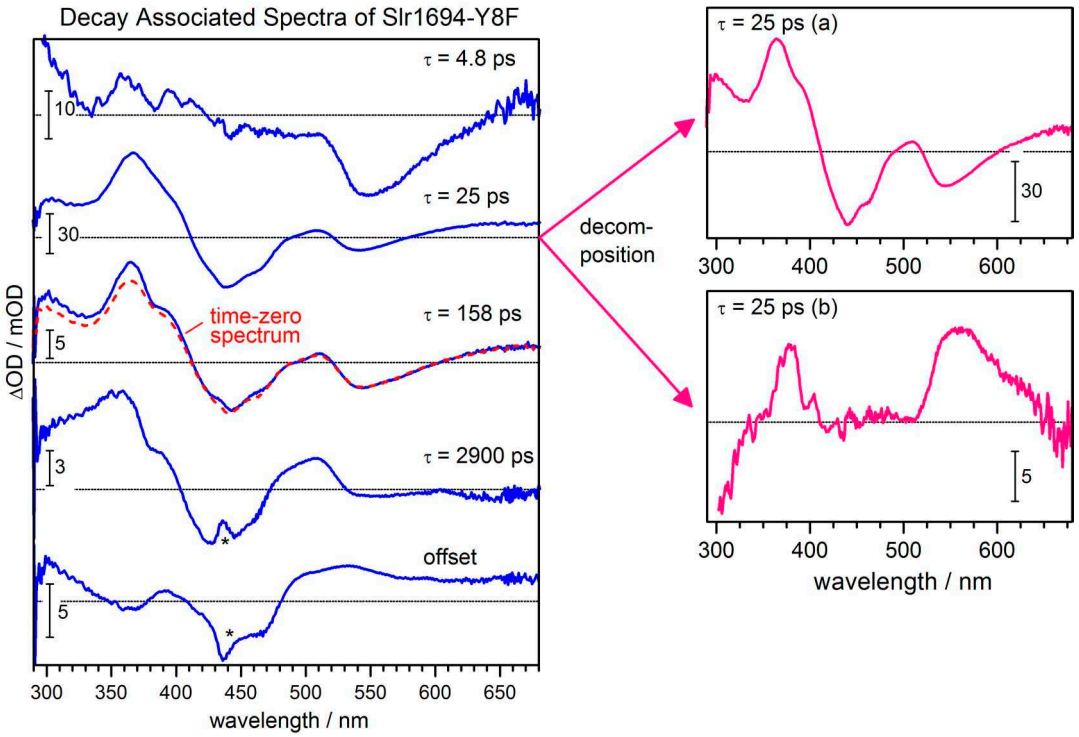

Figure 7.8: Decay associated spectra (DAS) from a multi-exponential global fit of transient absorption on the BLUF mutant Slr1694-Y8F with the time constants from table 7.1. For comparison, the extrapolated time-zero spectrum is shown in panel 3 (dashed red), scaled by a factor of 0.15. The DAS for $\tau = 25$ ps can be devided into the magenta spectra to the right. Artefacts from the scattering of the pump beam are indicated by asterisks.

the stimulated emission does not decay at early delay times. Instead, the 4.6 ps time constant describes subtle spectral changes, probably by solvation through the protein. One may conclude that reaction rates for the photoexcited chromophore are limited by protein dynamics.

Global Analysis and Mechanism

Decay Associated Spectra. A global fit is now performed on the full data set with the parameters from the previous analysis. The obtained decay associated spectra (DAS) are shown in Figure 7.8. As detailed in section 3.6, DAS do not necessarily represent spectra of photochemical intermediates, but report the spectral changes for a given exponential decay. The sum of all DAS is the transient spectrum, extrapolated to zero delay time. When scaling this time-zero spectrum by a factor of 0.15 (dashed red in panel three), it matches almost completely the DAS for $\tau = 160$ ps. This indicates that 15% of the initially excited flavin decays with 160 ps directly to the ground, without forming

detectable intermediates. This part of the population is assigned to one conformer of the photoreceptor (A).

Another extreme is the DAS for $\tau = 2900$ ps: It does not bear any sign of stimulated emission from S_1, but shows nonzero bleach amplitude. This indicates decay to the ground state from an electronic state, which is different from the initially excited S_1 state, *i.e* which corresponds to a photochemical intermediate. Product formation requires the existence of a second, reactive conformer (B).

The early evolution is characterized by the DAS for $\tau = 4.8$ ps. This spectrum has no significant bleach contribution, thus excluding that population flows back to the initial ground state at early times. The rise in the stimulated emission region in Figure 7.7 a is reproduced in the DAS as a negative band around 550 nm. Note that at this point it is not possible to distinguish between the decay of stimulated emission and the rise of a new absorption band. As shown in Section 6, solvation can induce a change of the stimulated emission intensity. However, since the presence of a photochemical intermediate was already confirmed, it appears reasonable to assign the 4.8 ps evolution to the population of a different electronic state of conformer B.

The interpretation of the DAS for $\tau = 25$ ps is more complicated. The shape resembles the spectrum of flavin in the first excited state, but with a decreased amplitude in the stimulated emission region. The analysis of the bleach signal in Figure 7.7 c already lead to the conclusion that a third conformer (C) exists that re-populates the ground state with 25 ps. The spectral appearance obtained here can be understood if one assumes that the 25 ps time constant describes two different processes: the return of excited flavin from S_1 to the ground state S_0, assigned to a conformer (C), and another process that has to be speciefied in the subsequent analysis. On this basis, the DAS can be decomposed into the two spectra shown in Figure 7.8, right. The new DAS labeled by $\tau = 25$ ps (b), is free from bleach signal, *i.e.* describes a process in the excited state manifold (or in a ground state, which differs from the initial S_0 electronic state). The broad absorption band around 560 nm links this process to the component in conformer B that rises with 4.8 ps. This analysis describes two processes with the same time constant. The real values may, of course, be slighty different, but close enough that they are not distinguished by the fit.

Kinetic Model and Species Associated Spectra

The information from the previous analysis can now be combined in the kinetic model for Slr1694-Y8F photochemistry shown in Figure 7.9. Within this model, for each species a transient spectrum is obtained. For the excited chromophore FAD^* three conformations can be distinguished, which are populated with the ratios 15:20:65 (A:B:C). Only B can react further to the intermediate Q1, whereas A and C directly return the ground state S_0 with 160 and 25 ps, respectively. Conversion of B occurs with 4.8 ps and is characterized by a loss of structure in the UV absorption bands and the rise of a broad absorption around 555 nm. With 25 ps this absorption decays, accompanied by spectral changes in the UV. The resulting spectrum for Q2 shows a hump at 386 nm, and a broad shoulder around 352 nm; in the visible a band is seen around 505 nm, which tails

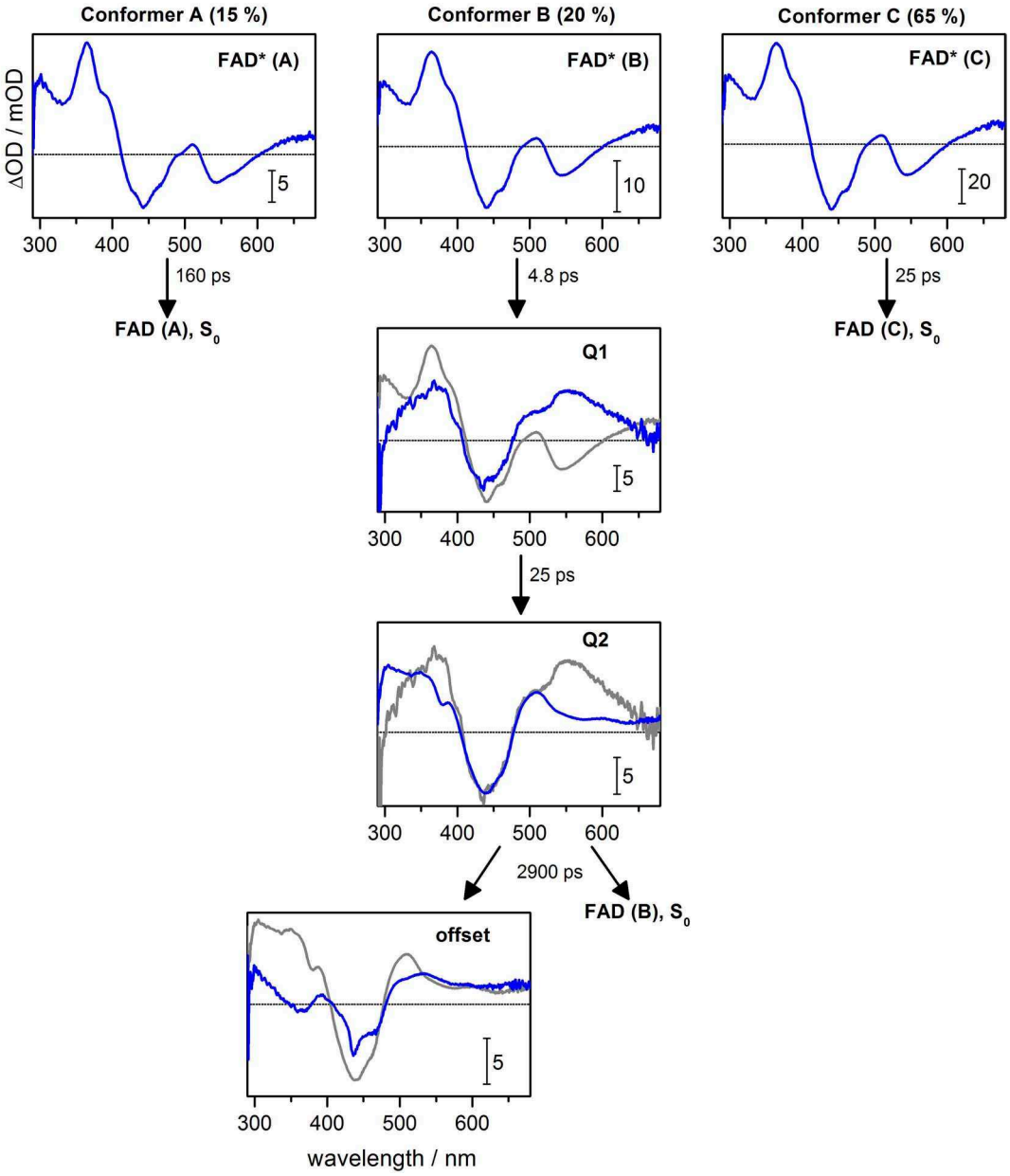

Figure 7.9: Photochemistry of Slr1694-Y8F: mechanism and species associated spectra. Blue spectra correspond to the spectrum of the actual species, the previous spectrum is shown in grey. Conversion times are indicated.

towards the red. The species Q2 decays with 2900 ps. Part of the population returns to the ground state, whereas the rest converts to another species to account for the long-time offset; a similar spectrum was found for the Slr1694-Y8W mutant.[246] The assignment of the offset to the B conformer alone is to some extend arbitrary, since also

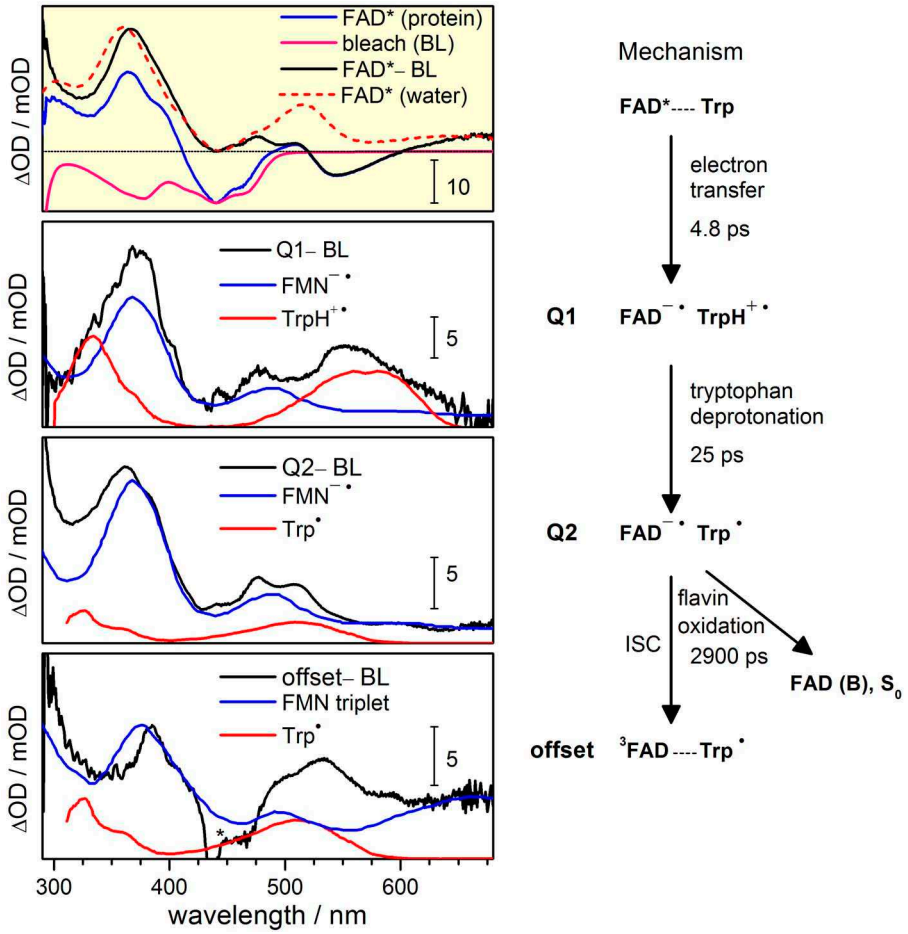

Figure 7.10: Photochemistry of Slr1694-Y8F: mechanism and species associated spectra. Blue spectra correspond to the spectrum of the actual species, the previous spectrum is shown black dashed. Conversion times are indicated.

conformers A and C could form the underlying species in a side reaction. However, it is noted already here that the broad absorption throughout the visble region indicates a contribution of the flavin triplet state to this spectrum; this assignment will be further substantiated below. For flavins, inter-system crossing takes typically several nanoseconds, both in the protein and in solution.[183] This agrees with an effective time constant of 2900 ps found in the current analysis. Since the excited conformers A and C decay significantly faster, their contribution should be small.

Mechanistic conclusions from the proposed model require an assignment of the spectral signatures in the spectra of Figure 7.9. Note that the term "species" collects all absorbing products that contribute to the associated spectrum.

The interpretion of transient absorption spectra is hampered by the superposition of

bleach, excited state absorption, and stimulated emission. In Chapter 6 a procedure was developed to decompose the spectrum into the components. Also here the bleach can be modeled by the scaled ground state absorption spectrum. The decomposition is shown for the FAD* spectrum in the top panel of Figure 7.10. The vibrational structure of the first absorption band is clearly reproduced in the transient absorption signal. The ground state spectrum is scaled to match the minimum at 440 nm (BL, magenta) and subtracted, resulting in the black spectrum (FAD*-BL). It resembles the previously obtained ESA spectrum of unbound FAD in water, extrapolated to zero delay time (dashed red). In the chromophore, the UV absorption band is 6 nm red-shifted, peaking at 367 nm. Also the blue shoulder of the ESA around 515 nm is revealed; the stimulated emission is not subtracted here.

According to the model in Figure 7.9 the intermediates Q1 and Q2 are formed from the initial FAD*(B) without loss of population to the ground state. Hence, the bleach stays constant in this model and can be taken from the decomposition of FAD*(B). Results are shown by the black lines in panels two and three. Since for the step Q1→offset conversion to the ground state appears as a side reaction, the bleach spectrum had to be adjusted again to obtain the corrected offset-spectrum in panel four (black).

The excited absorption of Q1 shows absorption bands at 373 and 480 nm, which match the spectrum of the flavin radical anion $FAD^{-\bullet}$. For comparison the spectrum of the flavin mononucleotide radical anion, $FMN^{-\bullet}$, from the flash photolysis experiments of ref. 253 is shown in blue. The broad absorption around 555 nm could have different origins. The neutral radical $FADH^{\bullet}$, for example, absorbs also in this region. Reduction of flavin to its semiquinone form, however, should leave a residue in the vicinity with electron deficiency, which should show up in the absorption spectrum as well. Indeed, the tryptophan radical cation $TrpH^{+\bullet}$ (red) has a matching absorption spectrum.[254] In the Slr1694 binding pocket, tryptophan-91 could act as a suitable electron donor. Crystal structures indicated different conformers of this amino acid: either buried in the protein, in close proximity to the chromophore, or oriented towards surface of the protein and solvent exposed. The latter arrangement would correspond to conformers A and C and would explain their lack of reactivity.

Upon formation of Q2, mainly the putative $TrpH^{+\bullet}$ band decays (panel three). The resulting spectrum resembles strongly the $FMN^{-\bullet}$ spectrum, confirming the previous assignment to the radical anion. The humps around 500 nm are assigned to vibrational band structure, which becomes stronger in the protein environment.[255] A typical reaction for a tryptophane radical cation is the release of a proton, generating the neutral radical $Trp^{\bullet}$. This species absorbs around 500 nm and below 400 nm, red line in panel three. The excited state absorption of Q2 shows in these regions upward deviation from the semiquinone spectrum, so that a formation of $Trp^{\bullet}$ appears reasonable. However, the effects are small, and additional spectroscopic information should be gathered in future to support this idea.

For the long-time offset, already a contribution of the flavin triplet spectrum was suggested. The corresponding spectrum of FMN in solution[253] agrees with the offset

spectrum below 475 nm[3] and above 600 nm. In between an additional absorption band is present in the species associated spectrum. As before, it could be assigned to a persistent fraction of $Trp^{\bullet}$. On the other hand, both return of $FAD^{-\bullet}$ to the ground state and formation of the triplet state require oxidation, and the question after the electron acceptor arises. This question should be addressed in future experiments.

7.5 Conclusions

The BLUF mutants BlrB-L66F and Slr1694-Y8F were studied by broadband transient absorption spectroscopy with femtosecond resolution. Recorded transient absorption spectra extend from the ultraviolet to the near-infrared spectral region without missing parts around the pump wavelength. Excitation at 440–480 nm assured that the sample is only excited in the first absorption band.

For BlrB-L66F the initial transient spectrum of the S_1 state interconverts without apparent intermediates with 190 ps to the spectrum of the signaling state. On the way, subtle spectral changes occur with 4.6 and 25 ps; they are assigned to a reorientation of the protein binding site.

For the Slr1694-Y8F mutant spectral intermediates are observed. Spectra obtained from a global analysis with a model of sequential interconversion suggest that flavin is reduced to the semiquinone $FAD^{-\bullet}$ by electron transfer from tryptophan-91. Broad visible absorption is assigned to the tryptophan radical cation $TrpH^{+\bullet}$, and its decay with 25 ps indicates deprotonation of $TrpH^{+\bullet}$ on this time scale; meanwhile flavin stays in the radical anion form. The signaling state is not formed by the Y8F mutant of Slr1694. Instead the semiquinone returns to the ground state with an effective time constant of 2900 ps, leaving an offset spectrum, which contains contributions from the triplet and another species, probably the neutral tryptophan radical $Trp^{\bullet}$. Additional exponential evolution with 25 and 160 ps was assigned to direct ground-state recovery in two non-reactive conformations of the protein.

The current results suggest that not only tyrosine-8 but also tryptophan-91 can act as electron donors for flavin reduction. Although not essential for signaling state formation, tryptophan-91 may contribute to the light-induced reactions of the wild-type photoreceptor. The similarity of time constants found in several BLUF domains for different processes could implicate that the rates of photoinduced reactions are controlled by response of the binding site.

The current experiments also demonstrate the limitations of transient absorption spectroscopy for the identification of spectral intermediates. Despite the large spectral range that is covered, assignments are based of only few broad absorption bands. In future, transient Raman spectra would provide a significantly higher information density. Then

[3]Note that the feature marked by an asterik originates from stray light from the pump beam.

intermediates could be identified with high confidence by their vibrational fingerprint. In addition, Raman spectroscopy will also provide details about the structural evolution during signaling state formation.

8 Outlook: Femtosecond Stimulated Raman Spectroscopy of Glucose Oxidase

8.1 Introduction

The previous chapter demonstrated the potential of femtosecond spectroscopy to reveal light-induced reactions in biological photoreceptors. Already in transient absorption measurements the response of the protein environment was seen as subtle spectral changes. Detailed information about the involved processes, like the controverse orientation of glutamine-50 requires structure-sensitive methods. Femtosecond stimulated Raman spectroscopy has not been used to study flavoproteins before, and its principle application will be shown here. The basis for such measurements was developed with the experiments on stilbene, cyanine, and the biologically relevant flavin chromophore, free in solution. Here first experiments on flavin in a protein environment are reported.

As a model compound, the glucose oxidase was chosen, a commercially available glycoprotein that contains noncovalently bound FAD as a cofactor; the crystal structure is

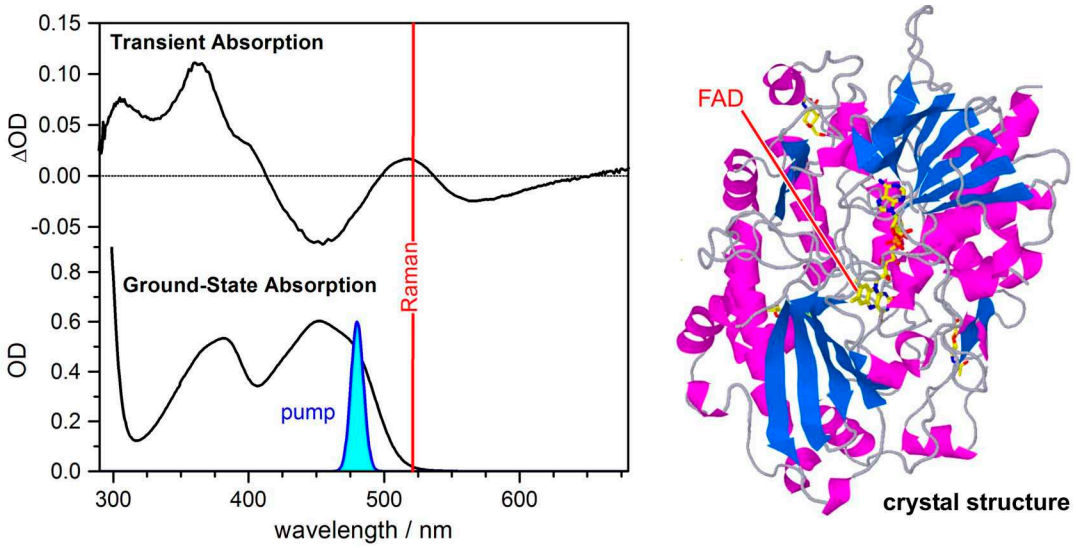

Figure 8.1: Left: Transient absorption (top) of glucose oxidase in citric acid/NaOH buffer (pH 5), 0.2 ps after excitation, and ground-state absorption (bottom) of the sample in a 1 mm cuvette. The actinic pump pulse is shown in blue, the Raman wavelength is marked by the red line. Right: crystal structure of glucose oxidase of *Aspergillus niger* from the RCSB protein database, ref. 256.

shown in Figure 8.1, right.[256] This enzyme binds to β-D-glucose and catalyzes the oxidation by molecular oxygen to glucono-δ-lactone.[257] Although glucose oxidase is naturally not photoactive, its illumination leads to the intermediate reduction of FAD, similar to the processes in flavin-based photoreceptors.[258] Since a proof-of-principle experiment is presented here, the details of the light-induced dynamics are not discussed.

8.2 Experimental Details

Glucose Oxidase from *Aspergillus niger* was purchased as a lyophilized powder from Sigma (type VII-S, 100000–250000 units/g) and used as received. The sample was dissolved in a citric acid/sodium hydroxide buffer at pH 5 (Merck *CertiPur*). The solution had an optical density of 0.3 on an optical path length of 0.5 mm.

Transient Raman Spectroscopy. The sample was excited with 0.4 μJ of 480 nm (30 fs fwhm) pulses from a NOPA. Narrowband Raman pulses around 521 nm (0.5 μJ) were provided by the home-built optical parametric amplifier (see Section 3.5.1); the spectral resolution was 11 cm^{-1}. Experiments were carried out under parallel polarization conditions. To replace the sample after each shot, the containing cell was shaken laterally with an oscillation frequency of 10 Hz and an amplitude of 5 cm; at the same time the cell was slowly moved in vertical direction. For presentation in Figure 8.2, the spectral evolution up to 0.5 ps was filtered by a 66 fs wide moving average in time, and the evolution up to 2.9 ps by a 114 fs moving average.

Transient Absorption Spectra were recorded with the pump-supercontinuum probe setup based on the FEMTOLASERS *sPro* laser system. The sample was excited with 440 nm pulses (50 fs fwhm, 0.5 μJ), which were obtained by mixing the 800 nm fundamental with the frequency-doubled output of the *TOPAS* parametric amplifier. The measurement was carried out under parallel polarization conditions. Sample replacement was achieved by the same moving cell as in the transient Raman experiment.

8.3 Results

The resonance conditions were already shown in Figure 8.1. The Raman beam overlaps at 521 nm with excited state absorption and stimulated emission, but is also preresonant with the ground-state absorption. Under similar conditions, induced Raman spectra were studied for the unbound chromophore in solution, see Chapter 6. There a complicated signal was observed, which was dominated by absorptive bands at the ground state frequencies, but contained also emissive and dispersive contributions.

Femtosecond stimulated Raman spectra from glucose oxidase are presented in Figure 8.2, top. At delay times > 0.5 ps the spectral shape resembles that of flavin in solution. A comparison with the ground-state stimulated Raman spectrum in Figure 8.2 shows that also here negative Raman signals occur at the ground state frequencies.

At earliest delay times (red spectrum), the signal is stronger and has a dispersive shape, *i.e.* inflection points are seen at the positions of the subsequently evolving Raman bands.

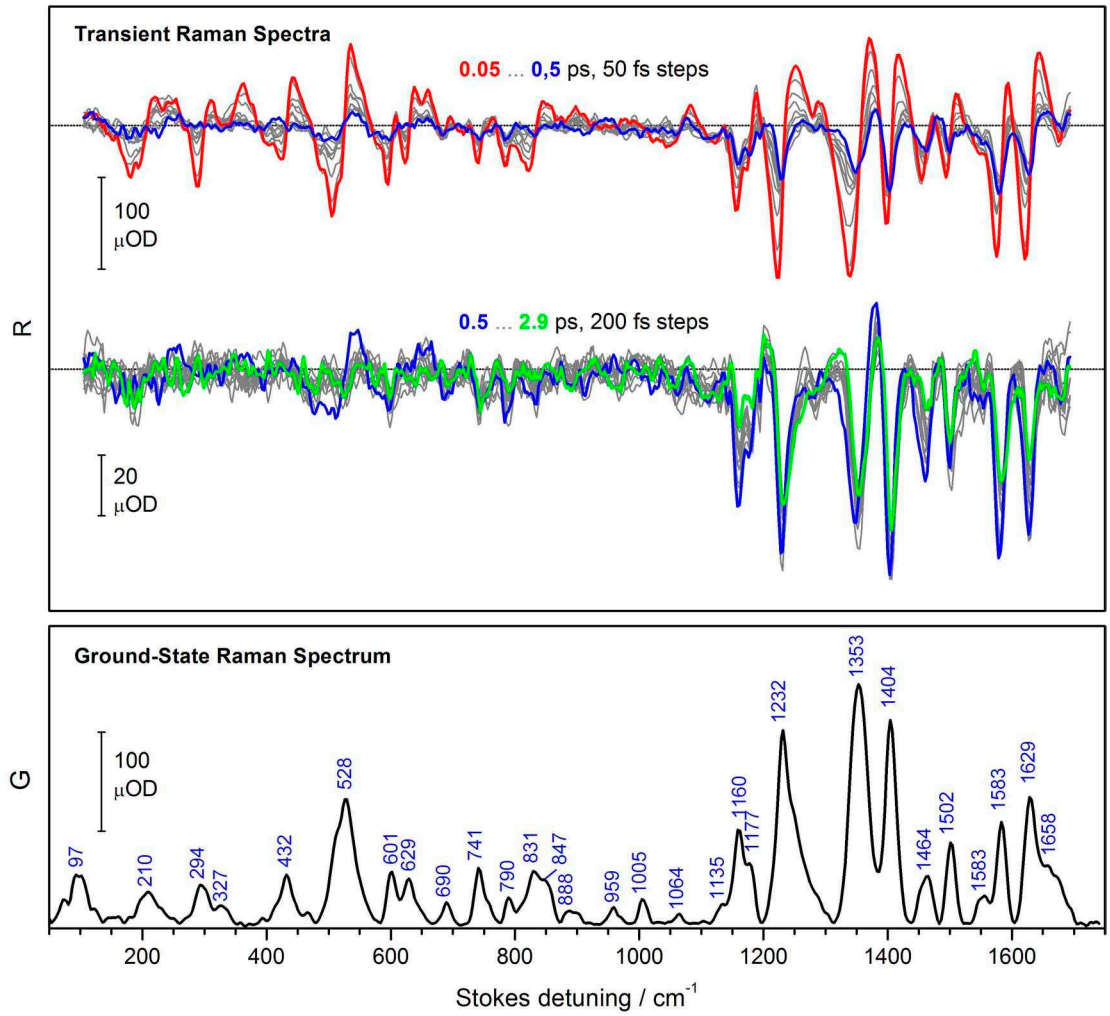

Figure 8.2: Stimulated Raman spectroscopy on Glucose Oxidase from *Aspergillus Niger*. Top: transient Raman spectra. Bottom: ground-state Raman spectrum. The sample was actinically excited at 480 nm, and the Raman pulse was tuned to 521 nm.

Within 500 fs the shape of the later spectra developes; this change is accompanied by a decrease in signal amplitude. The ultrafast evolution could reflect molecular relaxation at earliest times. But it is also possible that it originates from a fifth-order coherent contribution, when all three pulses (pump, Raman, and probe) overlap in time. Finally also population depletion by the Raman pulse should be considered, even though one would expect a signal change induced by this process rather on the 0.5–1 ps time scale. On account of the complicated signal, the discussion is not detailed further at this point.

In summary, the current results demonstrate that the Raman spectrometer developed in this work can be used to investigate biological samples. Resolved spectra were obtained

for the bound flavin chromophore in the ground and and excited state, and the temporal evolution of the spectra could be traced. Following the conclusions from Chapter 6, future measurements with Raman pulses around 780 nm should yield simpler spectra, which can be directly compared to quantum-chemical calculations. Measurements on BLUF photoreceptors should be possible without further complications. In fact, the Slr1694-Y8F sample was more stable during transient measurements than glucose oxidase under the current conditions.

9 Conclusions

The key achievement of this work was the development of a wavelength-tunable stimulated Raman spectrometer with femtosecond temporal resolution. The technique was used to study photoinduced relaxation processes in real time, by monitoring vibrational modes in the electronic excited state. In this way the method was advanced towards its application to biological photoreceptors.

Raman pulses were generated with high efficiency in a new narrowband optical parametric amplifier (*nb*-OPA). Output pulses are tunable throughout the visible. Although not shown here, it should also be possible to generate near-infrared pulses down to $\sim$ 1200 nm with this device. Raman spectra in the ground and excited state were recorded with 7.5–15 cm^{-1} spectral and 50–100 fs temporal resolution. In each individual measurement, transient spectra were obtained at up to 660 different delay times. To allow a detailed analysis of the measured evolution, an algorithm was developed to remove the background for all transient spectra of a dataset consistently.

A strong dependence of the stimulated Raman spectrum on the resonance conditions was found. To understand experimentally observed band shapes, the Raman signal was described by third-order perturbation theory and simulated for typical conditions.[1] The results indicate that the spectrum is best defined if the Raman pulse is only resonant with excited-state absorption. Then a direct comparison to calculated spectra is possible. A bleach signal from overlap with the $S_1 \leftarrow S_0$ transition can be subtracted and analyzed separately as shown in measurements on 1,1'-diethyl-2,2'-pyrido cyanine iodide, see below. Overlap with the stimulated emission, however, should be avoided, since it causes complex bandshapes that could not be decomposed in the current work.

Relaxation processes in the excited state were first studied for the photoswitch stilbene, starting from both the *cis* and the *trans* isomers. Intitial shift and decay of the Raman bands with 0.2–0.7 ps was interpreted in terms of intramolecular vibrational redistribution (IVR) and dynamic polar solvation. The subsequent dissipation of excess energy to the solvent was also seen as a frequency up-shift and narrowing of characteristic bands. Oscillations of Raman frequencies and amplitudes directly reported on the motion of wavepackets in the excited state. Anharmonic coupling was seen as a modulation of high-frequency bands with < 100 cm^{-1} by phenyl/ethylene torsion modes.

Transition over the isomerization barrier and internal conversion to the hot ground state was observed for a "parent" cyanine, 1,1'-diethyl-2,2'-pyrido cyanine iodide (PC).

[1] this part was supported Alexander Dobryakov.

From global analysis, Raman spectra were obtained for the Franck-Condon region, the intermediately populated hot ground state, and the two isomerization products *cis*- and *trans*-PC. Transient aborption and fluorescence upconversion experiments[2] in combination with quantum-chemical calculations[3] suggests a stepwise distortion of the excited chromophore.

Flavin is a cofactor in a number of photoreceptors. Flavin derivatives were first studied in solution, and the influence of different solvent environments was investigated by transient absorption and fluorescence upconversion measurements. A decomposition procedure for the transient absorption signal was shown. The experiments find a rise of the stimulated emission band in DMSO for excitation with excess energy. As an explanation, coupling of the $\pi\pi^*$ state to a nearby $n\pi^*$ state is suggested.

Raman spectra are reported for the ground and excited states; they are assigned with the help of quantum-chemical calculations[4]. The long-time evolution of the Raman signal reproduces the results from transient absorption and fluorescence. At short delay times, also for flavin wavepacket motion can be seen as oscillation of the transient Raman signal. Within the first picoseconds additional signal decay is observed, which is attributed to population depletion by the Raman pulse. This effect should be taken into account in future resonance Raman experiments.

As an application for Raman depletion, a new method is presented to mark vibrational wavepackets in the excited state.

BLUF photoreceptors contain the flavin chromophore in a non-covalently bound form. Here the mutants BlrB-L66F and Slr1694-Y8F were studied by transient absorption spectroscopy. BlrB-L66F forms the signaling state without detectable intermediates. Small spectral changes suggest a reorientation of the protein. Slr1694-Y8F does not undergo the photocycle, but —based on a global analysis— an intermediate reduction of FAD by a semi-conserved tryptophan is proposed.

Finally it is demonstrated that the developed femtosecond stimulated Raman spectrometer can also be used to study biological samples. Glucose oxidase served as a model compound, for which an ultrafast evolution of the transient Raman spectra could be resolved. In future, I expect that with this technique detailed insights can be obtained in light-induced conformational changes of proteins, for example BLUF domains.

[2]recorded by Mohsen Sajadi.
[3]provided by Fabrizio Santoro, Roberto Improta, and Vincenzo Barone.
[4]provided by Bastian Klaumünzer.

Bibliography

[1] H. Zewail. Femtochemistry: Atomic-scale dynamics of the chemical bond using ultrafast lasers (nobel lecture). *Angew. Chem. Int. Ed.*, 39:2586–2631, 2000.

[2] J. Assmann, M. Kling, and B. Abel. Watching photoinduced chemistry and molecular energy flow in solution in real time. *Angew. Chem. –Intern. Ed.*, 42:2226–2246, 2003.

[3] V. Sundström. Femtobiology. *Ann. Rev. Phys. Chem.*, 59:53–77, 2008.

[4] R. Berera, R. van Grondelle, and J. T. M. Kennis. Ultrafast transient absorption spectroscopy: Principles and application to photosynthetic systems. *Photosynth. Res.*, 101:105–118, 2009.

[5] M. Chergui and A. H. Zewail. Electron and x-ray methods of ultrafast structural dynamics: advances and applications. *ChemPhysChem*, 10:28–43, 2009.

[6] E. T. J. Nibbering, H. Fidder, and E. Pines. Ultrafast chemistry: Using time-resolved vibrational spectroscopy for interrogation of structural dynamics. *Ann. Rev. Phys. Chem.*, 56:337–3367, 2005.

[7] P. Kukura, D. W. McCamant, and R. A. Mathies. Femtosecond stimulated raman spectroscopy. *Ann. Rev. Phys. Cem.*, 58:461–488, 2007.

[8] M. Yoshizawa and M. Kurosawa. Femtosecond time-resolved raman spectroscopy using stimulated raman scattering. *Phys. Rev. A*, 61:013808, 1999.

[9] U. Brackmann. *Lambdachrome Laser Dyes*. Lambda Physik, Göttingen, Germany, 2nd edition, 1994.

[10] D. W. McCamant, P. Kukura, and R. A. Mathies. Femtosecond time-resolved stimulated raman spectroscopy: Application to the ultrafast internal conversion in β-carotene. *J. Phys. Chem. A*, 107:8208–8214, 2003.

[11] N. J. Miller, J. Sampson, L. P. Candeias, P. M. Bramley, and C. A. RiceEvans. Antioxidant activities of carotenes and xanthophylls. *FEBS Lett.*, 384:240–242, 1996.

[12] P. Kukura, D. W. McCamant, S. Yoon, D. B. Wandschneider, and R. A. Mathies. Structural observation of the primary isomerization in vision with femtosecond-stimulated raman. *Science*, 310:1006–1009, 2005.

[13] S. Bhattacharya, K. D. Ridge, B. E. Knox, and H. G. Khorana. Light-stable rhodopsin, 1. a rhodopsin analog reconstituted with a nonisomerizable 11-*cis* retinal derivative. *J. Biol. Chem.*, 267:6763–6769, 1992.

[14] D. W. McCamant, P. Kukura, and R. A. Mathies. Femtosecond stimulated raman study of excited-state evolution in bacteriorhodopsin. *J. Phys. Chem. B*, 109: 10449–10457, 2005.

[15] H. I. A. Mostafa. Effect of beta-particles on the retinal chromophore in bacteriorhodopsin of halobacterium salinarium. *Rad. Meas.*, 38:217–225, 2004.

[16] S. Laimgruber, H. Schachenmayr, B. Schmidt, W. Zinth, and P. Gilch. A femtosecond stimulated raman spectrograph for the near ultraviolet. *Appl. Phys. B*, 85:557–564, 2006.

[17] V. Leyva, I. Corral, T. Schmierer, B. Heinz, F. Feixas, A. Migani, L. Blancafort, P. Gilch, and L. Gonzalez. Electronic states of o-nitrobenzaldehyde: A combined experimental and theoretical study. *J. Phys. Chem. A*, 112:5046–5053, 2008.

[18] P. Kukura, R. Frontiera, and R. A. Mathies. Direct observation of anharmonic coupling in the time domain with femtosecond stimulated raman scattering. *Phys. Rev. Lett.*, 96:238303, 2006.

[19] S. Shim and R. A. Mathies. Development of a tunable femtosecond stimulated raman apparatus and its application to β-carotene. *J. Phys. Chem. B*, 112:4826–4832, 2008.

[20] R. R. Frontiera, S. Shim, and R. A. Mathies. Origin of negative and dispersive features in anti-stokes and resonance femtosecond stimulated raman spectroscopy. *J. Chem. Phys.*, 129:064507, 2008.

[21] J. Dasgupta, R. R. Frontiera, K. C. Taylor, J. C. Lagarias, and R. A. Mathies. Ultrafast excited-state isomerization in phytochrome revealed by femtosecond stimulated raman spectroscopy. *P. Natl. Acad. Sci. USA*, 106:1784–1789, 2009.

[22] T. Lamparter, B. Esteban, and J. Hughes. Phytochrome cph1 from the cyanobacterium synechocystis pcc6803 — purification, assembly, and quaternary structure. *Eur. J. Biochem.*, 268:4720–4730, 2001.

[23] C. Fang, R. R. Frontiera, R. Tran, and R. A. Mathies. Mapping gfp structure evolution during proton transfer with femtosecond raman spectroscopy. *Nature*, 462:200–204, 2009. ISSN 0028-0836.

[24] S. R. McRae, C. L. Brown, and G. R. Bushell. Rapid purification of egfp, eyfp, and ecfp with high yield and purity. *Prot. Expr. Pur.*, 41:121–127, 2005.

[25] T. Schmierer, S. Laimgruber, K. Haiser, K. Kiewisch, J. Neugebauer, and P. Gilch. Femtosecond spectroscopy on the photochemistry of *o*-nitrotoluene. *Phys. Chem. Chem. Phys.*, 12:15653–64, 2010.

[26] R. K. Bansal. *Synthetic Approaches in Organic Chemistry.* Jones & Bartlett Publishers, Stadbury, 1st edition, 1997.

[27] G. S. Levinson, W. T. Simpson, and W. Curtis. Electronic spectra of pyridocyanine dyes with assignments of transitions. *J. Am. Chem. Soc.*, 79:4314–4320, 1957.

[28] S. K. Chapman and G. A. Reid, editors. *Flavoprotein Protocols (Methods in Molecular Biology)*, volume 131. Humana Press, Totowa, New Jersey, 1999.

[29] J. L. Johnson, R. E. London, and K. V. Rajagopalan. Covalently bound phosphate residues in bovine milk xanthine oxidase and in glucose oxidase from aspergillus niger — a reevaluation. *P. Natl. Acad. Sci. USA*, 86:6493–6497, 1989.

[30] S. Mukamel. *Principles of Nonlinear Optical Spectroscopy.* Oxford University Press, New York, 1995.

[31] Y. J. Yan and S. Mukamel. Femtosecond pump-probe spectroscopy of polyatomic molecules in condensed phases. *Phys. Rev. A*, 41:6485–6504, 1990.

[32] S. Mukamel. Femtosecond optical spectroscopy — a direct look at elementary chemical events. *Ann. Rev. Phys. Chem.*, 41:647–681, 1990.

[33] R. F. Loring, Y. Y. Yan, and S. Mukamel. Time-resolved and frequency-resolved fluorescence line-shapes as a probe of solvation dynamics. *Chem. Phys. Lett.*, 135: 23–29, 1987.

[34] Y. J. Yan, L. E. Fried, and S. Mukamel. Ultrafast pump-probe spectroscopy — femtosecond dynamics in liouville space. *J. Phys. Chem.*, 93:8149–8162, 1989.

[35] S. A. Kovalenko, A. L. Dobryakov, J. Ruthmann, and N. P. Ernsting. Femtosecond spectroscopy of condensed phases with chirped supercontinuum probing. *Phys. Rev. A*, 59:2369–2384, 1999.

[36] A. L. Dobryakov, S. A. Kovalenko, and N. P. Ernsting. Electronic and vibrational coherence effects in broadband transient absorption spectroscopy with chirped supercontinuum probing. *J. Chem. Phys.*, 119:988–1002, 2003.

[37] A. L. Dobryakov, S. A. Kovalenko, and N. P. Ernsting. Coherent and sequential contributions to femtosecond transient absorption spectra of a rhodamine dye in solution. *J. Chem. Phys.*, 123:044502, 2005.

[38] A. L. Dobryakov, N. P. Ernsting, W. Galewa, C. Bressler, and M. Chergui. *Analysis and Control of Ultrafast Photoinduced Reactions, Springer Series in Chemical Physics.* Springer, Heidelberg, 2007.

[39] A. L. Dobryakov, J. L. P. Lustres, S. A. Kovalenko, and N. P. Ernsting. Femtosecond transient absorption with chirped pump and supercontinuum probe: Perturbative calculation of transient spectra with general lineshape functions, and simplifications. *Chem. Phys.*, 347:127–138, 2008.

[40] A.L. Dobryakov and N.P. Ernsting. Lineshapes for resonant impulsive stimulated raman scattering with chirped pump and supercontinuum probe pulses. *J. Chem. Phys.*, 129:184504, 2008.

[41] Z. G. Sun, J. Lu, D. H. Zhang, and S. Y. Lee. Quantum theory of (femtosecond) time-resolved stimulated raman scattering. *J. Chem. Phys.*, 128:144114, 2008.

[42] Z. Sun, X. Q. Qiu, J. Lu, D. H. Zhang, and S. Y. Lee. Three-state model for femtosecond broadband stimulated raman scattering. *J. Raman Spectrosc.*, 39: 1568–1577, 2008.

[43] Z. G. Sun, Z. Q. Jin, J. Lu, D. H. Zhang, and S. Y. Lee. Wave packet theory of dynamic stimulated raman spectra in femtosecond pump-probe spectroscopy. *J. Chem. Phys.*, 126:174104, 2007.

[44] S. Yoon, D. W. McCamant, P. Kukura, and R. A. Mathies. Dependence of line shapes in femtosecond broadband stimulated raman spectroscopy on pump-probe time delay. *J. Chem. Phys.*, 122:024505, 2005.

[45] S.-Y. Lee, D. Zhang, D. W. McCamant, P. Kukura, and R. A. Mathies. Theory of femtosecond stimulated raman spectroscopy. *J. Chem. Phys.*, 121:3632–3642, 2004.

[46] K. Niu, S. L. Cong, and S. Y. Lee. Femtosecond stimulated raman scattering for polyatomics with harmonic potentials: Application to rhodamine 6g. *J. Chem. Phys.*, 131:054311, 2009.

[47] V. I. Claessen, H. Engelkamp, P. C. M. Christianen, J. C. Maan, R. J. M. Nolte, K. Blank, and A. E. Rowan. Single-biomolecule kinetics: The art of studying a single enzyme. *Ann. Rev. Anal. Chem.*, 3:319–340, 2010.

[48] Philipp Kukura, Michele Celebrano, Alois Renn, and Vahid Sandoghdar. Single-molecule sensitivity in optical absorption at room temperature. *J. Phys. Chem. Lett.*, 1:3323–3327, 2010.

[49] S. Chong, W. Min, and X. S. Xie. Ground-state depletion microscopy: Detection sensitivity of single-molecule optical absorption at room temperature. *J. Phys. Chem. Lett.*, 1:3316–3322, 2010.

[50] A. Gaiduk, M. Yorulmaz, P. V. Ruijgrok, and M. Orrit. Room-temperature detection of a single molecule's absorption by photothermal contrast. *Science*, 330: 353–356, 2010.

[51] D. P. Craig and T. Thirunamachandran. *Molecular Quantum Electrodynamics.* Dover Publications, Inc., New York, 1984.

[52] N. Mataga and T. Kubota. *Molecular Interactions and Electronic Spectra.* Marcel Dekker, Inc., New York, 1970.

[53] S. A. Kovalenko, R. Schanz, H. Hennig, and N. P. Ernsting. Cooling dynamics of an optically excited molecular probe in solution from femtosecond broadband transient absorption spectroscopy. *J. Chem. Phys.*, 115:3256–3273, 2001.

[54] P. Hamm. Coherent effects in femtosecond infrared-spectroscopy. *Chem. Phys.*, 200:415–429, 1995.

[55] M. Chachisvilis, H. Fidder, and V. Sundstrom. Electronic coherence in pseudo-2-color pump-probe spectroscopy. *Chem. Phys. Lett.*, 234:141–150, 1995.

[56] M.B. Birks. *Photophysics of aromatic molecules.* Wiley-Interscience, 1970.

[57] W. H. Melhuish. Quantum efficiencies of fluorescence of organic substances — effect of solvent and concentration of fluorescent solute. *J. Phys. Chem.*, 65:229–235, 1961.

[58] T. Karstens and K. Kobs. Rhodamine b and rhodamine 101 as reference substances for fluorescence quantum yield measurements. *J. Phys. Chem.*, 84:1871–1872, 1980.

[59] P. F. Moulton. Spectroscopic and laser characteristics of ti:al_2o_3. *J. Opt. Soc. Am. B*, 3:125–133, 1986.

[60] Claude Rullière, editor. *Femtosecond Laser Pulses -Principles and Experiments.* Springer Science+Business Media, Inc., 2. edition, 2005.

[61] M. Ziolek, R. Naskrecki, and J. Karolczak. Some temporal and spectral properties of femtosecond supercontinuum important in pump-probe spectroscopy. *Opt. Commun.*, 241:221–229, 2004.

[62] L. J. Zhao, J. L. P. Lustres, V. Farztdinov, and N. P. Ernsting. Femtosecond fluorescence spectroscopy by upconversion with tilted gate pulses. *Phys. Chem. Chem. Phys.*, 7:1716–1725, 2005.

[63] M. Sajadi, T. Obernhuber, S. A. Kovalenko, M. Mosquera, B. Dick, and N. P. Ernsting. Dynamic polar solvation is reported by fluorescing 4-aminophthalimide faithfully despite h-bonding. *J. Phys. Chem. A*, 113:44–55, 2009.

[64] M. Sajadi, A. L. Dobryakov, E. Garbin, N. P. Ernsting, and S. A. Kovalenko. Time-resolved fluorescence spectra of cis-stilbene in hexane and acetonitrile. *Chem. Phys. Lett.*, 489:44–47, 2010.

[65] D. Polli, L. Luer, and G. Cerullo. High-time-resolution pump-probe system with broadband detection for the study of time-domain vibrational dynamics. *Rev. Sci. Instr.*, 78:103108, 2007.

[66] U. Megerle, I. Pugliesi, C. Schriever, C. F. Sailer, and E. Riedle. Sub-50 fs broadband absorption spectroscopy with tunable excitation: putting the analysis of ultrafast molecular dynamics on solid ground. *Appl. Phys. B-Lasers O.*, 96:215–231, 2009.

[67] C. Schriever, S. Lochbrunner, E. Riedle, and D. J. Nesbitt. Ultrasensitive ultraviolet-visible 20 fs absorption spectroscopy of low vapor pressure molecules in the gas phase. *Rev. Sci. Instr.*, 79:013107, 2008.

[68] A. L. Dobryakov, S. A. Kovalenko, A. Weigel, J. L. Perez-Lustres, J. Lange, A. Müller, and N. P. Ernsting. Femtosecond pump-supercontinuum-probe (pscp) spectroscopy: Optimized setup and signal analysis for single-shot spectral referencing. *Rev. Sci. Instr.*, 81:113106, 2010.

[69] G. Cerullo and S. De Silvestri. Ultrafast optical parametric amplifiers. *Rev. Sci. Instr.*, 74:1–18, 2003.

[70] J. Piel, M. Beutter, and E. Riedle. 20–50 fs pulses tunable acrosss the near infrared from a blue-pumped noncollinear parametric amplifier. *Opt. Lett.*, 25:180–182, 2000.

[71] G. Cerullo, M. Nisoli, S. Stagira, and S. De Silvestri. Sub-8-fs pulses from an ultrabroadband optical parametric amplifier in the visible. *Opt. Lett.*, 23:1283–1285, 1998.

[72] T. Kobayashi and A. Shirakawa. Sub-10-fs tunable pulses in visible and nir and visible sub-5-fs pulses generated by noncollinear opa. *J. Luminesc.*, 87–89:119–120, 2000.

[73] T. Kobayashi and A. Shirakawa. Tunable visible and near-infrared pulse generator in a 5 fs regime. *Appl. Phys. B*, 70:239–246, 2000.

[74] A. Shirakawa, I. Sakane, M. Takasaka, and T. Kobayashi. Sub-5-fs visible pulse generation by pulse-front matched noncollinear optical parametric amplification. *App. Phys. Lett.*, 74:2268–2271, 1999.

[75] S. Shim and R. A. Mathies. Generation of narrow-bandwidth picosedond visible pulses from broadband femtosecond pulses for femtosecond stimulated raman. *Appl. Phys. Lett.*, 89:121124–1–3, 2006.

[76] I. Szundi, J. W. Lewis, and D. S. Kliger. Deriving reaction mechanisms from kinetic spectroscopy. application to late rhodopsin intermediates. *Biophys. J.*, 73: 688–702, 1997.

[77] J. Zhao, M. M. Carrabba, and F. S. Allen. Automated fluorescence rejection using shifted excitation raman difference spectroscopy. *Appl. Spectrosc.*, 56:834–845, 2002.

[78] P. Matousek, M. Towrie, and A. W. Parker. Simple reconstruction algorithm for shifted excitation raman difference spectroscopy. *Appl. Spectrosc.*, 59:848–851, 2005.

[79] A. P. Shreve, N. J. Cherepy, and R. A. Mathies. Effective rejection of fluorescence interference in raman spectroscopy using a shifted excitation difference technique. *Appl. Spectr.*, 46:707–711, 1992.

[80] D. W. McCamant, P. Kukura, S. Yoon, and r. A. Mathies. Femtosecond broadband stimulated raman spectroscopy: Apparatus and methods. *Rev. Sci. Instr.*, 75: 4971–4980, 2004.

[81] P. J. Steinbach, R. Ionescu, and C. R. Matthews. Analysis of kinetics using a hybrid maximum-entropy/nonlinear-least-squares method: Application to protein folding. *Biophys. J.*, 82:2244–2255, 2002.

[82] C. Dugave and L. Demange. Cis-trans isomerization of organic molecules and biomolecules: Implications and applications. *Chem. Rev.*, 103:2475–2532, 2003.

[83] M. A. van der Horst and K. J. Hellingwerf. Photoreceptor proteins, "star actors of modern times": A review of the functional dynamics in the structure of representative members of six different photoreceptor families. *Acc. Chem. Res.*, 37:13–20, 2004.

[84] G. Likhtenshtein. *Stilbenes: Applications in Chemistry, Life Sciences and Materials Science*. Wiley-Vch, 1st edition, 2009.

[85] J. Saltiel, A. S. Waller, and D. F. Sears. Dynamics of *cis*-stilbene photoisomerization — the adiabatic pathway to excited *trans*-stilbene. *J. Photochem. Photobiol. A*, 65:29–40, 1992.

[86] J. A. Syage, P. M. Felker, and A. H. Zewail. Picosecond dynamics and photoisomerization of stilbene in supersonic beams. 2. reaction rates and potential energy surface. *J. Chem. Phys.*, 81:4706–4723, 1984.

[87] S. A. Kovalenko, A. L. Dobryakov, I. Ioffe, and N. P. Ernsting. Evidence for the phantom state in photoinduced cis-trans isomerization of stilbene. *Chem. Phys. Lett.*, 493:255–258, 2010.

[88] G. Rothenberger, D. K. Negus, and R. M. Hochstrasser. Solvent influence on photo-isomerization dynamics. *J. Chem. Phys.*, 79:5360–5367, 1983.

[89] S. H. Courtney, M. W. Balk, L. A. Philips, S. P. Webb, D. Yang, D. H. Levy, and G. R. Fleming. Unimolecular reactions in isolated and collisional systems — deuterium-isotope effect in the photoisomerization of stilbene. *J. Chem. Phys.*, 89: 6697–6707, 1988.

[90] M. Sumitani, N. Nakashima, and K. Yoshihara. Direct measurement of the reaction rate for cis-trans photoisomerization of stilbene. *Chem. Phys. Lett.*, 68:255–257, 1979.

[91] S. Abrash, S. Repinec, and R. M. Hochstrasser. The viscosity dependence and reaction coordinate for isomerization of *cis*-stilbene. *J. Chem. Phys.*, 93:1041–1053, 1990.

[92] R. J. Sension, S. T. Repinec, A. Z. Szarka, and R. M. Hochstrasser. Femtosecond laser studies of the *cis*-stilbene photoisomerization reactions. *J. Chem. Phys.*, 98: 6291–6315, 1993.

[93] D. C. Todd and G. R. Fleming. *Cis*-stilbene isomerization — temperature-dependence and the role of mechanical friction. *J. Chem. Phys.*, 98:269–279, 1993.

[94] S. T. Repinec, R. J. Sension, A. Z. Szarka, and R. M. Hochstrasser. Femtosecond laser studies of the *cis*-stilbene photoisomerization reactions — the *cis*-stilbene to dihydrophenanthrene reaction. *J. Phys. Chem. A*, 95:10380–10385, 1991.

[95] K. Ohmori. Wave-packet and coherent control dynamics. *Ann. Rev. Phys. Chem.*, 60:487–511, 2009.

[96] Y. Silberberg. Quantum coherent control for nonlinear spectroscopy and microscopy. *Ann. Rev. Phys. Chem.*, 60:277–292, 2009.

[97] M. Gruebele. Quantum dynamics and control of vibrational dephasing. *J. Phys.-Condens. Mat.*, 16:R1057–R1088, 2004.

[98] M. Greenfield, S. D. McGrane, and D. S. Moore. Control of *cis*-stilbene photochemistry using shaped ultraviolet pulses. *J. Phys. Chem. A*, 113:2333–2339, 2009.

[99] S. D. McGrane, R. J. Scharff, M. Greenfield, and D. S. Moore. Coherent control of multiple vibrational excitations for optimal detection. *New J. Phys.*, 11:105047, 2009.

[100] S. Takeuchi, S. Ruhman, T. Tsuneda, M. Chiba, T. Taketsugu, and T. Tahara. Spectroscopic tracking of structural evolution in ultrafast stilbene photoisomerization. *Science*, 322:1073–1077, 2008.

[101] L. Nikowa, D. Schwarzer, J. Troe, and J. Schroeder. Viscosity and solvent dependence of low-barrier processes — photoisomerization of *cis*-stilbene in compressed liquid solvents. *J. Chem. Phys.*, 97:4827–4835, 1992.

[102] K. Iwata and H. Hamaguchi. Vibrational cooling kinetics of s_1 *trans*-stilbene in sodium dodecyl sulfate micellar solution observed with picosecond time-resolved resonance raman spectroscopy. *J. Raman Spectrosc.*, 29:915–918, 1998.

[103] K. Iwata and H. O. Hamaguchi. Solute-solvent energy transfer and cooling kinetics of photoexcited s_1 *trans*-stilbene probed with picosecond raman spectroscopy: Comparison between chloroform and chloroform-d solutions. *Laser Chem.*, 19: 367–370, 1999.

[104] K. Iwata, R. Ozawa, and H. O. Hamaguchi. Analysis of the solvent- and temperature-dependent raman spectral changes of s_1 *trans*-stilbene and the mechanism of the trans to cis isomerization: Dynamic polarization model of vibrational dephasing and the c=c double-bond rotation. *J. Phys. Chem. A*, 106(14):3614–3620, 2002.

[105] K. Iwata, K. Yoshida, Y. Takada, and H. O. Hamaguchi. Vibrational cooling process of s_1 *trans*-stilbene in ionic liquids observed with picosecond time-resolved raman spectroscopy. *Chem. Lett.*, 36:504–505, 2007.

[106] R. E. Hester, P. Matousek, J. N. Moore, A. W. Parker, W. T. Toner, and M. Towrie. Vibrational mode-selective effects in the picosecond time-resolved resonance raman-spectrum of singlet excited *trans*-stilbene. *Chem. Phys. Lett.*, 208: 471–478, 1993.

[107] P. Matousek, A. W. Parker, W. T. Toner, M. Towrie, D. L. A. Defaria, R. E. Hester, and J. N. Moore. The anti-stokes resonance raman-spectrum of photoexcited s_1 *trans*-stilbene. *Chem. Phys. Lett.*, 237:373–379, 1995.

[108] H. Hamaguchi and K. Iwata. Exchange model of vibrational dephasing in s_1 *trans*-stilbene in solution and its possible correlation with the isomerization reaction. *Chem. Phys. Lett.*, 208:465–470, 1993.

[109] H. O. Hamaguchi. Solvent-induced dynamic polarization and vibrational dephasing of electronically excited molecules. *Mol. Phys.*, 89:463–471, 1996.

[110] V. Deckert, K. Iwata, and H. Hamaguchi. The exchange polarization model of photoisomerization: A rationale for profound solvent effects on photoisomerization of trans-stilbene and *all-trans* retinal. *J. Photochem. Photobiol. A*, 102:35–38, 1996.

[111] W. M. Kwok, C. Ma, D. Phillips, A. Beeby, T. B. Marder, R. L. Thomas, C. Tschuschke, G. Baranovic, P. Matousek, M. Towrie, and A. W. Parker. Time-resolved resonance raman study of s_1 *cis*-stilbene and its deuterated isotopomers. *J. Raman Spectrosc.*, 34:886–891, 2003.

[112] P. Matousek, A. W. Parker, D. Phillips, G. D. Scholes, W. T. Toner, and M. Towrie. A picosecond time-resolved resonance raman study of s_1 *cis*-stilbene. *Chem. Phys. Lett.*, 278:56–62, 1997.

[113] T. Elsaesser and W. Kaiser. Vibrational and vibronic relaxation of large polyatomic molecules in liquids. *Ann. Rev. Phys. Chem.*, 42:83–107, 1991.

[114] J. S. Baskin, L. Banares, S. Pedersen, and A. H. Zewail. Femtosecond real-time probing of reactions. 20. dynamics of twisting, alignment, and ivr in the *trans*-stilbene isomerization reaction. *J. Phys. Chem. A*, 100:11920–11933, 1996.

[115] A. Sakamoto, F. Tanaka, M. Tasumi, H. Torii, K. Kawato, and K. Furuya. Comparison of the raman spectrum of *trans*-stilbene in the s_1 state calculated by the cis method and the spectra observed under resonant and off-resonant conditions. *Vibr. Spectr.*, 42:176–182, 2006.

[116] H. Hamaguchi, T. Urano, and M. Tasumi. Transient resonance raman spectra and vibrational assignments of the s_1 state of *trans*-stilbene and its deuterated analogs. *Chem. Phys. Lett.*, 106:153–156, 1984.

[117] T. L. Gustafson, D. M. Roberts, and D. A. Chernoff. The structure of electronic excited states in *trans*-stilbene — picosecond transient stokes and anti-stokes raman spectra. *J. Chem. Phys.*, 81:3438–3433, 1984.

[118] K. Tsumura, K. Furuya, A. Sakamoto, and M. Tasumi. Vibrational analysis of *trans*-stilbene in the excited singlet state by time-dependent density functional theory: Calculations of the raman, infrared, and fluorescence excitation spectra. *J. Raman Spectrosc.*, 39:1584–1591, 2008.

[119] J. Tatchen and E. Pollak. Ab initio spectroscopy and photoinduced cooling of the *trans*-stilbene molecule. *J. Chem. Phys.*, 128:164303, 2008.

[120] H. Watanabe, Y. Okamoto, K. Furuya, A. Sakamoto, and M. Tasumi. Vibrational analysis of *trans*-stilbene in the ground and excited singlet electronic states revisited. *J. Phys. Chem. A*, 106:3318–3324, 2002.

[121] T. Urano, M. Maegawa, K. Yamanouchi, and S. Tsuchiya. Vibrational level structure and intermode coupling of s_1-*trans*-stilbene as studied by laser-induced fluorescence spectroscopy in a supersonic free jet. *J. Phys. Chem. A*, 93:3459–3465, 1989.

[122] A. A. Heikal, J. S. Baskin, L. Banares, and A. H. Zewail. Structural effects on the isomerization dynamics of *trans*-stilbenes: Ivr, microcanonical reaction rates, and the nature of the transition state. *J. Phys. Chem. A*, 101:572–590, 1997.

[123] D. A. Long. *The Raman Effect: A Unified Treatment of the Theory of Raman Scattering by Molecules.* John Wiley & Sons, Ltd, Chichester, England, 2002.

[124] D.C Harris and M. D. Bertolucci. *Symmetry and Spectroscopy —An Introduction to Vibrational and Electronic Spectroscopy.* Dover Publications, New York, 1989.

[125] R. D. Mehlenbacher, B. Lyons, K. C. Wilson, Y. Du, and D. W. McCamant. Theoretical analysis of anharmonic coupling and cascading raman signals observed with femtosecond stimulated raman spectroscopy. *J. Chem. Phys.*, 131:244512, 2009.

[126] K. C. Wilson, B. Lyons, R. Mehlenbacher, R. Sabatini, and D. W. McCamant. Two-dimensional femtosecond stimulated raman spectroscopy: Observation of cascading raman signals in acetonitrile. *J. Chem. Phys.*, 131:214502, 2009.

[127] R. J. Sension, S. T. Repinec, and R. M. Hochstrasser. Femtosecond laser study of energy disposal in the solution phase isomerization of stilbene. *J. Chem. Phys.*, 93:9185–9188, 1990.

[128] M. L. Horng, J. A. Gardecki, A. Papazyan, and M. Maroncelli. Subpicosecond measurements of polar solvation dynamics — coumarin 153 revisited. *J. Phys. Chem. A*, 99:17311–17337, 1995.

[129] H. Okamoto. Picosecond infrared spectroscopy of electronically excited *trans*-stilbene in solution in the fingerprint region. *J. Phys. Chem. A*, 103:5852–5857, 1999.

[130] J. L. Perez-Lustres, F. Rodriguez-Prieto, M. Mosquera, T. A. Senyushkina, N. P. Ernsting, and S. A. Kovalenko. Ultrafast proton transfer to solvent: Molecularity and intermediates from solvation- and diffusion-controlled regimes. *J. Am. Chem. Soc.*, 129:5408–5418, 2007.

[131] K. Iwata, R. Ozawa, and H. O. Hamaguchi. Analysis of the solvent- and temperature-dependent raman spectral changes of s_1 *trans*-stilbene and the mechanism of the trans to cis isomerization: Dynamic polarization model of vibrational dephasing and the c=c double-bond rotation. *J. Phys. Chem. A*, 106:3614–3620, 2002.

[132] H. Hamaguchi. Picosecond solvation dynamics of s_1 *trans*-stilbene by nanosecond transient raman spectroscopy with optical depletion timing. *J. Chem. Phys.*, 89: 2587–2588, 1988.

[133] W. L. Weaver, L. A. Huston, K. Iwata, and T. L. Gustafson. Solvent-solute interactions probed by picosecond transient raman spectroscopy — mode-specific vibrational dynamics in s_1 *trans*-stilbene. *J. Phys. Chem.*, 96:8956–8961, 1992.

[134] V. Karunakaran, M. Pfaffe, I. Ioffe, T. Senyushkina, S. A. Kovalenko, R. Mahrwald, V. Fartzdinov, H. Sklenar, and N. P. Ernsting. Solvation oscillations and excited-state dynamics of 2-amino- and 2-hydroxy-7-nitrofluorene and its 2 '-deoxyriboside. *J. Phys. Chem. A*, 112:4294–4307, 2008.

[135] A. B. Myers and R. A. Mathies. Excited-state torsional dynamics of *cis*-stilbene from resonance raman intensities. *J. Chem. Phys.*, 81:1552–1558, 1984.

[136] A. B. Myers, M. O. Trulson, and R. A. Mathies. Quantitation of homogeneous and inhomogeneous broadening mechanisms in *trans*-stilbene using absolute resonance raman intensities. *J. Chem. Phys.*, 83:5000–5006, 1985.

[137] N. Kozich and W. Werncke. Influence of vibrational cooling on the time-dependence of stokes and anti-stokes resonance raman scattering. *J. Mol. Struct.*, 735:145–151, 2005.

[138] K. Venugopal, L. P. Lustres, L. Zhao, N. P. Ernsting, and O. Seitz. Large dynamic stokes shift of dna intercalation dye thiazole orange has contribution from a high-frequency mode. *J. Am. Chem. Soc.*, 128:2954, 2006.

[139] P. Hunt and M. A. Robb. Systematic control of photochemistry: The dynamics of photoisomerization of a model cyanine dye. *J. Am. Chem. Soc.*, 127:5720, 2005.

[140] L. G. S. Brooker and G. H. Keyes. Studies in the cyanine dye series. iii improvements in the 2'-cyanine condensation. *J. Am. Chem. Soc.*, 57:2488–2492, 1935.

[141] T. Yanai, D. P. Tew, and N. C. Handy. A new hybrid exchange-correlation functional using the coulomb-attenuating method (cam-b3lyp). *Chem. Phys. Lett.*, 393:51–57, 2004.

[142] M. J. G. Peach, T. Helgaker, P. Salek, T. W. Keal, O. B. Lutnaes, D. J. Tozer, and N. C. Handy. Assessment of a coulomb-attenuated exchange-correlation energy functional. *Phys. Chem. Chem. Phys.*, 8:558–562, 2006.

[143] J. Tomasi, B. Mennucci, and R. Cammi. Quantum mechanical continuum solvation models. *Chem. Rev.*, 105:2999–3093, 2005.

[144] R. Improta, V. Barone, G. Scalmani, and M. J. Frisch. A state-specific polarizable continuum model time dependent density functional theory method for excited state calculations in solution. *J. Chem. Phys.*, 125:054103, 2006.

[145] R. Improta, G. Scalmani, M. J. Frisch, and V. Barone. Toward effective and reliable fluorescence energies in solution by a new state specific polarizable continuum model time dependent density functional theory approach. *J. Chem. Phys.*, 127: 074504, 2007.

[146] F. Santoro, R. Improta, A. Lami, J. jBoino, and V. Barone. Effective method to compute franck-condon integrals for optical spectra of large molecules in solution. *J. Chem. Phys. B*, 126:084509, 2007.

[147] F. Santoro, A. Lami, R. Improta, and V. Barone. Effective method to compute vibrationally resolved optical spectra of large molecules in the gas phase and in solution. *J. Chem. Phys.*, 126:184102, 2007.

[148] F. Santoro, A. Lami, R. Improta, J. Bloino, and V. Barone. Effective method for the computation of optical spectra of large molecules at finite temperature including duschinsky and herzberg-teller effect: The q_x band of porphyrin as a case study. *J. Chem. Phys.*, 128:224311, 2008.

[149] F. Santoro. Fcclasses, a fortran 77 code, 2010. URL `http://village.ipcf.cnr.it`.

[150] A. Losi. Flavin-based blue-light photosensors: A photobiophysics update. *Photochem. Photobiol.*, 83:1283–1300, 2007.

[151] K. J. Hellingwerf. Key issues in the photochemistry and signalling-state formation of photosensor proteins. *J. Photochem. Photobiol.*, 54:94–102, 2000.

[152] T. Kottke, J. Heberle, D. Hehn, B. Dick, and P. Hegemann. Phot-lov1: Photocycle of a blue-light receptor domain from the green alga *Chlamydomonas reinhardtii*. *Biophys. J.*, 84:1192–1201, 2003.

[153] T. Kottke, B. Dick, R. Fedorov, I. Schlichting, R. Deutzmann, and P. Hegemann. Irreversible photoreduction of flavin in a mutated phot-lov1 domain. *Biochemistry*, 42:9854–9862, 2003.

[154] T. Kottke, P. Hegemann, B. Dick, and J. Heberle. The photochemistry of the light-, oxygen-, and voltage-sensitive domains in the algal blue light receptor phot. *Biopolymers*, 82:373–378, 2006.

[155] M. T. A. Alexandre, T. Domratcheva, C. Bonetti, L. J. G. W. van Wilderen, R. van Grondelle, M. L. Groot, K. J. Hellingwerf, and J. T. M. Kennis. Primary reactions of the lov2 domain of phototropin studied with ultrafast mid-infrared spectroscopy and quantum chemistry. *Biophys. J.*, 97:227–237, 2009.

[156] K. Ataka, P. Hegemann, and J. Heberle. Vibrational spectroscopy of an algal phot-lov1 domain probes the molecular changes associated with blue-light reception. *Biophys. J.*, 84:466–474, 2003.

[157] J. P. Bouly, E. Schleicher, M. Dionisio-Sese, F. Vandenbussche, D. Van Der Straeten, N. Bakrim, S. Meier, A. Batschauer, P. Galland, R. Bittl, and M. Ahmad. Cryptochrome blue light photoreceptors are activated through interconversion of flavin redox states. *J. Biol. Chem.*, 282:9383–9391, 2007.

[158] A. Berndt, T. Kottke, H. Breitkreuz, R. Dvorsky, S. Hennig, M. Alexander, and E. Wolf. A novel photoreaction mechanism for the circadian blue light photoreceptor drosophila cryptochrome. *J. Biol. Chem.*, 282:13011–13021, 2007.

[159] Y. T. Kao, C. Tan, S. H. Song, N. Ozturk, J. Li, L. J. Wang, A. Sancar, and D. P. Zhong. Ultrafast dynamics and anionic active states of the flavin cofactor in cryptochrome and photolyase. *J. Am. Chem. Soc.*, 130:7695–7701, 2008.

[160] J. Brazard, A. Usman, F. Lacombat, C. Ley, M. M. Martin, P. Plaza, L. Mony, M. Heijde, G. Zabulon, and C. Bowler. Spectro-temporal characterization of the photoactivation mechanism of two new oxidized cryptochrome/photolyase photoreceptors. *J. Am. Chem. Soc.*, 132:4935–4945, 2010.

[161] K. Hasegawa, S. Masuda, and T. Ono. Structural intermediate in the photocycle of a bluf (sensor of blue light using fad) protein slr1694 in a cyanobacterium synechocystis sp pcc6803. *Biochemistry*, 43:14979–14986, 2004.

[162] S. Masuda, K. Hasegawa, A. Ishii, and T. Ono. Light-induced structural changes in a putative blue-light receptor with a novel fad binding fold sensor of blue-light

using fad (bluf); slr1694 of synechocystis sp pcc6803. *Biochemistry*, 43:5304–5313, 2004.

[163] P. Zirak, A. Penzkofer, C. Lehmpfuhl, T. Mathes, and P. Hegemann. Absorption and emission spectroscopic characterization of blue-light receptor slr1694 from synechocystis sp pcc6803. *J. Photochem. Photobiol. B*, 86:22–34, 2007.

[164] M. Unno, R. Sano, S. Masuda, T. A. Ono, and S. Yamauchi. Light-induced structural changes in the active site of the bluf domain in appa by raman spectroscopy. *J. Phys. Chem. B*, 109:12620–12626, 2005.

[165] C. Bonetti, T. Mathes, I. H. M. van Stokkum, K. M. Mullen, M. L. Groot, R. van Grondelle, P. Hegemann, and J. T. M. Kennis. Hydrogen bond switching among flavin and amino acid side chains in the bluf photoreceptor observed by ultrafast infrared spectroscopy. *Biophys. J.*, 95:4790–4802, 2008.

[166] M. Gauden, J. S. Grinstead, W. Laan, H. M. van Stokkum, M. Avila-Perez, K. C. Toh, R. Boelens, R. Kaptein, R. van Grondelle, K. J. Hellingwerf, and J. T. M. Kennis. On the role of aromatic side chains in the photoactivation of bluf domains. *Biochemistry*, 46:7405–7415, 2007.

[167] M. Gauden, I. H. M. van Stokkum, J. M. Key, D. C. Luhrs, R. Van Grondelle, P. Hegemann, and J. T. M. Kennis. Hydrogen-bond switching through a radical pair mechanism in a flavin-binding photoreceptor. *P. Natl. Acad. Sci. USA*, 103: 10895–10900, 2006.

[168] J. TM. Kennis and M.-L. Groot. Ultrafast spectroscopy of biological photoreceptors. *Curr. Opinion Struct. Biol.*, 17:623–630, 2007.

[169] A. L. Stelling, K. L. Ronayne, J. Nappa, P. J. Tonge, and S. R. Meech. Ultrafast structural dynamics in bluf domains: Transient infrared spectroscopy of appa and its mutants. *J. Am. Chem. Soc.*, 129:15556–15564, 2007.

[170] R. Takahashi, K. Okajima, H. Suzuki, H. Nakamura, M. Ikeuchi, and T. Noguchi. Ftir study on the hydrogen bond structure of a key tyrosine residue in the flavin-binding blue light sensor tepixd from thermosynechococcus elongatus. *Biochemistry*, 46:6459–6467, 2007.

[171] H. Yuan, S. Anderson, S. Masuda, V. Dragnea, K. Moffat, and C. Bauer. Crystal structures of the synechocystis photoreceptor slr1694 reveal distinct structural states related to signaling. *Biochemistry*, 45:12687–12694, 2006.

[172] K. H. Dudley, A. Ehrenberg, P. Hemmerich, and F. Müller. Spektren und strukturen der am flavin-redoxsystem beteiligten partikeln. *Helv. Chim. Act.*, 47:1354–1383, 1964.

[173] G. F. Li and K. D.n Glusac. Light-triggered proton and electron transfer in flavin cofactors. *J. Phys. Chem. A*, 112:4573–4583, 2008.

[174] C. Neiss and P. Saalfrank. Ab initio quantum chemical investigation of the first steps of the photocycle of phototropin: A model study. *Photochem. Photobiol.*, 77: 101–109, 2003.

[175] E. Sikorska, I. Khmelinskii, A. Komasa, J. Koput, L. F. V. Ferreira, J. R. Herance, J. L. Bourdelande, S. L. Williams, D. R. Worrall, M. Insinska-Rak, and M. Sikorski. Spectroscopy and photophysics of flavin related compounds: Riboflavin and *iso*-(6,7)-riboflavin. *Chem. Phys.*, 314:239–247, 2005.

[176] T. Climent, R. Gonzalez-Luque, M. Merchan, and L. Serrano-Andres. Theoretical insight into the spectroscopy and photochemistry of isoalloxazine, the flavin core ring. *J. Phys. Chem. A*, 110:13584–13590, 2006.

[177] S. Salzmann, V. Martinez-Junza, B. Zorn, S. E. Braslavsky, M. Mansurova, C. M. Marian, and W. Gartner. Photophysical properties of structurally and electronically modified flavin derivatives determined by spectroscopy and theoretical calculations. *J. Phys. Chem. A*, 113:9365–9375, 2009.

[178] H. A. Harbury, K. F. Lanoue, P. A. Loach, and R. M. Amick. Molecular interaction of isoalloxazine derivatives 2. *P. Natl. Acad. Sci. USA*, 45:1708–1717, 1959.

[179] R. J. Stanley and H. Jang. Electronic structure measurements of oxidized flavins and flavin complexes using stark-effect spectroscopy. *J. Phys. Chem. A*, 103:8976–8984, 1999.

[180] A. Weigel, A. L. Dobryakov, M. Veiga, and J. L. P. Lustres. Photoinduced processes in riboflavin: Superposition of $\pi\pi^*$-nπ^* states by vibronic coupling, transfer of vibrational coherence, and population dynamics under solvent control. *J. Phys. Chem. A*, 112:12054–12065, 2008.

[181] V. N. Petushkov, I. H. M. van Stokkum, B. Gobets, F. van Mourik, J. Lee, R. van Grondelle, and A. J. W. G. Visser. Ultrafast fluorescence relaxation spectroscopy of 6,7-dimethyl-(8-ribityl)-lumazine and riboflavin, free and bound to antenna proteins from bioluminescent bacteria. *J. Phys. Chem. B*, 107:10934–10939, 2003.

[182] P. Drössler, W. Holzer, A. Penzkofer, and P. Hegemann. ph dependence of the absorption and emisssion behaviour of riboflavin in aqueous solution. *Chem. Phys.*, 282:429–439, 2002.

[183] S. D. M. Islam, A. Penzkofer, and P. Hegemann. Quantum yield of triplet formation of riboflavin in queous solution and of flavin mononucleotide bound to the lov1 domain of phot1 from *Chlamydomonas reinhardtii*. *Chem. Phys.*, 291:97–114, 2003.

[184] P. Drössler, W. Holzer, A. Penzkofer, and P. Hegemann. Fluorescence quenching of riboflavin in aqueous solution by methionin and cystein. *Chem. Phys.*, 286: 409–420, 2003.

[185] G. Porcal, S. G. Bertolotti, C. M. Previtah, and M. V. Encinas. Electron transfer quenching of singlet and triplet excited states of flavins and lumichrome by aromatic and aliphatic electron donors. *Phys. Chem. Chem. Phys.*, 5:4123–4128, 2003.

[186] A. Penzkofer, A. K. Bansal, S. H. Song, and B. Dick. Fluorescence quenching of flavins by reductive agents. *Chem. Phys.*, 336:14–21, 2007.

[187] N. Mataga, H. Chosrowjan, Y. Shibata, and F. Tanaka. Ultrafast fluorescence quenching dynamics of flavin chromophores in protein nanospace. *J. Phys. Chem. B*, 102:7081–7084, 1998.

[188] N. Mataga, H. Chosrowjan, Y. Shibata, F. Tanaka, Y. Nishina, and K. Shiga. Dynamics and mechanisms of ultrafast fluorescence quenching reactions of flavin chromophores in protein nanospace. *J. Phys. Chem. B*, 104:10667–10677, 2000.

[189] N. Mataga, H. Chosrowjan, S. Taniguchi, F. Tanaka, N. Kido, and M. Kitamura. Femtosecond fluorescence dynamics of flavoproteins: Comparative studies on flavodoxin, its site-directed mutants, and riboflavin binding protein regarding ultrafast electron transfer in protein nanospaces. *J. Phys. Chem. B*, 106:8917–8920, 2002.

[190] R. J. Stanley and A. W. MacFarlane. Ultrafast excited state dynamics of oxidized flavins: Direct observations of quenching by purines. *J. Phys. Chem. A*, 104: 6899–6906, 2000.

[191] P. A. W. van den Berg, K. A. Feenstra, A. E. Mark, H. J. C. Berendsen, and A. J. W. G. Visser. Dynamic conformations of flavin adenine dinucleotide: Simulated molecular dynamics of the flavin cofactor related to the time-resolved fluorescence characteristics. *J. Phys. Chem. B*, 106:8858–8869, 2002.

[192] J. R. Barrio, G. L. Tolman, N. J. Leonard, R. D. Spencer, and G. Weber. Flavin 1, n-6 ethenoadenine dinucleotide — dynamic and static quenching of fluorescence. *P. Natl. Acad. Sci. USA*, 70:941–943, 1973.

[193] M. Grininger, F. Seiler, K. Zeth, and D. Oesterhelt. Dodecin sequesters fad in closed conformation from the aqueous solution. *J. Mol. Biol.*, 364:561–566, 2006.

[194] M. Raszka and N. O. Kaplan. Intramolecular hydrogen-bonding in flavin adenine dinucleotide. *P. Natl. Acad. Sci. USA*, 71:4546–4550, 1974.

[195] H. Chosrowjan, S. Taniguchi, N. Mataga, F. Tanaka, and A. J. W. G. Visser. The stacked flavin adenine dinucleotide conformation in water is fluorescent on picosecond timescale. *Chem. Phys. Lett.*, 378:354–358, 2003.

[196] G. F. Li and K. D. Glusac. The role of adenine in fast excited-state deactivation of fad: A femtosecond mid-ir transient absorption study. *J. Phys. Chem. B*, 113: 9059–9061, 2009.

[197] S. Stob, J. Kemmink, and R. Kaptein. Intramolecular electron-transfer in flavin adenine dinucleotide — photochemically induced dynamic nuclear-polarization study at high and low magnetic fields. *J. Am. Chem. Soc.*, 111:7036–7042, 1989.

[198] M. M. N. Wolf, C. Schumann, R. Gross, T. Domratcheva, and R. Diller. Ultrafast infrared spectroscopy of riboflavin: Dynamics, electronic structure, and vibrational mode analysis. *J. Phys. Chem. B*, 112:13424–13432, 2008.

[199] M. Kondo, J. Nappa, K. L. Ronayne, A. L. Stelling, P. J. Tonge, and S. R. Meech. Ultrafast vibrational spectroscopy of the flavin chromophore. *J. Chem. Phys. B*, 110:20107–20110, 2006.

[200] A. Weigel and N. P. Ernsting. Excited stilbene: Intramolecular vibrational redistribution and solvation studied by femtosecond stimulated raman spectroscopy. *J. Phys. Chem. B*, 114:7879–7893, 2010.

[201] M. Abe, Y. Kyogoku, T. Kitagawa, K. Kawano, N. Ohishi, A. Takai-Suzuki, and K. Yagi. lnfrared spectra and molecular association of lumiflavin and riboflavin derivatives. *Spec. Acta Part A: Mol. Spec.*, 42:1059 – 1068, 1986.

[202] M. Abe and Y. Kyogoku. Vibrational analysis of flavin derivatives: Normal coordinate treatments of lumiflavin. *Spec. Acta Part A: Mol. Spec.*, 43:1027–1037, 1987.

[203] B. Klaumünzer, D. Kröner, and P. Saalfrank. (td-)dft calculation of vibrational and vibronic spectra of riboflavin in solution. *J. Phys. Chem. B*, 114:10826–10834, 2010.

[204] A. Mühlpfordt, R. Schanz, N. P. Ernsting, V. Farztdinov, and S. Grimme. Coumarin 153 in the gas phase: optical spectra and quantum chemical calculations. *Phys. Chem. Chem. Phys.*, 1:3209–3218, 1999.

[205] C. Lee, W. Yang, and R. G. Parr. Development of the colle-salvetti correlation-energy formula into a functional of the electron density. *Phys. Rev. B*, 37:785–789, 1988.

[206] A. D. Becke. Density-functional thermochemistry. iii. the role of exact exchange. *J. Chem. Phys.*, 98:5648–5652, 1993.

[207] J. Andzelm N. Godbout, D. R. Salahub and E. Wimmer. Optimization of gaussian-type basis sets for local spin density functional calculations. part i. boron through neon, optimization technique and validation. *Can. J. Chem.*, 70:560–571, 1992.

[208] M. J. Frisch, G. W. Trucks, H. B. Schlegel, G. E. Scuseria, M. A. Robb, J. R. Cheeseman, G. Scalmani, V. Barone, B. Mennucci, G. A. Petersson, H. Nakatsuji, M. Caricato, X. Li, H. P. Hratchian, A. F. Izmaylov, J. Bloino, G. Zheng, J. L. Sonnenberg, M. Hada, M. Ehara, K. Toyota, R. Fukuda, J. Hasegawa, M. Ishida, T. Nakajima, Y. Honda, O. Kitao, H. Nakai, T. Vreven, Montgomery Jr. J. A.,

J. E. Peralta, F. Ogliaro, M. Bearpark, J. J. Heyd, E. Brothers, K. N. Kudin, V. N. Staroverov, R. Kobayashi, J. Normand, K. Raghavachari, A. Rendell, J. C. Burant, S. S. Iyengar, J. Tomasi, M. Cossi, N. Rega, J. M. Millam, M. Klene, J. E. Knox, J. B. Cross, V. Bakken, C. Adamo, J. Jaramillo, R. Gomperts, R. E. Stratmann, O. Yazyev, A. J. Austin, R. Cammi, C. Pomelli, J. W. Ochterski, R. L. Martin, K. Morokuma, V. G. Zakrzewski, G. A. Voth, P. Salvador, J. J. Dannenberg, S. Dapprich, A. D. Daniels, O. Farkas, J. B. Foresman, J. V. Ortiz, J. Cioslowski, and D. J. Fox. Gaussian 09 Revision A.02, 2009. Gaussian Inc. Wallingford CT 2009.

[209] S. Mertuš, E. Scrocco, and J. Tomasi. Electrostatic interaction of a solute with a continuum. direct utilization of ab initio molecular potentials for the prevision of solvent effects. *Chem.Phys.*, 55:117–129, 1981.

[210] G. Scalmani, M. J. Frisch, B. Mennucci, J. Tomasi, R. Cammi, and V. Barone. Geometries and properties of excited states in the gas phase and in solution: Theory and application of a time-dependent density functional theory polarizable continuum model. *J. Chem. Phys.*, 124:094107, 2006.

[211] D. J. Tannor and E. J. Heller. Polyatomic raman scattering for general harmonic potentials. *J. Chem. Phys.*, 77:202–218, 1982.

[212] Eric J. Heller. Time-dependent variational approach to semiclassical dynamics. *J. Chem. Phys.*, 64:63–73, 1976.

[213] Eric J. Heller. Time-dependent approach to semiclassical dynamics. *J. Chem. Phys.*, 62:1544–1555, 1975.

[214] T. Petrenko and F. Neese. Analysis and prediction of absorption band shapes, fluorescence band shapes, resonance raman intensities, and excitation profiles using the time-dependent theory of electronic spectroscopy. *J. Chem. Phys.*, 127:164319, 2007.

[215] Frank Neese. Orca 2.8, 2010. Universität Bonn.

[216] Karl Zenichowski, Marcel Gothe, and Peter Saalfrank. Exciting flavins: Absorption spectra and spin-orbit coupling in light-oxygen-voltage (lov) domains. *J. Photochem. Photobiol. A*, 190:290 – 300, 2007.

[217] K. Nishimoto, Y. Watanabe, and K. Yagi. Hydrogen-bonding of flavoprotein. 1. effect of hydrogen-bonding on electronic-spectra of flavoprotein. *Biochim. Biophys. Acta*, 526:34–41, 1978.

[218] T. B. Melo, M. A. Ionescu, G. W. Haggquist, and K. R. Naqvi. Hydrogen abstraction by triplet flavins. i: Time-resolved multi-channel absorption spectra of flash-irradiated riboflavin solutions in water. *Spectrochim. Acta Part A — Mol. Biomol. Spectrosc.*, 55:2299–2307, 1999.

[219] R. A. Copeland and T. G. Spiro. Ultraviolet resonance raman spectroscopyof flavin monocucleotide and flavin adenine dinucleotide. *J. Phys. Chem. A*, 90:6648–6654, 1986.

[220] W. D. Bowman and T. G. Spiro. Normal mode analysis of lumiflavin and interpretation of resonance raman spectra of flavoproteins. *Biochemistry*, 20:3313–3318, 1981.

[221] I. Hazekawa, Y. Nishina, K. Sato, M. Shichiri, R. Miura, and K. Shiga. A raman study on the c(4)=o stretching mode of flavins in flavoenzymes: Hydrogen bonding at the c(4)=o moiety. *J. Biochem. (Tokyo)*, 121:1147–1154, 1997.

[222] T. Kitagawa, Y. Nishina, Y. Kyogoku, T. Yamano, N. Ohishi, A. Takai-Suzuki, and K. Yagi. Resonance raman spectra of carbon-13-labeled and nitrogen-15-labeled riboflavin bound to egg-white flavoprotein. *Biochemistry*, 18:1804–1808, 1979.

[223] T. Kitagawa, Y. Nishina, K. Shiga, H. Watari, Y. Matsumura, and T. Yamano. Resonance raman evidence for charge-transfer interactions of phenols with the flavin mono-nucleotide of old yellow enzyme. *J. Am. Chem. Soc.*, 101:3376–3378, 1979.

[224] J. Schmidt, P. Coudron, A. W. Thompson, K. L. Watters, and J. T. McFarlandD. Hydrogen-bonding between flavin and protein — a resonance raman study. *Biochemistry*, 22:76–84, 1983.

[225] M. Kim and P. R. Carey. Observation of a carbonyl feature for riboflavin bound to riboflavin-binding protein in the red-excited raman spectrum. *J. Am. Chem. Soc.*, 115:7015–7016, 1993.

[226] G. Cerullo, L. Luer, C. Manzoni, S. De Silvestri, O. Shoshana, and S. Ruhman. Time-domain investigation of excited-state vibrational motion in organic molecules by stimulated emission pumping. *J. Phys. Chem. A*, 107:8339–8344, 2003.

[227] T. Hornung, H. Skenderovic, and M. Motzkus. Observation of *all-trans*-β-carotene wavepacket motion on the electronic ground and excited dark state using degenerate four-wave mixing (dfwm) and pump-dfwm. *Chem. Phys. Lett.*, 402:283–288, 2005.

[228] R. M. Bowman, M. Dantus, and A. H. Zewail. Femtosecond transition-state spectroscopy of iodine — from strongly bound to repulsive surface dynamics. *Chem. Phys. Lett.*, 161:297–302, 1989.

[229] J. Du, Z. Wang, W. Feng, K. Yoshino, and T. Kobayashi. Simultaneous measurement of electronic and vibrational dynamics to clarify a geometrical relaxation process in a conjugated polymer. *Physical Review B*, 77:195205, 2008.

[230] D. Schwarzer, J. Troe, and M. Zerezke. The role of local density in the collisional deactivation of vibrationally highly excited azulene in supercritical fluids. *J. Chem. Phys.*, 107:8380–8390, 1997.

[231] J. L. N. Lustres, S. A. Kovalenko, M. Mosquera, T. Senyushkina, W. Flasche, and N. P. Ernsting. Ultrafast solvation of n-methyl-6-quinolone probes local ir spectrum. *Angewandte Chemie-International Edition*, 44:5635–5639, 2005.

[232] N. P. Ernsting, J. Breffke, D. Y. Vorobyev, D. A. Duncan, and I. Pfeffer. Subpicosecond. fluorescence evolution of amino-cyano-stilbenes in methanol: polar solvation obeys continuum theory without evidence of twisting. *Phys. Chem. Chem. Phys.*, 10:2043–2049, 2008.

[233] A. Möglich, X. J. Yang, R. A. Ayers, and K. Moffat. Structure and function of plant photoreceptors. *Annual Review of Plant Biology, Vol 61*, 61:21–47, 2010.

[234] E. Silva and A. M. Edwards, editors. *Flavins: Photochemistry and Photobiology*. Royal Society of Chemistry, Cambridge, 1st edition, 2006.

[235] M. Gomelsky and G. Klug. Bluf: A novel fad-binding domain involved in sensory transduction in microorganisms. *Trends Biochem. Sci.*, 27:497–500, 2002.

[236] K. Okajima, Y. Fukushima, H. Suzuki, A. Kita, Y. Ochiai, M. Katayama, Y. Shibata, K. Miki, T. Noguchi, S. Itoh, and M. Ikeuchi. Fate determination of the flavin photoreceptions in the cyanobacterial blue light receptor tepixd (t110078). *J. Mol. Biol.*, 363:10–18, 2006.

[237] M. Gomelsky and S. Kaplan. Appa, a redox regulator of photosystem formation in rhodobacter sphaeroides 2.4.1, is a flavoprotein - identification of a novel fad binding domain. *J. Biol. Chem.*, 273:35319–35325, 1998.

[238] S. Braatsch, M. Gomelsky, S. Kuphal, and G. Klug. A single flavoprotein, appa, integrates both redox and light signals in *Rhodobacter sphaeroides*. *Mol. Microbiol.*, 45:827–836, 2002.

[239] M. Ntefidou, M. Iseki, M. Watanabe, M. Lebert, and D. P. Hader. Photoactivated adenylyl cyclase controls phototaxis in the flagellate euglena gracilis. *Plant Physiol.*, 133:1517–1521, 2003.

[240] T. R. M. Barends, E. Hartmann, J. J. Griese, T. Beitlich, N. V. Kirienko, D. A. Ryjenkov, J. Reinstein, R. L. Shoeman, M. Gomelsky, and I. Schlichting. Structure and mechanism of a bacterial light-regulated cyclic nucleotide phosphodiesterase. *Nature*, 459:1015–U150, 2009.

[241] A. Jung, T. Domratcheva, M. Tarutina, Y. Wu, W. Ko, R. L. Shoeman, M. Gomelsky, K. H. Gardner, and I. Schlichting. Structure of a bacterial bluf photoreceptor: Insights into blue light-mediated signal transduction. *Proc. Nat. Ac. Sci.*, 102: 12350–12355, 2005.

[242] A. Kita, K. Okajima, Y. Morimoto, M. Ikeuchi, and K. Miki. Structure of a cyanobacterial bluf protein, tll0078, containing a novel fad-binding blue light sensor domain. *J. Mol. Biol.*, 349:1–9, 2005.

[243] J. S. Grinstead, M. Avila-Perez, K. J. Hellingwerf, R. Boelens, and R. Kaptein. Light-induced flipping of a conserved glutamine sidechain and its orientation in the appa bluf domain. *J. Am. Chem. Soc.*, 128:15066–15067, 2006.

[244] S. Anderson, V. Dragnea, S. Masuda, J. Ybe, K. Moffat, and C. Bauer. Structure of a novel photoreceptor, the bluf domain of appa from rhodobacter sphaeroides. *Biochemistry*, 44:7998–8005, 2005.

[245] J. S. Grinstead, S. T. D. Hsu, W. Laan, A. M. J. J. Bonvin, K. J. Hellingwerf, R. Boelens, and R. Kaptein. The solution structure of the appa bluf domain: Insight into the mechanism of light-induced signaling. *ChemBioChem*, 7:187–193, 2006.

[246] C. Bonetti, M. Stierl, T. Mathes, I. H. M. van Stokkum, K. M. Mullen, T. A. Cohen-Stuart, R. van Grondelle, P. Hegemann, and J. T. M. Kennis. The role of key amino acids in the photoactivation pathway of the synechocystis slr1694 bluf domain. *Biochemistry*, 48:11458–11469, 2009.

[247] W. Laan, M. A. van der Horst, I. H. van Stokkum, and K. J. Hellingwerf. Initial characterization of the primary photochemistry of appa, a blue-light-using flavin adenine dinucleotide-domain containing transcriptional antirepressor protein from rhodobacter sphaeroides: A key role for reversible intramolecular proton transfer from the flavin adenine dinucleotide chromophore to a conserved tyrosine? *Photochem. Photobiol.*, 78:290–297, 2003.

[248] B. J. Kraft, S. Masuda, J. Kikuchi, V. Dragnea, G. Tollin, J. M. Zaleski, and C. E. Bauer. Spectroscopic and mutational analysis of the blue-light photoreceptor appa: A novel photocycle involving flavin stacking with an aromatic amino acid. *Biochemistry*, 42:6726–6734, 2003.

[249] Q. Wu, W. H. Ko, and K. H. Gardner. Structural requirements for key residues and auxiliary portions of a bluf domain. *Biochemistry*, 47:10271–10280, 2008.

[250] S. Masuda, K. Hasegawa, and T. Ono. Light-induced structural changes of apoprotein and chromophore in the sensor of blue light using fad (bluf) domain of appa for a signaling state. *Biochemistry*, 44:1215–1224, 2005.

[251] M. Gauden, S. Yeremenko, W. Laan, I. H. M. van Stokkum, J. A. Ihalainen, R. van Grondelle, K. J. Hellingwerf, and J. T. M. Kennis. Photocycle of the flavin-binding photoreceptor appa, a bacterial transcriptional antirepressor of photosynthesis genes. *Biochemistry*, 44:3653–3662, 2005.

[252] V. Dragnea, M. Waegele, S. Balascuta, C. Bauer, and B. Dragnea. Time-resolved spectroscopic studies of the appa blue-light receptor bluf domain from rhodobacter sphaeroides. *Biochemistry*, 44:15978–15985, 2005.

[253] M. Sakai and H. Takahashi. One-electron photoreduction of flavin mononucleotide: time-resolved resonance raman and absorption study. *J. Mol. Struc.*, 379:9–18, 1996.

[254] C. Aubert, M. H. Vos, P. Mathis, A. P. M. Eker, and K. Brettel. Intraprotein radical transfer during photoactivation of dna photolyase. *Nature*, 405:586–590, 2000.

[255] W. Holzer, A. Penzkofer, M. Fuhrmann, and P. Hegemann. Spectroscopic characterization of flavin mononucleotide bound to the lov1 domain of phot1 from *Chlamydomonas reinhardtii*. *Biochemistry*, 75:479–487, 2002.

[256] G. Wohlfahrt, S. Witt, J. Hendle, D. Schomburg, H. M. Kalisz, and H. J. Hecht. 1.8 and 1.9 angstrom resolution structures of the penicillium amagasakiense and aspergillus niger glucose oxidases as a basis for modelling substrate complexes. *Acta Crystallographica Section D-biological Crystallography*, 55:969–977, 1999.

[257] V. Leskovac, S. Trivic, G. Wohlfahrt, J. Kandrac, and D. Pericin. Glucose oxidase from aspergillus niger: the mechanism of action with molecular oxygen, quinones, and one-electron acceptors. *International Journal of Biochemistry & Cell Biology*, 37:731–750, 2005.

[258] J. Pan, M. Byrdin, C. Aubert, A. P. M. Eker, K. Brettel, and M. H. Vos. Excited-state properties of flavin radicals in flavoproteins: Femtosecond spectroscopy of dna photolyase, glucose oxidase, and flavodoxin. *J. Phys. Chem. B*, 108:10160–10167, 2004.

[259] R. H. Duurkens, M. B. Tol, E. R. Geertsma, H. P. Permentier, and D. J. Slotboom. Flavin binding to the high affinity riboflavin transproter ribu. *J. Biol. Chem.*, 282: 10380–10386, 2007.

Danksagung

Die vorliegende Arbeit entstand in der Zeit zwischen Februar 2006 und Dezember 2010 am Institut für Chemie der Humboldt-Universität zu Berlin in der Arbeitsgruppe von Prof. Nikolaus Ernsting. An dieser Stelle danke ich allen, die mich in dieser Zeit unterstützt haben.

Insbesondere danke ich *Prof. Nikolaus Ernsting* für das interessante Thema und die Betreuung meiner Doktorarbeit. Ich danke ihm für die Unterstützung dabei, selbstständige wissenschaftliche Arbeit zu entwickeln und Ideen experimentell zu verwirklichen.

Großer Dank gilt auch den anderen Mitgliedern der Arbeitsgruppe:

Dr. Luis Perez-Lustres für die Zusammenarbeit bei der Untersuchung von Flavin und flavinbasierten Photorezeptoren,
Dr. Sergey Kovalenko für die Unterstützung bei den zeitaufgelösten Messungen,
Dr. Alexander Dobryakov für die Simulationen der Ramansignale und die geduldigen Diskussionen über nichtlineare Optik,
Mohsen Sajadi Hezaveh und *Xinxing Zhang* für die Unterstützung bei den femtosekundenaufgelösten Fluoreszenzmessungen und für interessante Diskussionen,
Matthias Pfaffe und *Priv. Doz. Rainer Mahrwald* für die Synthese von 1,1'-Diethyl-2,2'-pyridocyaniniodid (PC),
Lars Dehmel für seine stete Hilfsbereitschaft,
Dr. Horst Hennig dafür, dass er sein Büro für das Schreiben dieser Arbeit zur Verfügung gestellt hat,
Heiderose Steingräber, *Iris Suter* und *Sabrina Penn* für das angenehme Klima und die administrative Unterstützung.

Für die Unterstützung bei den Messungen an biologischen Photorezeptoren und die Anstellung zu Beginn meiner Doktorarbeit danke ich *Prof. Peter Hegemann*. Für die Bereitstellung der Proben und die Hilfestellung bei der Handhabung danke ich *Dr. Tilo Mathes*.

Weiterhin danke ich

Bastian Klaumünzer und *Prof. Peter Saalfrank* für die quanten-chemischen Rechnungen an Flavin.
Prof. Fabrizio Santoro, *Dr. Roberto Improta* und *Prof. Vincenzo Barone* für die quanten-chemischen Rechnungen an PC.
Dr. Jens Lange für die Entwicklung der Elektronik für die transiente Absorption und

das Schneiden der Raman-Chopperscheibe,
Prof. Eberhard Riedle für hilfreiche Vorschläge für die Verwirklichung des *nb*-OPA.

Der experimentelle Teil dieser Arbeit hat sehr von der fachkundigen Unterstützung durch die Werkstätten profitiert. Ausdrücklich bedanke ich mich bei den Mitarbeitern der *feinmechanischen Werkstatt*, der *Elektronikwerkstatt* und der *feinoptischen Werkstatt* in Göttingen.

Für finanzielle Unterstützung dieser Arbeit bedanke ich mich bei

dem *Fonds der Chemischen Industrie* für ein Kekulé-Stipendium,
dem *Sonderforschungsbereich 450* "Analyse und Steuerung ultraschneller photoinduzierter Reaktionen",
dem *Exzellenzcluster 304* "Unifying Concepts in Catalysis", gefördert durch die Deutsche Forschungsgemeinschaft.

Bei *meinen Eltern* und bei *Alexandra Lauer* bedanke ich mich für die fortwährende Unterstützung.

Selbständigkeitserklärung

Ich erkläre, dass ich die vorliegende Arbeit selbständig und nur unter Verwendung der angegebenen Literatur und Hilfsmittel angefertigt habe.

Ich besitze keinen entsprechenden Doktorgrad und habe mich anderwärts nicht um einen Doktorgrad beworben.

Die dem Promotionsverfahren zugrundeliegende Promotionsordnung vom 1. September 2005 ist mir bekannt.

Berlin, den 23.12.2010 Alexander Weigel